Influence of neutral particles on edge dynamics of magnetically confined plasmas

Thrysøe, Alexander Simon

Publication date:
2018

Document Version
Publisher's PDF, also known as Version of record

Influence of neutral particles on edge dynamics of magnetically confined plasmas

Thesis submitted for the degree of
Doctor of Philosophy

Department of Physics
Technical University of Denmark

Technical University of Denmark

Alexander Simon Thrysøe

Influence of neutral particles on edge dynamics of magnetically confined plasmas

Supervisor: Prof. Volker Naulin

Co-supervisors: Prof. Jens Juul Rasmussen
Dr. Jens Madsen

Technical University of Denmark

Examiners:

Chairman:

Submitted to the Technical University of Denmark
on April 23rd 2018.

Abstract

Thermonuclear fusion of light atomic nuclei in future reactors promises a source of electric energy which is clean, safe, and sustainable. A propitious design for such reactor is the tokamak, in which hot plasma is suspended in a twisted toroidal magnetic field. The geometry of toroidal confinement results in turbulent transport of particles and heat from the confined bulk region radially outwards towards the first wall of the vacuum chamber. The plasma passes through the edge layer of the confined region, for which the conditions have been found to be defining for the overall plasma confinement. This makes the plasma edge a region of uttermost importance to understand, if energy from reactor based fusion is to be realized.

In the scrape-off layer (SOL) region, between the edge region and the first wall, plasma is transported outwards in field-aligned filaments. The SOL is characterized by open magnetic field lines which terminate on material surfaces, and it is significantly colder and less dense than the confined plasma. This allows for maintaining a considerable population of neutral particles. It has been experimentally observed that the presence of neutrals influences the conditions in the edge region. This makes the understanding of transport of neutrals and their interactions with the edge and SOL plasma equally important.

In this work a novel numerical model for describing the transport of neutral particles, in particular the interactions with the electrons and ions, is formulated. Both molecular and atomic neutral species are included in the model to account for various neutral-plasma interactions. The model for the neutrals is coupled to an existing drift-fluid model for edge and SOL plasma, and the combined model is applied in a series of studies on the effect of neutral interactions on the plasma and vice versa.

Particularly the relative roles of molecules and atoms in the plasma fuelling process, as well as the local effect that the field-aligned plasma filaments have on the neutral densities, are elucidated. The effect of the molecular puffing rate on the plasma turbulence characteristics is likewise investigated.

Keywords: Plasma-neutral interactions, plasma turbulence, neutral transport, drift-fluid equations, tokamak fuelling, numerical modelling

Resumé

Termonuklear fusion af lette atomkerner vil i fremtidige reaktorer kunne levere en kilde til elektrisk energi, som er ren, sikker og bæredygtig. Et lovende design for en sådan reaktor er den såkaldte tokamak, hvori varmt plasma er indesluttet af et snoet toroidalt magnetfelt. Den toroidale indeslutning resulterer i en turbulent transport af partikler og varme fra det indesluttede område radielt udad mod væggen af vakuum kammeret. Plasmaet passerer gennem det indesluttede plasmas randområde, for hvilket betingelserne er altafgørende for den overordnede plasma indeslutning. Dette gør randen af plasmaet til et område, som er meget vigtigt at forstå, hvis energi fra reaktorbaseret fusion skal realiseres.

I *scrape-off layer* (SOL) området, som findes mellem plasma-randen og reaktorvæggen, tranporteres plasma udad i filamenter, som strækker sig langs de magnetiske feltlinjer. SOL området er karakteriseret ved åbne magnetiske feltlinjer, som slutter på materialeoverflader, og dette område er signifikant koldere og mindre tæt end det indesluttede plasma volumen. Dette tillader for en anseelig bestand af ikke-ioniserede neutrale partikler at eksistere. Det er eksperimentelt observeret, at tilstedeværelsen af neutrale partikler kan påvirke betingelserne i plasma-rand området, hvilket gør forståelsen af transport af neutrale partikler, og deres vekselvirkning med rand- og SOL-plasmaet, tilsvarende vigtig.

I denne afhandling formuleres en ny numerisk model, som beskriver transporten af neutrale partikler, og i særdeleshed deres vekselvirkning med elektroner og ioner. Både neutrale molekyler og atomer er indeholdt i modellen, således at der tages højde for en række vekselvirkninger mellem neutrale- og plasmapartikler. Modellen for neutrale partikler er koblet til en eksisterende drift-fluid model for rand- og SOL-plasma, og den kombinerede model er anvendt i en række af studier af effekten af de neutrale partiklers påvirkning af plasmaet og omvendt.

Specielt er den relative rolle for molekyler og atomer i processen hvor partikler transporteres ind i det indesluttede område, samt den lokale effekt som plasmafilamenter har på tætheden af neutrale partikler, belyst. Ligeledes undersøges effekten af tilførselsraten af molekyler på karakteristikaene for plasmaturbulensen.

Acknowledgements

I would like to thank my supervisor Volker Naulin, and co-supervisors Jens Juul Rasmussen and Jens Madsen for guidance and support throughout this project. I appreciate the help and understanding that I have been met with on all matters. Our discussions and shared aim towards understanding the significance of neutral particles have been both educational and inspiring.

My gratitude extends to all members of the plasma physics and fusion energy group here at DTU. I would in particular like to thank Anders Henry Nielsen for his expertise on the HESEL model, Mirko Salewski from whom I initially learned about the Danish activities in fusion research, and Søren Bang Korsholm for providing me the opportunities to escape the office and disseminate our work to an audience beyond the fusion community.

I have been lucky to share the many highs and lows of the past years with a dynamical and gregarious group of office mates counting Asger Schou Jacobsen, Aslak Sindbjerg Poulsen, Bernhard Schießl, Galina Avdeeva, Jeppe Miki Busk Olsen, Mads Givskov Senstius, Michael Løiten Magnussen, and Søren Kjer Hansen. Of those Michael deserves special thanks for our many discussions on physics, his perpetual help solving my numerical issues, and for the friendship with him and his wife outside of work.

I would like to thank Cecilie Thrysøe, Kim Oskar Lewis, and Michael Løiten Magnussen for proofreading the manuscript of the thesis.

Last but not least I would like to thank my close friends and family for their support, interest, and understanding during the course of the project. The greatest of thanks, however, are due to my wife Cecilie with whom I have shared the most immense moments in the past years. My daily struggles with equations and numerics have been less disheartening knowing, that I get to spend my afternoons and evenings with you and our son.

Contents

Chapter 1

Introduction

This chapter provides an introduction to fusion energy in general and to selected generic topics which are of particular relevance to the main content of the thesis. In Section 1.1 research in fusion energy is motivated. A viable reactor design for energy production from fusion energy is the so-called tokamak, which confines fusion plasma magnetically and for which the principles are reviewed in Sec. 1.2. The edge region of the confined plasma has proved to be of particular interest, as it dictates the overall confinement properties of the device. Section 1.3 provides an overview of plasma transport near the edge region, in which there also is a significant population of neutral particles. The importance of understanding the interactions between neutral particles and plasma is stressed out in Sec. 1.4, which provides a short introduction to the various reasons for injecting neutrals and examples of how the neutrals may interact with the plasma. The structure of the remaining thesis is provided in Sec.1.5.

1.1 Fusion and society

To maintain the standard of living of today's society and also to allow for further growth due to increasing living standards and global population, energy has to be extracted from natural resources and converted into, e.g., electrical energy. Electric energy is generated either from intermittent sources such as wind or solar energy, or from base-load power plants, such as coal or nuclear

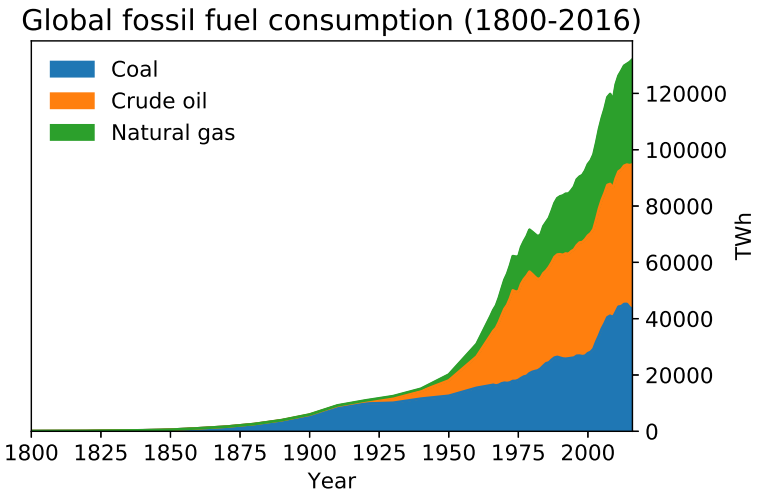

Figure 1.1: Long-term global consumption of primary fossil fuels measured in terawatt-hours (TWh). Data obtained from [1].

power plants. In 2016 the global energy consumption of fossil fuels, i.e., coal, crude oil, and natural gas, constituted 85.5 % of the total primary energy consumption that year [1]. The large-scale consumption of fossil fuels has contributed to allowing humanity to advance throughout the past centuries, due to its high mobility, energy density, and availability. The global fossil fuel consumption as a function of time is shown in Fig. 1.1.

However, combustion of fossil fuels results in emission of carbon-dioxide into the Earth's atmosphere. Carbon-dioxide is a greenhouse gas due to its effect on transfer of infra-red light through the atmosphere. It thus belongs to a group atmospheric gases of which the amounts have increased drastically since mid-20$^{\text{th}}$ century due to human activity. These gases are responsible for the current warming of Earth's climate system [2]. Although the long-term implications of the global warming are yet to be experienced, it is concluded in [2] that:

> *"Continued emission of greenhouse gases will cause further warming and long-lasting changes in all components of the climate system, increasing the likelihood of severe, pervasive and irreversible impacts for people and ecosystems. Limiting climate change would require substantial and sustained reductions in greenhouse gas emissions which, together with adaptation, can limit climate change risks."*

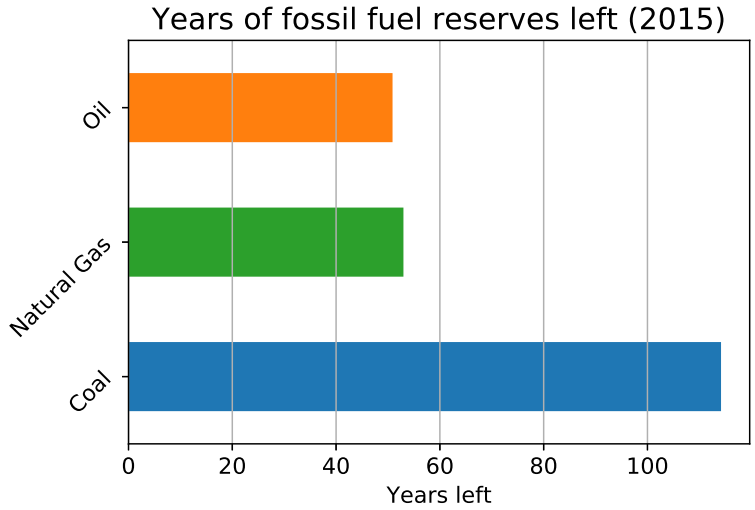

Figure 1.2: Remaining years of global reserves of primary fossil fuels. Data obtained from [1].

In addition to the effect of fossil fuel combustion on the global environment, the limited availability of fossil fuels is another reason to seek out alternative fuels. Best estimates on the amount of fossil fuel reserves are presented in Fig. 1.2, and it is evident, that even if global warming was not an issue, humanity would be facing a scarcity crisis as the World's fossil fuel reserves are to be depleted within this century.

The impact of fossil fuel combustion on the global environment, and the finiteness of this energy source present a great incentive to seek out alternative energy sources, which are more clean and renewable than fossil fuels. The remaining 14.5 % of the global primary energy consumption is constituted by energy sources, which do not pose the same disadvantages as the fossil fuels. Those include nuclear fission, hydroelectricity, solar, wind, and other renewable energy sources [1]. While providing clean and renewable sources, most of the alternatives to fossil fuels lack major advantages of fossil fuels, such as availability and high energy density. Of the above energy sources, only nuclear fission is applicable as a geographically independent base-load power source. The advantages of energy from nuclear fission are, however, tainted with historical accidents and public distrust [3]. Nuclear fission also produces long-lived radioactive waste from the fission process. Recent and future generations of nuclear fission power plants do, however, limit the issues of safety and radioactive waste of the older reactor models [4, 5].

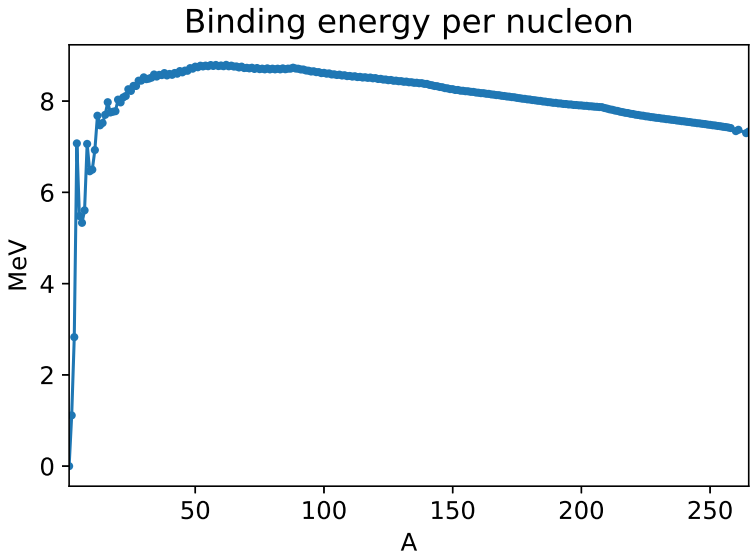

Figure 1.3: Experimentally measured binding energy per nucleon for common isotopes of nucleon number A. Data obtained from [6].

In fission power plants, heavy atomic nuclei are split into lighter nuclei accompanied by energetic neutrons and radiation. An example of a neutron-induced fission reaction is that of uranium-235,

$$ {}^{1}_{0}\mathrm{n} + {}^{235}_{92}\mathrm{U} \rightarrow {}^{139}_{56}\mathrm{Ba} + {}^{94}_{36}\mathrm{Kr} + 3\,{}^{1}_{0}\mathrm{n} + 177\,\mathrm{MeV}\,. \tag{1.1} $$

In Figure 1.3 the binding energy per nucleon is shown. It is observed, that moving from heavy nuclei with large values of nucleon number A to lighter nuclei (though heavier than iron), the binding energy per nucleon increases, which results in a release of energy. From Figure 1.3 it is likewise observed, that merging very light nuclei into heavier nuclei is another path for increasing the binding energy per nucleon and thus release energy. This process is known as nuclear fusion.

Nuclear fusion is the process that drives the stars. In the Sun (and other smaller stars) the dominant reaction chain is that of proton-proton fusion [7], where protons in a series of steps fuse into helium-4 nuclei. It is also possible to create the conditions for nuclear fusion in reactors. For the charged nuclei to fuse, their mutual Coulomb repulsion has to be overcome so that the distance of the nuclei is small enough for the strong nuclear force to dominate. This can be achieved in thermonuclear fusion, where the nuclei

are energized through heating processes, to obtain a temperature in the range of 150 million °C. Around this temperature one of the most viable reactor-relevant fusion processes, namely that of deuterium ${}^{2}_{1}\mathrm{D}$ and tritium ${}^{3}_{1}\mathrm{T}$, has the optimal conditions for energy production. The deuterium-tritium fusion process is

$$ {}^{2}_{1}\mathrm{D} + {}^{3}_{1}\mathrm{T} \rightarrow {}^{4}_{2}\mathrm{He} + {}^{1}_{0}\mathrm{n} + 17.6\,\mathrm{MeV}\,. \tag{1.2} $$

The released energy of 17.6 MeV is carried by the reaction products. The alpha particle has 3.5 MeV, and the neutron carries an energy of 14.1 MeV.

Deuterium is a stable isotope found in nature and accounts for approximately 0.0156 % of hydrogen in the oceans, from where it can be separated for by various techniques. Tritium, on the other hand, has a half-life of approximately 12.32 years and is thus required to be bred for fusion purposes. Present fusion power plant designs incorporate the breeding of tritium on-site, where interactions of the energetic neutron produced in the fusion reaction in (1.2) with ${}^{6}_{3}\mathrm{Li}$ allows for both energy dissemination and tritium production, without the need to transport radioactive fuel to the power plant [8]. It is estimated, that the World oceans hold enough deuterium for fusion energy to theoretically cover the global energy usage (at the current consumption rate) for tens of billions of years. Unlike nuclear fission power plants, the nuclear fusion reaction is not a chain reaction, and the risk of a reactor melt-down is thus absent.

The global need for a clean, safe, and sustainable energy source for base-load power plants has never been more urgent. With effectively limitless available fuel, no production of long-lived radioactive waste, no risk of reactor meltdown, and an enormous fuel energy density, application of future thermonuclear fusion reactors may be an important piece in the puzzle of reducing the future global greenhouse gas emissions. In the following chapter the design of such reactors, and some of the resulting engineering and physical issues that prevent fusion energy to be harnessed today, are presented.

1.2 Fusion plasmas and tokamaks

The temperature required for sustaining fusion reactions is much higher than what any material can tolerate. This poses an obvious challenge in finding a suitable container for the fusion processes to take place in. When the

fuel is heated to such extreme temperatures, it exists in the plasma state, where the charged electrons and ions are no longer bound in atoms. As charged particles interact with magnetic fields it is possible to construct a 'magnetic bottle', and thus prevent the bulk plasma from touching the first wall directly. The charged particles orbit the magnetic field lines, which in principle allows for confining the plasma in the plane perpendicular to the magnetic field. For the plasma to be confined parallel to the magnetic field, the field lines must end on themselves, or at least have a geometry which limits the amount of heat and particles that are transported along the open magnetic field lines and eventually terminate on material surfaces. The most researched magnetic confinement configuration traps the plasma in a toroidal magnetic field, which has a finite poloidal component as well, which is obtained by driving a current in the plasma. Such device is called tokamak.

The first tokamaks were tested in the late 1950s and 1960s at the Kurchatov Institute in Moscow. In 1968 the first ever quasi-stationary high-temperature plasma was achieved on the T-3 tokamak [9], with a measured temperature of over 1 keV. The breakthrough sparked the fusion research worldwide and resulted in conversion of existing experiments, as well as the construction of new large tokamak experiments, such as the Joint European Torus (JET) in Oxfordshire, UK. JET remains the World's largest operating tokamak. Its successor ITER is currently under construction in Cadarache, France. Although the tokamak design has been overall successful in confining plasmas at fusion conditions, there are still major challenges to overcome for the tokamak design to be truly victorious. Some of the most serious obstacles are caused by cross-field turbulent transport of heat and particles away from the confined region, and towards the first wall of the chamber. Cross-field transport is an important topic for this thesis in particular, and it is treated in Sec. 1.3. Before progressing to this topic, a general introduction to the tokamak design, and the conditions for what makes a 'good' confined plasma, are reviewed.

Figure 1.4 shows sketches of the design of a generic tokamak. Figure 1.4a depicts the toroidal field coils, which generate the toroidal magnetic field component that confines the plasma. The inner poloidal field coils function as a primary loop of a transformer and the plasma forms the secondary loop. This allows driving a toroidal current in the plasma, which results in a poloidal magnetic field component. The resulting field is helical, and effectively shorts out the upper and lower parts of the plasma volume, which for reasons that are explained in Sec. 1.3 is necessary for confining the plasma

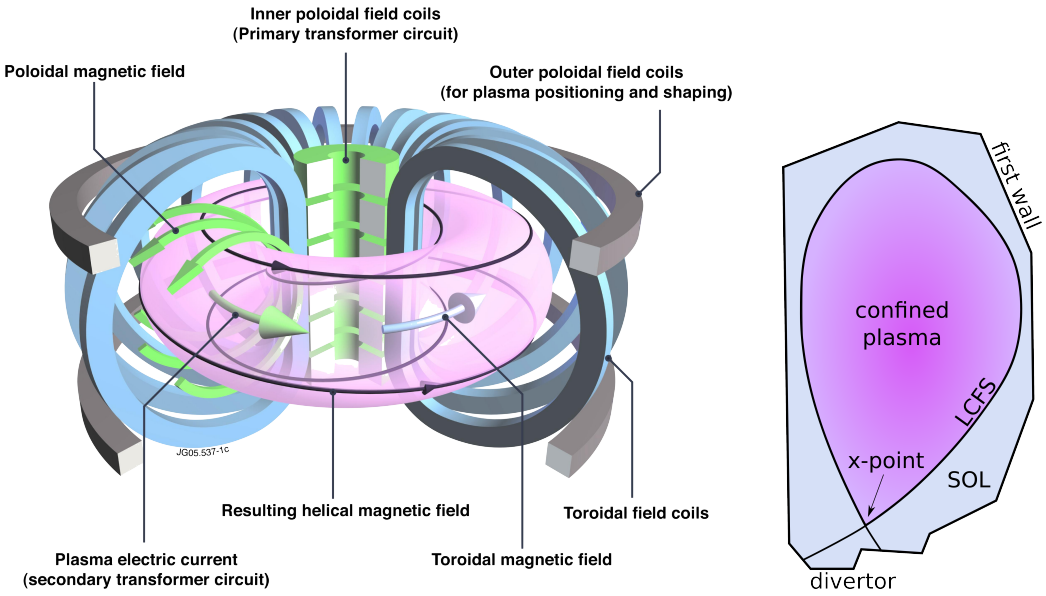

(a) (b)

Figure 1.4: (a) Simplified tokamak design, showing the machine main components, graphic obtained from [10]. (b) Cross-section of diverted confined plasma.

toroidally. In Figure 1.4b the cross-section of a diverted plasma is shown. In this geometry the SOL plasma is transported along the open magnetic field lines, and the majority of the energy is disposed onto the divertor plates which are more durable than the first wall. Diverted geometries have proved to yield higher energy confinement times than those for limited plasmas, in particular due to the enhanced removal of impurities [11].

The design of the device determines the plasma fields, and thus the overall performance of a tokamak. There are numerous parameters that enter this equation, such as materials, geometry, magnitude and shape of generated external fields, etc. It is, however, possible to formulate a generic criterion for generating a surplus of energy in a tokamak from fusion reactions. The following derivation is present in most introductory text books, such as [12]. Consider the parameter Q, defined by the ratio of the output power generated from fusion reactions P_{fusion} to the auxiliary power to the system required to sustain the plasma temperature P_{aux}

$$Q = \frac{P_{\text{fusion}}}{P_{\text{aux}}} \,. \tag{1.3}$$

At the $Q = 1$ state the reactor produces as much power as it consumes

and is said to break-even. Ideally the power from the fusion reactions can itself sustain the temperature, and thus $P_{\text{aux}} \to 0$, results in $Q \to \infty$. This state is denoted ignition. The highest value of Q obtained in experiments is $Q = 0.65$ at JET in 1997. The heating power required for obtaining ignition comes from the α-particles produced in (1.2) and is given by

$$P_\alpha = \tfrac{1}{5} P_{\text{fusion}} = n_{\text{D}} n_{\text{T}} \langle \sigma_{\text{fusion}} v \rangle E_\alpha V = \tfrac{1}{4} n_{\text{e}} \langle \sigma_{\text{fusion}} v \rangle E_\alpha V \,, \tag{1.4}$$

where $n_{\text{D}} = n_{\text{T}} = \frac{1}{2} n_{\text{e}}$ are the densities of deuterium, tritium and electrons, $\langle \sigma_{\text{fusion}} v \rangle$ is the reaction rate coefficient for fusion reactions, $E_\alpha = 3.5\,\text{MeV}$ is the energy of the produced α-particle, and V is the plasma volume. The plasma loses energy either to transport of particles, heat, and momentum, or to bremsstrahlung in the bulk volume. The power loss from the latter is given by

$$P_{\text{Brms}} = C_{\text{B}} T_{\text{e}}^{\frac{1}{2}} n_{\text{e}}^2 V \,, \tag{1.5}$$

where C_{B} is a constant independent of the plasma fields, and T_{e} is the electron temperature. The power loss due to transport (at steady state) is written as

$$P_{\text{trans}} = \frac{W}{\tau_{\text{E}}} \,, \tag{1.6}$$

where $W = 3 n_{\text{e}} k_{\text{B}} T_{\text{e}} V$ is the plasma thermal kinetic energy, k_{B} is the Boltzmann constant, and τ_{E} is the characteristic energy confinement time. Thus, at steady state the power balance is $P_\alpha + P_{\text{aux}} = P_{\text{Brms}} + P_{\text{trans}}$, which by combining Eqns. (1.3)-(1.6) yields

$$\left(\frac{5+Q}{4Q} \right) n_{\text{e}}^2 \langle \sigma_{\text{fusion}} v \rangle E_\alpha V = C_{\text{B}} T_{\text{e}}^{\frac{1}{2}} n_{\text{e}}^2 V + \frac{3 n_{\text{e}} k_{\text{B}} T_{\text{e}} V}{\tau_{\text{E}}} \,. \tag{1.7}$$

The equation is readily rewritten to a more convenient form yielding the product of the electron density and the confinement time

$$n_{\text{e}} \tau_{\text{E}} = \frac{3 k_{\text{B}} T_{\text{e}}}{\frac{(5+Q)\langle \sigma_{\text{fusion}} v \rangle E_\alpha}{4Q} - C_{\text{B}} T_{\text{e}}^{\frac{1}{2}}} \,, \tag{1.8}$$

known as the Lawson criterion [13]. It is common to augment the Lawson criterion with the energy transformation efficiency η of the device, which is usually assumed to be $\eta = \frac{1}{3}$ following [14], and which result in

$$n_{\text{e}} \tau_{\text{E}} = \frac{3\,(1-\eta)\, k_{\text{B}} T_{\text{e}}}{\eta \frac{(5+Q)\langle \sigma_{\text{fusion}} v \rangle E_\alpha}{4Q} - C_{\text{B}}\,(1-\eta)\, T_{\text{e}}^{\frac{1}{2}}} \,. \tag{1.9}$$

The optimal conditions for D-T break-even is at $T_\mathrm{e} \approx 15\,\mathrm{keV}$, and that for ignition is $T_\mathrm{e} \approx 30\,\mathrm{keV}$, for which the Lawson criterion (1.9) becomes

$$\begin{aligned} n_\mathrm{e}\tau_\mathrm{E} &\approx 1.0 \cdot 10^{20}\,\mathrm{m}^{-3}\mathrm{s}\,, \quad \text{for} \quad Q = 1\,, \\ n_\mathrm{e}\tau_\mathrm{E} &\approx 2.7 \cdot 10^{20}\,\mathrm{m}^{-3}\mathrm{s}\,, \quad \text{for} \quad Q \to \infty\,. \end{aligned} \tag{1.10}$$

The Lawson criterion in (1.10) provide quantitative estimates for conditions necessary for realizing reactor-based fusion. The parameters that determine whether break-even (or ignition) is achieved at sufficiently high temperature are thus the plasma density and the energy confinement time. An obvious goal for fusion yield experiments is thus to increase those parameters. There is, however, an empirical limit to the maximum density of the confined plasma dictated by the Greenwald density limit [15], which is given by

$$n_{\mathrm{e},20} \leq \frac{I_\mathrm{p}}{\pi a^2}\,, \tag{1.11}$$

where $n_{\mathrm{e},20}$ is the electron density in units of $10^{20}\,\mathrm{m}^{-3}$, I_p is the plasma current in units of MA, and a is the minor radius in units of m. Since the Greenwald density limit puts an upper bound on the average density of the toroidally confined plasma, one of the major tasks of current tokamak experiments is to understand, and potentially control, the transport dynamics in the plasma edge region so that the energy confinement time can be enhanced. The background for understanding the edge transport is given in the following section.

1.3 Turbulence and transport

The message from the former section is that the reason a net energy production from fusion has not been achieved yet, is because it has not been possible to obtain an energy confinement time τ_E, which is large enough to fulfill the Lawson criterion in (1.10). It is difficult to obtain a high energy confinement time, because of cross-field transport of heat, momentum, and particles away from the region of closed magnetic field lines. The cross-field transport necessarily involves the plasma edge region, which functions as a boundary condition for the bulk plasma. The existence of the H-mode [16] is an example of how conditions in the edge can affect the overall confinement

and highlights the importance of understanding this particular region of the plasma.

The cross-field edge and SOL transport is highly intermittent and subject to strong turbulence, which shares the same characteristics across devices of all sizes [17]. The density fluctuations span a broad frequency spectrum of $\nu = 10 - 1000\,\mathrm{kHz}$, with a relative fluctuation amplitude, that can be as large as of the order of unity. The size of the coherent turbulent structures is extremely anisotropic, and the shape is determined by the magnetic field lines. Perpendicular to the field lines the size of the structures is of the order of millimetres to centimetres, whereas parallel to the field lines they typically extend tens of metres. The large difference of perpendicular and parallel transport with respect to the magnetic field lines allows for decoupling those directions when constructing edge and SOL plasma transport models, which is also the strategy applied in Sec. 2.1.2. The field-aligned structures that intermittently emerge from the edge region and propagate outwards through the SOL towards the first wall are generally referred to as blobs.

Turbulent dynamics in magnetically confined plasmas was acknowledged early in the development of the tokamak design, and the topic gained particular attention during the 1970s, where more advanced diagnostics and signal processing tools were developed [17]. Today a variety of diagnostic techniques exist, which allows for obtaining information of the turbulent plasma fields in the edge and SOL regions. One example is Langmuir probes [18]. Langmuir probes are electrically biased probes that are inserted into the SOL and far edge plasmas. They provide temporally resolved information on the fluctuating plasma and electromagnetic fields in a wide range of frequencies. It is also possible to utilize the scattering or reflection of electromagnetic waves on the charged particles. Opposed to the Langmuir probes this technique do not perturb the plasma, but the techniques come with other disadvantages such as poor spatial resolution, or poor performance when the relative fluctuations are large [19, 20]. A set of diagnostic tools which are particularly relevant for this work are those which utilize the optical line emission that occur after the electrons interact with neutral particles. The technique covers beam emission spectroscopy [21, 22] and gas puff imaging [23], of which the latter is discussed in more detail in Sec. 4.3.

In order to understand the transport mechanism of plasma filaments, the dynamics of magnetically confined charged particles are reviewed. A more detailed analysis of mechanisms driving blob transport can be found in, e.g., [24, 25, 26]. Consider a particle with charge q in a homogeneous magnetic

field with a finite, but small compared to the Larmor radius, gradient length scale, and assume that the temporal variation of $\boldsymbol{B}$ is much slower than the cyclotron period of ions. The particle will experience a force due to the electric and magnetic fields according to the Lorentz force law

$$m\,\mathrm{d}_t\boldsymbol{v} = q\left(\boldsymbol{E} + \boldsymbol{v}\times\boldsymbol{B}\right)\,, \tag{1.12}$$

where m is the mass, and $\boldsymbol{v}$ is the velocity of the particle. Following the lines of most plasma physics introductory textbook (such as [27, 28]), the position $\boldsymbol{x}(t)$ and velocity $\boldsymbol{v}(t)$ of the particle is decomposed into those of its slow guiding center motion, described by $\boldsymbol{x}_{\mathrm{gc}}(t), \boldsymbol{v}_{\mathrm{gc}}(t)$ and its fast gyro-motion $\boldsymbol{x}_{\mathrm{gm}}(t), \boldsymbol{v}_{\mathrm{gm}}(t)$, i.e.,

$$\boldsymbol{x}(t) = \boldsymbol{x}_{\mathrm{gc}}(t) + \boldsymbol{x}_{\mathrm{gm}}(t)\,, \qquad \boldsymbol{v}(t) = \boldsymbol{v}_{\mathrm{gc}}(t) + \boldsymbol{v}_{\mathrm{gm}}(t)\,, \tag{1.13}$$

where $\langle\boldsymbol{x}_{\mathrm{gm}}(t)\rangle = \langle\boldsymbol{v}_{\mathrm{gm}}(t)\rangle = 0$ for the average $\langle\cdot\rangle$ over a cyclotron period. By Taylor expanding the electric and magnetic fields, subtracting equation for the fast gyro-motion, i.e., $m\,\mathrm{d}_t\boldsymbol{v}_{\mathrm{gm}}(t) = q\boldsymbol{v}_{\mathrm{gm}}(t)\times\boldsymbol{B}(\boldsymbol{x}_{\mathrm{gm}}(t))$, and decomposing the variables into terms perpendicular and parallel to $\boldsymbol{B}$, the perpendicular guiding center component of (1.12) reads

$$\begin{aligned} m\,\mathrm{d}_t\boldsymbol{v}_{\perp\mathrm{gc}} = q\Bigg[&\boldsymbol{E}_\perp(\boldsymbol{x}_{\mathrm{gc}}(t)) + \langle\boldsymbol{v}_{\mathrm{gm}}(t)\times(\boldsymbol{x}_{\mathrm{gm}}(t)\cdot\nabla)\,\boldsymbol{B}\rangle_\perp \\ &-\frac{mv_{\parallel\mathrm{gc}}^2}{B^2}\boldsymbol{B}\cdot\nabla\boldsymbol{B} + \boldsymbol{v}_{\mathrm{gc}}\times\boldsymbol{B}\Bigg]\,. \end{aligned} \tag{1.14}$$

Each term of the expression in (1.14) corresponds to a force acting on the guiding center, and thus results in a drift of the guiding center position. Some of the forces drive electrons and ions in opposite directions and result in polarization of coherent structures, which proves to be a key mechanic in blob transport. In tokamaks the magnetic field has a finite gradient of $\boldsymbol{B}$ and result in a drift term, corresponding to the second term of (1.14), and is an example of a charge-separating force. The expression for the so-called grad-B drift is

$$\boldsymbol{v}_{\nabla B} = -\frac{mv_{\mathrm{gm}}^2}{2qB^3}\nabla B\times\boldsymbol{B}\,. \tag{1.15}$$

The grad-B drift separates ions and electrons perpendicular to the magnetic field, due to the dependence on the sign of q. The charge accumulation results in an electric field perpendicular to $\boldsymbol{B}$, and the magnitude of another drift,

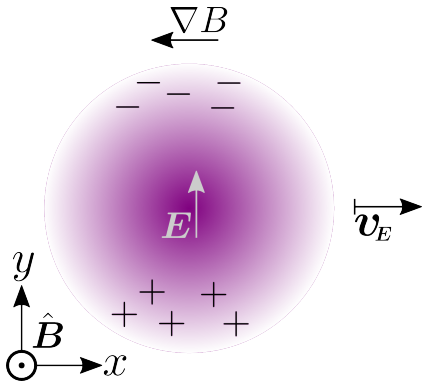

Figure 1.5: The dominant mechanics, i.e., charge separation and $\boldsymbol{E}\times\boldsymbol{B}$ drift, driving outwards cross-field transport of plasma in field-aligned blob filaments.

namely that resulting from the first term of (1.14), increases. This drift is called the $\boldsymbol{E}\times\boldsymbol{B}$ (E-cross-B) drift, and is given by

$$\boldsymbol{v}_E = \frac{\boldsymbol{E}\times\boldsymbol{B}}{B^2} \ . \tag{1.16}$$

The $\boldsymbol{E}\times\boldsymbol{B}$ drift has, opposed to the grad-B drift, no charge dependence, and ions and electrons are thus translated in the same direction. In the outboard SOL of tokamaks, the polarization of blobs by charge-separating drifts, and advection by the $\boldsymbol{E}\times\boldsymbol{B}$ drift due to the resulting electric field, is what is theorized to cause the radial outwards bulk motion of blob filaments as depicted in Fig. 1.5. If no current had been driven in the bulk plasma, this would be subject to the same process, resulting in an immediate loss of confinement. However, having a poloidal component in the magnetic field prevents the polarization of the bulk plasma, and thus secures the overall confinement. There is, however, no known method to avoid the generation and propagation of filamentary structures, and the resulting loss of particles and heat.

The mechanics for creation of field-aligned filaments near the LCFS is not yet entirely understood, although certain parameters are known to be important for the process. One is the presence of a sheared poloidal flow near the LCFS , which is typically weak in the so-called low-confinement mode (L-mode), and stronger in the high-confinement mode (H-mode). Another parameter that drives the creation of blobs is the type linear instability which causes the initial perturbation to grow. The driving instabilities count the interchange mode, the ballooning mode, and the drift-wave instability,

and may differ depending on the magnetic topology. The last topic in the introduction concerns the origin of neutral particles in tokamak plasmas and it is reviewed in the following section.

1.4 Neutrals and plasmas

The far edge and SOL regions of magnetically confined plasmas are generally substantially colder than the bulk plasma. This allows for a significant population of neutral molecules and atoms to exist in a statistical equilibrium with the plasma, balanced by ionization, which moves particles from the neutral to the plasma population, and recombination and recycling processes, where ions and electrons reunite and result in neutral atoms or molecules. Neutral particles originate from a variety of processes. They are either created from recombined or recycled plasma, or they are injected into the vacuum chamber for fuelling or diagnostics purposes. Below is a brief overview of the effect of neutrals on the plasma, and vice-versa. A more detailed analysis of plasma-neutral interactions is provided in Sec. 2.2.1.

Turbulent processes, reviewed in Sec. 1.3, result in a large transport of particles away from the plasma. This has a beneficial effect as impurities that have sputtered off from material surfaces and polluted the plasma, and eventually helium from fusion processes, otherwise accumulate in the bulk plasma. The intended hydrogen isotopes for the fusion process, however, are also removed by cross-field transport, and it is thus necessary to fuel the plasma during the discharge to maintain the density. As the plasma is confined by a magnetic field, it is not possible to inject charged particles directly. The charged particles would gyrate the (open) magnetic field lines, and thus result in little to no fuelling. The solution is to inject neutral particles; transport of neutrals is naturally not affected by the presence of electromagnetic fields, and in principle all injected neutrals could reach the confined region where they are ionized and contribute to the desired bulk plasma density. However, due to the presence of charged particles in the SOL region not all injected neutrals reach the region of closed magnetic field lines before they are ionized.

There exists various methods for injecting neutrals for fuelling purposes. The perhaps simplest technique is to place valves at designated locations at the first wall, which can be opened and allow for neutral molecules at

room temperature to enter the vacuum chamber. This technique is called gas puffing. It is the same technique for introducing neutrals as is used in gas puff imaging diagnostics. As will be apparent from Chpt. 4, the blobs ionize a substantial amount of thermal neutrals in the SOL region. One of the main objectives of this work is to qualify and quantify the relevant interactions between SOL and edge plasmas and neutral particles by numerical means. Two other fuelling methods are designed with the purpose of deeper penetration and thus a higher efficiency due to less SOL losses. For supersonic molecular beam injection (SMBI) the neutral molecules are injected with an inwards directed velocity of the order of km/s [29], which results in molecular dissociative and ionization processes closer to, or even inside, the edge region. The second method is to shoot frozen fuel pellets at high speed into the vacuum chamber, which result in a much deeper fuelling than that of gas puffing and SMBI [30]. In this work only the gas puffing scheme is considered, although the analytical and numerical foundation to study SMBI fuelling is also provided for future applications.

Neutral particles are not only injected for fuelling purposes. As mentioned in Sec. 1.3 some diagnostic techniques for measuring the plasma density and temperatures also involve adding neutrals to the system, mainly for the purpose of becoming excited and subsequently radiate light which is then measured. This is the working principle of both gas puff imaging and beam emission spectroscopy. High energy atomic beams in the 100 keV range, known as neutral beams, are a common method of heating the plasma through charge-exchange collisions, and also allow for diagnostics of fast ions in the core as well. Only simulation relevant for gas puff imaging technique, however, can be obtained from the analytical and numerical tools provided in this work. A final application for neutral particles in confined plasmas is protection of material surfaces and components. Through collisions between charged and neutral particles, the hot plasma looses energy and damage from the filaments on the reactor is thus reduced.

Although neutrals are applied for diagnostics of plasma fields, the neutral fields themselves are difficult to measure. The conditions near the plasma are typically too hostile for conventional probes, and the neutrals do not interact with electromagnetic waves in a manner that allows for such diagnostics, as is the case for charged particles. The light from gas puff imaging measurements does contain information about the neutral atom density, as the emitted light is proportional to that. The atom density can thus in principle be deduced, if the other fields that correlate with the measured light intensity are known. For obtaining information of the neutral energy distribution, the Doppler

shift of the measured signal can be utilized as is done in [31, 32]. The deduction of neutral fields from data is, however, not a standard procedure at most experiments, so information obtained from numerical simulations can illuminate mechanics that are otherwise inaccessible.

In recap; neutrals are injected into the plasma for the purpose of fuelling, diagnostic, and heating, or to influence the temperature in the edge and SOL regions. They are also created in a dynamical statistical equilibrium between the plasma and the existing neutrals, and the material surfaces. In Section 1.3 the importance of the plasma edge conditions on the overall confinement is accentuated, and as a natural extension, the injection of neutrals influences the overall confinement through the interactions with the edge and SOL plasma. It has been observed in experiments, that puffing neutrals into the chamber can result in various distinguishable SOL conditions, such as detachment [33, 34] and shoulder formation [35], and trigger transitions from H-mode to L-mode [36]. The analytical and numerical results presented in this thesis aim towards enhancing the understanding of neutral transport, and the neutral-plasma interactions, which may be one small piece in the puzzle of realizing reactor-based fusion as a future source of energy. In the following section the points made in the introduction chapter are reviewed, and the structure of the remaining parts of the thesis is outlined.

1.5 Thesis overview

The introductory chapter can be summarized as follows. Our global society requires a huge and increasing production of electric energy from base-load power plants for sustaining the current standard of living. Thermonuclear fusion is proposed as a possible future solution, where reactor based fusion of the hydrogen isotopes deuterium and tritium potentially provides an energy source which is clean, safe, and sustainable. The most researched design for a thermonuclear reactor is the tokamak, which confines hot fusion plasma magnetically in a toroidal configuration. The fusion gain is dictated by the plasma density and temperature, and by the energy confinement time which is determined by losses due to turbulent transport in the plasma edge and SOL regions. Neutral particles have a direct impact on the plasma fields in the edge and SOL regions, and increased knowledge of the transport of neutrals and their interaction with plasma may provide a path to enhancing the plasma confinement and limit the damages from the plasma filaments on

material surfaces.

In addition to conducting experiments in tokamak test reactors, knowledge of the plasma edge and SOL dynamics is obtained from analytical and numerical models. This work presents a novel fluid-like model for neutral molecules and atoms in the edge and SOL regions of a magnetically confined plasma. The model describes transport of neutral particles that experience a long mean-free path between collisions, as well as source terms resulting from interactions between the neutrals and charged particles. The model is coupled to an existing numerical model for edge and SOL plasma to provide a scheme in which the effects of neutrals on edge and SOL plasma, and vice-versa, can be studied in a dynamical, self-consistent manner.

In Chapter 2 the theoretical foundation for the combined plasma-neutral model is provided. Section 2.1 displays the steps necessary to take for constructing a plasma drift-fluid model, starting from the kinetic equations for ions and electrons. The derivation introduces source terms from elastic and inelastic collisions between charged and neutral particles. This results in the formulation of the well-known two-fluid equations augmented with neutral sources in Sec. 2.1.1, the continued approximation into the so-called drift-fluid models in Sec. 2.1.2, and the overview of the so-called HESEL model [37, 38] in Sec. 2.1.3. Section 2.2 similarly covers the derivation of the neutral transport and interaction model. Section 2.2.1 provides a detailed overview of the origin of neutrals, and the physical foundations of the neutral model and the source terms included in Sec. 2.1. A fluid-like transport model for neutrals, which takes into account the long mean-free path between collisions in the SOL region, is subsequently derived in Sec. 2.2.2. The combined neutral-HESEL (nHESEL) model is presented in Sec. 2.3.

Chapter 3 concerns the transition from the mathematical model of Chpt. 2 to a numerical model. The implementation of the model in a numerical framework is described in Sec. 3.1. For the numerical model to be trustworthy the numerical methods are verified in Sec. 3.2, and validation of the model is discussed in Sec. 3.3.

The results of various study cases are presented in Chpt. 4. The chapter is built around three papers provided in Secs. 4.1 - 4.3, which investigative various phenomena that result from interactions between plasmas and neutrals. The results presented in the papers are obtained using the nHESEL model or predecessor models thereof. The chapter subsequently presents three conference papers in Sec. 4.4 on similar topics, which are referenced in

the discussions of the three primary papers. Finally a selection of preliminary, non-published results are presented in Sec. 4.5.

Chapter 5 provides a review of the thesis content, where the primary conclusions of the thesis are presented in Sec. 5.1. Following the conclusions is Sec. 5.2, in which future applications for, and improvements of, the nHESEL model are discussed.

Chapter 2

Theory

This chapter provides the theoretical background for deriving the models which are used in the studies of neutral-plasma interactions in Chpt. 4. The chapter has three sections, of which the latter, Sec. 2.3, summarizes the full nHESEL model obtained in the former two sections. Section 2.1 concerns the modelling of the plasma, and systematically displays how sources from neutral interactions enter fluid and drift-fluid equations. This is applied to the HESEL model [37, 38], which constitutes the plasma part of the nHESEL equations. In Section 2.2 the sources of neutral particles in a tokamak plasma and the transport of neutrals in the dilute SOL region are discussed, and a fluid-like model consistent with the SOL and far edge conditions is derived. It is this model that constitutes the neutral part of the nHESEL model.

2.1 Modelling plasmas

One of the challenges in modelling plasmas is that the scales of spatial and temporal dynamics span several orders of magnitudes. Thus, to describe collective plasma phenomena, e.g., coherent structures in the SOL, dynamics at much smaller length scales and much faster time scales can be averaged out to obtain a model that gives physical insight to the relevant dynamics and is computationally viable to solve.

The first step for obtaining a mathematical description for plasma pro-

cesses is the single particle description, where the smallest and fastest dynamics are described in an exact model. A plasma of N particles, i.e., $N/2$ ions and $N/2$ electrons, is described by classical electrodynamics by solving the equation of motion with the Lorentz force

$$m_\sigma \mathrm{d}_t \boldsymbol{v}_\sigma = q_\sigma \left(\boldsymbol{E} + \boldsymbol{v}_\sigma \times \boldsymbol{B} \right) , \tag{2.1}$$

for each of the N particles, where m_σ is the mass, and q_σ is the electric charge for species σ, and $\boldsymbol{E}$ and $\boldsymbol{B}$ are the electric and magnetic fields, which are obtained by the Maxwell equations, and thus couple the equations of motion for all particles. The number of equations to be solved in order to describe a plasma is usually huge, and even by computational means impossible for plasmas as voluminous and dense as those in tokamaks.

If the particle velocities are distributed according to a well defined distribution function, the number of free variables can be reduced by treating the motions statistically and average out the individual particle orbits. This is the kinetic theory, which describes the evolution of the electron and ion velocity distribution functions through the Vlasov equation

$$\partial_t f_\sigma + \boldsymbol{v} \cdot \nabla f_\sigma + \tfrac{q_\sigma}{m_\sigma} \left(\boldsymbol{E} + \boldsymbol{v} \times \boldsymbol{B} \right) \cdot \nabla_{\boldsymbol{v}} f_\sigma = 0 \, , \tag{2.2}$$

where $f_\sigma = f_\sigma(\boldsymbol{x}(t), \boldsymbol{v}(t))$ is the distribution function for species σ.

By integrating out the velocity dependence, the Vlasov equation reduces to the fluid equations and changes from describing microscopic to macroscopic fields by the evolution of the densities, bulk velocities, and pressures. The plasma two-fluid equations are the foundation of the studies in this work, and are treated in detail in Sec. 2.1.1. Most numerical models that simulate the edge and SOL regions are based on equations that are derived from the two-fluid equations. An incomplete list of current numerical models counts the codes based on convective transport, e.g., SOLPS [39], UEDGE [40], and EDGE2D [41], and drift-fluid based codes, e.g., Tokam-3D [42], HERMES [43], GBS [44], and HESEL [37, 38].

Yet another step towards simplifying the plasma equations is by considering the electrons and ions as one fluid, and thus obtaining the MHD equations, which are applicable for describing more global phenomena than those of relevance to this work.

2.1.1 Two-fluid equations

In this section the derivation of the two-fluid equations, initially carried out by Braginskii [45], is reviewed. In addition to the original fluid equations, the derivation includes the source terms that originate from both elastic and inelastic collisions between charged particles and neutrals. The section has three parts; first the derivation of the two-fluid equations from the kinetic equation is outlined, secondly an appropriate closure scheme for the plasma two-fluid equations is discussed, and lastly the explicit expressions for the collisional terms are provided.

Fluid equations

In this section the two-fluid equations are derived by taking velocity space moments of the kinetic Boltzmann equation

$$\boxed{\partial_t f_\sigma + \nabla \cdot (\boldsymbol{v} f_\sigma) + \cdot \nabla_{\boldsymbol{v}} (\boldsymbol{a}_\sigma f_\sigma) = \mathcal{C}_\sigma + \mathcal{S}_\sigma \,.} \tag{2.3}$$

Here $f_\sigma = f_\sigma(\boldsymbol{x}(t), \boldsymbol{v}(t))$ is the distribution function for species σ, $\boldsymbol{a}_\sigma$ is the acceleration caused by the electric and magnetic fields, $\mathcal{C}_\sigma = \sum_\alpha \mathcal{C}_{\sigma\alpha}$ is the sum of the collision operators for elastic collisions of species σ with species α, and $\mathcal{S}_\sigma = \sum_\alpha \mathcal{S}_{\sigma\alpha}$ is the sum of the collision operators for inelastic collisions of species σ with species α.

The **zeroth order** velocity space moment is

$$\int \mathrm{d}\boldsymbol{v} \left[\partial_t f_\sigma + \nabla \cdot (\boldsymbol{v} f_\sigma) + \cdot \nabla_{\boldsymbol{v}} (\boldsymbol{a}_\sigma f_\sigma)\right] = \int \mathrm{d}\boldsymbol{v} \left[\mathcal{C}_\sigma + \mathcal{S}_\sigma\right] . \tag{2.4}$$

The integrals are readily evaluated, keeping in mind that $\boldsymbol{x}$, $\boldsymbol{v}$, and t are independent variables, and defining the particle number density

$$n_\sigma = \int \mathrm{d}\boldsymbol{v}\, f_\sigma \,, \tag{2.5}$$

and the particle flow velocity

$$\boldsymbol{u}_\sigma = \frac{1}{n_\sigma} \int \mathrm{d}\boldsymbol{v}\, \boldsymbol{v} f_\sigma \,, \tag{2.6}$$

the zeroth order moment result in the continuity equation

$$\partial_t n_\sigma + \nabla \cdot (n_\sigma \boldsymbol{u}_\sigma) = S^n_\sigma \,. \tag{2.7}$$

The integral of the third term on the left-hand side (LHS) in (2.4) vanish as a result of Gauss' theorem, and the elastic collision operator term on the right-hand side (RHS) likewise integrates to zero. The latter results from demanding particle conservation in elastic collisions, i.e.,

$$\int \mathrm{d}\boldsymbol{v}\, \mathcal{C}_{\sigma\alpha} = 0 \,. \tag{2.8}$$

The velocity space integral of the inelastic collision operator, e.g., that for ionization of atoms, result in a density source term

$$S^n_\sigma = \int \mathrm{d}\boldsymbol{v}\, \mathcal{S}_\sigma \,, \tag{2.9}$$

for which an explicit expression in terms of dynamical fields is given in the third part of the section.

In order to calculate the time evolution of the particle number density from (2.7), knowledge of the particle flow velocity is required. Such knowledge is provided by the momentum equation, which result from the **first order** velocity space moment of the Boltzmann equation

$$m_\sigma \int \mathrm{d}\boldsymbol{v}\, \boldsymbol{v} \left[\partial_t f_\sigma + \nabla \cdot (\boldsymbol{v} f_\sigma) + \cdot \nabla_{\boldsymbol{v}} (\boldsymbol{a}_\sigma f_\sigma)\right] = m_\sigma \int \mathrm{d}\boldsymbol{v}\, \boldsymbol{v} \left[\mathcal{C}_\sigma + \mathcal{S}_\sigma\right] \,. \tag{2.10}$$

For practical reasons all terms are multiplied by the particle mass m_σ when calculating the first moment. Carrying out the integrals on the LHS requires a bit more vector algebra than for the zeroth moment. The first term simply integrates to the time derivative of the momentum density $n_\sigma m_\sigma \boldsymbol{u}_\sigma$ by Eqn. (2.6). The second term describes the divergence of the flow of the momentum, i.e., the stress tensor

$$\mathbf{P}_\sigma = \int \mathrm{d}\boldsymbol{v}\, m_\sigma \boldsymbol{v}\boldsymbol{v} f_\sigma \,. \tag{2.11}$$

By writing the velocity as a sum of the mean and random velocities, the stress tensor can be written as

$$\mathbf{P}_\sigma = \mathbf{p}_\sigma + m_\sigma n_\sigma \boldsymbol{u}_\sigma \boldsymbol{u}_\sigma \,, \tag{2.12}$$

where $\mathbf{p}_\sigma$ is the pressure tensor. The pressure tensor itself often is split into its diagonal and off-diagonal terms

$$\mathbf{p}_\sigma = p_\sigma \mathbf{I} + \boldsymbol{\pi}_\sigma \,, \tag{2.13}$$

where p_σ is the scalar pressure, and $\boldsymbol{\pi}_\sigma$ is the generalized viscosity tensor. For the third term in the LHS of (2.10) the acceleration from the Lorentz force is written explicitly, that is, $\boldsymbol{a}_\sigma = \frac{q_\sigma}{m_\sigma}(\boldsymbol{E} + \boldsymbol{v} \times \boldsymbol{B})$, and integrates to $-q_\sigma n_\sigma (\boldsymbol{E} + \boldsymbol{u}_\sigma \times \boldsymbol{B})$ by integration by parts. The first term of the RHS of (2.10) describes the collisional friction force $\boldsymbol{R}_\sigma = \sum_\alpha \boldsymbol{R}_{\sigma\alpha}$ due to elastic collisions, which is constrained by demanding momentum conservation in elastic collisions of species σ with other species α

$$\boldsymbol{R}_{\sigma\alpha} = -\boldsymbol{R}_{\alpha\sigma} \,, \tag{2.14}$$

where $\boldsymbol{R}_{\sigma\alpha} = m_\sigma \int \mathrm{d}\boldsymbol{v}\, \boldsymbol{v} \mathcal{C}_{\sigma\alpha}$, so that $\sum_\sigma \boldsymbol{R}_\sigma = 0$. The second term on the RHS of (2.10) is the inelastic momentum source given by

$$\boldsymbol{S}^u_\sigma = m_\sigma \int \mathrm{d}\boldsymbol{v}\, \boldsymbol{v} \mathcal{S}_\sigma \,, \tag{2.15}$$

which, as for the density source, is explicated in the last part of the section. Collecting all terms from (2.10) result in

$$\begin{aligned} m_\sigma \partial_t (n_\sigma \boldsymbol{u}_\sigma) + \nabla p_\sigma + \nabla \cdot \boldsymbol{\pi}_\sigma + m_\sigma \nabla \cdot (n_\sigma \boldsymbol{u}_\sigma \boldsymbol{u}_\sigma) \\ - q_\sigma n_\sigma (\boldsymbol{E} + \boldsymbol{u}_\sigma \times \boldsymbol{B}) = \boldsymbol{R}_\sigma + \boldsymbol{S}_\sigma \,. \end{aligned} \tag{2.16}$$

Finally the continuity equation (2.7) is multiplied by $m_\sigma \boldsymbol{u}_\sigma$ and subtracted from (2.16) to obtain the evolution of the momentum, rather than the momentum density. The resulting equation is

$$\begin{aligned} m_\sigma n_\sigma \partial_t \boldsymbol{u}_\sigma + m_\sigma n_\sigma \boldsymbol{u}_\sigma \cdot \nabla \boldsymbol{u}_\sigma + \nabla p_\sigma + \nabla \cdot \boldsymbol{\pi}_\sigma - q_\sigma n_\sigma (\boldsymbol{E} + \boldsymbol{u}_\sigma \times \boldsymbol{B}) \\ = \boldsymbol{R}_\sigma + \boldsymbol{S}^u_\sigma - m_\sigma \boldsymbol{u}_\sigma \boldsymbol{S}^n_\sigma \,. \end{aligned} \tag{2.17}$$

The last step, where the continuity equation has been subtracted from the momentum density equation, is important to include in the presence of a density source, i.e., when the RHS of (2.7) is no longer zero. The resulting sink term on the RHS of the momentum equation (2.17) describes a loss of momentum due to the creation of particles at zero fluid velocity. As for the case of the particle flux density in the continuity equation, which required the calculation of the next moment of the Boltzmann equation, the terms originating from the stress tensor likewise demand knowledge of the evolution of the higher order moment of (2.3).

The **second order** velocity space moment of the Boltzmann equation is

$$\begin{aligned} \tfrac{1}{2}m_\sigma \int \mathrm{d}\boldsymbol{v}\, v^2 \left[\partial_t f_\sigma + \nabla\cdot(\boldsymbol{v} f_\sigma) + \cdot\nabla_{\boldsymbol{v}}\left(\boldsymbol{a}_\sigma f_\sigma\right)\right] \\ = \tfrac{1}{2}m_\sigma \int \mathrm{d}\boldsymbol{v}\, v^2 \left[\mathcal{C}_\sigma + \mathcal{S}_\sigma\right]. \end{aligned} \tag{2.18}$$

The integrals are again solved term by term, applying the same techniques as for the first moment. Splitting the velocity into mean and random parts allows for writing the first term on the LHS

$$\tfrac{1}{2}m_\sigma \int \mathrm{d}\boldsymbol{v}\, v^2 \partial_t f_\sigma = \partial_t\left(\tfrac{3}{2}p_\sigma + \tfrac{1}{2}m_\sigma n_\sigma u_\sigma^2\right). \tag{2.19}$$

The second term of (2.18) is the spatial derivative of the energy flux density and can be written

$$\nabla\cdot\left(\tfrac{1}{2}m_\sigma \int \mathrm{d}\boldsymbol{v}\, \boldsymbol{v} v^2 f_\sigma\right) = \boldsymbol{q}_\sigma + \mathbf{p}_\sigma\cdot\boldsymbol{u}_\sigma + \tfrac{3}{2}p_\sigma\boldsymbol{u}_\sigma + \tfrac{1}{2}m_\sigma n_\sigma u_\sigma^2\boldsymbol{u}_\sigma\,, \tag{2.20}$$

where $\boldsymbol{q}_\sigma = m_\sigma\int \mathrm{d}\boldsymbol{v}\, w_\sigma^2\boldsymbol{w}_\sigma f_\sigma$ is the heat flux, and $\boldsymbol{w}_\sigma = \boldsymbol{v} - \boldsymbol{u}_\sigma$ is the random velocity part. The last term on the LHS of (2.18) readily integrates to $-q_\sigma n_\sigma \boldsymbol{E}\cdot\boldsymbol{u}_\sigma$, and the energy density equation reads

$$\begin{aligned} \partial_t\left(\tfrac{3}{2}p_\sigma + \tfrac{1}{2}m_\sigma n_\sigma u_\sigma^2\right) + \nabla\cdot\left(\boldsymbol{q}_\sigma + \mathbf{p}_\sigma\cdot\boldsymbol{u}_\sigma + \tfrac{3}{2}p_\sigma\boldsymbol{u}_\sigma + \tfrac{1}{2}m_\sigma n_\sigma u_\sigma^2\boldsymbol{u}_\sigma\right) \\ - q_\sigma n_\sigma \boldsymbol{E}\cdot\boldsymbol{u}_\sigma = Q_\sigma + S_\sigma^p\,. \end{aligned} \tag{2.21}$$

Here $Q_\sigma = \frac{1}{2}m_\sigma\int \mathrm{d}\boldsymbol{v}\, v^2\mathcal{C}_\sigma$ defines the collisional energy transfer rate between species σ and other species present, and similar for inelastic collisions

$$S_\sigma^p = \tfrac{1}{2}m_\sigma \int \mathrm{d}\boldsymbol{v}\, v^2\mathcal{S}_\sigma\,. \tag{2.22}$$

As for the momentum, energy is conserved in elastic collisions

$$Q_{\sigma\alpha} = -Q_{\alpha\sigma}\,, \tag{2.23}$$

where $Q_\sigma = \sum_\alpha Q_{\sigma\alpha}$. Similar to the case of the first moment of the Boltzmann equation, the energy density equation contains the lower order equations, and (2.7) multiplied with $\frac{1}{2}mu_\sigma^2$, and the inner product of (2.17) with $\boldsymbol{u}_\sigma$, can thus be subtracted from (2.24) to yield

$$\begin{aligned} \tfrac{3}{2}\partial_t p_\sigma + \tfrac{3}{2}\nabla\cdot(\boldsymbol{u}_\sigma p_\sigma) + \mathbf{p}_\sigma : \nabla\boldsymbol{u}_\sigma + \nabla\cdot\boldsymbol{q}_\sigma = Q_\sigma - \boldsymbol{u}_\sigma\cdot\boldsymbol{R}_\sigma + S_\sigma^p \\ - \boldsymbol{u}_\sigma\cdot\boldsymbol{S}_\sigma^u + \tfrac{1}{2}m_\sigma u_\sigma^2 S_\sigma^n\,, \end{aligned} \tag{2.24}$$

where the double-dot operation is defined by $\mathbf{a} : \nabla \boldsymbol{b} \equiv a_{\alpha\beta}\partial_\alpha b_\beta$. As for the lower moment equations, the energy density equation contains a term, namely the heat flux $\boldsymbol{q}_\sigma$, of which the temporal evolution is defined by the third moment of the Boltzmann equation. It is a feature of the fluid equations always to include the lower moment equations, as well as a higher order term. It is therefore also necessary to introduce an approximation, that closes the system of fluid equations, and this is often done at this point in the derivation. A common closure procedure for is that of the Chapman-Enskog scheme, which assumes some length scale, either the elastic collisional mean-free path or the Lamor radius, of the particles to be small compared to the macroscopic length scales. The Chapman-Enskog closure is explained in more detail in the following part. Below the obtained set of fluid equations is re-stated for future reference. The two-fluid equations with neutral source terms are constituted by the continuity equation

$$\boxed{\mathrm{d}_{t,\sigma} n_\sigma + n_\sigma \nabla \cdot \boldsymbol{u}_\sigma = S_\sigma^n \,,} \tag{2.25}$$

the momentum equation

$$\boxed{\begin{aligned} m_\sigma n_\sigma \mathrm{d}_{t,\sigma} \boldsymbol{u}_\sigma + \nabla p_\sigma + \nabla \cdot \boldsymbol{\pi}_\sigma - q_\sigma n_\sigma \left(\boldsymbol{E} + \boldsymbol{u}_\sigma \times \boldsymbol{B}\right) = \boldsymbol{R}_\sigma + \boldsymbol{S}_\sigma^u \\ - m_\sigma \boldsymbol{u}_\sigma S_\sigma^n \,, \end{aligned}} \tag{2.26}$$

and the energy equation

$$\boxed{\begin{aligned} \tfrac{3}{2}\mathrm{d}_{t,\sigma} p_\sigma + \tfrac{5}{2} p_\sigma \nabla \cdot \boldsymbol{u}_\sigma + \boldsymbol{\pi}_\sigma : \nabla \boldsymbol{u}_\sigma + \nabla \cdot \boldsymbol{q}_\sigma = Q_\sigma - \boldsymbol{u}_\sigma \cdot \boldsymbol{R}_\sigma + S_\sigma^p \\ - \boldsymbol{u}_\sigma \cdot \boldsymbol{S}_\sigma^u + \tfrac{1}{2} m_\sigma u_\sigma^2 S_\sigma^n \,, \end{aligned}} \tag{2.27}$$

where $\mathrm{d}_{t,\sigma} = \partial_t + \boldsymbol{u}_\sigma \cdot \nabla$ is the material derivative. The fluid equations were originally derived in [45], but without the inclusion of the inelastic source terms. Similar results on the integrated inelastic source terms are also found in [46, 47]. The original Braginskii paper provides approximations for the source terms, $\boldsymbol{R}_\sigma$ and Q_σ, and viscosity, originating from elastic collisions. Those approximations are reviewed after the fluid closure part, with the addition that collisions with neutrals are also included. Explicit expressions for the inelastic source terms are likewise provided in this section.

Fluid closure

Besides the lack of a closed form for the collisional terms, which are provided in the following part, the evolution of the fields described in the two-fluid

equations in (2.25)-(2.27) is still undetermined due to the presence of the heat flux, for which the dynamics are described by the next velocity space moment of the kinetic equation. This equation would, however, depend on a higher moment term as well. It is an inherit feature of the fluid equations that each equation depend on a variable provided by the next order equation, and the only way to obtain a set of well-defined equations is to close the system by describing the unknown variables in terms of lower-moment fields. For a consistent model an asymptotic closure scheme (opposed to a truncation scheme), which involves expanding the kinetic equation in some small parameter, is required. The closure scheme applied to obtain the Braginskii equations is the Chapman-Enskog closure [48], which depends on the ratio of either the collisional short mean-free path for a collisional plasma or Larmor radius l for a magnetized plasma, to the macroscopic variation length scales L of the plasma, $\epsilon = \frac{l}{L}$.

The core of the Chapman-Enskog scheme is assuming that the distribution function entering the kinetic equation (2.3) can be written on the form

$$f = f_0 + f_1 \,, \tag{2.28}$$

where f_0 is the leading order Maxwellian contribution to the distribution function, and f_1 is a perturbation to this, assumed to be smaller than the former by the order of ϵ. By linearizing the kinetic equation an integral equation for f_1 in terms of f_0 can be obtained and solved by truncating a rapidly converging Laguerre polynomial expansion. This results in a closed form of f_1 depending only on lower-moment plasma fields, and the appropriate moments of the distribution function can be taken to obtain the heat flux and collisional terms.

The heat flux densities for electrons and ions in the magnetized limit are [45]

$$\begin{aligned} \boldsymbol{q}_\mathrm{e} = & -k_{\mathrm{e}\parallel}\nabla_\parallel T_\mathrm{e} - k_{\mathrm{e}\perp}\nabla_\perp T_\mathrm{e} - k_{\mathrm{e}\times}\hat{\boldsymbol{B}}\times\nabla_\perp T_\mathrm{e} \\ & - 0.71\frac{T_\mathrm{e}}{e}\boldsymbol{j}_\parallel + \frac{3}{2}\frac{T_\mathrm{e}}{\Omega_\mathrm{e}\tau_e e}\hat{\boldsymbol{B}}\times\boldsymbol{j}_\perp \,, \end{aligned} \tag{2.29}$$

$$\boldsymbol{q}_\mathrm{i} = -k_{\mathrm{i}\parallel}\nabla_\parallel T_\mathrm{i} - k_{\mathrm{i}\perp}\nabla_\perp T_\mathrm{i} - k_{\mathrm{i}\times}\hat{\boldsymbol{B}}\times\nabla_\perp T_\mathrm{i} \,. \tag{2.30}$$

Here $\hat{\boldsymbol{B}}$ is the magnetic field unit vector, $\boldsymbol{j}_{\parallel,\perp}$ are the parallel and perpendicular components of the electric current, and the thermal conductivities

are

$$k_{\mathrm{e}\parallel} = 3.2\frac{\tau_{\mathrm{e}} n_{\mathrm{e}} T_{\mathrm{e}}}{m_{\mathrm{e}}}\,, \qquad k_{\mathrm{e}\perp} = 4.7\frac{n_{\mathrm{e}} T_{\mathrm{e}}}{\tau_{\mathrm{e}} m_{\mathrm{e}} \Omega_{\mathrm{e}}^2}\,, \qquad k_{\mathrm{e}\times} = -\frac{5}{2}\frac{n_{\mathrm{e}} T_{\mathrm{e}}}{m_{\mathrm{e}} \Omega_{\mathrm{e}}}\,, \tag{2.31}$$

$$k_{\mathrm{i}\parallel} = 3.9\frac{\tau_{\mathrm{i}} n_{\mathrm{i}} T_{\mathrm{i}}}{m_{\mathrm{i}}}\,, \qquad k_{\mathrm{i}\perp} = 2\frac{n_{\mathrm{i}} T_{\mathrm{i}}}{\tau_{\mathrm{i}} m_{\mathrm{i}} \Omega_{\mathrm{i}}^2}\,, \qquad k_{\mathrm{i}\times} = \frac{5}{2}\frac{n_{\mathrm{i}} T_{\mathrm{i}}}{m_{\mathrm{i}} \Omega_{\mathrm{i}}}\,, \tag{2.32}$$

where $\tau_{\mathrm{e,i}}$ are the self-collision times for electrons and ions, which are treated in more detail in the following section. The viscosity is found in a similar manner and provided in [45].

With the set of fluid equations systematically closed, the remainder of the section is dedicated to obtaining explicit expressions for both the elastic and inelastic source terms on the RHSs of (2.25)-(2.27).

Source terms

In this section the source terms from elastic collisions, i.e., $\boldsymbol{R}_\sigma$ and Q_σ, and from inelastic collisions, i.e., S_σ^n, $\boldsymbol{S}_\sigma^u$, and S_σ^p, are derived for electrons and ions $\sigma = \mathrm{e}, \mathrm{i}$. Due to conservation of momentum and energy in elastic collisions, i.e., (2.14) and (2.23), it suffices to identify the pairs $\sigma\alpha = (\mathrm{ei}, \mathrm{en}, \mathrm{in})$ for $\boldsymbol{R}_\sigma$ and Q_σ. The inelastic source terms are calculated from the kinetic collision sources similar to [45], whereas the elastic collisions are obtained in a more heuristic manner.

For **elastic** collisions, it is enlightening to estimate the magnitudes and rates of momentum and energy transfer before reviewing the analytical expressions for the collisional terms. When a particle a collide (head-on) with another particle b, the maximum loss of momentum and energy of particle a in a collision time τ_a is determined by the equations for conservation of momentum and energy

$$m_{\mathrm{a}} v_{\mathrm{a}0} + m_{\mathrm{b}} v_{\mathrm{b}0} = m_{\mathrm{a}} v_{\mathrm{a}1} + m_{\mathrm{b}} v_{\mathrm{b}1}\,, \tag{2.33}$$

$$\tfrac{1}{2} m_{\mathrm{a}} v_{\mathrm{a}0}^2 + \tfrac{1}{2} m_{\mathrm{b}} v_{\mathrm{b}0}^2 = \tfrac{1}{2} m_{\mathrm{a}} v_{\mathrm{a}1}^2 + \tfrac{1}{2} m_{\mathrm{b}} v_{\mathrm{b}1}^2\,, \tag{2.34}$$

where $m_\sigma, v_{\sigma 0}, v_{\sigma 1}$ are the mass, initial velocity, and final velocity of particle $\sigma = \mathrm{a}, \mathrm{b}$. To estimate the momentum and energy transferred in collisions in a partly ionized plasma, such as that in the SOL and edge regions, the above equations are evaluated in the limits of large mass ratios and zero mass difference between particles a and b. Assuming that the target particle

is initially at rest, i.e., $v_{\mathrm{b}0} = 0$, the transfer of momentum from particle a to b is

$$\frac{m_{\mathrm{b}} v_{\mathrm{b}1}}{m_{\mathrm{a}} v_{\mathrm{a}0}} = \frac{2}{\frac{m_{\mathrm{a}}}{m_{\mathrm{b}}} + 1} \rightarrow \begin{cases} 2 & \text{for} \quad m_{\mathrm{a}} \ll m_{\mathrm{b}} \\ 1 & \text{for} \quad m_{\mathrm{a}} = m_{\mathrm{b}} \\ 2\frac{m_{\mathrm{b}}}{m_{\mathrm{a}}} & \text{for} \quad m_{\mathrm{a}} \gg m_{\mathrm{b}} \end{cases}, \tag{2.35}$$

and the transfer of energy is similarly

$$\frac{m_{\mathrm{b}} v_{\mathrm{b}1}^2}{m_{\mathrm{a}} v_{\mathrm{a}0}^2} = \frac{4\frac{m_{\mathrm{a}}}{m_{\mathrm{b}}}}{\left(\frac{m_{\mathrm{a}}}{m_{\mathrm{b}}} + 1\right)^2} \rightarrow \begin{cases} 4\frac{m_{\mathrm{a}}}{m_{\mathrm{b}}} & \text{for} \quad m_{\mathrm{a}} \ll m_{\mathrm{b}} \\ 1 & \text{for} \quad m_{\mathrm{a}} = m_{\mathrm{b}} \\ 4\frac{m_{\mathrm{b}}}{m_{\mathrm{a}}} & \text{for} \quad m_{\mathrm{a}} \gg m_{\mathrm{b}} \end{cases}. \tag{2.36}$$

The analysis reveals, that for a plasma with light species (such as electrons) and heavy species (such as ions or atoms), the momentum is transferred in just one collision except for that for heavy on light collisions, where a number of collisions similar to the mass ratio are required. For species of similar mass the energy is transferred in one collision, but requires a number of collisions similar to the mass ratio to transfer energy between species of in different mass classes. The collision frequency is neither the same for collisions between similar and different species, and is even different for self-collisions in light and heavy populations. Again a crude estimate provides the collision time (i.e., the inverse frequency) as the mean-free path divided by the relative thermal velocity

$$\tau \sim \frac{\lambda}{v_{\mathrm{th}}} \sim \frac{1}{n\sigma} \left(\frac{m}{T}\right)^{\frac{1}{2}}, \tag{2.37}$$

where σ is the collisional cross-section. For charged particle collisions this is due to Coulomb collisions and can be approximated by the square of the mean-distance of closest approach, which can be found by equating the thermal energy to the electrostatic potential, and result in $\sigma \approx \left(\frac{e^2}{4\pi\epsilon_0 T}\right)^2$, where ϵ_0 is the vacuum permittivity. The resulting collision time for charged particle collisions is

$$\tau \sim \frac{16\pi^2 \epsilon_0^2 m^{\frac{1}{2}} T^{\frac{3}{2}}}{e^4 n}, \tag{2.38}$$

where the relative velocity, and thus the mass dependence, is defined by that of the electrons if they participate in the collision. This orders the charged particle collisions as

$$\tau_{\mathrm{ee,ei}} \sim \sqrt{\frac{m_{\mathrm{e}}}{m_{\mathrm{i}}}} \tau_{\mathrm{ii}}, \tag{2.39}$$

for $T_\mathrm{e} \sim T_\mathrm{i}$. The expression for the charged particle collision times is consistent with that derived more formally in [45]. For collisions involving neutral particles, which is treated in more detail in Sec. 2.2.2, the cross-section is determined by assuming the particles as hard spheres, i.e., $\sigma_\mathrm{ab} = \pi \left(r_\mathrm{a} + r_\mathrm{b}\right)^2$ for colliding particles of radii $r_\mathrm{a,b}$ and thus from (2.37) it is found that

$$\tau_\mathrm{en} \sim \sqrt{\frac{m_\mathrm{e}}{m_\mathrm{i}}}\tau_\mathrm{in} \sim \frac{1}{\pi a_0^2 n_\mathrm{n}} \left(\frac{m_\mathrm{e}}{T_\mathrm{e}}\right)^{\frac{1}{2}} , \tag{2.40}$$

for $T_\mathrm{e} \sim T_\mathrm{i}$. The estimates for the momentum and energy transfer in (2.35) and (2.36), combined with the collision times (2.39) and (2.40) reveal that electrons experience collisions at a rate comparable to the square root of the mass ratio more often than ions do, but the rate at which energy is transferred to heavier particles is down by the mass ratio. Ions on the other hand transfer all their energy and momentum in one elastic collision with neutrals. The relative importance of collisions between charged particles and neutrals is, however, not determined by this estimate, but can be found from comparing the collision times τ_ii and τ_in, which yields

$$\frac{\nu_\mathrm{ii}}{\nu_\mathrm{in}} = \frac{\tau_\mathrm{in}}{\tau_\mathrm{ii}} = \frac{e^4}{\left(4\pi\right)^3 \epsilon_0^2 a_0^2} \frac{n_\mathrm{i}}{n_\mathrm{n}} T_\mathrm{i}^{-2} \sim 60 \frac{n_\mathrm{i}}{n_\mathrm{n}} \left(T_\mathrm{i}(\mathrm{eV})\right)^{-2} , \tag{2.41}$$

where $T_\mathrm{i}(\mathrm{eV})$ is the ion temperature measured in eV. The effect of the actual Coulomb collisions is even larger than estimated due to the effect of many deflections at small angles [49]. Thus, unless the plasma is weakly ionized, the ions, and in particular the electrons, experience collisions with charged particles at a much higher frequency than with neutrals. This does, however, not mean that neutrals are insignificant to edge plasmas, but their influence is mainly mediated through the inelastic sources. Before deriving the source terms for inelastic collisions, the explicit source terms resulting from elastic collisions are provided.

Elastic collisions between different species result in frictious force terms $\boldsymbol{R}_\mathrm{ei,en,ie,in}$ in the momentum equations, and heating terms $Q_\mathrm{ei,en,ie,in}$ in the energy equations. Assuming that species σ and n have Maxwellian velocity distributions with bulk velocities $\boldsymbol{u}_{\sigma,\mathrm{n}}$ allows to obtain approximate expressions [45] for the friction forces from charged particle collisions with neutrals

$$\boxed{\boldsymbol{R}_{\sigma\mathrm{n}} = -n_\sigma n_\mathrm{n} m_{\sigma\mathrm{n}} \alpha'_{\sigma\mathrm{n}} \left(\boldsymbol{u}_\sigma - \boldsymbol{u}_\mathrm{n}\right) ,} \tag{2.42}$$

where $m_{\sigma\mathrm{n}} = m_\sigma m_\mathrm{n} / \left(m_\sigma + m_\mathrm{n}\right)$ is the reduced mass and

$$\alpha'_{\sigma\mathrm{n}} = \tfrac{4}{3}\sigma_{\sigma\mathrm{n}} \left(\frac{8}{\pi}\frac{T_\sigma}{m_{\sigma\mathrm{n}}}\right)^{\frac{1}{2}} . \tag{2.43}$$

The charged particle collisions result in the friction terms

$$\begin{aligned}\boldsymbol{R}_{\rm ei} = &-\frac{m_{\rm e}n_{\rm e}}{\tau_{\rm ei}}\left[0.51\left(\boldsymbol{u}_{\rm e,\parallel}-\boldsymbol{u}_{\rm i,\parallel}\right)+\left(\boldsymbol{u}_{\rm e,\perp}-\boldsymbol{u}_{\rm i,\perp}\right)\right]\\ &-0.71n_{\rm e}\nabla T_{\rm e}-\frac{3}{2}\frac{n_{\rm e}}{\Omega_{\rm ce}\tau_{ei}}\hat{\boldsymbol{B}}\times\nabla T_{\rm e}\,.\end{aligned} \tag{2.44}$$

The collisional heating terms are

$$\boxed{Q_{\sigma{\rm n}} = 3\frac{m_{\rm n}}{m_\sigma}\frac{n_{\rm n}}{\tau_{\sigma{\rm n}}}\left(T_{\rm n}-T_\sigma\right)\,,} \qquad Q_{\rm ie} = 3\frac{m_{\rm e}}{m_{\rm i}}\frac{n_{\rm e}}{\tau_{\rm ei}}\left(T_{\rm e}-T_{\rm i}\right)\,, \tag{2.45}$$

and that for heat generated in the electrons by ions has additional terms from frictious heating,

$$Q_{\rm ei} = \boldsymbol{R}_{\rm ei}\cdot\left(\boldsymbol{u}_{\rm i}-\boldsymbol{u}_{\rm e}\right)+3\frac{m_{\rm e}}{m_{\rm i}}\frac{n_{\rm e}}{\tau_{\rm ei}}\left(T_{\rm i}-T_{\rm e}\right)\,, \tag{2.46}$$

which are in principle also present in the ion collisional heating term (2.45), but of negligible magnitude. This concludes the analysis of elastic collisions.

The **inelastic** collisions considered here are electron impact dissociation (dis) ($\mathrm{H}_2+e\rightarrow 2\mathrm{H}+e$), molecular assisted ionization (m.iz) ($\mathrm{H}_2+e\rightarrow \mathrm{H}_2^+ + 2e\rightarrow \mathrm{H}+\mathrm{H}^+ + 2e$), and atomic ionization (iz) ($\mathrm{H}+e\rightarrow \mathrm{H}^+ + 2e$), as well as ion-atom charge-exchange collisions (cx) ($\mathrm{H}+\mathrm{H}^+\rightarrow \mathrm{H}^+ + \mathrm{H}$). The physical reasons for including those collisions are given in Sec. 2.2.1. The corresponding collision operators, which are added to yield $\mathcal{S}_{\rm e,i}$ are

$$\mathcal{S}_{\rm e,i}^{\rm m.iz} = f_{\rm m}\int {\rm d}\boldsymbol{v}\, f_{\rm e}\sigma_{\rm m.iz}v_{\rm rel}\,, \tag{2.47}$$

$$\mathcal{S}_{\rm e,i}^{\rm iz} = f_{\rm a}\int {\rm d}\boldsymbol{v}\, f_{\rm e}\sigma_{\rm iz}v_{\rm rel}\,, \tag{2.48}$$

$$\mathcal{S}_{\rm i}^{\rm cx} = f_{\rm a}\int {\rm d}\boldsymbol{v}\, f_{\rm i}\sigma_{\rm cx}v_{\rm rel} - f_{\rm i}\int {\rm d}\boldsymbol{v}\, f_{\rm a}\sigma_{\rm cx}v_{\rm rel}\,. \tag{2.49}$$

Here $f_{\rm a}$ is the distribution function for neutral atoms, and $f_{\rm m}$ is that for molecules. Dissociation of molecules is not a fluid source of charged particles, momentum, or heat (except from the sink in electron energy that corresponds to the dissociation potential) and does not appear in the above. The neutral kinetic source terms are

$$\mathcal{S}_{\rm m}^{\rm dis} = -\tfrac{1}{2}\mathcal{S}_{\rm a}^{\rm dis} = -f_{\rm m}\int {\rm d}\boldsymbol{v}\, f_{\rm e}\sigma_{\rm dis}v_{\rm rel}\,, \tag{2.50}$$

$$\mathcal{S}_{\rm m}^{\rm m.iz} = -\mathcal{S}_{\rm a}^{\rm m.iz} = -\mathcal{S}_{\rm e,i}^{\rm m.iz}\,, \tag{2.51}$$

$$\mathcal{S}_{\rm a}^{\rm iz} = -\mathcal{S}_{\rm e,i}^{\rm iz}\,, \tag{2.52}$$

$$\mathcal{S}_{\rm a}^{\rm cx} = -\frac{m_{\rm i}}{m_{\rm a}}\mathcal{S}_{\rm i}^{\rm cx}\,, \tag{2.53}$$

where m_a is the atom mass. For reasons that have to do with the choice of neutral model, the corresponding fluid source terms are not calculated here, but discussed in Sec. 2.2.2. The next step is to calculate the source terms that result from taking velocity moments of (2.47)-(2.49), and thus derive the explicit expressions for the source terms in (2.9), (2.15), and (2.22) similar to [47]. For the interactions under consideration, the electron and ion density sources in (2.9) are

$$S_\sigma^n = \sum_\rho S_{\sigma,\rho}^n \,, \tag{2.54}$$

where $S_{\sigma,\rho}^n = \int \mathrm{d}\boldsymbol{v}\, \mathcal{S}_\sigma^\rho$, and $\rho = \mathrm{m.iz}, \mathrm{iz}$. It is apparent from the reactions, that neither dissociation nor charge-exchange collisions constitute a density source for the charged particles. The expression for molecular assisted ionization is

$$S_{\sigma,\mathrm{m.iz}}^n = \int \mathrm{d}\boldsymbol{v}\, \mathcal{S}_\mathrm{e,i}^\mathrm{m.iz} = \iint \mathrm{d}\boldsymbol{v}\mathrm{d}\boldsymbol{v}'\, f_\mathrm{m}(\boldsymbol{v}') f_\mathrm{e}(\boldsymbol{v}) \sigma_\mathrm{m.iz}(v_\mathrm{rel}) v_\mathrm{rel} \,, \tag{2.55}$$

where all velocity dependencies have been written explicitly. For all electron impact collisions it is assumed that the electron thermal speed $w = |\boldsymbol{w}|$, where $\boldsymbol{w} = \boldsymbol{v} - \boldsymbol{u}_\mathrm{e}$, is much higher than both the fluid speed, as well as the neutral fluid and thermal speeds. This allows for writing the relative velocity

$$v_\mathrm{rel} = |\boldsymbol{v} - \boldsymbol{v}'| \approx w \,, \tag{2.56}$$

and assuming a Maxwellian velocity distribution for the electrons, the integrals of (2.62) decouple and allows for writing

$$S_{\sigma,\mathrm{m.iz}}^n = \int \mathrm{d}\boldsymbol{v}'\, f_\mathrm{m}(\boldsymbol{v}') \int \mathrm{d}\boldsymbol{w}\, f_\mathrm{e}(\boldsymbol{w}) \sigma_\mathrm{m.iz}(w) w = n_\mathrm{m} n_\mathrm{e} \langle \sigma_\mathrm{m.iz} w \rangle \,, \tag{2.57}$$

and $\langle \cdot \rangle$ denotes the statistical average over velocity space

$$\langle ... \rangle \equiv \frac{\int \mathrm{d}\boldsymbol{v}\, ... f(\boldsymbol{v})}{\int \mathrm{d}\boldsymbol{v}\, f(\boldsymbol{v})} \,, \tag{2.58}$$

and where (2.5) has been applied to obtain the molecular and electron densities. The procedure for obtaining $S_{\sigma,\mathrm{iz}}^n$ is identical for that for $S_{\sigma,\mathrm{m.iz}}^n$, and result in

$$S_{\sigma,\mathrm{iz}}^n = n_\mathrm{a} n_\mathrm{e} \langle \sigma_\mathrm{iz} w \rangle \,, \tag{2.59}$$

where n_a is the atom density. The electron and ion density source (2.54) thus reads

$$\boxed{S_{e,i}^n = n_\mathrm{e} \left(n_\mathrm{a} \langle \sigma_\mathrm{iz} w \rangle + n_\mathrm{m} \langle \sigma_\mathrm{m.iz} w \rangle \right) \,,} \tag{2.60}$$

and describes the creation of charged particles from ionization of molecules and atoms.

The technique for obtaining the first order moment of the kinetic sources is similar to that for the zeroth moment. The momentum fluid source term is given by

$$\boldsymbol{S}_{\sigma}^{u} = \sum_{\rho} \boldsymbol{S}_{\sigma,\rho}^{u} \,, \tag{2.61}$$

with the structural difference from (2.54) that the sum for the ion momentum source now also includes a contribution from charge-exchange collisions, i.e., $\rho = \mathrm{m.iz}, \mathrm{iz}, \mathrm{cx}$. As for the density source, the contributions from molecular assisted ionization and atomic ionization are of the same form, and the former result from

$$\begin{aligned} \boldsymbol{S}_{\sigma,\mathrm{m.iz}}^{u} &= m_{\sigma} \int \mathrm{d}\boldsymbol{v}\, \boldsymbol{v} \mathcal{S}_{\mathrm{e,i}}^{\mathrm{m.iz}} \\ &= m_{\sigma} \iint \mathrm{d}\boldsymbol{v} \mathrm{d}\boldsymbol{v}'\, \boldsymbol{v}' f_{\mathrm{m}}(\boldsymbol{v}') f_{\mathrm{e}}(\boldsymbol{v}) \sigma_{\mathrm{m.iz}}(v_{\mathrm{rel}}) v_{\mathrm{rel}} \,. \end{aligned} \tag{2.62}$$

The decoupling of the integrals yields

$$\begin{aligned} \boldsymbol{S}_{\sigma,\mathrm{m.iz}}^{u} &= m_{\sigma} \int \mathrm{d}\boldsymbol{v}'\, \boldsymbol{v}' f_{\mathrm{m}}(\boldsymbol{v}') \int \mathrm{d}\boldsymbol{w}\, f_{\mathrm{e}}(\boldsymbol{w}) \sigma_{\mathrm{m.iz}}(w) w \\ &= m_{\sigma} \boldsymbol{u}_{\mathrm{m}} n_{\mathrm{m}} n_{\mathrm{e}} \langle \sigma_{\mathrm{m.iz}} w \rangle = m_{\sigma} \boldsymbol{u}_{\mathrm{m}} S_{\sigma,\mathrm{m.iz}}^{n} \,, \end{aligned} \tag{2.63}$$

where $\boldsymbol{u}_{\mathrm{m}}$ is the molecule fluid velocity. Similarly the momentum source resulting from atomic ionization is

$$\boldsymbol{S}_{\sigma,\mathrm{iz}}^{u} = m_{\sigma} \boldsymbol{u}_{\mathrm{a}} S_{\sigma,\mathrm{iz}}^{n} \,, \tag{2.64}$$

where $\boldsymbol{u}_{\mathrm{a}}$ is the atom fluid velocity. The electron momentum source thus reads

$$\boxed{\boldsymbol{S}_{\mathrm{e}}^{u} = m_{\mathrm{e}} \left(\boldsymbol{u}_{\mathrm{m}} S_{\mathrm{e,m.iz}}^{n} + \boldsymbol{u}_{\mathrm{a}} S_{\mathrm{e,iz}}^{n} \right) \,.} \tag{2.65}$$

The charge-exchange contribution to the ion momentum source is somewhat more difficult to obtain, as the collision involves particles of similar mass, which prevents the convenient decoupling of the velocity space integrals. It is possible to approximate the kinetic collision operator (2.49) following [47, 50], so that

$$\mathcal{S}_{\mathrm{i}}^{\mathrm{cx}} \approx \sigma_{\mathrm{cx}} \left(v_{\mathrm{i}}^{*} n_{\mathrm{i}} f_{\mathrm{a}} - v_{\mathrm{a}}^{*} n_{\mathrm{a}} f_{\mathrm{i}} \right) \tag{2.66}$$

where $\sigma_{\rm cx}$ is the cross-section for charge-exchange collisions, and $v^*_\sigma \equiv v_{{\rm T}\sigma}\big(\frac{4}{\pi}+|\boldsymbol{v}-\boldsymbol{v}_\sigma|^2/v^2_{{\rm T}\sigma}\big)^{1/2}$, for $\sigma = {\rm i,a}$. By decomposing the velocity into its mean and random components, the first moment of (2.49) can thus be approximated to

$$\begin{aligned}\boldsymbol{S}^u_{\rm i,cx} &\approx m_{\rm i}\int {\rm d}\boldsymbol{v}\,\boldsymbol{v}\sigma_{\rm cx}\left(v^*_{\rm i}n_{\rm i}f_{\rm a} - v^*_{\rm a}n_{\rm a}f_{\rm i}\right)\\ &= m_{\rm i}\left(n_{\rm i}\int {\rm d}\boldsymbol{v}\,\boldsymbol{v}\sigma_{\rm cx}v^*_{\rm i}f_{\rm a} - n_{\rm a}\int {\rm d}\boldsymbol{v}\,\boldsymbol{v}\sigma_{\rm cx}v^*_{\rm a}f_{\rm i}\right)\\ &= m_{\rm i}\left(\boldsymbol{u}_{\rm a}-\boldsymbol{u}_{\rm i}\right)S_{\rm cx} + \boldsymbol{R}_{\rm ia,cx} - \boldsymbol{R}_{\rm ai,cx}\,,\end{aligned} \tag{2.67}$$

where the charge-exchange reaction rate is

$$\begin{aligned}S_{\rm cx} &\equiv n_{\rm i}\int {\rm d}\boldsymbol{v}\,\sigma_{\rm cx}v^*_{\rm i}f_{\rm a} = n_{\rm a}\int {\rm d}\boldsymbol{v}\,\sigma_{\rm cx}v^*_{\rm a}f_{\rm i}\\ &\approx \sigma(v_{\rm cx})v_{\rm cx}n_{\rm i}n_{\rm a}\,,\end{aligned} \tag{2.68}$$

with the charge-exchange velocity $v_{\rm cx} = \big(\frac{4}{\pi}v^2_{T{\rm i}}+\frac{4}{\pi}v^2_{T{\rm a}}+u^2_{\rm ia}\big)^{1/2}$, $\boldsymbol{u}_{\rm ia}\equiv|\boldsymbol{u}_{\rm i}-\boldsymbol{u}_{\rm a}|$, and the friction terms are

$$\begin{aligned}\boldsymbol{R}_{\alpha\beta,{\rm cx}} &= m_{\rm i}\sigma_{\rm cx}n_\alpha\int {\rm d}\boldsymbol{v}\,\boldsymbol{w}v^*_\alpha f_\beta\\ &\approx (1-2\delta_{\alpha,{\rm i}})\,m_{\rm i}\sigma_{\rm cx}(v_{\rm cx})n_{\rm i}n_{\rm a}\boldsymbol{u}_{\rm ia}v^2_{T\beta}\left(\tfrac{16}{\pi}v^2_{T\alpha}+\tfrac{9\pi}{4}v^2_{T\beta}+4u^2_{ia}\right)^{-\frac{1}{2}}\end{aligned} \tag{2.69}$$

for $\alpha\beta = {\rm ai,ia}$ and thus the ion momentum source is

$$\boxed{\boldsymbol{S}^u_{\rm i} = m_{\rm i}\left[\boldsymbol{u}_{\rm m}S^n_{\rm i,m.iz} + \boldsymbol{u}_{\rm a}S^n_{\rm i,iz} + \left(\boldsymbol{u}_{\rm a}-\boldsymbol{u}_{\rm i}\right)S_{\rm i,cx}\right] + \boldsymbol{R}_{\rm ia,cx} - \boldsymbol{R}_{\rm ai,cx}\,.} \tag{2.70}$$

The interpretation of the physics of the momentum sources (2.65) and (2.70) is discussed in Sec. 2.1.2.

The second order moment of the kinetic source terms result in electron and ion pressure source terms

$$S^p_\sigma = \sum_\rho S^p_{\sigma,\rho}\,, \tag{2.71}$$

where, as for the momentum source, $\rho = {\rm m.iz,iz,cx}$, and $S^p_{\sigma,\rho} = \frac{1}{2}m_\sigma\int {\rm d}\boldsymbol{v}\,v^2\mathcal{S}^\rho_\sigma$. Again by splitting the neutral velocity into its random and mean components and decoupling the integrals, the contributions to (2.22) from electron impact

reactions are

$$\begin{aligned} S^p_{\sigma,\mathrm{m.iz}} &= \tfrac{1}{2} m_\sigma \iint \mathrm{d}\boldsymbol{v}\mathrm{d}\boldsymbol{v}'\, v'^2 f_\mathrm{m}(\boldsymbol{v}') f_\mathrm{e}(\boldsymbol{v}) \sigma_\mathrm{m.iz}(v_\mathrm{rel}) v_\mathrm{rel} \\ &= \tfrac{1}{2} m_\sigma \left(u_\mathrm{m}^2 \int \mathrm{d}\boldsymbol{v}'\, f_\mathrm{m}(\boldsymbol{v}') + \int \mathrm{d}\boldsymbol{v}'\, w'^2 f_\mathrm{m}(\boldsymbol{v}') \right) \int \mathrm{d}\boldsymbol{w}\, f_\mathrm{e}(\boldsymbol{w}) \sigma_\mathrm{m.iz}(w) w \\ &= \tfrac{1}{2} m_\sigma \left(u_\mathrm{m}^2 n_\mathrm{m} + \tfrac{3}{2} n_\mathrm{m} v_{T\mathrm{m}}^2 \right) n_\mathrm{e} \langle \sigma_\mathrm{m.iz} w \rangle = \tfrac{1}{2} m_\sigma \left(u_\mathrm{m}^2 + \tfrac{3}{2} v_{T\mathrm{m}}^2 \right) S^n_{\sigma,\mathrm{m.iz}} \,, \end{aligned} \tag{2.72}$$

assuming a Maxwellian velocity distribution for f_m, and similar

$$S^p_{\sigma,\mathrm{iz}} = \tfrac{1}{2} m_\sigma \left(u_\mathrm{a}^2 + \tfrac{3}{2} v_{T\mathrm{a}}^2 \right) S^n_{\sigma,\mathrm{iz}} \,. \tag{2.73}$$

For both ionization processes the source terms (2.72) and (2.73) represent the addition of kinetic energy and heat to the existing energy density, that result from producing new particles at a finite velocity or temperature. For every inelastic collision in the model, an additional term has to be added to the electron pressure source, namely that which represents the loss of energy to the inelastic process, e.g., the ionization energy for atoms, or the ionization and dissociation energies for molecules. The resulting electron pressure source is

$$\boxed{\begin{aligned} S^p_\mathrm{e} = &\left[\tfrac{1}{2} m_\mathrm{e} \left(u_\mathrm{a}^2 + \tfrac{3}{2} v_{T\mathrm{a}}^2 \right) - \phi_\mathrm{iz} \right] S^n_{\mathrm{e,iz}} \\ &+ \left[\tfrac{1}{2} m_\mathrm{e} \left(u_\mathrm{m}^2 + \tfrac{3}{2} v_{T\mathrm{m}}^2 \right) - \phi_\mathrm{m.iz} \right] S^n_{\mathrm{e,m.iz}} - \phi_\mathrm{dis} S_\mathrm{e,dis} \,, \end{aligned}} \tag{2.74}$$

where $S_\mathrm{e,dis} = n_\mathrm{m} n_\mathrm{e} \langle \sigma_\mathrm{dis} w \rangle$. It is observed that the electron energy density source is has two types of contributions; the first is from the creation of kinetic electrons, and the second is from the loss of energy due to the reaction potentials. The reaction energy losses do not enter the ion pressure equation, which instead has a contribution from heating from charge-exchange collisions

$$\begin{aligned} S^p_\mathrm{i,cx} &= \int \mathrm{d}\boldsymbol{v}\, v^2 \mathcal{S}^\mathrm{cx}_\mathrm{i} \\ &= \int \mathrm{d}\boldsymbol{v}\, v^2 \left[f_\mathrm{a}(v) \int \mathrm{d}\boldsymbol{v}'\, f_\mathrm{i}(v') \sigma_\mathrm{cx} v_\mathrm{rel} - f_\mathrm{i}(v) \int \mathrm{d}\boldsymbol{v}'\, f_\mathrm{a}(v) \sigma_\mathrm{cx} v_\mathrm{rel} \right] . \end{aligned} \tag{2.75}$$

As for the momentum source, and again following [47, 50], several approximations to the velocity integrals can be made, which allow for writing the above as

$$\begin{aligned} S^p_{i,cx} \approx &\tfrac{1}{2} m_\mathrm{i} \left(u_\mathrm{a}^2 - u_\mathrm{i}^2 \right) S^\mathrm{cx}_\mathrm{i} + \boldsymbol{u}_\mathrm{a} \cdot \boldsymbol{R}^\mathrm{cx}_\mathrm{ia} - \boldsymbol{u}_\mathrm{i} \cdot \boldsymbol{R}^\mathrm{cx}_\mathrm{ai} \\ &+ \tfrac{1}{2} m_\mathrm{i} \int \mathrm{d}\boldsymbol{v}\, w^2 \left(n_\mathrm{i} v^*_\mathrm{i} \sigma_\mathrm{cx} f_\mathrm{a} - n_\mathrm{a} v^*_\mathrm{a} \sigma_\mathrm{cx} f_\mathrm{i} \right) . \end{aligned} \tag{2.76}$$

The terms represent energy exchange from exchange of momentum, as well as frictious heating. The last term represents the change in energy density from heat transfer, and with $Q^{\mathrm{cx}}_{\alpha\beta} \equiv \frac{1}{2} m_{\mathrm{i}} \int \mathrm{d}\boldsymbol{v}\, w^2 n_\alpha v^*_\alpha \sigma_{\mathrm{cx}} f_\beta$, for $\alpha\beta = \mathrm{ai}, \mathrm{ia}$, the heat transfer terms can be approximated to

$$Q^{\mathrm{cx}}_{\alpha\beta} \approx \tfrac{3}{4} m_{\mathrm{i}} \sigma_{\mathrm{cx}} n_{\mathrm{i}} n_{\mathrm{a}} v^2_{T\beta} \left(\tfrac{4}{\pi} v^2_{T\alpha} + \tfrac{64\pi}{9} v^2_{T\beta} + u^2_{ia} \right)^{\frac{1}{2}} . \tag{2.77}$$

The energy density source terms from charge-exchange adds to those of (2.72) and (2.73) to yield the inelastic ion pressure source

$$\boxed{\begin{aligned} S^p_{\mathrm{i}} = {} & \tfrac{1}{2} m_{\mathrm{i}} \left[\left(u^2_{\mathrm{a}} + \tfrac{3}{2} v^2_{T\mathrm{a}} \right) S^n_{\mathrm{i,iz}} + \left(u^2_{\mathrm{m}} + \tfrac{3}{2} v^2_{T\mathrm{m}} \right) S^n_{\mathrm{i,m.iz}} + \left(u^2_{\mathrm{a}} - u^2_{\mathrm{i}} \right) S^{\mathrm{cx}}_{\mathrm{i}} \right] \\ & + \boldsymbol{u}_{\mathrm{a}} \cdot \boldsymbol{R}^{\mathrm{cx}}_{\mathrm{ia}} - \boldsymbol{u}_{\mathrm{i}} \cdot \boldsymbol{R}^{\mathrm{cx}}_{\mathrm{ai}} + Q^{\mathrm{cx}}_{\mathrm{ia}} - Q^{\mathrm{cx}}_{\mathrm{ai}} , \end{aligned}} \tag{2.78}$$

where the first two terms are similar to those of the electron pressure equation (2.74). The third term is of the same origin and represents the change in energy due to removing and adding ions with different kinetic energies. The last terms are caused by frictious heating and heat transfer in charge-exchange collisions.

This concludes the formal derivation of the source terms, both from elastic and inelastic collisions with neutrals, for the two-fluid equations. Although the present model only contains a limited number of interactions, the procedure which is mapped out here is generic, and should easily provide other inelastic source terms, such as that for recombination of electrons and ions into atoms, of atoms into molecules, or other dissociation channels for molecules.

Before seeking out a fluid model for describing the transport of neutral fields, a series of approximations are introduced in the following section to rewrite the two-fluid equations in terms of the so-called fluid drift velocities. This allows for obtaining a set of drift-fluid equations that resolve the coherent SOL dynamics spatially and temporally, and which are the foundation of the plasma part of the nHESEL equations.

2.1.2 Drift-fluid equations

Although the momentum equations are complete after the analysis presented in Sec. 2.1.1, further approximations to the system can be made, which both reduce the number of fields and also give insight into the defining transport

mechanism at time- and length-scales of interest. The technique applied here is called drift-ordering [37, 51, 52]. The procedure is initiated by decomposing the momentum equation (2.26) into terms that are parallel or perpendicular to the magnetic field lines, and order the terms of the latter. For the sake of readability the species index σ is implicit in the following derivation. The perpendicular part of the momentum equation can be written

$$\begin{aligned} \mathbf{0} = \frac{1}{\Omega_{\mathrm{ci}}} \mathrm{d}_t \boldsymbol{u}_\perp + \frac{\nabla_\perp p}{nqB} + \frac{(\nabla \cdot \boldsymbol{\pi})_\perp}{nqB} - \frac{\boldsymbol{E}_\perp}{B} - \boldsymbol{u}_\perp \times \hat{\boldsymbol{B}} \\ - \frac{\boldsymbol{R}_\perp}{nqB} - \frac{\boldsymbol{S}^u_\perp}{nqB} + \frac{m\boldsymbol{u}_\perp S^n}{nqB} \,, \end{aligned} \tag{2.79}$$

where $\hat{\boldsymbol{B}}$ is the magnetic field unit vector, and the perpendicular projection of some vector $\boldsymbol{a}$ is

$$\boldsymbol{a}_\perp \equiv \boldsymbol{a} - \hat{\boldsymbol{B}}\hat{\boldsymbol{B}} \cdot \boldsymbol{a} \,, \tag{2.80}$$

which also defines the perpendicular derivative for $\boldsymbol{a} = \nabla$.

Drift ordering is an iterative method for ordering the terms in equations (2.79) according to their relative magnitude. This will then subsequently allow for ordering $\boldsymbol{u}_\perp$ and simplify the fluid equations in the limit where the drift-ordering is valid. The ordering is obtained by assuming the defining time- and length-scales are much larger than those set by the gyro-motion of charged particles. The characteristic time-scales related to the temporal derivative and advection terms

$$|\partial_t| \sim \omega_{\mathrm{char}} \,, \qquad |\boldsymbol{u} \cdot \nabla| \sim |\boldsymbol{u} \cdot \boldsymbol{k}_{\mathrm{char}}| \,, \tag{2.81}$$

are both assumed small compared to the ion (and thus the electron) cyclotron frequency $\Omega_{\mathrm{ci}} = q_{\mathrm{i}}B/m_{\mathrm{i}}$, i.e.,

$$\frac{|\omega_{\mathrm{char}}|}{|\Omega_{\mathrm{ci}}|}, \frac{|\boldsymbol{u} \cdot \boldsymbol{k}_{\mathrm{char}}|}{|\Omega_{\mathrm{ci}}|} \ll 1 \,. \tag{2.82}$$

This assumption naturally orders the first term with the time derivative in (2.79)

$$\frac{1}{\Omega_{\mathrm{ci}}} \mathrm{d}_t \boldsymbol{u}_\perp = \left[\frac{\partial_t}{\Omega_{\mathrm{ci}}} + \frac{\boldsymbol{u} \cdot \nabla}{\Omega_{\mathrm{ci}}} \right] \boldsymbol{u}_\perp \,. \tag{2.83}$$

Likewise, the collision frequency between particles ν is assumed small compared to the cyclotron frequency

$$\frac{\nu}{\Omega_{\mathrm{ci}}} \ll 1 \,, \tag{2.84}$$

which affects the friction term as $\boldsymbol{R} \propto \nu n m$ according to (2.44), and thus

$$\frac{\boldsymbol{R}}{nqB} \propto \frac{\nu n m}{nqB} = \frac{\nu}{\Omega_{\mathrm{ci}}} \,. \tag{2.85}$$

The assumption on the collision frequency likewise orders the perpendicular viscous term $\frac{(\nabla\cdot\boldsymbol{\pi})_\perp}{nqB}$, as well as the inelastic source terms $\frac{\boldsymbol{S}^u_\perp}{nqB}$ and $\frac{m\boldsymbol{u}_\perp S^n}{nqB}$. All considered time-scale setting quantities are assumed to be of the same order, i.e.,

$$\frac{\nu}{\Omega_{\mathrm{ci}}} \sim \frac{\Omega_{\mathrm{char}}}{\Omega_{\mathrm{ci}}} \sim \frac{\boldsymbol{u}\cdot\boldsymbol{k}_{\mathrm{char}}}{\Omega_{\mathrm{ci}}} \,, \tag{2.86}$$

and all terms proportional to these factors are labelled with an ϵ. Note that the ϵ is only a label of smallness, that indicates the order of a given term, and not a small factor itself. Terms labelled with ϵ^0 are thus larger than those with ϵ^1, which are larger than ϵ^2 terms, and so forth. There is no reason to assume that the remaining terms in (2.79) are small, and they will thus carry the ϵ^0 label. The labelled perpendicular momentum equation reads

$$\begin{aligned} \boldsymbol{0} =& \epsilon^0 \left[\frac{\nabla_\perp p}{nqB} - \frac{\boldsymbol{E}_\perp}{B} - \boldsymbol{u}_\perp \times \hat{\boldsymbol{B}} \right] \\ &+ \epsilon^1 \left[\frac{1}{\Omega_{\mathrm{ci}}} \mathrm{d}_t \boldsymbol{u}_\perp + \frac{(\nabla\cdot\boldsymbol{\pi})_\perp}{nqB} - \frac{\boldsymbol{R}_\perp}{nqB} - \frac{\boldsymbol{S}^u_\perp}{nqB} + \frac{m\boldsymbol{u}_\perp S^n}{nqB} \right] . \end{aligned} \tag{2.87}$$

Each term carries the unit of velocity, and it is natural to assume that there likewise exists an ordering of the fluid velocities, i.e., that one can write

$$\boldsymbol{u}_\perp = \epsilon^0 \boldsymbol{u}_{\perp,0} + \epsilon^1 \boldsymbol{u}_{\perp,1} + \epsilon^2 \boldsymbol{u}_{\perp,2} + \dots \,. \tag{2.88}$$

Such ordering allows for solving the momentum equation iteratively. Working only to first order, it is sufficient to assume that the fluid velocity can be written $\boldsymbol{u}_\perp = \epsilon^0 \boldsymbol{u}_{\perp,0} + \epsilon^1 \boldsymbol{u}_{\perp,1}$. With this ordering the momentum equation reads

$$\begin{aligned} \boldsymbol{0} =& \epsilon^0 \left[\frac{\nabla_\perp p}{nqB} - \frac{\boldsymbol{E}_\perp}{B} - \left(\epsilon^0 \boldsymbol{u}_{\perp,0} + \epsilon^1 \boldsymbol{u}_{\perp,1}\right) \times \hat{\boldsymbol{B}} \right] \\ &+ \epsilon^1 \left[\frac{1}{\Omega_{\mathrm{ci}}} \mathrm{d}_t \left(\epsilon^0 \boldsymbol{u}_{\perp,0} + \epsilon^1 \boldsymbol{u}_{\perp,1}\right) + \frac{(\nabla\cdot\boldsymbol{\pi})_\perp}{nqB} - \frac{\boldsymbol{R}_\perp}{nqB} - \frac{\boldsymbol{S}^u_\perp}{nqB} \right. \\ &\left. + \frac{m\left(\epsilon^0 \boldsymbol{u}_{\perp,0} + \epsilon^1 \boldsymbol{u}_{\perp,1}\right) S^n}{nqB} \right] . \end{aligned} \tag{2.89}$$

Note that the material derivative also contains $\boldsymbol{u}_\perp$ and must also be ordered accordingly.

The ordered momentum equation (2.89) can now be solved iteratively order by order. To 0^{th} order it reads

$$\frac{\nabla_\perp p}{nqB} - \frac{\boldsymbol{E}_\perp}{B} - \boldsymbol{u}_{\perp,0} \times \hat{\boldsymbol{B}} = \boldsymbol{0}\,. \tag{2.90}$$

Crossing the equation with $\hat{\boldsymbol{B}}$ from the right allows for solving for $\boldsymbol{u}_{\perp,0}$, as for some vector $\boldsymbol{a}$

$$\left(\boldsymbol{a} \times \hat{\boldsymbol{B}}\right) \times \hat{\boldsymbol{B}} = \left(\boldsymbol{a} \cdot \hat{\boldsymbol{B}}\right) \hat{\boldsymbol{B}} - \left(\hat{\boldsymbol{B}} \cdot \hat{\boldsymbol{B}}\right) \boldsymbol{a} = -\boldsymbol{a} \tag{2.91}$$

which allows for rewriting (2.91) to

$$\boxed{\boldsymbol{u}_{\perp,0} = -\frac{\nabla_\perp p \times \hat{\boldsymbol{B}}}{qnB} - \frac{\nabla_\perp \phi \times \hat{\boldsymbol{B}}}{B}\,,} \tag{2.92}$$

where the electrostatic approximation has been applied to write $\boldsymbol{E}_\perp = -\nabla_\perp \phi$. The first term in (2.92) is recognized as the diamagnetic drift $\boldsymbol{u}_d$, and the second term as the $E\times B$ drift $\boldsymbol{u}_E$. The $E\times B$ drift already emerged in (1.16) from the analysis of single particle motion in Sec. 1.3, and is perhaps best understood in the particle picture. A gyrating particle experiencing an electric field perpendicular to its plane of gyration is accelerated by the field in half of the orbit, and decelerated in the other half. The acceleration increases the gyration velocity, and thus the Larmor radius, resulting in an orbital motion that does not close upon itself, but instead effectively advects the particle in a direction perpendicular to the electric and magnetic fields. The diamagnetic drift can also be understood in the particle picture, where a pressure gradient perpendicular to the plane of gyration effectively causes more particles in a local volume element to move in one direction, perpendicular to the pressure gradient, than in the opposite. The particles, however, stay in their orbits and the diamagnetic drift is thus not advecting any particles as is the case for the $E\times B$ drift.

The 1^{st} order perpendicular terms are now obtained by subtracting the 0^{th} order equation from (2.89) and truncate higher-order terms, which yields

$$\boldsymbol{0} = \boldsymbol{u}_{\perp,1} \times \hat{\boldsymbol{B}} + \frac{1}{\Omega_{\text{ci}}}\, \mathrm{d}_t \boldsymbol{u}_{\perp,0} + \frac{(\nabla \cdot \boldsymbol{\pi})_\perp}{nqB} - \frac{\boldsymbol{R}_\perp}{nqB} - \frac{\boldsymbol{S}^u_\perp}{nqB} + \frac{m\boldsymbol{u}_{\perp,0} S^n}{nqB}\,. \tag{2.93}$$

The equation is now solved by inserting $\boldsymbol{u}_{\perp,0}$ from (2.92), and again crossing the equation with $\hat{\boldsymbol{B}}$, applying (2.91). This allows for solving for $\boldsymbol{u}_{\perp,1}$ and yields

$$\boxed{\begin{aligned}\boldsymbol{u}_{\perp,1} = &-\frac{1}{\Omega_{\mathrm{ci}}}\mathrm{d}_t\left(\frac{\nabla_\perp p}{qnB}+\frac{\nabla_\perp \phi}{B}\right)-\frac{(\nabla\cdot\boldsymbol{\pi})_\perp\times\hat{\boldsymbol{B}}}{nqB}\\ &+\frac{\boldsymbol{R}_\perp\times\hat{\boldsymbol{B}}}{nqB}+\frac{\boldsymbol{S}^u_\perp\times\hat{\boldsymbol{B}}}{nqB}-\left(\frac{\nabla_\perp p}{qnB}+\frac{\nabla_\perp\phi}{B}\right)\frac{mS^n}{nqB}.\end{aligned}} \tag{2.94}$$

The first two terms on the RHS are identified as well-known drifts, namely the polarization drift $\boldsymbol{u}_p$, and the viscous drift $\boldsymbol{u}_\pi$. The third term $\boldsymbol{u}_R$ is the sum of the resistive drift and the so-called Pedersen drift [53] which results from elastic collisions with neutrals. By the perpendicular projections of (2.42) and (2.44) the $\boldsymbol{u}_{\mathrm{e},R}$ reads

$$\begin{aligned}\boldsymbol{u}_{\mathrm{e},R} = &-\frac{\boldsymbol{R}_{\mathrm{e}\perp}\times\hat{\boldsymbol{B}}}{n_{\mathrm{e}}eB}=\frac{1}{n_{\mathrm{e}}eB}\Bigg[\frac{m_{\mathrm{e}}n_{\mathrm{e}}}{\tau_{\mathrm{ei}}}\left[(\boldsymbol{u}_{\mathrm{e},d}+\boldsymbol{u}_E)-(\boldsymbol{u}_{\mathrm{i},d}+\boldsymbol{u}_E)\right]\\ &+0.71n_{\mathrm{e}}\nabla_\perp T_{\mathrm{e}}+\frac{3}{2}\frac{n_{\mathrm{e}}}{\Omega_{\mathrm{ce}}\tau_{ei}}\hat{\boldsymbol{B}}\times\nabla_\perp T_{\mathrm{e}}\\ &+n_{\mathrm{e}}n_{\mathrm{n}}m_{\mathrm{en}}\tfrac{4}{3}\pi a_0^2\left(\frac{8}{\pi}\frac{T_{\mathrm{e}}}{m_{\mathrm{en}}}\right)^{\frac{1}{2}}\left((\boldsymbol{u}_{\mathrm{e},d}+\boldsymbol{u}_E)-\boldsymbol{u}_{\mathrm{n},\perp}\right)\Bigg]\times\hat{\boldsymbol{B}}\\ =&\Bigg[\frac{1}{n_{\mathrm{e}}m_{\mathrm{e}}\tau_{\mathrm{ei}}\Omega_{\mathrm{ce}}^2}\nabla_\perp(p_{\mathrm{e}}+p_{\mathrm{i}})\times\hat{\boldsymbol{B}}\\ &+\frac{0.71}{eB}\nabla_\perp T_{\mathrm{e}}+\frac{3}{2}\frac{1}{\Omega_{\mathrm{ce}}^2 m_{\mathrm{e}}\tau_{ei}}\nabla_\perp T_{\mathrm{e}}\times\hat{\boldsymbol{B}}\\ &+\frac{8\sqrt{2}}{3\pi^{\frac{3}{2}}\Omega_{\mathrm{ce}}\tau_{\mathrm{en}}}\left[\left(\frac{\nabla_\perp p_{\mathrm{e}}}{en_{\mathrm{e}}B}-\frac{\nabla_\perp\phi}{B}\right)\times\hat{\boldsymbol{B}}-\boldsymbol{u}_{\mathrm{n},\perp}\right]\Bigg]\times\hat{\boldsymbol{B}}\\ =&-\frac{\nabla_\perp(p_{\mathrm{e}}+p_{\mathrm{i}})}{n_{\mathrm{e}}m_{\mathrm{e}}\tau_{\mathrm{ei}}\Omega_{\mathrm{ce}}^2}+\frac{0.71}{eB}\nabla_\perp T_{\mathrm{e}}\times\hat{\boldsymbol{B}}-\frac{3}{2}\frac{\nabla_\perp T_{\mathrm{e}}}{\Omega_{\mathrm{ce}}^2 m_{\mathrm{e}}\tau_{ei}}\\ &+\frac{8\sqrt{2}}{3\pi^{\frac{3}{2}}\Omega_{\mathrm{ce}}\tau_{\mathrm{en}}}\left[\left(\frac{\nabla_\perp\phi}{B}-\frac{\nabla_\perp p_{\mathrm{e}}}{en_{\mathrm{e}}B}\right)-\boldsymbol{u}_{\mathrm{n},\perp}\times\hat{\boldsymbol{B}}\right].\end{aligned} \tag{2.95}$$

The first term involving only the pressure gradients is the drift due to the collisional friction force, the following two terms containing the temperature gradients constitute the thermal force drift, and the last term is the Pedersen drift $\boldsymbol{u}_{\mathrm{e},R_{\mathrm{n}}}$ caused by neutral collisions. Returning to (2.94) the last two terms appear when inelastic momentum or density source terms from plasma-neutral interactions are present, and are denoted the momentum source drift

$\boldsymbol{u}_{S^u}$ and the density source drift $\boldsymbol{u}_{S^n}$. The polarization drift arises since the charged particles are accelerated when the leading order drifts vary in time. The acceleration causes a motion of the particles as if they are influenced by an inertial force equal to the product of their mass and the acceleration, and thus result in an inertial drift term. The viscous drift, and the frictious part of the resistive drift, including the Pedersen drift, are caused by change in momentum due to collisions with other particles, whereas the thermal force part of the resistive drift is caused by the temperature dependence in the collisionality (2.38), and thus changes along the gradient of that, resulting in a net motion in the gyration plane perpendicular to $\nabla_\perp T$. For the inelastic source drifts it is advantageous to consider both terms at once, i.e.,

$$\begin{aligned}\boldsymbol{u}_{\mathrm{i}S^n} + \boldsymbol{u}_{\mathrm{i}S^u} &= \frac{m_\mathrm{i}\boldsymbol{u}_{\mathrm{i},\perp,0}S_\mathrm{i}^n \times \hat{\boldsymbol{B}}}{nqB} - \frac{\boldsymbol{S}_{\mathrm{i},\perp}^u \times \hat{\boldsymbol{B}}}{nqB} \\ &= \frac{(\boldsymbol{u}_{\mathrm{m},\perp} - \boldsymbol{u}_{\mathrm{i},\perp,0})\, S_{\mathrm{i,m.iz}}^n \times \hat{\boldsymbol{B}}}{n_\mathrm{i}\Omega_\mathrm{ci}} + \frac{(\boldsymbol{u}_{\mathrm{a},\perp} - \boldsymbol{u}_{\mathrm{i},\perp,0})\, S_{\mathrm{i,iz}}^n \times \hat{\boldsymbol{B}}}{n_\mathrm{i}\Omega_\mathrm{ci}} \\ &\quad + \frac{(\boldsymbol{u}_{\mathrm{a},\perp} - \boldsymbol{u}_{\mathrm{i},\perp,0})\, S_{\mathrm{i,cx}} \times \hat{\boldsymbol{B}}}{n_\mathrm{i}\Omega_\mathrm{ci}} + \frac{\boldsymbol{R}_{\mathrm{ia,cx},\perp} \times \hat{\boldsymbol{B}}}{n_\mathrm{i}eB} - \frac{\boldsymbol{R}_{\mathrm{ai,cx},\perp} \times \hat{\boldsymbol{B}}}{n_\mathrm{i}eB}\,.\end{aligned} \tag{2.96}$$

The inelastic source drifts reveal two types of contributions to the drifts; those from density sources (including that for charge-exchange collisions), and those from the friction force between ions and atoms in charge-exchange collisions. The density sources are observed to vanish if the neutral velocity equals that of the ions, which indicates the physical nature of the drift. The drift arises when neutrals, which typically have a much lower bulk speed than the ions, are created, resulting in ions that move much slower than the average ions. This is expressed in the drift-fluid equations as negative drifts proportional to the ion sources. The last two terms are, like the frictious drift resulting from collisions, except in this case the collisions are those from charge-exchange, and the sum of the two terms represent the loss of momentum due to charge-exchange collisions with neutral atoms. For the electron source drifts only the first two terms of (2.96), with charge and mass replaced by those of the electron, are present.

This concludes the drift ordering, as the fluid velocity

$$\boxed{\boldsymbol{u}_\perp = \boldsymbol{u}_{\perp,0} + \boldsymbol{u}_{\perp,1}\,,} \tag{2.97}$$

can now be reinserted in the continuity (2.25) and heat (2.27) equations, resulting in two equations for the densities and two equations for the pressures,

assuming that the parallel velocities are accounted for, e.g., by parametrizing the transport. Using quasi-neutrality and subtracting the two density equations yields a system of one density equation, one equation for the vorticity and two heat equations. This set of equations is denoted the drift-fluid equations. In the following the drift-fluid equations are examined in more detail, and a series of additional approximations result in the so-called HESEL equations [37] augmented with neutral source terms.

The direct application of the drift-ordering to the continuity equation in (2.25) result in the electron density equation

$$\begin{aligned}\partial_t n_\mathrm{e} &= S_\mathrm{e}^n - \nabla\cdot\left[n_\mathrm{e}\left(\boldsymbol{u}_{\mathrm{e},\perp}+\boldsymbol{u}_{\mathrm{e},\parallel}\right)\right] \\ &= S_\mathrm{e}^n - \nabla\cdot\left[n_\mathrm{e}\left(\boldsymbol{u}_{\mathrm{e},d}+\boldsymbol{u}_E+\boldsymbol{u}_{\mathrm{e},p}+\boldsymbol{u}_{\mathrm{e},\pi}+\boldsymbol{u}_{\mathrm{e},R}+\boldsymbol{u}_{\mathrm{e},S^u}+\boldsymbol{u}_{\mathrm{e},S^n}+\boldsymbol{u}_{\mathrm{e},\parallel}\right)\right] .\end{aligned} \tag{2.98}$$

The electron density equation (2.98) is in principle valid as is, but can be simplified as some drift terms are formally smaller by the electron mass. The negligible terms are the polarization drift $\boldsymbol{u}_{\mathrm{e},p}$ as well as the elastic and inelastic neutral drift terms $\boldsymbol{u}_{\mathrm{e},R_\mathrm{n}}$, $\boldsymbol{u}_{\mathrm{e},S^u}$, and $\boldsymbol{u}_{\mathrm{e},S^n}$, and the electron viscous drift $\boldsymbol{u}_{\mathrm{e},\pi}$, which also proves to be a ϵ^2 term as found in [37].

Thus, the electron density equation in (2.98) is reduced to

$$\boxed{\partial_t n_\mathrm{e} = S_\mathrm{e}^n - \nabla\cdot\left[n_\mathrm{e}\left(\boldsymbol{u}_{\mathrm{e},d}+\boldsymbol{u}_E+\boldsymbol{u}_{\mathrm{e},R}+\boldsymbol{u}_{\mathrm{e},\parallel}\right)\right] .} \tag{2.99}$$

For the ion density equation, neglecting the small drift terms in the corresponding electron density equation is not possible, and all terms in the ion version of (2.98) are retained. This result in the ion density equation

$$\begin{aligned}\partial_t n_\mathrm{i} = S_\mathrm{i}^n - \nabla\cdot\Big[n_\mathrm{i}\big(&\boldsymbol{u}_{\mathrm{i},d}+\boldsymbol{u}_E+\boldsymbol{u}_{\mathrm{i},p}+\boldsymbol{u}_{\mathrm{i},\pi}+\boldsymbol{u}_{\mathrm{i},R} \\ &+\boldsymbol{u}_{\mathrm{i},S^u}+\boldsymbol{u}_{\mathrm{i},S^n}+\boldsymbol{u}_{\mathrm{i},\parallel}\big)\Big] .\end{aligned} \tag{2.100}$$

The assumption of quasi-neutrality, i.e., that $n_\mathrm{e} = n_\mathrm{i}$, can be applied to trade one of the density equations (typically the more complicated ion density equation) for an equation for the vorticity $\omega = \nabla^2\phi$. Assuming a quasi-neutral plasma and for equal density sources $S_\mathrm{e}^n = S_\mathrm{i}^n$, subtracting (2.99) from (2.100) yields the vorticity equation

$$\boxed{\begin{aligned}0 = \nabla\cdot\Big[n_\mathrm{e}\big(&(\boldsymbol{u}_{\mathrm{i},d}-\boldsymbol{u}_{\mathrm{e},d})+\boldsymbol{u}_{\mathrm{i},p}+\boldsymbol{u}_{\mathrm{i},\pi}+\boldsymbol{u}_{\mathrm{i},R_\mathrm{n}} \\ &+\boldsymbol{u}_{\mathrm{i},S^u}+\boldsymbol{u}_{\mathrm{i},S^n}\big)+\tfrac{1}{e}\boldsymbol{j}_\parallel\Big] .\end{aligned}} \tag{2.101}$$

It may not be clear from the above that this equation describes the evolution of the vorticity, but the time derivative of the (generalized) vorticity emerges from the divergence of the ion polarization and viscous drifts.

The equations for the energy densities are obtained directly from inserting (2.97) into (2.24), and result in

$$\begin{aligned}
&\tfrac{3}{2}\partial_t p_\mathrm{e} + \tfrac{3}{2}\nabla\cdot\left[p_\mathrm{e}\left(\boldsymbol{u}_{\mathrm{e},d}+\boldsymbol{u}_E+\boldsymbol{u}_{\mathrm{e},R}+\boldsymbol{u}_{\mathrm{e},\parallel}\right)\right] \\
&\qquad + p_\mathrm{e}\nabla\cdot\left(\boldsymbol{u}_{\mathrm{e},d}+\boldsymbol{u}_E+\boldsymbol{u}_{\mathrm{e},R}+\boldsymbol{u}_{\mathrm{e},\parallel}\right) + \nabla\cdot\boldsymbol{q}_\mathrm{e} \\
&\quad = Q_\mathrm{e} - \left(\boldsymbol{u}_{\mathrm{e},d}+\boldsymbol{u}_E\right)\cdot\boldsymbol{R}_\mathrm{e} + S^p_\mathrm{e} \\
&\qquad - \left(\boldsymbol{u}_{\mathrm{e},d}+\boldsymbol{u}_E\right)\cdot\boldsymbol{S}^u_\mathrm{e} + \tfrac{1}{2}m_\mathrm{e}\left(\boldsymbol{u}_{\mathrm{e},d}+\boldsymbol{u}_E\right)^2 S^n_\mathrm{e}\,,
\end{aligned} \tag{2.102}$$

and

$$\begin{aligned}
&\tfrac{3}{2}\partial_t p_\mathrm{i} + \tfrac{3}{2}\nabla\cdot\big[p_\mathrm{i}\big(\boldsymbol{u}_{\mathrm{i},d}+\boldsymbol{u}_E+\boldsymbol{u}_{\mathrm{i},p}+\boldsymbol{u}_{\mathrm{i},\pi}+\boldsymbol{u}_{\mathrm{i},R} \\
&\qquad\qquad + \boldsymbol{u}_{\mathrm{i},S^u}+\boldsymbol{u}_{\mathrm{i},S^n}+\boldsymbol{u}_{\mathrm{i},\parallel}\big)\big] \\
&\qquad + p_\mathrm{i}\nabla\cdot\left(\boldsymbol{u}_{\mathrm{i},d}+\boldsymbol{u}_E+\boldsymbol{u}_{\mathrm{i},p}+\boldsymbol{u}_{\mathrm{i},\pi}+\boldsymbol{u}_{\mathrm{i},R}+\boldsymbol{u}_{\mathrm{i},S^u}+\boldsymbol{u}_{\mathrm{i},S^n}+\boldsymbol{u}_{\mathrm{i},\parallel}\right) \\
&\qquad + \boldsymbol{\pi}_\mathrm{i} : \nabla\left(\boldsymbol{u}_{\mathrm{i},d}+\boldsymbol{u}_E\right) + \nabla\cdot\boldsymbol{q}_\mathrm{i} \\
&\quad = Q_\mathrm{i} - \left(\boldsymbol{u}_{\mathrm{i},d}+\boldsymbol{u}_E\right)\cdot\boldsymbol{R}_\mathrm{i} + S^p_\mathrm{i} \\
&\qquad - \left(\boldsymbol{u}_{\mathrm{i},d}+\boldsymbol{u}_E\right)\cdot\boldsymbol{S}^u_\mathrm{i} + \tfrac{1}{2}m_\mathrm{i}\left(\boldsymbol{u}_{\mathrm{i},d}+\boldsymbol{u}_E\right)^2 S^n_\mathrm{i}\,.
\end{aligned} \tag{2.103}$$

The term with the electron viscosity vanish, as this is formally of order ϵ^2 [54]. The parallel velocity is still undefined at this point, and thus requires for the parallel momentum equation to be solved, unless parallel transport is parametrized as in the following section.

The drift-fluid equations constituted by that for the evolution of the electron density (2.99), the vorticity (2.101), and of the electron and ion pressures (2.102) and (2.103), are subject to yet another series of approximations before the nHESEL equations are obtained. The approximations concern the terms involving the velocities that do not originate from neutral interactions and are thus for the purpose of this work of less interest. In the following section the necessary steps to obtain the nHESEL equations are outlined.

2.1.3 nHESEL equations

In this section the final steps necessary for deriving the nHESEL equations, i.e., the original HESEL (**H**ot **E**dge **S**OL **EL**ectrostatic) equations [37] aug-

mented with **n**eutral interactions from the drift-fluid equations in (2.99), (2.101), (2.102), and (2.103) are outlined. The derivations utilize cancellation of terms from different velocity drifts, as well as a number of approximations to the fields, in order to simplify the system of equations. The derivations concern only the fields resulting in the original HESEL equations, and do not involve the neutral source terms as such. For this reason the path to the HESEL equations is only outlined here, as the focus remains on the influence of the neutral source terms, and for detailed calculations the reader is referred to some of the original HESEL papers [37, 55].

For the diamagnetic terms, i.e., $\nabla \cdot (n_\mathrm{e} \boldsymbol{u}_{\mathrm{e},d})$ in the density equation, and $\frac{3}{2}\nabla \cdot (p_\sigma \boldsymbol{u}_{\sigma,d}) + p_\sigma \nabla \cdot \boldsymbol{u}_{\sigma,d} + \nabla \cdot \left(\frac{5}{2} \frac{p_\sigma}{q_\sigma B} \hat{\boldsymbol{B}} \times \nabla T_\sigma \right)$ in the pressure equation, for which the last term is the divergence of the diamagnetic heat flux, the following common feature is present

$$\nabla \cdot (n_\mathrm{e} \boldsymbol{u}_{\mathrm{e},d}) = \nabla \cdot \left(\frac{\nabla_\perp p_\mathrm{e} \times \hat{\boldsymbol{B}}}{eB} \right) , \tag{2.104}$$

$$\begin{aligned} \frac{3}{2}\nabla \cdot (p_\sigma \boldsymbol{u}_{\sigma,d}) + p_\sigma \nabla \cdot \boldsymbol{u}_{\sigma,d} + \nabla \cdot \left(\frac{5}{2} \frac{p_\sigma}{q_\sigma B} \hat{\boldsymbol{B}} \times \nabla T_\sigma \right) \\ = \frac{5}{2} \nabla \times \frac{\hat{\boldsymbol{B}}}{q_\sigma B} \cdot \nabla \left(p_\sigma T_\sigma \right) , \end{aligned} \tag{2.105}$$

that is, in a uniform magnetic field the diamagnetic fluxes are incompressible, and the diamagnetic drift do not contribute to the advection of the fields. This feature is also present in the particle description and is known as diamagnetic cancellation [55]. The diamagnetic drift also vanishes in the vorticity equation due to the so-called gyro-viscous cancellation, in which the diamagnetic drift is cancelled by the viscous part of the stress tensor [56]. The vorticity equation (2.101) is now considered, for which the polarization heat flux and anisotropic pressure terms are neglected, and the magnetic unit vector is moved into the material derivative in the polarization drift, i.e., $\Omega_\mathrm{ci}^{-1} \hat{\boldsymbol{B}} \times \mathrm{d}_t \boldsymbol{u}_{\mathrm{i},\perp,0} \approx \Omega_\mathrm{ci}^{-1} \mathrm{d}_t (\hat{\boldsymbol{B}} \times \boldsymbol{u}_{\mathrm{i},\perp,0})$. The ion viscosity tensor is formally decomposed into a parallel part $\boldsymbol{\pi}_{\mathrm{i},\parallel}$, a gyro-frequency dependent cross-field part $\boldsymbol{\pi}_{\mathrm{i},\perp}$, and a gyro-viscous part $\boldsymbol{\pi}_\mathrm{i}^*$, so that $\boldsymbol{\pi}_\mathrm{i} = \boldsymbol{\pi}_{\mathrm{i},\parallel} + \boldsymbol{\pi}_{\mathrm{i},\perp} + \boldsymbol{\pi}_\mathrm{i}^*$. The drifts resulting from the former two parts are treated in the parallel parametrization and collection of collisional terms respectively, whereas the gyro-viscous

drift enters the vorticity equation along with the polarization drift and yields

$$\begin{aligned}\nabla \cdot (n\boldsymbol{u}_{\mathrm{i},p} + n\boldsymbol{u}_{\mathrm{i},\pi^*}) \approx -\nabla \cdot \Bigg(& \frac{n}{\Omega_{\mathrm{ci}}} \mathrm{d}_t \nabla_\perp \phi^* \\ & + \nabla \cdot \left[n \left(-\frac{T_\mathrm{i}}{B} \nabla \times \frac{\hat{\boldsymbol{B}}}{q_\mathrm{i} B} \cdot \nabla \nabla_\perp \phi^* \right) \right] \Bigg) ,\end{aligned} \tag{2.106}$$

where the last term is a remnant from the gyro-viscous cancellation which only contribute if $\hat{\boldsymbol{B}}$ is inhomogeneous and is neglected in the following, and the notation $\nabla_\perp \phi^* = B^{-1} \nabla_\perp \phi + (q_\mathrm{i} n B)^{-1} \nabla_\perp p_\mathrm{i}$ has been introduced. In the material derivative only the dominant advective $E \times B$ drift is retained. Moreover the so-called thin-layer approximation, which is similar to the Boussinesq approximation in neutral fluid dynamics [57], is applied which effectively pulls the density outside the divergence in (2.106) by neglecting particle density variations in this term.

The collisional terms, i.e., those containing the resistive drift, the conductive heat flux, the heat transfer, and the cross-field parts of the viscosity tensor are now considered. By neglecting the temperature gradient terms in the divergence of the resistive flux result in particle density diffusion due to the approximate resistive drift

$$\boldsymbol{u}_{\mathrm{e},R} \approx -D_\mathrm{e} \left(1 + \frac{T_{\mathrm{i}0}}{T_{\mathrm{e}0}} \right) \nabla_\perp \ln n \,, \tag{2.107}$$

with $D_\mathrm{e} = \rho_{\mathrm{e}0}^2 / \tau_{\mathrm{ei}0}$, where the terms labelled with subscript-zero are defined in terms of characteristic fields $n_0, T_{\mathrm{e,i}\,0}$. A similar approximation is applied to the electron pressure equation to write the resistive energy flux in terms of D_e. The ion pressure equation also applies the approximation in (2.107), as well as approximating the perpendicular ion heat flux by

$$\boldsymbol{q}_{\mathrm{i}\perp} \approx 2 n D_\mathrm{i} \nabla_\perp T_\mathrm{i} \,, \tag{2.108}$$

with constant diffusion coefficient $D_\mathrm{i} = T_{\mathrm{i}0} / (\tau_{\mathrm{ii}0} m_\mathrm{i} \Omega_{\mathrm{ci}0}^2)$. In a similar manner the heat transfer terms from elastic collisions are evaluated at constant collision time. The cross-field parts of the viscosity tensor result in diffusion of viscosity through divergence of the viscous flux due to the thin-layer approximation, and likewise introduce viscous heating terms to the ion pressure equation. The divergence of the viscous energy flux is formally small, and neglected in the ion pressure equation. The diffusion coefficients resulting from

the above analysis are subject to further modification due to neoclassical effects, which effectively modifies the diffusion coefficient by

$$D_{\mathrm{e,i}} \to \left(1 + \tfrac{R}{a} q_{95}\right) D_{\mathrm{e,i}} \,, \tag{2.109}$$

due to the q^2 factor in the Pfirsch-Schlüter diffusion coefficient [58]. Here q is the safety factor, which expresses the magnetic field line pitch, and q_{95} is the safety factor at 95 % of the minor radius a. R is the major radius of the tokamak.

Finally the parallel losses in the SOL region are parametrized in a manner that result in various sink terms to the field equations. Parallel transport results in sinks, as blobs are predominantly born at the out-board mid-plane, and expand along the magnetic field lines, leading to a loss of heat and particles. The particle damping rate is

$$\frac{1}{\tau_n} = \frac{2u_{\mathrm{i}\parallel}}{L} \,, \tag{2.110}$$

with the parallel blob length approximately given by $L \approx q_{95} R$. As vorticity is generated and transported by blobs, it is assumed that the damping rate of vorticity is identical to that of the density, and the expansion likewise result in parallel advection of electron and ion pressure with damping times $\tau_{p_{\mathrm{e,i}}} = \frac{2}{9}\tau_n$. For the electron pressure equation the parallel heat fluxes in (2.29), as well as the parallel advection term, are subject to parametrization. Due to quasi-neutrality the electron parallel velocity must be similar to that of the ions and the thermal heat flux, i.e., the fourth term of (2.29), is formally small compared to the divergence of the parallel pressure flux, and thus neglected. The parallel electron heat conduction, i.e., the first term of (2.29), on the other hand comes with a temperature dependency of $k_{\mathrm{e}\parallel} \propto T_{\mathrm{e}}^{\frac{5}{2}}$. The perpendicular fluid closure which depend on a short collisional mean-free path is however invalid and the heat transport is exceeded by Spitzer-Härm heat conduction [59] at lower collisionalities, which allows for parametrizing the parallel electron heat flux as

$$\nabla_\parallel \cdot \boldsymbol{q}_{\mathrm{e}\parallel} \approx -\frac{T_{\mathrm{e}}^{\frac{7}{2}}}{\tau_{\mathrm{SH}}} \,, \tag{2.111}$$

with the Spitzer-Härm damping rate

$$\frac{1}{\tau_{\mathrm{SH}}} = 3.16 \frac{n_0 \tau_{\mathrm{ei}0}}{m_{\mathrm{e}} T_{\mathrm{e}0}^{\frac{3}{2}} L_\parallel^2} \,, \tag{2.112}$$

where $L_\parallel$ is the parallel connection length. Parallel ion heat conduction is neglected, as the parallel ion heat transport is dominated by advection. Finally divergence of the parallel current is assumed to be defined from the sheath-dampening [60] of the fields averaged in the parallel direction

$$\tfrac{1}{e}\nabla\cdot\boldsymbol{j}_\parallel \approx \frac{en_0\langle c_\mathrm{s}\rangle}{L_\parallel}\left[1+\exp\left(\log\sqrt{\frac{m_\mathrm{i}}{2\pi m_\mathrm{e}}}-\frac{e\langle\phi\rangle}{\langle T_\mathrm{e}\rangle}\right)\right], \tag{2.113}$$

where $c_\mathrm{s}=\sqrt{(T_\mathrm{e}+T_\mathrm{i})/m_\mathrm{i}}$ is the ion sound speed. This concludes the review of the approximations that take the drift-fluid equations to the HESEL equations.

In summary; due to the gyro-viscous and diamagnetic cancellations only the $E\times B$ drift advects the plasma fields, the thin-layer approximation allows for neglecting density variations in the polarization flux of the vorticity equation, approximations on collisional drifts introduce (neoclassical) diffusive terms in the density, vorticity, and pressure equations, and the parallel terms are parametrized due to parallel expansion of blobs resulting in advective loss of density and pressures, loss of vorticity due to advection and parallel current, and Spitzer-Harm parallel electron heat conduction. Before writing out the nHESEL equations, the curvature operator is introduced. The curvature operator $\mathcal{K}$ is defined on a field f as

$$\mathcal{K}(f)\equiv-\nabla\cdot\left(\frac{\nabla_\perp f\times\hat{\boldsymbol{B}}}{B}\right), \tag{2.114}$$

which allows for re-writing terms containing the divergence, e.g., of $E\times B$-drift and diamagnetic flux

$$\nabla\cdot\boldsymbol{u}_E=\mathcal{K}(\phi), \tag{2.115}$$
$$\nabla\cdot(n_\sigma\boldsymbol{u}_{\sigma,d})=\tfrac{1}{q_\sigma}\mathcal{K}(p_\sigma), \tag{2.116}$$

and thus write the remaining terms that do not originate from collisional or parallel drifts in a more compact manner.

The HESEL equations augmented with neutral source terms read

$$\mathrm{d}_t n+n\mathcal{K}(\phi)-\mathcal{K}(p_\mathrm{e})=\Lambda_n+\Sigma_n, \tag{2.117}$$
$$\nabla\cdot\left(\mathrm{d}_t^0\nabla_\perp\phi^*\right)-\mathcal{K}(p_\mathrm{e}+p_\mathrm{i})=\Lambda_\omega+\Sigma_\omega, \tag{2.118}$$
$$\tfrac{3}{2}\mathrm{d}_t p_\mathrm{e}+\tfrac{5}{2}p_e\mathcal{K}(\phi)-\tfrac{5}{2}\mathcal{K}(p_\mathrm{e}^2/n)=\Lambda_{p_\mathrm{e}}+\Sigma_{p_\mathrm{e}}, \tag{2.119}$$
$$\tfrac{3}{2}\mathrm{d}_t p_\mathrm{i}+\tfrac{5}{2}p_i\mathcal{K}(\phi)+\tfrac{5}{2}\mathcal{K}\left(p_\mathrm{i}^2/n\right)-p_\mathrm{i}\mathcal{K}(p_\mathrm{e}+p_\mathrm{i})=\Lambda_{p_\mathrm{i}}+\Sigma_{p_\mathrm{i}}, \tag{2.120}$$

where terms from collisional drifts and parametrization of parallel dynamics are contained in the Λ terms on the RHS

$$\Lambda_n = D_{\mathrm{e}}(1+\tau)\nabla_\perp^2 n - \sigma(x)\frac{n}{\tau_n}\,, \tag{2.121}$$

$$\Lambda_\omega = \tfrac{3}{10}D_{\mathrm{i}}\nabla_\perp^2\nabla_\perp^2\phi^* - \sigma(x)\left[\frac{w}{\tau_n}+\Sigma\right]\,, \tag{2.122}$$

$$\begin{aligned}\Lambda_{p_{\mathrm{e}}} = {} & D_{\mathrm{e}}(1+\tau)\nabla\cdot(T_{\mathrm{e}}\nabla_\perp n) + D_{\mathrm{e}}(1+\tau)\nabla_\perp \ln n\cdot\nabla_\perp p_{\mathrm{i}} \\ & + \tfrac{11}{12}D_{\mathrm{e}}\nabla\cdot(n\nabla_\perp T_{\mathrm{e}}) - 3\frac{m_{\mathrm{e}}}{m_{\mathrm{i}}}\nu_{\mathrm{ei0}}(p_{\mathrm{e}}-p_{\mathrm{i}}) \\ & - \sigma(x)\left[\frac{9}{2}\frac{p_{\mathrm{e}}}{\tau_n} + \frac{T_{\mathrm{e}}^{7/2}}{\tau_{\mathrm{SH}}}\right]\,,\end{aligned} \tag{2.123}$$

$$\begin{aligned}\Lambda_{p_{\mathrm{i}}} = {} & \tfrac{5}{2}D_{\mathrm{e}}(1+\tau)\nabla\cdot(T_{\mathrm{i}}\nabla_\perp n) - D_{\mathrm{e}}(1+\tau)\nabla_\perp \ln n\cdot\nabla_\perp p_{\mathrm{i}} \\ & + 2D_{\mathrm{i}}\nabla\cdot(n\nabla_\perp T_{\mathrm{i}}) + \tfrac{3}{10}D_{\mathrm{i}}\left[\left(\partial_{xx}^2\phi^* - \partial_{yy}^2\phi^*\right)^2 + 4\left(\partial_{xy}^2\phi^*\right)^2\right] \\ & + 3\frac{m_{\mathrm{e}}}{m_{\mathrm{i}}}\nu_{\mathrm{ei0}}(p_{\mathrm{e}}-p_{\mathrm{i}}) - \sigma(x)\left[p_{\mathrm{i}}\Sigma - \frac{9}{2}\frac{p_{\mathrm{i}}}{\tau_n}\right]\,.\end{aligned} \tag{2.124}$$

Only the $E\times B$ drift advects the plasma fields, which result in the modified material derivatives of (2.117)-(2.120) on the form

$$\mathrm{d}_t = \partial_t + B^{-1}\{\phi,\cdot\} \qquad\qquad \mathrm{d}_t^0 = \partial_t + \{\phi,\cdot\}\,, \tag{2.125}$$

where the advection by the $E\times B$ drift is written as the anti-symmetric brackets, which for some f and g is given by

$$\{f,g\} = \partial_x f\partial_y g - \partial_y f\partial_x g\,. \tag{2.126}$$

The variables of the nHESEL equations are gyro-Bohm normalized, so that

$$\Omega_{\mathrm{ci}}t\to t\,,\qquad \frac{x}{\rho_s}\to x\,,\qquad \frac{T_{\mathrm{e,i}}}{T_{\mathrm{e0}}}\to T_{\mathrm{e,i}}\,,\qquad \frac{e\phi}{T_{\mathrm{e0}}}\to\phi\,,\qquad \frac{n}{n_0}\to n\,, \tag{2.127}$$

where $\rho_{\mathrm{s}} = \sqrt{\frac{T_{\mathrm{e0}}}{m_{\mathrm{i}}\Omega_{\mathrm{ci}}^2}}$ is the cold-ion hybrid thermal gyro-radius. $\phi^* = \phi + p_{\mathrm{i}}$ is the generalized potential, $D_{\mathrm{e,i}}$ are the neoclassical electron and ion diffusion coefficients, $\tau = T_{\mathrm{i0}}/T_{\mathrm{e0}}$ is the reference ion-electron temperature ratio, and ν_{ei0} is proportional to the electron-ion collision frequency. The parameters $\sigma(x)$, τ_n, w, Σ, and τ_{SH} all originate from parameterization of parallel losses and are described in detail in [37].

The addition of neutral interactions to the HESEL equations are contained in the source terms $\Sigma_{n,\omega,p_{\mathrm{e}},p_{\mathrm{i}}}$. The definition of the source terms in

the drift-fluid approximation follows directly from the drift-fluid equations (2.99), (2.101), (2.102), and (2.103) and result in

$$\boxed{\begin{aligned}
\Sigma_n &= S^n \,, && (2.128)\\
\Sigma_\omega &= -\nabla\cdot\left[n_\mathrm{e}\left(\boldsymbol{u}_{\mathrm{i},R_\mathrm{n}}+\boldsymbol{u}_{\mathrm{i},S^u}+\boldsymbol{u}_{\mathrm{i},S^n}\right)\right] \,, && (2.129)\\
\Sigma_{p_\mathrm{e}} &= Q_{\mathrm{e},n}+S^p_\mathrm{e}-\boldsymbol{u}_{\mathrm{e},\perp,0}\cdot\left(\boldsymbol{R}_{\mathrm{e},n}+\boldsymbol{S}^u_\mathrm{e}\right)+\tfrac{1}{2}m_\mathrm{e}\boldsymbol{u}^2_{\mathrm{e},\perp,0}S^n \,, && (2.130)\\
\Sigma_{p_\mathrm{i}} &= -\tfrac{3}{2}\nabla\cdot\left[p_\mathrm{i}\left(\boldsymbol{u}_{\mathrm{i},R_\mathrm{n}}+\boldsymbol{u}_{\mathrm{i},S^u}+\boldsymbol{u}_{\mathrm{i},S^n}\right)\right]\\
&\quad -p_\mathrm{i}\nabla\left(\boldsymbol{u}_{\mathrm{i},R_\mathrm{n}}+\boldsymbol{u}_{\mathrm{i},S^u}+\boldsymbol{u}_{\mathrm{i},S^n}\right) && (2.131)\\
&\quad +Q_{\mathrm{i},n}+S^p_\mathrm{i}-\boldsymbol{u}_{\mathrm{i},\perp,0}\cdot\left(\boldsymbol{R}_{\mathrm{i},n}+\boldsymbol{S}^u_\mathrm{i}\right)+\tfrac{1}{2}m_\mathrm{i}\boldsymbol{u}^2_{\mathrm{i},\perp,0}S^n \,.
\end{aligned}}$$

where S^n is the density source given in (2.60), $Q_{\mathrm{e,i},n}$ are the terms for heating due to elastic collisions given in (2.45), $S^p_{\mathrm{e,i}}$ are the pressure source terms from (2.74) and (2.78), $\boldsymbol{u}_{\mathrm{e,i},\perp,0}$ are the leading order drift velocities given in (2.92), $\boldsymbol{R}_{\mathrm{e,i},n}$ are the frictious forces due to collisions with neutrals and are found in (2.42), and the inelastic momentum sources $\boldsymbol{S}^u_{\mathrm{e,i}}$ are given in (2.65) and (2.70). The drifts from neutral sources $\boldsymbol{u}_{\mathrm{i},S^u}, \boldsymbol{u}_{\mathrm{i},R_n}, \boldsymbol{u}_{\mathrm{i},S^n}$, i.e., the momentum source drift, Pedersen drift, and density source drift are provided in (2.94) and (2.95). Note that the electron transport is only directly affected by the inelastic source terms, and not through the correction to the drift velocity from neutral interactions. Note also that the terms in (2.128)-(2.131) should be normalized according to the convention of (2.127). This concludes the part of the nHESEL equations that concerns the transport of charged particles. In the following section a model for neutral particle transport is derived, and the full model is reviewed in Sec. 2.3.

2.2 Modelling neutrals

In this section the physical foundation for the choice of neutral model is explained. It has been established that the neutral model should be fluid-like to resolve the same dynamics as that of the plasma model at a similar computational time scale. This leaves for two major features of the model to be decided on; which interactions are to be included in the model, and which type of fluid transport model does most accurately describe the dynamics of the neutral particles?

This work is by no means the first attempt to model neutrals in a plasma. Neutral dynamics are commonly described either by kinetic models, such

as the EIRENE code [61], KN1D [62], DEGAS 2 [63], and in [64], which solve equations similar to the neutral version of (2.3), or the dynamics are described by fluid models. Already in Braginskii's paper from 1965 [45] a neutral transport model is included in the form of a three-component model for electrons, ions, and neutrals, under the assumption of a high collisionality between the ions and neutral particles. Diffusive models for neutrals are commonly found in the literature, e.g., in [65, 66] where the diffusion of neutral atoms is assumed to be driven mainly by charge-exchange collisions. The assumption that charge-exchange collisions define the neutral transport is extended in [67], and include higher moment terms such as neutral viscosity and thermal conductivity. It is also common to include an advective term in the neutral density transport equations if neutrals enter the system at a high directed velocity, e.g., for supersonic molecular beams as in [68, 69]. Finally more location specific fluid models target, e.g., the divertor region as is the case in [70, 71]. Many neutral fluid models a high collisionality of neutrals is either assumed or not discussed, which allows for applying the Chapman-Enskog scheme to close the neutral transport equations. In this work, however, the collisional long mean-free path experienced by neutrals in the SOL and edge regions in tokamak plasmas is adressed, and a different closure scheme is used to obtain a neutral transport equation that is valid at any collisionality.

In Section 2.2.1 possible life-cycles of neutrals, starting with a thermal neutral molecule, are reviewed. This provides an understanding of the basic processes that involve neutrals in a tokamak, and aids in deciding on the interactions and neutral species to include. Once the relevant interactions and neutral species are determined the transport of the neutrals is discussed. Neutral transport described by a fluid model proves to be a non-trivial subject, as the neutrals experience a mean-free path between collisions which is much longer than any local length-scales in typical SOL and far-edge plasmas. The long mean-free path prevents the conventional assumption for closing the set of neutral fluid equations in the Chapman-Enskog scheme, and thus requires for another approach for obtaining the transport equations. This issue is covered in Sec. 2.2.2.

2.2.1 Interactions

Consider a neutral thermal hydrogen isotope molecule, e.g. from gas puffing, entering a vacuum chamber containing a confined plasma volume. The

molecule may collide with other neutrals in the SOL, or at some point with the first wall where it is reflected or absorbed and maybe released at some later point. Most likely, however, the molecule will encounter a charged particle, and undergo one of many possible interactions. In [72] cross-sections and corresponding reaction rates for a large number of proton and electron collision processes with H_2 and H are provided. Common for those are, that for SOL relevant temperatures, the cross sections for charged particle collisions with thermal molecules is much larger for electrons than for ions. The inelastic molecule and charged particle collisions result in one of three outcomes for the molecule; excitation of the vibrational or electron states of the molecule, dissociation of the molecule into its atomic components, or ionization of the molecule into H_2^+. Those processes are discussed separately in the following.

The inclusion of **excitation of molecules** (and atoms), i.e.,

$$\mathrm{H}_2 + \mathrm{e, p} \rightarrow \mathrm{H}_2^* + \mathrm{e, p}\,, \tag{2.132}$$

in fluid models is usually accommodated for by introducing an additional fluid species for each excited state. The excitations will thus result in identical density source and sink terms for the two species. This method, however, would require for a larger number of coupled differential equations to be solved. Another, maybe less elegant, solution is to simply neglect the reactions that result in excited molecular states, and thus avoid the considering the excited molecules entirely. The latter approach is applied for the neutral model at hand, and is to some extend justified by the short lifetime of the excited states of both molecules and atoms, which typically have a lifetime of the order of $1 - 100\,\mathrm{ns}$ [73, 74], which is similar to time scales set by the inverse ion gyro-frequency. By neglecting the excited states, there is, however, a sink of electron temperature and potentially a source of neutral atoms which are not accounted for. The following assumptions are thus made on the neutral model:

- thermal molecules enter the system,
- only electron impact reactions on molecules are considered, and
- reactions leading to excited molecular and atomic states are neglected.

The list of assumptions will expand, as the possible fates of the initial molecule are explored.

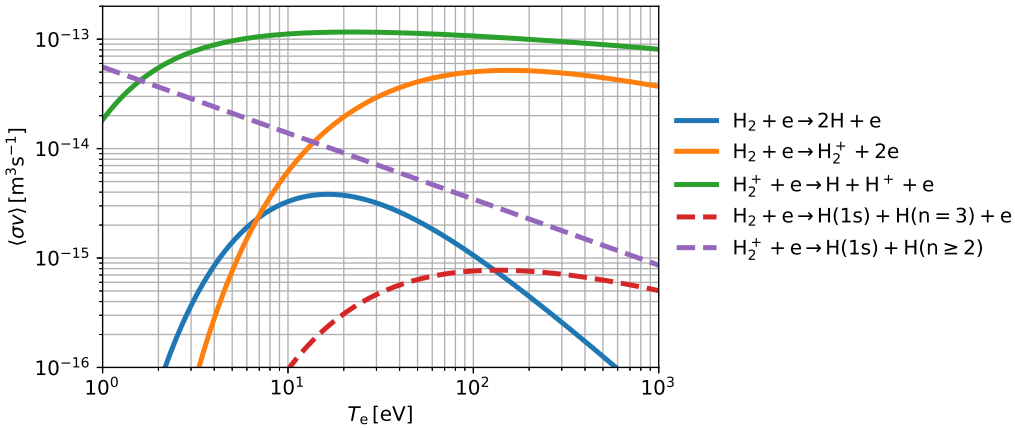

Figure 2.1: Reaction rates for electron impact dissociation and ionization processes of H_2. The reactions plotted with solid lines are included in the model, whereas those with dashed lines are examples of reactions involving excited atomic states.

Dissociation of molecules into two atoms, i.e.,

$$H_2 + e \rightarrow 2H + e\,, \tag{2.133}$$

occurs at relatively high cross-section and can follow various paths. The dominant dissociative processes are obtained from [72] and shown in Fig. 2.1. Common for the dissociation products are, that they carry the molecular binding energy of the order of eVs kinetically, and dissociation thus results in energetic non-thermal neutral atoms. Those atoms are in the literature referred to as *Franck-Condon* neutrals [75]. For the same reasons as for the molecules, treatment of atomic exited states is omitted. Thus only one dissociative process is included in the model, namely that which results in ground state Franck-Condon atoms of an energy of roughly 2 eV, as the dissociation potential for H_2 is approximately 4.52 eV [76].

The **ionization hydrogen molecules** into H_2^+, i.e.,

$$H_2 + e \rightarrow H_2^+ + 2e\,, \tag{2.134}$$

is another process which occurs at a high cross-section. The inclusion of H_2^+ into the HESEL model may be very interesting, but also beyond the scope of this work and an assumption on the H_2^+ molecules is required. Since the ionized molecules are retained by their orbit around the magnetic field lines, and the reaction rate for dissociation of H_2^+ is very high (see Fig. 2.1), it

is assumed that the ionized molecules are dissociated instantaneously after their creation, i.e.,

$$\mathrm{H_2 + e \rightarrow H_2^+ + 2e \rightarrow H + H^+ + 2e}\,, \tag{2.135}$$

and the resulting neutral atom is a Franck-Condon neutral. The ionization energy of $\mathrm{H_2}$ is 15.4 eV and the dissociation energy of $\mathrm{H_2^+}$ is 2.65 eV [77]. Thus, the model is augmented with another pair of assumptions:

- ionization of molecules is treated as a one-step molecular assisted ionization process, and
- atoms originate from dissociation and molecular assisted ionization, and have a characteristic temperature of 2 eV.

This almost concludes the life-cycle of molecules. In review, thermal molecules enter the system, and result either in electrons and ions through molecular assisted ionization, or in energetic 2 eV Franck-Condon neutrals. The latter requires for a dynamic treatment of the neutral atoms, and will be done in a manner similar to that of molecules in the following. After that a few more interactions involving molecules and atoms are discussed when reviewing plasma-wall interactions.

Consider now a 2 eV Franck-Condon neutral originating from a dissociated molecule. As for the thermal molecule, this will experience a limited life-time, and at some point either hit the wall or interact with a charged particle. The plasma-wall interaction, and the resulting neutral source, is only weakly included in the model derived here and discussed at the end of the section. As for the molecules, cross-sections for electron impact collisions dominate over those from ion impacts, except for the so-called charge-exchange collision. Here the electron from the neutral particle is donated to an ion upon impact, resulting again in a neutral atom and an ion, but with the initial energies and momenta exchanged. For the electron impact collisions, ionization of atoms is the only process that does not involve excited states. Ionization is thus the only atomic reaction to be considered in this model, except for charge-exchange collisions. The two collisional reactions are reviewed in the following, starting with atomic ionization.

Electron impact **ionization of atoms**, i.e.,

$$\mathrm{H + e \rightarrow H^+ + 2e}\,, \tag{2.136}$$

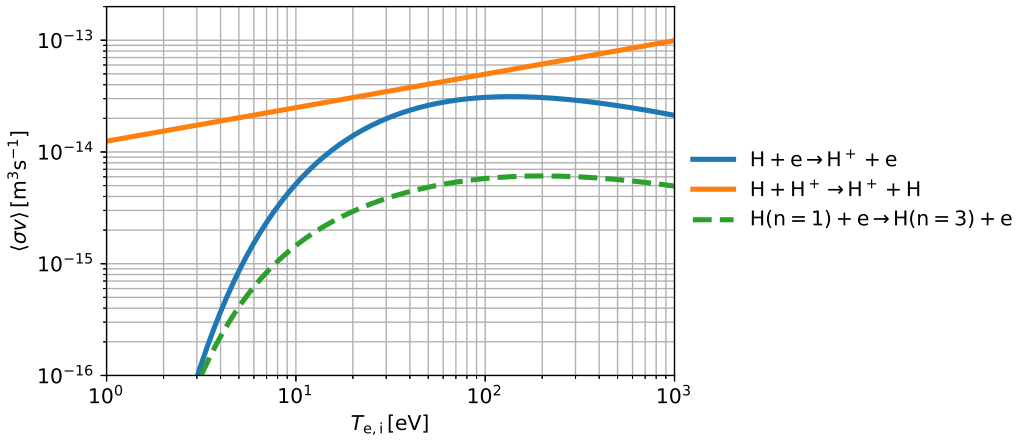

Figure 2.2: Reaction rates for electron and ion impact collisions with H. The reactions plotted with solid lines are included in the model, whereas that with dashed lines is an example of a reaction involving excited atomic states.

is the main mechanism for fuelling the bulk plasma. This reaction occurs for atoms at all energies, and the ionization potential for hydrogen is approximately 13.6 eV. As for the molecules, the model does not include excited atomic states, which effectively would lower the excitation threshold, as the ionization can happen in multiple steps. The reaction rate for atomic ionization is shown in Fig. 2.2, together with other common atomic collisional reactions.

The last interaction to be included in the model, is **charge-exchange collisions** between atoms and ions. In the charge-exchange collision, an electron is transferred from an atom to an ion, i.e.,

$$\mathrm{H} + \mathrm{H}^+ \rightarrow \mathrm{H}^+ + \mathrm{H}\,, \tag{2.137}$$

which does not introduce a density source or sink, but effectively swaps the momenta and energies of the two colliding particles. The charge-exchange collisions heat a fraction of the neutral atoms in the SOL to the temperature of the edge ions, which allow the neutral atoms to penetrate deep into the plasma before being ionized. In order to account for this energetic subpopulation of neutral atoms, the charge-exchanged neutrals are treated as a separate atomic species, with a characteristic ion-like temperature. This adds to the list of assumptions:

- Franck-Condon atoms that have undergone a charge-exchange collision

with an ion are treated as a separate atomic species.

This concludes the overview of dominant plasma-neutral volume interactions in the SOL and edge regions of a tokamak. A substantial fraction of plasma-neutral interactions do, however, happen at material surfaces. When hot plasma filaments reach the vacuum chamber wall, or are terminated at the divertor, various outcomes depending on the plasma temperature and surface material result from the impact. In the nHESEL model surface interactions are parametrized in a simple manner, leaving space for future improvement. For the sake of completeness, and as a first encounter to the physical processes for possible future collaborators on the neutral model, a brief review of the dominant plasma-surface interactions follows, before discussing the neutral transport model in the following section.

When charged or neutral particles hit material surfaces, such as the first wall, various possible release mechanism depending on, e.g., temperature and surface material, determine the product. There exists an exhaustive number of possible recycling channels, and only a few typical recycling processes are listed here, on which more information can be found in, e.g., [78, 79, 80]. A group of recycling processes result in neutral atoms, and are thus of the form

$$\mathrm{H}, \mathrm{H}^+ \xrightarrow{\text{recycling}} \mathrm{H}\,, \tag{2.138}$$

and count reflection, sputtering, and desorption induced by the impacting particle. Depending on the conditions, a reflected particle can retain most of the impact energy, whereas neutral atoms from sputtering of hydrogen-saturated metals or desorption are released from the material and typically have energies of a few eVs. It is also possible that molecules are released, i.e.,

$$\mathrm{H}, \mathrm{H}^+ \xrightarrow{\text{recycling}} \mathrm{H}_2\,, \tag{2.139}$$

through thermal desorption due to heating of the wall, or by the so-called Langmuir-Hinshelwood and Eley-Rideal reactions, where either the captured particles diffuse in the material to the surface where they recombine to molecules under desorption, or an impacting particle recombines with a material captured atom into a molecule.

Although recycling processes are not included in this model, except from a partial reflection of neutrals explained in Sec. 3.1, the products of plasma-wall recycling are observed to fit well into the neutral populations included

in the model. Methods for accounting for recycling in future versions of the neutral model are suggested in Sec. 5.2.

In recap; this section has provided the physical foundation for considering molecules, as well as atoms at two characteristic energies in a neutral model. The molecules are thermal, whereas the atoms have either energies of a few eV from the dissociation energy of molecules, or a temperature comparable to that of the edge ions due to charge-exchange collisions. In the following section the transport of neutral particles in the fluid picture is examined and results in a three-species fluid model for neutral particles at the characteristic energies above.

2.2.2 Transport

With the set of characteristic neutral species, i.e., thermal molecules, Franck-Condon atoms originating from dissociation, and energetic atoms from charge exchange collisions with ions, a fluid transport model for the neutrals is sought out. A straightforward way to approach this task is to start with the kinetic equation (2.3), and follow the recipe of Sec. 2.1.1. This will result in a set of fluid equations for neutral density, momentum, and temperature, as was found for the charged particles, but without the acceleration terms from electromagnetic interactions. A crucial step in the derivation of the fluid equations is the closure, which is typically obtained by the Chapman-Enskog scheme reviewed in Sec. 2.1.1, and where a short mean-free path between collisions is to be assumed. As will be apparent from the following analysis this assumption, however, is not valid when describing the neutral particles in the SOL region.

Expanding upon the analysis in the last part of Sec. 2.1.1, a neutral particle moving at speed v is considered. The neutral particles are assumed to be hard spheres of diameter d, and collisions between two such particles (or between a neutral and a charged particle) occur, if the distance between their centre approaches d. Along the path of motion, the neutral will thus collide with any other particle within the collisional cross-section

$$\sigma = \pi d^2 \,. \tag{2.140}$$

The cylindrical volume that is swept by the particle during the time t is $V = \sigma v t$, and the number of collisions in this time is thus $N = \sigma v t n$, where

n is the particle number density. The collision time τ is defined as the characteristic time for one collision to happen, i.e., $N = 1$ for $t = \tau$. For a Maxwellian velocity distribution, the characteristic speed can be assumed to be the thermal speed $v_{\mathrm{th}} = \sqrt{2T/m}$, and as in (2.37) the collision time thus becomes

$$\tau = \frac{1}{\sigma v_{\mathrm{th}} n} = \frac{1}{\sigma n}\sqrt{\frac{m}{2T}}\,. \tag{2.141}$$

The corresponding mean-free path between collisions is given by

$$\lambda = \tau v_{\mathrm{th}} = \frac{1}{\sigma n}\,, \tag{2.142}$$

and thus only depend on the cross-section, and particle density. Note that for inelastic collisions with charged particles, the mean-free path will have a temperature dependency, as the average reaction rate $\langle \sigma v \rangle$ is primarily defined by the charged particle speed, and the mean-free path thus reads

$$\lambda = \frac{v_{th}}{\langle \sigma v \rangle n} = \frac{1}{\langle \sigma v \rangle n}\sqrt{\frac{2T}{m}}\,. \tag{2.143}$$

This results in a penetration depth of neutrals into the plasma pedestal that is dependent on the neutral temperature, and which is numerically confirmed as reported in Chpt. 4. For the consideration at hand, however, the neutral mean-free path (2.142) is temperature independent. To assess whether a high collisionality can be assumed, the neutral mean-free path is compared to other SOL-relevant perpendicular length-scales. Two intuitively meaningful measures are the SOL width, and the typical perpendicular width of blob filaments; the former is, at least for the larger machines, of the order of ten centimetres, and the latter typically a few centimetres. Thus, for a collisional closure to be valid, λ should be in the sub-centimetre range. The typical SOL plasma density for medium-sized devices is in the order of $10^{18}\,\mathrm{m}^{-3}$, and possibly higher in blobs, and that of neutrals is assumed to be similar. A somewhat high estimate on the value of n is thus $n = 10^{19}\,\mathrm{m}^{-3}$. For the collisional cross-section in (2.140), an atomic diameter of twice the Bohr radius $d = 2 \cdot 0.53 \cdot 10^{-10}\,\mathrm{m}$ is used, yielding a cross section of $\sigma = 3.53 \cdot 10^{-20}\,\mathrm{m}^2$ and an approximate neutral collisional mean-free path (2.142) of

$$\lambda \approx 3\,\mathrm{m}\,. \tag{2.144}$$

This value is too large to assume a high neutral collisionality, and the conventional closure scheme for the SOL, and even the plasma edge, regions is thus invalid.

A natural response to this estimate would be to abandon the quest for a fluid description of neutrals, as the above calculations clearly disfavours such an approach. The literature on transport in the long mean-free path limit is likewise sparse. One paper [81], however, treats a similar situation, namely that of parallel transport of particles and heat for supra-thermal electrons in a tokamak plasma. Weakly collisional transport dynamics are also considered in [82, 83]. The general idea of [81] is to replace the mean-free path as the small-parameter required for expanding the velocity distribution function with an assumed small Maxwellian source term. The source term thus acts as a linear perturbation to the lowest-order Maxwellian velocity distribution, and allows for obtaining expressions for the particle and heat fluxes at any collisionality. In [81] the derivations are carried out for the one-dimensional steady-state case. Here, the analysis is attempted extended to three dimensions and includes momentum sources, but towards the end it reverts to the results of the simpler analysis in [81] for calculation reasons.

Similar to (2.3) the (static) kinetic equation for the neutrals is

$$\boxed{\boldsymbol{v}\cdot\nabla f(\boldsymbol{x},\boldsymbol{v}) = \mathcal{C}(f) + \mathcal{S}(\boldsymbol{x},\boldsymbol{v})\,,} \tag{2.145}$$

where f is the neutral velocity distribution function, $\mathcal{C}$ is an appropriate elastic collision operator, and $\mathcal{S}$ is the assumed small Maxwellian source term. The linearly perturbed Maxwellian distribution function is written

$$f = f_0\left(1+\hat{f}_1\right)\,, \tag{2.146}$$

where $f_0(n,T) = \frac{n}{\pi^{3/2}v_{\mathrm{th}}^3}\exp\left(-v^2/v_{\mathrm{th}}^2\right)$, and the hat denotes the normalized term $\hat{f}_1 = f_1/f_0$. By allowing for density, momentum, and temperature perturbations, i.e.,

$$n\to n+n_1\,,\qquad \boldsymbol{v}\to\boldsymbol{v}+\boldsymbol{v}_1\,,\qquad T\to T+T_1\,, \tag{2.147}$$

where the perturbations fulfill

$$n_1 = \int \mathrm{d}\boldsymbol{v}\, f_1\,, \tag{2.148}$$

$$\boldsymbol{v}_1 = \frac{1}{n}\int \mathrm{d}\boldsymbol{v}\,\boldsymbol{v} f_1 \tag{2.149}$$

$$T_1 = 2\frac{T}{n}\int \mathrm{d}\boldsymbol{v}\,\left(\frac{v^2}{v_{\mathrm{th}}^2}-\frac{3}{2}\right) f_1\,, \tag{2.150}$$

the collision operator is constructed so that it drives the f_1 towards the perturbed Maxwellian f_1^* given by

$$\hat{f}_1^* = (n_1\partial_n + \boldsymbol{v}_1 \cdot \nabla_{\boldsymbol{v}} + T_1\partial_T) \ln f_0 \,. \tag{2.151}$$

The above is readily evaluated and yields

$$\hat{f}_1^* = \frac{n_1}{n} + 2\frac{\boldsymbol{v}_1 \cdot \boldsymbol{v}}{v_{\rm th}^2} + \frac{T_1}{T}\left(\frac{v^2}{v_{\rm th}^2} - \frac{3}{2}\right) , \tag{2.152}$$

where negative signs on the second and third terms have been absorbed into the perturbations. The collision operator is thus similar to that for the Krook-model [84], which conserves particles, momentum, and energy according to (2.8), (2.14), and $\int \mathrm{d}\boldsymbol{v}\left(\frac{v^2}{v_{\rm th}^2} - \frac{3}{2}\right)\mathcal{C} = 0$, ensured by the restrictions in (2.148) - (2.150). The collision operator acts on a non-Maxwellian perturbation to the distribution function according to

$$\mathcal{C}(f_1) = -\nu\left\{f_1 - \left[\frac{n_1}{n} + 2\frac{\boldsymbol{v}_1 \cdot \boldsymbol{v}}{v_{\rm th}^2} + \frac{T_1}{T}\left(\frac{v^2}{v_{\rm th}^2} - \frac{3}{2}\right)\right] f_0\right\} . \tag{2.153}$$

The kinetic Maxwellian (small) source term is similarly assumed to be of the form

$$\mathcal{S} = \frac{f_0}{n}\left[\mathcal{S}_n(\boldsymbol{x}) + \frac{\boldsymbol{v}}{v_{\rm th}} \cdot \boldsymbol{\mathcal{S}}_u(\boldsymbol{x}) + \left(\frac{v^2}{v_{\rm th}^2} - \frac{3}{2}\right)\mathcal{S}_p(\boldsymbol{x})\right] , \tag{2.154}$$

with the particle density $\mathcal{S}_n$, momentum density $\boldsymbol{\mathcal{S}}_u$, and energy density $\mathcal{S}_p$ sources.

The source in (2.154) is considered a perturbation to a system in equilibrium, so that to lowest order (2.145) is

$$\boldsymbol{v} \cdot \nabla f_0 = \mathcal{C}(f_0) \,, \tag{2.155}$$

and the first order perturbation is described by

$$\boldsymbol{v} \cdot \nabla f_1 = \mathcal{C}(f_1) + \mathcal{S} \,. \tag{2.156}$$

The next step in the kinetic analysis is to solve (2.156) for f_1. (2.156) is linear in f_1 and is readily solved by Fourier transformation $\mathcal{F}$, using

$$f_k \equiv \mathcal{F}(f_1) = \int \mathrm{d}\boldsymbol{x}\, e^{i\boldsymbol{k}\cdot\boldsymbol{x}} f_1(\boldsymbol{x}) \,. \tag{2.157}$$

The Fourier transform of (2.156) is

$$\begin{aligned} i\boldsymbol{v}\cdot\boldsymbol{k}f_k + \nu\left\{f_k - \mathcal{F}\left[\frac{n_1}{n} + 2\frac{\boldsymbol{v}\cdot\boldsymbol{v}_1}{v_{\rm th}^2} + \frac{T_1}{T}\left(\frac{v^2}{v_{\rm th}^2} - \frac{3}{2}\right)\right] f_0\right\} \\ = \frac{f_0}{n}\mathcal{F}\left[\mathcal{S}_n + \frac{\boldsymbol{v}}{v_{\rm th}}\cdot\boldsymbol{\mathcal{S}}_u + \left(\frac{v^2}{v_{\rm th}^2} - \frac{3}{2}\right)\mathcal{S}_p\right], \end{aligned} \tag{2.158}$$

which is rearranged to provide the Fourier transformed perturbed distribution function

$$f_k = \frac{f_0/n}{\nu - i\boldsymbol{k}\cdot\boldsymbol{v}} F_k(v)\,, \tag{2.159}$$

with

$$F_k(v) = \sigma_n + \nu\tau_n + \frac{\boldsymbol{v}}{v_{\rm th}}\cdot(\boldsymbol{\sigma}_u + \nu\boldsymbol{\tau}_u) + \left(\frac{v^2}{v_{\rm th}^2} - \frac{3}{2}\right)(\sigma_T + \nu\tau_T)\,. \tag{2.160}$$

Here the σ's are the Fourier transformed source terms, and the τ's are those for the perturbations, i.e.,

$$\sigma_n = \mathcal{F}\left(\mathcal{S}_n\right)\,, \qquad \tau_n = \int \mathrm{d}\boldsymbol{v}\, f_k\,, \tag{2.161}$$

$$\boldsymbol{\sigma}_u = \mathcal{F}\left(\boldsymbol{\mathcal{S}}_u\right)\,, \qquad \boldsymbol{\tau}_u = 2\int \mathrm{d}\boldsymbol{v}\, \frac{\boldsymbol{v}}{v_{\rm th}} f_k\,, \tag{2.162}$$

$$\sigma_T = \mathcal{F}\left(\mathcal{S}_p\right)\,, \qquad \tau_T = 2\int \mathrm{d}\boldsymbol{v}\left(\tfrac{v^2}{v_{\rm th}^2} - \tfrac{3}{2}\right) f_k\,. \tag{2.163}$$

The final step in the kinetic analysis is to substitute (2.159) into the transformed perturbations (2.161) - (2.163). This yields three coupled integral equations for the τ_i, which in principle can be solved to obtain the Fourier transform of the perturbations. This is, however, a challenging task and a more simple approach could be possible. For this we define τ_i', which is that belonging to the decoupled equations corresponding to (2.159) - (2.163), e.g., for τ_n' it is assumed that $\boldsymbol{\sigma}_u = \boldsymbol{\tau}_u = \sigma_T = \tau_T = 0$, and similar for the other perturbations, so that they are considered independent of one another. This reformulates the problem into three decoupled integral equations that can be

solved to yield

$$\tau_n' = \frac{\sigma_n \tilde{Z}_0(\boldsymbol{k})}{\pi^{\frac{3}{2}} v_{\text{th}}^3 - \nu \tilde{Z}_0(\boldsymbol{k})}\,, \tag{2.164}$$

$$\boldsymbol{\tau}_u' = \frac{2\boldsymbol{\sigma}_u \tilde{Z}_2(\boldsymbol{k})}{\pi^{\frac{3}{2}} v_{\text{th}}^5 - 2\nu \tilde{Z}_2(\boldsymbol{k})}\,, \tag{2.165}$$

$$\tau_T' = \frac{\sigma_T \left(4\tilde{Z}_4(\boldsymbol{k}) - 12 v_{\text{th}}^2 \tilde{Z}_2(\boldsymbol{k}) + 9 v_{\text{th}}^4 \tilde{Z}_0(\boldsymbol{k})\right)}{2\pi^{\frac{3}{2}} v_{\text{th}}^7 - \nu \left(4\tilde{Z}_4(\boldsymbol{k}) - 12 v_{\text{th}}^2 \tilde{Z}_2(\boldsymbol{k}) + 9 v_{\text{th}}^4 \tilde{Z}_0(\boldsymbol{k})\right)}\,, \tag{2.166}$$

with

$$\tilde{Z}_j(\boldsymbol{k}) = \int \mathrm{d}\boldsymbol{v}\, v^j \frac{\exp(-v^2/v_{\text{th}}^2)}{\nu - i\boldsymbol{k}\cdot\boldsymbol{v}}\,, \tag{2.167}$$

and subsequently inserted into (2.159) and (2.160) to finalize the analysis.

By decoupling the perturbations as suggested above, however, an essential cross-field dependency on the Fourier transformed source terms, found in the 1D case without velocity perturbation in [81], is lost. There is no reason to believe that a similar dependence exists for the coupled case of the above analysis, but as the solution to the integral equation system has proved too difficult to obtain for now, the simpler 1D case with $\boldsymbol{\sigma}_u = \boldsymbol{\tau}_u = 0$ is considered for the remainder of the analysis, and the system of integral equations is left for a future challenge. For this case it is found in [81] that the Fourier transformed perturbations have the form

$$\tau_n = \frac{2\sigma_n\zeta\left[(1+\zeta^2-2\zeta^4)\bar{Z}(\zeta) - 2\zeta^3\right] + \sigma_T\left[2\zeta + (2\zeta^2-1)\,\bar{Z}(\zeta)\right]}{\nu\left[2\left(\zeta^2-1\right) + \left(2\zeta^3 - 3\zeta\right)\bar{Z}(\zeta)\right]}\,, \tag{2.168}$$

$$\tau_T = \frac{(2\sigma_n - \sigma_T)\,\zeta\left[2\zeta + (2\zeta^2-1)\,\bar{Z}(\zeta)\right]}{\nu\left[2\left(\zeta^2-1\right) + \left(2\zeta^3 - 3\zeta\right)\bar{Z}(\zeta)\right]}\,, \tag{2.169}$$

where $\zeta = \frac{-i}{k\lambda}$ with the mean-free path $\lambda = \frac{v_{\text{th}}}{\nu}$ and

$$\bar{Z}(\zeta) = \frac{1}{\lambda\zeta\pi^{\frac{1}{2}}}\tilde{Z}_0(k)\,. \tag{2.170}$$

Following the usual recipe for obtaining the Fourier transformed flux terms by integrating (2.159) and thus close the set of equations as is done in the Chapman-Enskog scheme, is not possible in this expansion as the procedure

simply reproduces the conservation laws. Instead it is observed that the Fourier transform of the fields, i.e., (2.168) and (2.169) has the property that

$$\tau_n + \tau_T = -\frac{2\zeta^2\sigma_n}{\nu}\,, \tag{2.171}$$

and as the Fourier transform of the particle flux Γ_k is given by the density source, this can be written in terms of the fields as

$$\Gamma_k = \frac{i\sigma_n}{k} = -\tfrac{1}{2}\nu\lambda^2 n\left(-ik\frac{\tau_n + \tau_T}{n}\right)\,. \tag{2.172}$$

The inverse Fourier transform of (2.172) yields the particle flux

$$\boxed{\Gamma = -\tfrac{1}{2}\nu\lambda^2 n\partial_x \log p\,.} \tag{2.173}$$

This expression is somewhat surprising, as particle transport is driven by local gradients at any collisionality ν. In a similar manner the heat flux in the long collisional mean-free path limit is found to be

$$q(x) = \frac{nv_{\rm th}}{\pi^{\frac{3}{2}}T}\int \mathrm{d}x' \frac{T(x-x') - T(x+x')}{x'}\,, \tag{2.174}$$

which by the integral over the full domain reflects the non-locality of the transport that usually results from a low collisionality.

The attempt to obtain another closure for the particle transport is partially successful. The results from [81] display how fluxes can be obtained beyond the short mean-free path limit, but for the heat flux (and most likely also for the momentum flux) the expression is not in a closed form and in terms of local gradients. This is, however, the case for the particle flux, which is driven by the pressure gradient.

For the neutral model initiated in Sec. 2.2.1 some decisions on describing the transport is made on background of the analysis presented here. Since the higher moment fluxes require integration across the full domain, and the mean-free path between collisions is several orders of magnitudes larger than the domain considered in Chpts. 3 and 4, the corresponding neutral momentum and temperature fields are assumed constant. Using non-local neutral flux terms similar to that of the heat flux in (2.174) may provide a more complex model, but it is not necessarily more correct than that of constant fields due to the small ratio of the extend of the domain to the mean-free path. The analysis in Sec. 2.2.1 suggests two atomic neutral species at

characteristic temperatures of $\sim 2\,\mathrm{eV}$ and $\sim T_\mathrm{i}\big|_\mathrm{LCFS}$, and a neutral species of thermal molecules. This results in a three species fluid-like model for the neutral particles, where particle transport is described by diffusion through (2.173), which in the isothermal form becomes

$$\Gamma = -D\partial_x n\,, \tag{2.175}$$

with diffusion coefficient $D = \frac{1}{2}\frac{v_\mathrm{th}^2}{\nu}$.

The transport equations for the neutrals are extended to three dimensions, with the temporal dependency naively introduced, and thus read

$$\boxed{\partial_t n_\mathrm{n} - \nabla\cdot(D_\mathrm{n}\nabla n_\mathrm{n}) = S_\mathrm{n}^n\,,} \tag{2.176}$$

for neutral species denoted n = *cold* for the cold (thermal) molecules, and n = *warm*, *hot* for the Frack-Condon and charge-exchanged atoms respectively. The diffusion coefficients depend linearly on the neutral temperature, which thus, together with the source term, determine the characteristic gradient length-scale for the neutral profiles. The inelastic sources couple the neutral equations to each other, as well as to the plasma equations, and result from atomic ionization, molecular assisted ionization, dissociation, and atom-ion charge-exchange collisions. The sources of neutral densities correspond to those derived in Sec. 2.1.1 and read

$$\boxed{\begin{aligned} S_\mathrm{cold}^n &= -n_\mathrm{e} n_\mathrm{cold}\left(\langle\sigma_\mathrm{Iz}v\rangle + \langle\sigma_\mathrm{Dis}v\rangle\right)\,, && (2.177)\\ S_\mathrm{warm}^n &= n_\mathrm{e}\left[n_\mathrm{cold}\left(\langle\sigma_\mathrm{Iz}v\rangle + 2\langle\sigma_\mathrm{Dis}v\rangle\right) - n_\mathrm{warm}\left(\langle\sigma_\mathrm{iz}v\rangle + \langle\sigma_\mathrm{cx}v\rangle\right)\right]\,, && (2.178)\\ S_\mathrm{hot}^n &= n_\mathrm{e}\left(n_\mathrm{warm}\langle\sigma_\mathrm{cx}v\rangle - n_\mathrm{hot}\langle\sigma_\mathrm{cx}v\rangle\right)\,. && (2.179) \end{aligned}}$$

If the neutrals have a directed velocity $\boldsymbol{u}_\mathrm{n}$, (2.176) can be extended by adding an advective term

$$\partial_t n_\mathrm{n} - \nabla\cdot(D_\mathrm{n}\nabla n_\mathrm{n} - \boldsymbol{u}_\mathrm{n} n_\mathrm{n}) = S_\mathrm{n}^n\,, \tag{2.180}$$

this feature has, however, not been utilized in the results presented in Chpt. 4.

This concludes the derivation of the neutral model. It is clear from the analysis that due to the long mean-free path between collisions for SOL and far edge relevant parameters, the fluid description is not suitable for describing transport of neutral particles. The demand of a fluid-like model may, however, be retained for the purpose of having equations with a similar formulation as those for the plasma fields, which allows for a temporal

resolution. This is necessary, e.g., if the effect of dynamical plasma fields, such as those for blobs, on neutrals, and vice versa, is to be treated in a self-consistent manner. The neutral collisional long mean-free path prevents the usual Chapman-Enskog closure scheme from being applied, and the transport of higher moment fields is non-local in its nature. It is, however, possible to have particle transport driven by local pressure gradients, even in the long mean-free path limit, as long as the source term is Maxwellian and acts as a perturbation to a Maxwellian distribution function. The resulting neutral transport is described by Fick's law, where the diffusion coefficient for the neutral density is proportional to the temperature of the neutrals, and the neutral model describes three neutral species at characteristic temperatures, for which the transport equations are coupled through inelastic sources. Due to the temperature dependence of the diffusion coefficient, and the inclusion of dominant source terms, the simulations are expected to provide length-scales for the neutral density gradients, and thus source terms, that are spatially and temporally consistent with the plasma dynamics.

It should be noted that the existence of populations of neutral particles at discrete energies is not entirely theoretical. Analyses of experimental measurements, e.g. [31, 32], indicate that neutral hydrogen atoms belong to certain 'velocity classes', for which most atoms belong to the classes of the order of 1 eV, but a substantial amount also fall into the class with energy of approximately 20 eV.

The following section concludes the theory chapter with a review of the combined nHESEL model, that describes the evolution of plasma and neutral fields in the edge and SOL regions at the out-board mid-plane of a tokamak plasma.

2.3 Combined model equations

In this short section the complete nHESEL model is reviewed, and the references to the transport and source equations are collected for convenience. The nHESEL model is a combined plasma-neutral model. It consists of the original HESEL drift-fluid based plasma transport equations augmented with source terms that result from interaction with neutrals, and of a neutral model for diffusive transport of molecules and atoms.

The nHESEL equations describe coherent transport of electron density, modified vorticity, and electron and ion pressures at time-scales much larger than that set by the inverse ion cyclotron frequency in a 2D slab perpendicular to the magnetic field lines at the out-board mid-plane of a tokamak plasma. The transport equations are stated in (2.117)-(2.120), with the collisional and parallel terms defined in (2.121)-(2.124). Plasma and neutrals interact through elastic collisions, as well as ionization of molecules and atoms, dissociation of molecules, and charge-exchange collisions between ions and atoms. The source terms from plasma-neutral interactions are provided in (2.128)-(2.131)

The neutral model describes one molecular species and two atomic species. It is assumed that the molecules are thermal, and dissociate into atoms with an energy of 2 eV, which can then be further energized in charge-exchange collisions to obtain an ion-like temperature. All neutral particles are assumed to remain in the excitational ground-state, and only partial reflection of neutrals on the first-wall is included to resemble the interactions at this physical boundary. The model is derived without the usual assumption of a short mean-free path between collisions, which prevents closed expressions for the evolution of higher-moment fluid variables. The neutral transport equations are given in (2.176), and the associated density source terms in (2.177)-(2.179).

Before applying the nHESEL model in various studies presented in Chpt. 4, the numerical implementation as well as discussions on verification and validation are presented in Chpt. 3.

Chapter 3

Numerical implementation

With the system of combined neutral-plasma equations at hand, all that is left to do is to fix the values of the free parameters, such as electron and ion edge densities and pressures, and flux of neutral molecules into the system, and solve the system of equations. It would be presumptuous to seek out analytical solutions to a set of seven coupled differential equations like those of the nHESEL model. Instead computational means are applied in order to obtain numerical approximate solutions.

In this chapter it is described how the equations are implemented in the BOUT++ framework [85]. The BOUT++ framework applies the finite difference method to discretize and solve the set of coupled differential equations in a specified domain. The implementation of the model into BOUT++, including the choice of domain, boundary conditions, and normalizations, is described in Sec. 3.1.

A model for a physical system may be useless, or even misleading, if it fails to include the determining physical properties of the system, or if the numerical machinery does not solve the underlying mathematical model as intended. For those reasons it is essential to validate and verify the numerical model. The verification of the nHESEL model is described in Sec. 3.2, and the validation of the model is discussed in Sec. 3.3.

3.1 Implementation in BOUT++

The nHESEL model has been implemented in the BOUT++ framework [85], which is an open source generic numerical tool tailored for solving plasma transport equations in an arbitrary magnetic field geometry, and allows the user to decide on the equations to be solved, which temporal solver to apply, and the spatial numerical discretization schemes. The default magnetic field direction in BOUT++ is in the negative y-direction, resulting in the nHESEL equations to be formulated in the xz-plane. For the results presented here, however, the transformations $z \to y$ and $y \to -z$ have been made to follow the more common procedure of aligning the magnetic field with the z-axis.

3.1.1 Finite difference schemes

The nHESEL model is solved in a slab at the out-board mid-plane with Euclidian geometry, depicted in Fig. 3.1. For the spatial derivatives a second order centred finite difference scheme is applied, i.e., for a field f the spatial derivative on grid-point x_i is given by

$$\begin{aligned} f'(x_i) &= \frac{f(x_{i+1}) - f(x_{i-1})}{2\Delta x} + \mathcal{O}(\Delta x^2)\,, \\ f''(x_i) &= \frac{f(x_{i+1}) - 2f(x_i) + f(x_{i-1})}{\Delta x^2} + \mathcal{O}(\Delta x^2)\,, \end{aligned} \tag{3.1}$$

where Δx is the grid spacing. The nHESEL model also has numerous uses of anti-symmetric brackets, $\{\cdot,\cdot\}$, which in the simplest numerical implementation results in consecutive use of different finite difference operators. This has been shown [86] to lead to artificial generation of, e.g., energy, which can be avoided by applying the so-called Arakawa bracket scheme in which the anti-symmetric bracket is discretized in a somewhat complicated manner involving the fields in the brackets evaluated at all of the eight surrounding grid-points. Forward time stepping is carried out adaptively by one of various possible temporal solvers offered in the BOUT++ framework. For the results presented here, the pvode solver [87] is applied, with an absolute tolerance of 10^{-10}, relative tolerance of 10^{-5}, and a maximum number of iterations allowed per time step before convergence is reached of 10^5.

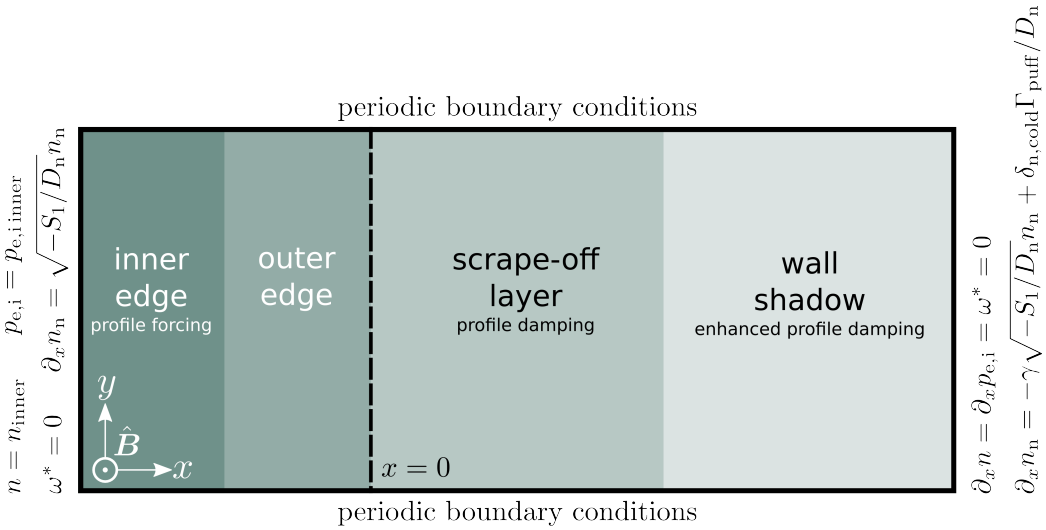

Figure 3.1: Domain for the combined HESEL-neutral simulations, where the x-coordinate correspond to the radial direction and the y-coordinate correspond to the poloidal direction. In the inner part of the edge region, marked by the darkest area, the plasma density and pressure fields are relaxed towards fixed prescribed profiles, which result in a dynamically imposed boundary condition towards the core. In the SOL region the plasma fields are damped according to parametrized parallel transport. The dashed line shows the location of the LCFS at $x = 0$.

3.1.2 Boundary conditions

In the poloidal direction the boundaries are periodic, and only radial boundary conditions on the inner boundary towards the core region and on the outer boundary towards the first wall are imposed. For the plasma fields in the nHESEL model, the inner boundary is defined by an artificial source which relaxes the density and temperature profiles towards a prescribed profile. This forcing of the profiles is described in Sec. 3.1.3, and the prescribed profiles likewise define the Dirichlet boundary condition. Typical values are

$$n = n_{\text{inner}} = 1.5\, n_0\,, \quad p_\text{e} = p_{\text{e,inner}} = 10\, n_0 T_{\text{e}0}\,, \quad p_\text{i} = p_{\text{i,inner}} = 5\, n_0 T_{\text{e}0}\,, \tag{3.2}$$

where $n_0, T_{\text{e}0}$ are the gyro-Bohm normalization parameters in Sec. 2.1. Near the outer boundary the above fields are strongly influenced by the enhanced parallel losses, also described in Sec. 3.1.3, and obey Neumann boundary conditions at the boundary, i.e.,

$$\partial_x n = \partial_x p_{\text{e,i}} = 0\,. \tag{3.3}$$

The modified vorticity is not subject to the forcing in the inner edge region, and on both inner and outer boundaries it retains Dirichlet values of zero

$$\omega^* = 0\,. \tag{3.4}$$

The neutral boundary conditions are found from the two assumptions. On the wall, a fraction of the neutrals γ are absorbed after colliding with the wall, and the remaining fraction $1-\gamma$ of neutrals are reflected. On the inner boundary, it is assumed that in the deep edge or core the neutrals are ionized and/or dissociated completely, which gives an exponential source dependence on the flux on the boundary. In both cases, it is assumed that the fluctuations on the boundaries and gradients in the non-radial plane are negligible, and thus the temporal derivative and poloidal spatial derivative vanish in the neutral transport equation for species n

$$\partial_t n_\text{n} - \nabla\cdot(D_\text{n}\nabla n_\text{n}) = S_\text{n}\,, \tag{3.5}$$

and thus on the boundaries one has

$$\partial_x\left(D_\text{n}\partial_x n_\text{n}\right) = -S_\text{n}\,. \tag{3.6}$$

The particle flux is identified as $\Gamma_\text{n} = -D_\text{n}\partial_x n$. The source term is assumed constant around the boundary and can be split into $S = S_0 + S_1 n$, where

neither S_0 nor S_1 depend on n. The above differential equation can readily be solved to yield the density at the boundary

$$n_{\mathrm{n}}(x) = c_1 \exp\left(\sqrt{-\frac{S_1}{D_{\mathrm{n}}}}x\right) + c_2 \exp\left(-\sqrt{-\frac{S_1}{D_{\mathrm{n}}}}x\right) - \frac{S_0}{S_1}\,. \tag{3.7}$$

For the edge boundary it is assumed that far into the edge region ($x \ll 0$), the neutral density should go to 0, i.e.,

$$\lim_{x\to-\infty} n_{\mathrm{n}}(x) = 0\,. \tag{3.8}$$

This demands for S_0/S_1 to go to zero in the deep edge, and determines $c_2 = 0$. The first condition is automatically satisfied, since it will depend linearly on other neutral densities, which should also go to zero in that limit. Fixing the constant c_1 can be omitted by demanding a finite flux boundary condition, i.e.,

$$-\Gamma_{\mathrm{n}} = D_{\mathrm{n}}\partial_x n_{\mathrm{n}} = \sqrt{-D_{\mathrm{n}}S_1}\,n_{\mathrm{n}}\,. \tag{3.9}$$

In the collisions between neutrals and the wall due to thermal motion, a fraction γ of the neutrals is assumed to be absorbed by the wall, and the remaining $1-\gamma$ reflected. The flux is derived as for (3.9), but with opposite sign, and thus reads

$$\Gamma_{\mathrm{n}} = -\left[D_{\mathrm{n}}\partial_x n_{\mathrm{n}} - (1-\gamma)D_{\mathrm{n}}\partial_x n_{\mathrm{n}}\right] = -\gamma D_{\mathrm{n}}\partial_x n_{\mathrm{n}}\,, \tag{3.10}$$

which agrees with the intuition that if the wall is completely reflecting ($\gamma = 0$) the boundary condition is a zero-flux Neumann. And if the wall absorbs all particles that hit it ($\gamma = 1$), the flux equals that caused by diffusion out of the system. Again (3.7) can be applied to find a closed expression for the flux by demanding that, if the neutrals could penetrate the wall, the density should vanish for large x, i.e., $c_1 = 0$, and thus

$$\Gamma_{\mathrm{n}} = -\gamma\sqrt{-D_{\mathrm{n}}S_1}\,n_{\mathrm{n}} + \Gamma_{\mathrm{puff}}\delta_{\mathrm{n,cold}}\,. \tag{3.11}$$

Here $\Gamma_{\mathrm{puff}}\delta_{\mathrm{cold}}$ is added to account for the inwards flux of cold neutrals from gas puffing, which should only affect the cold neutral flux.

Length-scales in this normalization scheme are determined by both ρ_s and $n_0^{1/3}$, and care must be taken when normalizing the equations. The flux

is measured in physical units of $[\Gamma] = \mathrm{L}^{-2}\mathrm{T}^{-1}$, so the RHS of (3.9) must be normalized by $\mathrm{L}^2\mathrm{T}^1$. This is obtained consistently by the transformations

$$n_\mathrm{n} \to \frac{n_\mathrm{n}}{n_0}\,, \qquad S_n \to \frac{S_\mathrm{n}}{n_0\Omega_\mathrm{ci}}\,, \qquad D_\mathrm{n} \to \frac{D_\mathrm{n}}{\rho_s^2\Omega_\mathrm{ci}}\,, \tag{3.12}$$

and the dimensionless Neumann flux on the edge-boundary thus is

$$\Gamma_\mathrm{n} = \frac{1}{n_0\rho_s\Omega_\mathrm{ci}}\sqrt{-D_\mathrm{n}S_\mathrm{n}}n_\mathrm{n}\,. \tag{3.13}$$

Likewise on the wall-boundary one finds

$$\Gamma_\mathrm{n} = -\frac{1}{n_0\rho_s\Omega_\mathrm{ci}}\left[\gamma\sqrt{-D_\mathrm{n}S_\mathrm{n}}n_\mathrm{n} + \Gamma_\mathrm{puff}\delta_\mathrm{n,cold}\right]\,. \tag{3.14}$$

In BOUT++ the boundary conditions must be applied manually in a finite difference form. A one-sided discretization scheme with 2^nd order accuracy is used, i.e.,

$$f'(x_i) = \frac{-f(x_{i+2}) + 4f(x_{i+1}) - 3f(x_i)}{2\Delta x} + \mathcal{O}(\Delta x^2)\,, \tag{3.15}$$

for x_i at the inner boundary, and

$$f'(x_i) = \frac{3f(x_i) - 4f(x_{i-1}) + f(x_{i-2})}{2\Delta x} + \mathcal{O}(\Delta x^2)\,, \tag{3.16}$$

for x_i at the outer boundary.

This concludes the boundary conditions section, and the simulation domain and typical parameters are presented in the following section.

3.1.3 Domain and normalizations

The domain and normalizations reflect the experimental conditions which are simulated, and will thus vary for each study case. There are certain restrictions on the parameters that effectively result from the approximations of the drift-ordering, i.e., the code can only resolve dynamics that are much slower than the time-scale set by the gyro-frequency, and length-scales much larger than the Larmor radius. Typical values for a simulation of a medium-sized tokamak are presented in the following.

The fields are normalized according to the gyro-Bohm normalization convention presented in Sec. 2.1. The normalization constants for a typical simulation are

$$\begin{aligned} \Omega_{\mathrm{ci}} &= 9.57 \cdot 10^{7}\,\mathrm{s}^{-1}\,, & \rho_{\mathrm{s}} &= 3.23 \cdot 10^{-4}\,\mathrm{m}\,, \\ n_0 &= 1.50 \cdot 10^{19}\,\mathrm{m}^{-3}\,, & T_{\mathrm{e0}} &= 20\,\mathrm{eV}\,. \end{aligned} \tag{3.17}$$

For enhanced computational speed the neutral transport equations in nHESEL are typically solved with fixed diffusion coefficients of

$$D_{\mathrm{hot}} = 10^{1} D_{\mathrm{warm}} = 10^{3} D_{\mathrm{cold}} = 10^{2} \rho_{\mathrm{s}}^{2} \Omega_{\mathrm{ci}}\,. \tag{3.18}$$

The remaining free parameters for the neutrals are the inwards flux of cold neutrals from the wall, Γ_{puff}, and the wall reflection coefficient γ, which is introduced in Sec. 3.1.2. The paper presented in Sec. 4.2 effectively presents a four-point scan in Γ_{puff}.

The typical domain extends $225\,\rho_{\mathrm{s}}$ in the x-direction, and $75\,\rho_{\mathrm{s}}$ in the y-direction (which is the z-direction when implemented in BOUT++), and is perpendicular to the magnetic field. The domain is subdivided into the inner edge, outer edge, SOL, and wall shadow regions, which typically cover respectively $\frac{1}{6}$, $\frac{1}{6}$, $\frac{1}{3}$, and $\frac{1}{3}$ of the radial extend. In the inner edge region, the electron and ion density and pressure fields are forced towards a fixed profile, resulting in an effective source term of the form

$$S_{\mathrm{force}}(x) = \frac{\frac{1}{2}\left[1 - \tanh\left(\frac{2}{3}\left(x - \frac{1}{2} x_{\mathrm{LCFS}}\right)\right)\right]}{\tau_{\mathrm{force}}} (f - f_{\mathrm{force}})\,, \tag{3.19}$$

for $f = n, p_{\mathrm{e,i}}$, and where x_{LCFS} is the distance to the LCFS from the innermost domain boundary, i.e., $\frac{1}{6}$ of the domain width, and a typical value for the characteristic forcing time is $\tau_{\mathrm{force}} = 50\,\Omega_{\mathrm{ci}}^{-1}$. The values of f_{force} are defined by the corresponding inner boundary Dirichlet conditions, $n_{\mathrm{inner}}, p_{\mathrm{e,i\,inner}}$

$$n_{\mathrm{force}} = n_{\mathrm{inner}}\,, \qquad p_{\mathrm{e,i\,force}} = p_{\mathrm{e,i\,inner}} + \frac{x}{x_{\mathrm{LCFS}}} \left(1 - p_{\mathrm{e,i\,inner}}\right)\,, \tag{3.20}$$

where x measures the distance from the inner boundary. In the outer edge region, the fields evolve without the direct influence of the forcing source. The SOL region have a damping term that parametrizes the parallel losses, and enters the transport equations (2.121)-(2.124) in terms proportional to $\sigma(x)$, which is a step-function that is zero in the edge region, and 1 in the SOL region. In the wall shadow region, the parallel losses are enhanced fourfold. The domain sketched in Fig. 3.1.

In the following section the nHESEL code is verified by the method of manufactured solutions, and following that is a discussion on the validation of the neutral part of the model.

3.2 Verification

The implementation of the nHESEL model into the BOUT++ framework allows for obtaining approximate numerical solutions to the system of equations. When discretizing and solving mathematical models numerically there is always a risk that the implementation is faulty, and it is thus essential to verify the numerical code to ensure that is solves the system of equations correctly and at the desired precision. Verification of numerical models is treated in detail in [88]. It should be emphasized that the verification process do not provide any information on whether the mathematical model is suitable for describing the physical system, neither if the numerical methods are applicable for the equations to be solved. The assessment of whether the (numerical) solution to the model equations describe the physical features that it is meant to simulate is the core of the validation process, and is for the nHESEL model discussed in Sec. 3.3.

The essential step when moving from an analytical to a numerical model is the discretization of the fields onto a numerical grid, and in particular the discretization of the differential operators. The latter naturally introduces an error, as the discretization involves truncating a series expansion of the differential operator term. As mentioned in Sec. 3.1 the second order centred scheme is applied for spatial discretization, i.e., for some field f at x_i the derivatives are approximated by the terms in (3.1), and thus truncated at terms of order Δx^2 and higher. The global error $\|e\|_{l^n}$ measured by the l^n-norm is given by

$$\|e\|_{l^n} = \|f_{\text{true}} - f_{\text{num}}\|_{l^n} \ , \tag{3.21}$$

where f_{true} is the analytical solution to a field f on all grid points, and f_{num} is that acquired by numerical means. Theory of linear partial differential equations dictates, that for the discretization scheme to be consistent and stable the error must converge to the order of the truncation error, i.e., order 2 for the nHESEL model, when the grid-point spacing approaches zero. The core of the verification process is to prove that this is true for the numerical model.

The analytical solution f_{true} to the fields relevant for the physical system is, however, not known. The absence of an analytical solution was after all the reason for seeking out a numerical solution in the first place. But as the verification process only concerns the numerics, and not the correspondence of the solution to a physical system, the numerical framework can be tested on a so-called manufactured solution, for which f_{true} can be obtained. The technique is known as verification by the method of manufactured solutions (MMS) and is described in detail in [89]. The model is written on the form

$$\mathcal{L}(f) = 0\,, \tag{3.22}$$

where $\mathcal{L}$ is a non-linear operator, containing the spatial and temporal derivatives that make out, e.g., the nHESEL model, acting on some solution field f. For the MMS technique an arbitrary solution, f_{M}, that has defined derivatives and which fulfils the boundary conditions of the model, is acted upon by $\mathcal{L}$. This result in a source term S on the RHS of (3.22), i.e.,

$$\mathcal{L}(f_{\text{M}}) = S\,. \tag{3.23}$$

The source term S results from applying the model on a manufactured solution, and has nothing to do with the sources otherwise treated in the thesis, e.g., those arising from neutral-plasma interactions. Since f_{M} is the analytical solution to (3.23), this set of equations, which is the original model augmented with an additional source term, is now solved numerically to obtain a solution f_{num}, which allows for calculating the global error

$$\|e\|_{l^n} = \|f_{\text{M}} - f_{\text{num}}\|_{l^n}\ . \tag{3.24}$$

For the numerical scheme to be verified (3.24) must convergence at the truncation order.

The nHESEL model is verified by the MMS technique, for all dynamical fields $f = \ln n_{\text{e}}, \ln p_{\text{e}}, \ln p_{\text{i}}, \omega^*, \ln n_{\text{cold}}, \ln n_{\text{warm}}, \ln n_{\text{hot}}$. All constants in the model are redefined to be of order unity, so that all terms are weighted more equally. The numerical model is solved for a series of grid-point spacings Δx, and the resulting errors in the l^2-norm and in the l^∞-norm are calculated and shown in Fig. 3.2. It is observed for the grid-point spacing approaching zero, the error norm for all fields converge at the truncation error order of 2. The BOUT++ framework, and thus the built-in differential operators, have previously been verified by MMS as reported in [90].

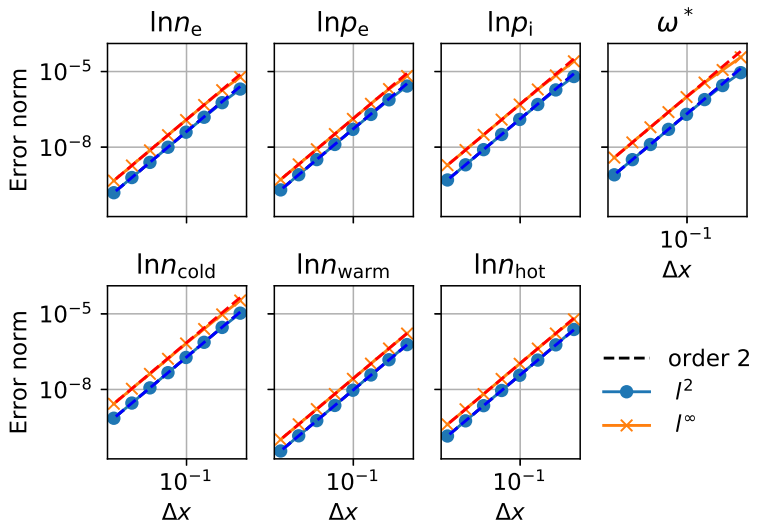

Figure 3.2: Convergence rate of error norms as a function of grid-point spacing for solving the nHESEL model with manufactured solutions and resulting source terms.

3.3 Validation

With assurance from the method of manufactured solutions that the numerical scheme discretizes and solves the nHESEL model equations at the expected order, the next question is whether the model describes the physical system that it simulates well. The plasma field transport is governed by the HESEL equations, which have proved in multiple publications [91, 92, 93, 94] to mimic the outboard-midplane plasma dynamics at various machines well. The neutral part of the nHESEL model, on the other hand, is novel and the focus will be on the validity of this.

It is important to keep the expected performance of the neutral model in mind; the fluid-like description of the neutrals at long mean-free path allows for a dynamical model that represents transport phenomena at time scales similar to those of drift-fluid models, but also comes with limitations. Excitations of atoms and molecules are not considered, which prevents a range of dissociation and ionization paths to be taken into account. Wall recycling of charged particles to neutrals is likewise not included. Both effects influence the sources of molecules and atoms separately, and may thus affect the absolute values of the neutral densities, as well as the density ratio of molecules to atoms. On the other hand the model is tailored to describe

neutrals at various characteristic temperatures, and the dominant inelastic interactions are included. This should produce characteristic length scales for the neutral densities, and provide realistic spatial source terms.

Ideally experimentally measured plasma field profiles would be put into the neutral model, and the resulting neutral density fields could be compared to those measured. This would allow for assessing whether the model succeeds to provide realistic neutral density and source term profiles, and thus validate the neutral model. Unfortunately experimental data on neutral fields are sparse, and validation of the code against experimental data has not been possible.

Another, though less credible, solution is to benchmark the code against those for comparable models. For this purpose a qualitative comparison with an EIRENE simulation is provided [95]. EIRENE is a steady state kinetic model for neutral molecules and atoms [61], which from inputted plasma fields provides neutral profiles that are comparable to those obtained from the neutral part of nHESEL. Several remarks are necessary to make in this context. EIRENE and nHESEL are very different models, with diverging focal points. The neutral part of nHESEL, in addition to yield source profiles, seeks out to provide a dynamical response to turbulent plasma fields from a simplified description of the atomic processes. EIRENE on the other hand treats atomic and molecular physics in great detail, but provides steady state solutions. Moreover a comparison of only the neutral part of the model does not give any validation to the source drift terms in nHESEL, and primarily evaluates the transport aspect of the neutral code. With those limitations in mind a comparison is valuable, at least for the purpose of assessing whether the neutral model fulfils its purpose of providing the same characteristic length scales at steady state.

Interpolated profiles from the SOLPS code [39] for the electron density n_e and the electron and ion temperatures $T_\mathrm{e,i}$ are shown for an H-mode shot at the ASDEX Upgrade tokamak in Fig. 3.3, with the LCFS at $r = 0$. Results from simulations by the 1D version of the neutral part of nHESEL, as well as from EIRENE, are for the molecule densities shown in Fig. 3.4, and for the atom densities in Fig. 3.5. The neutral part of the nHESEL model is solved with Neumann boundary conditions, and the flux of molecules into the system is matched to that of the EIRENE model on the outer boundary.

For the molecule densities in Fig. 3.4 it is observed, that the overall, and in particular the SOL, profiles are both quantitatively and qualitatively

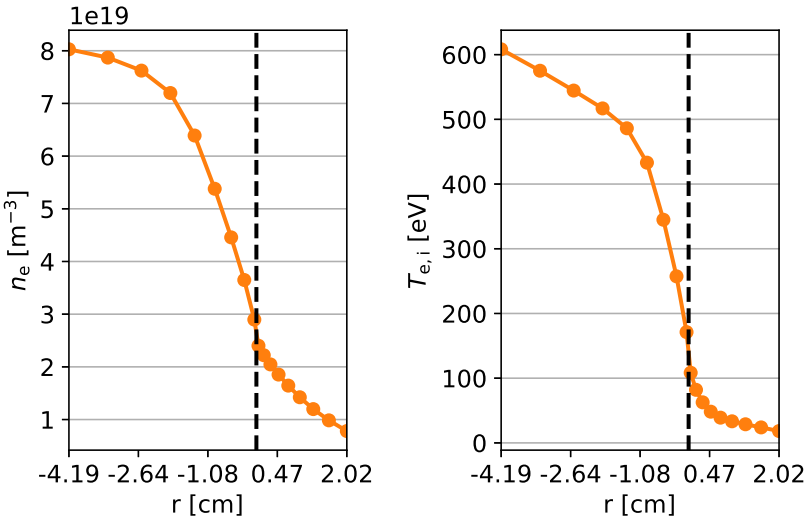

Figure 3.3: Radial interpolated profiles for electron and ion densities and temperatures, for which the interactions with the nHESEL and EIRENE neutral models result in the profiles for neutral densities shown in Figs. 3.4 and 3.5. The dashed line in these and the following plots indicate the position of the LCFS.

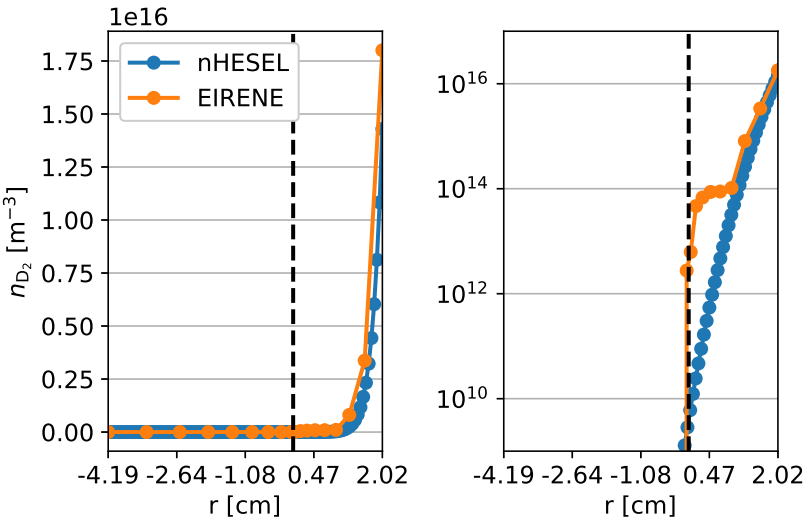

Figure 3.4: Profiles for the deuterium molecule densities in a linear plot (left) and a single logarithmic plot (right) for the neutral models nHESEL and EIRENE. The flux of molecules into the system in the nHESEL model is matched to that of the EIRENE model.

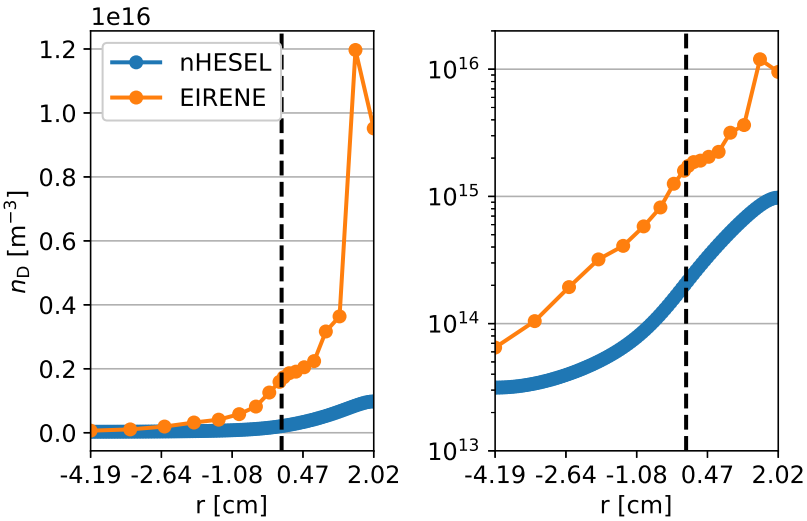

Figure 3.5: Profiles for the deuterium atom densities in a linear plot (left) and a single logarithmic plot (right) for the neutral models nHESEL and EIRENE. The atom density in the nHESEL model experience Neumann boundary conditions, and the profile is thus entirely determined by those of the plasma fields and neutral molecules. Note that the grid point spacing for the nHESEL model is so small, that the points appear to form a thick solid line.

consistent. The density profile provided by EIRENE has a bump near the LCFS which is not reproduced by the nHESEL neutral model, but densities from both models rapidly fall to zero inside the LCFS, and have similar fall off length scales in the outer SOL region.

The atom densities shown in Fig. 3.5, on the other hand, differ by a as much as an order of magnitude. The reasons for the discrepancy could be neglecting dissociation channels, which would, however, lower the molecule density if included, as well as the lack of surface recycling effects in the nHESEL model. The models do, however, show consistency in the characteristic length scales in most of the domain, which is after all the primary feature expected from the nHESEL neutral model in this comparison.

The analysis is in many ways superficial, and in particular benchmarking nHESEL to a time-dependent model would add to the validity of the neutral part of nHESEL. There is, however, cross-model consistency of char-

acteristic length-scales of the molecule and atom densities, and more suitable benchmarkings can hopefully be conducted in the future.

The comparison of the neutral part of the nHESEL model to EIRENE concludes the chapter on numerical implementation, and in the following chapter a series of studies using the nHESEL model are presented.

Chapter 4

Results

The nHESEL model, summarized in Sec. 2.3, which self-consistently describe transport of and interactions between plasma and neutrals in the edge and SOL regions, is applied for various study cases presented in this chapter. The main part of the chapter consists of three papers, of which two are published in peer reviewed journals, and one has been submitted, and covers Secs. 4.1 - 4.3. In addition to those papers, three non-peer reviewed conference papers are presented in Sec. 4.4, as well as a selection of non-published results in Sec. 4.5.

The peer-reviewed papers are presented in chronological order. The first paper in Sec. 4.1 discusses the so-called mean-field models, where the dynamical electron and ion fields are replaced by their temporal mean values to ease computations. The paper moreover describe a 1D predecessor to the nHESEL model, which asserts the influence of blobs on the density of neutral atoms. The paper in Sec. 4.2 can be viewed as the core paper for the work of the thesis. It presents an overview of the theory given in Chpt. 2, and mainly focuses on the effects of source terms, originating from interactions with neutrals, on the edge plasma. As for the first paper, the effect of blobs on the neutral density is studied in Sec. 4.3. The results from the latter is obtained from the nHESEL model, and thus include the effect of dissociation of molecules, which proves to be quintessential to the fluctuations of the neutral atomic density in the SOL.

Each of the main papers are preceded by an introduction to the paper, which functions as an extended abstract to the papers, where the relation to

the nHESEL model and main results are reviewed. The papers are likewise succeeded by a discussion on the results in connection to the similar findings, and the thesis as a whole.

4.1 The influence of blobs on neutral particles in the scrape-off layer

4.1.1 Prelude

As an initial steps towards formulating the nHESEL model, the paper presented here provides a 1D fluid model for neutral atoms in a dynamic SOL, where the atoms are at different characteristic temperatures.

The paper has three main sections. In the first section, the underlying considerations for formulating a neutral model with discrete isothermal subspecies is reviewed. The arguments are similar to those presented in Sec. 2.2, and based on the collisional long mean-free path of neutrals in the SOL, and the creation of Franck-Condon neutrals at distinct energies. The second section assesses the validity of the so-called mean-field approximation under the conditions present in a turbulent SOL. In the mean-field approximation, it is assumed that the average of the product of plasma fields is the same as the product of the average fields. The approximation thus neglects the field fluctuation correlation term, which is shown to be significant in the SOL region, based on HESEL simulations. The third section provide the 1D radial neutral model, and applies it to two study-cases, and compares the influence of the plasma field perturbations on the neutral densities to a similar 2D model perpendicular to the magnetic field lines.

The neutral model consists of three neutral atomic species, where the 'cold' atoms correspond to the 'warm' atoms of the nHESEL model, and the 'warm' atoms of the model presented here have been left out in the final model. The plasma fields are given by a static background, on which a Gaussian field perturbation is created at the LCFS and propagates radially outwards through the SOL. The two study-cases are both based on a scan in the blob emergence frequency, and consider the effect of this on the ionization fraction between the SOL and edge regions, and the flux of neutral particles across the LCFS.

It is found that the fraction of ionization in the SOL region to that of the ionization in the whole domain increases almost linearly with the blob frequency in the applied frequency domain. The linear dependence on the blob frequency is most likely a result of the enhanced average electron pressure in the SOL as a result of a shorter blob waiting time, as the blob frequency is low enough for the neutral profiles return to inter-blob steady state values between each blob. The fraction of SOL ionization to that of the ionization in the whole domain is, however, larger than that obtained using the mean-field approximation over a blob period for all blob occurrence frequencies. The latter displays the importance of taking the plasma field correlation into account even for simple models.

The inwards net flux of neutral atoms across the LCFS can be used as a proxy for the plasma fuelling rate. As for the first study-case, this quantity is simulated as a function of the blob frequency, and shows a sub-linear decrease for increasing blob occurrence frequencies. Also in this case all values are below that obtained by applying the mean-field approximation. The effect of the blobs on the neutral density flux is compared to a similar 2D model, in which the blobs are simulated as 2D local Gaussian perturbations. In the latter case, the results are reproduced, but to a smaller extend, as the relative size of the blob to the whole domain is smaller for the 2D model.

Thus, the paper stresses the importance of including the correlation terms for the plasma field variables in numerical models, and shows with two examples the effect of using the mean-field approximation instead of the full signal, when calculating reaction rates from plasma-neutral interactions. It was published in *Plasma Physics and Controlled Fusion* (Vol. 58, Issue 4) on 22 February 2016, and the paper presented in the following is the preprint of [96].

The Influence of Blobs on Neutral Particles in the Scrape-Off Layer

Alexander S. Thrysøe[1*], Laust E. H. Tophøj[1], Volker Naulin[1], Jens Juul Rasmussen[1], Jens Madsen[1], Anders H. Nielsen[1]

[1]PPFE, Department of Physics, DTU, DK-2800 Kgs. Lyngby, Denmark

Abstract

Interactions between plasma and neutrals are investigated with particular attention to the influence of large amplitude blob structures that mediate a significant particle and energy transport through the Scrape-Off Layer (SOL). We perform a statistical analysis of the mean-field approximation for plasma parameters in the SOL, and this approximation is shown to be poor in a SOL with a high level of fluctuations, as the plasma fields are strongly correlated. A 1D neutral fluid model which account for both cold and hot neutrals is formulated and the effects of blobs on the ionization in the SOL and edge are investigated. Simulations suggest that neutrals originating from dissociation of hydrogen molecules only fuel in the outermost edge region of the plasma, whereas hot neutrals from charge exchange collisions penetrate deep into the bulk plasma. The results are recovered in a simplified 2D model.

1 Introduction

Transport from the bulk plasma edge to the chamber wall of a magnetically confined plasma is found to be highly intermittent [1, 2, 3]. A significant part of heat and particles is carried across the magnetic field lines in field-aligned filaments of enhanced plasma pressure. Such filaments are usually denoted blobs. The region outside the plasma edge is characterized by open magnetic field lines and referred to as the Scrape-Off Layer (SOL). The plasma temperatures in the SOL are much lower that those of the bulk plasma [1, 2]. This allows for the existence of neutral atoms, which are otherwise not present due to a high ionization rate at temperatures above the ionization energy.

Neutrals can originate from plasma-wall interactions or be puffed into the chamber for fueling or imaging purposes. Another technique for fueling, which is not studied in this paper, is supersonic molecular beam injection which have

*alec@fysik.dtu.dk

a directed flow, where the speed of neutral molecules is much larger than that for gas puffed molecules.

Neutrals from gas-puffing, on the other hand, are at room temperature and their mean-free path for ionization is short compared to the width of the SOL, but similar to the perpendicular length scale of blobs [4]. This indicates that the influence of the intermittent structures on the neutrals differs significantly from what one would find from approximating the blobs by mean density and temperature. In a quiet SOL the ionization will be weak due to the low temperature, but the blobs come with an enhanced temperature and density, and may thus lead to a significant increase in ionization.

In this paper the feasibility of computing quantities from knowledge of mean fields in the plasma is discussed on the background of results obtained from a numerical edge/SOL turbulence code. We show that the mean-field approximation for the electron impact ionization rate is poor in the SOL region, due to the strong correlation between plasma density and temperatures in blobs, and the strong temperature dependence of the electron impact ionization rate coefficient.

The blob-neutral interactions are further investigated in a simpler 1D model, that takes into account the most dominant reactions between the plasma and neutral particles. The model includes hot neutral particles produced in charge exchange collisions between cold neutrals and hot plasma. The results suggest that the cold neutrals only penetrate the edge with a few centimeters, whereas hot neutrals fuel tens of centimeters inside the LCFS due to their longer ionization mean-free path. The fueling rate of the two species is comparable, even though the hot neutral density is typically an order of magnitude smaller than that of cold neutrals. This illustrates the importance of including hot charge exchanged neutrals in the model. We also find that the fraction of ionization occurring in the SOL increases with increasing blob frequency.

The structure of the paper is as follows. In Sec. 2 the interactions between plasma and neutrals are described, and mean-free paths for ionization and charge-exchange interactions at different neutral temperatures are discussed. Section 3 contains a critical analysis of the mean-field approximation in the SOL. In Sec. 4 a 1D model is used to analyze the interactions between blobs and neutrals. We compare the ionization in the SOL and edge regions, and the neutral density flux across the LCFS. In this section we also present results from a simplified 2D model and compare those to the 1D results. The conclusions are summarized in Sec. 5.

2 Plasma-Neutral Interactions

For a given collision reaction between two species of number density n_1 and n_2, the reaction rate is given by

$$\nu_R = n_1 n_2 \langle \sigma_R v_r \rangle, \tag{1}$$

where $\sigma_R = \sigma_R(v_r)$ is the cross-section of reaction R, and v_r is the relative velocity of species 1 and 2. The brackets $\langle \cdot \rangle$ indicate the average over the velocity distributions of the species. The velocity averaged quantity is known as the rate coefficient

$$k_R \equiv \langle \sigma_R v_r \rangle. \tag{2}$$

The rate coefficient thus determines the rate of a given reaction, say electron impact ionization. As long as many-body interactions can be neglected, it is independent of the densities of the species. In the following, we shall discuss the behavior of the reaction rate, and how temporally averaging its factors affect this.

We assume that the neutrals consist of atomic hydrogen. In actual fueling scenarios molecular gas is injected, so we assume the dissociation of those molecules to occur so far out in the SOL that it is reasonable to only include the neutral atoms in the model. It should also be mentioned that a proper inclusion of molecular interactions should account for the energy required to dissociate hydrogen molecules (which is roughly 4.5 eV, see e.g. [5]).

The hydrogen molecule dissociation introduce an atomic neutral density source, and the atoms resulting from the dissociation will carry the molecular binding energy of a few eV. We will refer to the neutral atoms originating from molecular dissociation as cold neutrals. In the literature those neutrals are referred to as Franck-Condon neutrals [6].

The molecules may also be ionized to so-called dihydrogen cations (H_2^+), and the ionization energy for this process is 15.6 eV. Note that this ionization energy is close to that of atomic hydrogen. The inclusion of H_2 has been omitted, as it is believed to dissociate in the far SOL.

Simple estimates (see, e.g., [6]) allow for expressing the rate coefficient for electron impact ionization, radiative recombination, and charge-exchange for ground-state hydrogen as

$$k_{\mathrm{iz}} = 2 \cdot 10^{-13} \frac{\sqrt{T_\mathrm{e}/T_*}}{6 + T_\mathrm{e}/T_*} \exp\left(-\frac{T_*}{T_\mathrm{e}}\right) \quad \mathrm{m^3 s^{-1}}\,, \tag{3}$$

$$k_{\mathrm{rc}} = 7 \cdot 10^{-20} \sqrt{\frac{T_*}{T_\mathrm{e}}} \quad \mathrm{m^3 s^{-1}}\,, \tag{4}$$

$$k_{\mathrm{cx}} = 3.2 \cdot 10^{-28} \left(\frac{3}{2} \cdot T_\mathrm{i}\right)^{-0.2} \sqrt{\frac{3T_\mathrm{i}}{m_\mathrm{i}}} \quad \mathrm{m^3 s^{-1}}\,, \tag{5}$$

where T_* is the ionization potential (13.6 eV for hydrogen) and temperatures are inserted in eV. Here, (3-4) are taken from [7], and (5) is stated by assuming the charge-exchange cross section $\sigma = 8{\cdot}10^{-19}(\frac{3}{2}T_\mathrm{i})^{-0.2}\,\mathrm{m}^2$ estimated from Fig. 10.8 of [7] and using the ion sound speed. The reaction rates are plotted in Fig. 1. Note that we do not consider the recombination reaction in this paper, as it is several orders of magnitudes smaller than ionization and charge exchange in the domain of interest.

The mean-free path of species 1 for some reaction R with species 2 is given by [7]

$$\lambda^1_\mathrm{mfp} = \frac{v_\mathrm{th}}{n_2\langle\sigma_\mathrm{R} v_r\rangle}\,, \tag{6}$$

where v_th is the thermal velocity of species 1. If the mean free path is larger than the domain, the reactions occur at an equal rate throughout the system. If on the other hand the mean-free path of neutrals for, e.g., ionization is much smaller than the system, there will be a localized plasma source. In Fig. 2a the mean-free path for cold neutral atoms is shown as a function of plasma temperature and density. It is seen that the cold neutral mean-free path in the SOL is roughly 10 cm for ionization and 5 cm for charge exchange collisions, for typical SOL conditions of medium sized tokamaks. This is smaller than or comparable to the typical SOL width, and this suggests that the flux of cold neutrals across the LCFS is small compared to that of the neutrals puffed into the system. The charge exchange collisions does, however, change a hot ion and a cold neutral to a cold ion and a hot neutral and thus source warmer species of neutrals with a larger mean-free path.

In Fig. 2b the ionization mean-free path of neutrals of temperature $T = 50$ eV is depicted. The mean-free path for hot neutrals is much larger than the SOL width, and these are expected to mainly be ionized within the first 10 cm of the edge region.

3 Averaging Correlated Signals

We begin with a generic discussion on averaging of fluctuating signals. Other statistical treatments of blobs are presented in [8, 9], where stochastic models for the plasma density fluctuations are presented. A critical assessment of the mean-field approximation is also discussed in [10]. The conclusions from our analysis of the mean-field approximation are consistent with those presented there.

Without loss of generality an intermittent field $a(t)$ can be written as the sum of a temporally averaged part $\bar{a} \equiv \langle a\rangle$ and a fluctuation part $\tilde{a}(t)$, as $a(t) = \bar{a} + \tilde{a}(t)$. Note that the average here is different from that defined in the previous section. The average of a product of two signals $a(t)$ and $b(t)$ is

$$\langle a(t)b(t)\rangle = \bar{a}\bar{b} + \langle\tilde{a}\tilde{b}\rangle\,. \tag{7}$$

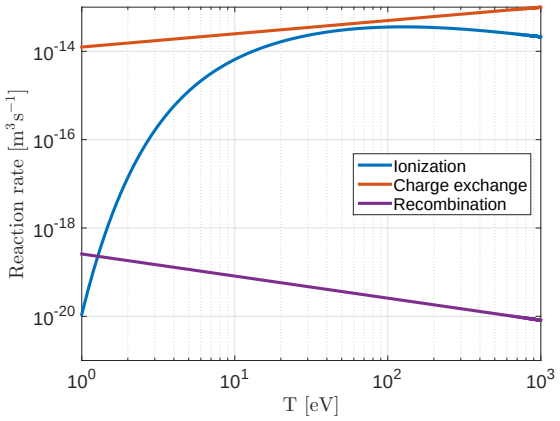

Figure 1: Dominant reaction rates for plasma-neutral interactions, given by (3,4,5). Stangeby [6], p.35.

Expressing the average of the product as the product of the averages, i.e., by ignoring the second term on the right hand side of (7), the *cross-correlation* $\langle \tilde{a}\tilde{b} \rangle$ of the signals is neglected. In the case of edge/SOL turbulence, this cross-correlation may be significant, if the signal relates to, e.g., the density and temperature.

This feature can be illustrated by a simple example. Consider a signal a having two levels. At a fraction δ of time, $a = A$, and a fraction $1-\delta$ of time, $a = \Lambda A$ with $\Lambda<1$. We consider the averaging procedure for the square of this signal, as a proxy for two perfectly correlated signals. Now, $\langle a \rangle = [\delta+(1-\delta)\Lambda]A$, and $\langle a^2 \rangle = [\delta + (1-\delta)\Lambda^2]A^2$, so the difference between including both terms in (7) and only the first is

$$\frac{\langle a^2 \rangle}{\langle a \rangle^2} = 1 + \frac{\delta(1-\delta)}{(\delta+\Lambda)^2}\,. \tag{8}$$

Now, for typical SOL conditions found in simulations (cf. Fig. 3), $\Lambda \sim 5\%$ and $\delta \sim 15\%$, leading to

$$\frac{\langle a \rangle^2}{\langle a^2 \rangle} \approx 0.24\,. \tag{9}$$

On the other hand, the average of a single function, say f, of a signal $a(t)$,

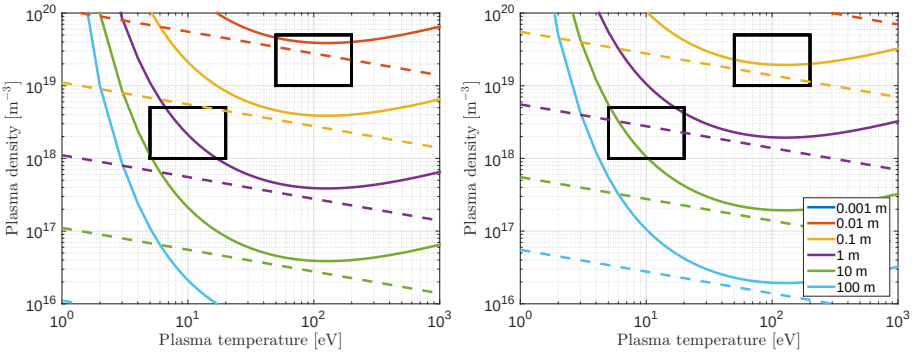

(a) (b)

Figure 2: Mean free paths for cold neutral atoms at $T_\mathrm{n} = 2\,\mathrm{eV}$ (a) and hot neutral atoms at $T_\mathrm{n} = 50\,\mathrm{eV}$ (b) for ionization (solid) and charge exchange (dashed) reactions. The lower left rectangle indicates the typical SOL parameter domain and the upper right rectangle the typical edge parameter domain.

can be expressed by Taylor-expanding f around $\bar{a}$,

$$\begin{aligned}\langle f(a)\rangle &= \left\langle f(\bar{a}) + f'(\bar{a})\tilde{a} + \frac{1}{2}f''(\bar{a})\tilde{a}^2 + \frac{1}{6}f'''(\bar{a})\tilde{a}^3 + \ldots \right\rangle \\ &= f(\bar{a}) + \frac{1}{2}f''(\bar{a})\langle\tilde{a}^2\rangle + \frac{1}{6}f'''(\bar{a})\langle\tilde{a}^3\rangle + \ldots\,. \end{aligned} \tag{10}$$

Thus, a simple estimate of $\langle f\rangle$ by $f(\bar{a})$ misses contributions from each moment of $\tilde{a}$. Note that the term linear in $\tilde{a}$ vanishes on averaging by definition.

Applying this observation to the ionization density at different radial positions in a slab geometry with radial coordinate x, poloidal coordinate y and of poloidal width L_y, one takes the average

$$\langle S(x)\rangle \equiv \frac{1}{L_y T}\int_0^T \mathrm{d}t \int_0^{L_y} \mathrm{d}y \;\; S(x,y,t)\,. \tag{11}$$

Defining S as the plasma density source from ionization of neutrals, we have $\langle S\rangle = \langle n_\mathrm{n}\, n_\mathrm{e}\, k_\mathrm{iz}(T_\mathrm{e})\rangle$. We expand each physical quantity in a mean and a fluctuation term, i.e. $f \equiv \langle f\rangle + \tilde{f}$, as in (7). Numerical simulations (see Sec. 4.3) suggest, that the neutral density fluctuations are rather small (of order 10% of the mean) for typical plasma conditions. For now, we therefore neglect these fluctuations, and

$$\begin{aligned}\langle S\rangle &= \langle n_\mathrm{n}\rangle\langle n_\mathrm{e} k_\mathrm{iz}\rangle \\ &= \langle n_\mathrm{n}\rangle\left(\langle n_\mathrm{e}\rangle\langle k_\mathrm{iz}\rangle + \langle\tilde{n}_\mathrm{e}\tilde{k}_\mathrm{iz}\rangle\right)\,. \end{aligned} \tag{12}$$

Consider the terms in (12). In a blob-turbulence dominated scenario, the fluctuations of density and temperature are strongly correlated, so we expect the term $\langle \tilde{n}_\mathrm{e} \tilde{k}_\mathrm{iz} \rangle$ to play a major role.

On the contrary, a mean field approximation would use only the term $\langle n_\mathrm{e} \rangle \langle k_\mathrm{iz} \rangle$ or $\langle n_\mathrm{e} \rangle k_\mathrm{iz}(\langle T_\mathrm{e} \rangle)$, which might be even worse, due to the strong temperature dependence of k_iz, cf. Eq. (3).

The strong correlation between the density and the ionization rate coefficient in edge/SOL simulations is shown in Fig. 3a. In Fig. 3b the effect of applying the mean-field approximation is demonstrated by comparing the ionization rate to that where the full reaction rate is averaged (solid lines). This result shows that by applying a mean-field approximation the average ionization rate is about a factor of 4 too low in the SOL region, consistent with what was estimated in (9).

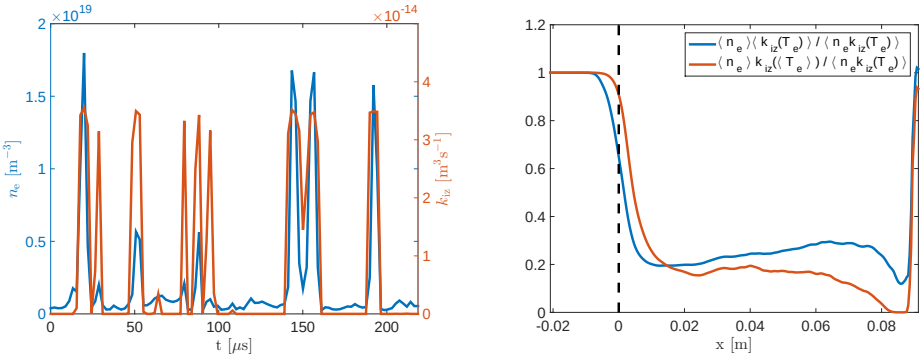

(a) (b)

Figure 3: The effect of fluctuations on the ionization rates. (a) shows time signals of plasma density (blue) and ionization rate coefficient $k_\mathrm{iz} = \langle \sigma_\mathrm{iz} v_r \rangle$ (red) at a fixed position $x = 2\,\mathrm{cm}$, $y = 2\,\mathrm{cm}$. The fluctuations in density and rate coefficient are clearly highly correlated. (b) depicts the radial (y-averaged) profile of the approximations $\langle n_\mathrm{e} \rangle \langle k_\mathrm{iz} \rangle$ (blue curve) and $\langle n_\mathrm{e} \rangle\, k_\mathrm{iz}(\langle T_\mathrm{e} \rangle)$ (red curve) normalized by the actual ionization rate per neutral atom $\langle n_\mathrm{e} k_\mathrm{iz}(T_\mathrm{e}) \rangle$, cf. (12). Both approximations underestimate the ionization rate by a factor of about 4 over most of the SOL, where the fluctuations dominate the mean fields. The plasma conditions are taken from HESEL simulations, cf. Sec. 4.3.

4 1D model

In order to illustrate the influence of blobs on the ionization of neutrals we start from a simplified 1D model. The radial evolution is modeled in a domain

extending from 10 cm inside the plasma edge and out to the wall. This allows for modeling the SOL dynamics as well as comparing ionization profiles for the SOL and edge regions. The model represent the plasma as a static profile with a fixed density and temperature in the SOL and edge regions. To model the blob, we consider a Gaussian perturbation of density and temperature in the SOL propagating radially outwards. In all simulations a constant radial blob velocity of 5 $\frac{\mathrm{km}}{s}$ is used.

The neutrals are assumed to evolve according to a diffusion model with an effective diffusion coefficient, and are modeled as a 3-species fluid with a different temperature for each species. This assumption gives a simplified description of neutrals compared to that of a kinetic model, but we trust that it bears out the key issues and conclusions in a qualitative way. A diffusion driven transport of neutrals is also investigated in [11], and another model for multi-species neutrals can be found in [12]. [13] considers a slightly different ionization cross section expansion in temperature and density than that of (3), but as for this paper, the ionizing effect on neutral particles by blobs is considered without feedback to the blobs.

The cold neutrals are at room temperature and enter the system at the outer wall. Through charge exchange collisions with the plasma the cold neutrals are either converted into warm neutrals at SOL temperature or hot neutrals at edge temperature. The warm neutrals are created in charge exchange collisions with the SOL background plasma, and the hot neutrals from collisions with the edge plasma and blobs.

The diffusion equation for the neutrals can be written

$$\partial_t n_\sigma - \partial_x \left(D_\sigma \partial_x n_\sigma \right) = S_\sigma \,, \tag{13}$$

where $\sigma = \mathrm{n_{cold}}, \mathrm{n_{warm}}, \mathrm{n_{hot}}$. The diffusion coefficient is given by

$$D_\sigma = \frac{T_\sigma}{k_{\mathrm{eff}} m_\sigma n} \,, \tag{14}$$

where k_{eff} is an effective reaction rate coefficient driving the diffusion, m_σ is the mass of the neutrals and n is the sum of all densities. The sources and sinks on the RHS of (13) are characterized by the ionization and charge exchange collisions and are given by

$$S_{\mathrm{n_{cold}}} = -\left(k_{\mathrm{cx}} + k_{\mathrm{iz}}\right) n_{\mathrm{n_{cold}}} n_{\mathrm{p}} \,, \tag{15}$$

$$S_{\mathrm{n_{warm}}} = k_{\mathrm{cx}} \left[\left(n_{\mathrm{n_{cold}}} + n_{\mathrm{n_{hot}}} \right) n_{\mathrm{p_{bkgd}}} - n_{\mathrm{n_{warm}}} n_{\mathrm{p_{blob}}} \right] - k_{\mathrm{iz}} n_{\mathrm{n_{warm}}} n_{\mathrm{p}} \,, \tag{16}$$

$$S_{\mathrm{n_{hot}}} = k_{\mathrm{cx}} \left[\left(n_{\mathrm{n_{cold}}} + n_{\mathrm{n_{warm}}} \right) n_{\mathrm{p_{blob}}} - n_{\mathrm{n_{hot}}} n_{\mathrm{p_{bkgd}}} \right] - k_{\mathrm{iz}} n_{\mathrm{n_{hot}}} n_{\mathrm{p}} \,, \tag{17}$$

where $n_{\mathrm{p_{blob}}}$ is the density of the perturbation, $n_{\mathrm{p_{bkgd}}}$ is the plasma background density and $n_{\mathrm{p}} = n_{\mathrm{p_{bkgd}}} + n_{\mathrm{p_{blob}}}$ is the total plasma density. The rate coefficients are calculated from the proper temperatures, i.e., $k_{\mathrm{iz}} n_{\mathrm{p_{bkgd}}}$ is calculated using the background temperature, whereas $k_{\mathrm{iz}} n_{\mathrm{p_{blob}}}$ is calculated from the blob temperature. An example of the profiles during a blob event (that is, when one Gaussian perturbation is created at the edge and propagates through the SOL

to the wall) is given in Fig. 4. It should be noted that the profiles depend on the temperatures and plasma density chosen. In this paper we use $n_{\mathrm{p_{bkgd}}} = 2 \cdot 10^{19}\,\mathrm{m}^{-3}$ for the plasma edge background density, $n_{\mathrm{p_{bkgd}}} = 1 \cdot 10^{18}\,\mathrm{m}^{-3}$ for the density in the SOL, and $T_{\mathrm{n_{hot}}} = 40\,\mathrm{eV}$, $T_{\mathrm{n_{warm}}} = 10\,\mathrm{eV}$ and $T_{\mathrm{n_{cold}}} = 2\,\mathrm{eV}$ for the neutral temperatures. We are using an effective reaction rate coefficient for the neutral diffusion of $k_{\mathrm{eff}} = 5 \cdot 10^{-14}\,\mathrm{m^3 s^{-1}}$.

The neutral density boundary conditions on the inner boundary are

$$\partial_x n_\sigma = \sqrt{\frac{k_{\mathrm{iz}} n_{\mathrm{p}}}{D_\sigma}} n_\sigma \,, \tag{18}$$

for $\sigma = \mathrm{n_{warm}}, \mathrm{n_{hot}}, \mathrm{n_{cold}}$, which is found by assuming that the neutral density is going to zero far in the edge due to ionization. On the wall we assume partial absorption of neutrals and thus

$$-\partial_x n_\sigma = -\frac{\gamma}{D_\sigma} \sqrt{\frac{T_\sigma}{2\pi m_{\mathrm{n}}}} \tag{19}$$

for $\sigma = \mathrm{n_{warm}}, \mathrm{n_{hot}}$. γ determines how large a fraction of the wall-hitting neutrals which are absorbed in the first wall. The simulations are run with $\gamma = 0.5$ corresponding to half the neutrals being recycled. Finally

$$-\partial_x D_{\mathrm{n_{cold}}} n_{\mathrm{n_{cold}}} = 10^{22}\,\mathrm{m^{-2} s^{-1}} \,, \tag{20}$$

to represent a cold neutral influx from, e.g., gas puffing.

4.1 Ionization in SOL and edge

It is important to provide an estimate of the radial distribution of the plasma source from ionization of neutrals in a tokamak device. This can for example be used for the purpose of estimating the fueling rate, if using gas puffing in future machines such as ITER and beyond.

Using the 1D model we simulate the neutral response to a series of blob events appearing with a given frequency. This allows for computing the ionization source profiles. The inclusion of hot neutrals in the model also gives insight into the fueling mechanism. It is expected from Fig. 2 that hot neutrals will penetrate far deeper into the edge region. However, the cold neutral density is much larger than that of hot neutrals, thus the fueling rate of the two species appears to be comparable.

In Fig. 4 we show profiles of the densities in the SOL and edge regions. The left column depicts profiles for when the blob is near the edge of the plasma, and the right column when the blob is near the chamber wall. In the top frames of Fig. 4 the plasma density profiles are displayed.

In the middle frames the neutral densities are shown. It is observed that the cold neutral density falls off exponentially in the SOL, but with a mean-free path of a few SOL widths, whereas the warm and hot neutral density is

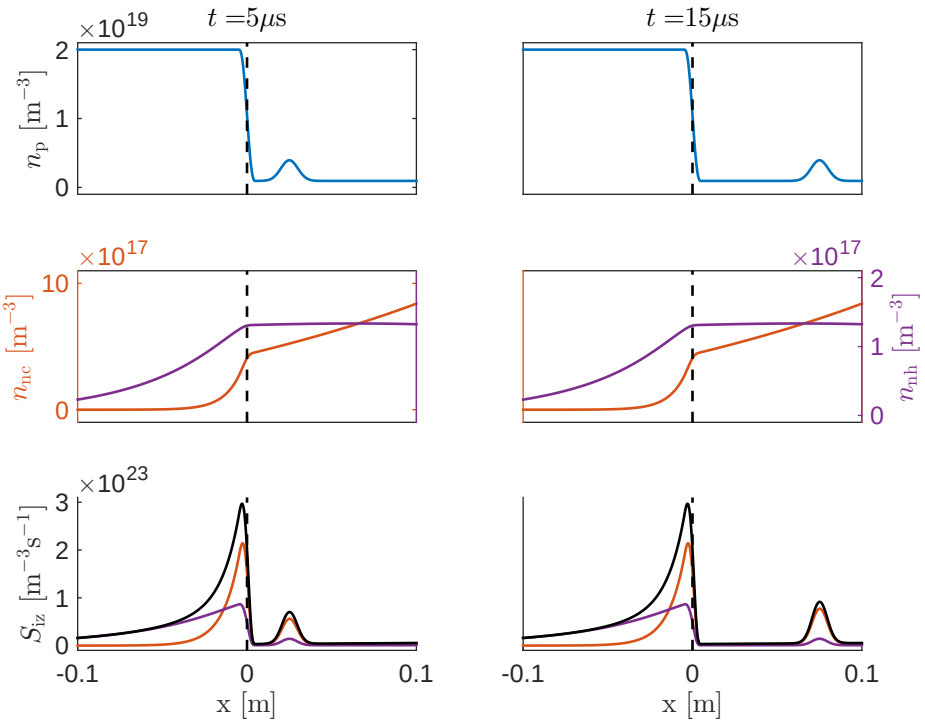

Figure 4: Plasma (top), and cold and sum of warm and hot neutrals (middle) density profiles during a blob event. The bottom frames depict ionization rates for the cold and the sum of warm and hot neutrals for the two blob positions. In the middle and bottom frames the red curves refer to cold neutrals, the purple curves to warm and hot neutrals and the black curves to the sum of all neutrals. Note that the axis for hot neutral density is two orders of magnitudes smaller than that for cold neutral density.

roughly constant in this region. The density of cold, warm and hot neutrals falls off exponentially in the edge region, but at a much shorter length scale for cold neutrals than that for warm and hot. The observed results reflect the dependency of the mean-free paths shown in Fig. 2.

The bottom frames of Fig. 4 depict the ionization rate during the blob event. As one may expect the ionization in the SOL rises significantly when the blob reaches the regions of high neutral density.

Note that the fluctuation level of the 1D model is much lower than that produced by the HESEL code, which was used to construct Fig. 3.

Figure 5a shows the same type of profiles as in the bottom frames of Fig. 4, except that the profiles have been averaged over a full blob period. The fre-

quency of the blob events applied in this case is 10 kHz. It is observed that the the ionization of cold neutrals dominate in the SOL region, ionization of hot neutrals dominate deep inside the edge region, and the the ionization rate of the two is comparable in the outer edge.

Spatially integrating the profiles reveals that roughly $10-15\%$ of the ionization occurs in the SOL, and $85-90\%$ in the edge region. The same procedure have been carried out for various blob frequencies and Fig. 5b shows a tendency that the higher frequency, the larger a fraction of neutrals are ionized in the SOL.

Thus in a SOL with more frequent blob events, the ionization rises compared to that in the edge and is in general higher than that of a SOL, where the plasma profiles are temporarily averaged. An equivalent conclusion has been made in, e.g., [14, 15], where it is found, that including fluctuations instead of using averaged values moves the ionization source outwards towards the wall.

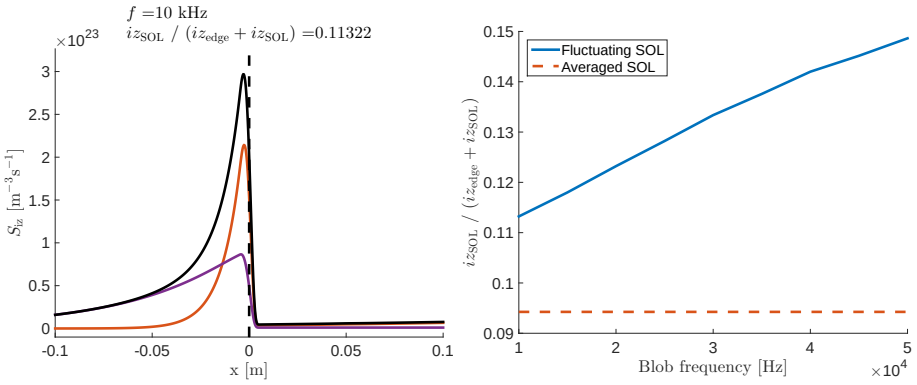

(a) (b)

Figure 5: The ionization rate for the event pictured in Fig. 4 averaged over a blob period (a), where the colors have the same meaning as in Fig. 4, and the fraction of averaged ionization in the SOL as a function of blob frequencies (b).

4.2 Neutral Flux across LCFS

As a continuation of Sec. 4.1 it is interesting to monitor the neutral flux across LCFS as function of time. This quantity can also serve as a proxy for the fueling rate, if it is assumed that all neutral particles crossing LCFS are ionized inside the bulk plasma.

The inward neutral density flux across LCFS as a function of time is shown in Fig. 6a for blob frequencies of 10 kHz. The blobs decrease the neutral density

slightly in the SOL, and the neutral flux across the LCFS is affected accordingly. This can be seen in Fig. 6a as short dips in the flux level, which is particularly significant for the cold neutrals.

As was done for the ionization rates in the previous section, the inward neutral density flux for various blob frequencies are compared. The result is shown in Fig. 6b. It is observed that the neutral flux across LCFS decreases with increasing blob frequency. Even though the average pressure is the same for all frequencies, a more turbulent SOL leads to more ionization in the SOL and thus a smaller fueling rate.

The results from this and the previous section suggest that warm and hot neutrals produced in charge exchange collisions are responsible for the majority of the ionization in the deep edge region, but that the cold neutrals from dissociated molecules can fuel at an equal level in the outer edge region. During a blob event, more neutrals are ionized in the SOL, which lead to a smaller flux across the LCFS, in particular for cold neutrals.

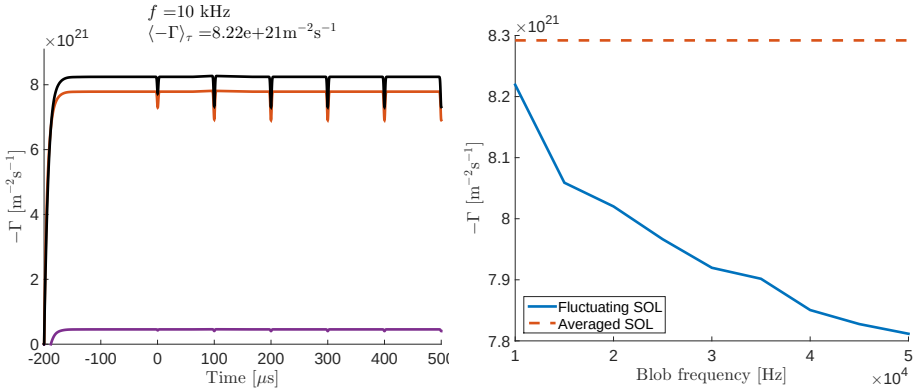

(a) (b)

Figure 6: The inward neutral density flux across LCFS as a function of time (a), where the colors have the same reference as in Fig. 4, and the average inward neutral flux during a blob period as a function of the blob frequency (b).

4.3 Comparison with 2D model

Blobs are localized in time, and spatially in the poloidal plane perpendicular to the magnetic field. By determining the effect of blobs from a 1D model, one undesirably neglect important dynamics that are present in higher dimensions. In particular it is observed, that in the 1D model the blob lowers the cold neutral density as it propagates through. In a 2D slab model the refilling is not only from the neutrals in front of the blob, but is assisted by the surrounding

cold neutrals. This allows for maintaining a more constant level of cold neutral density and the decrease in neutral flux across the LCFS after a blob event do not occur to the same extent. Note that extending from a 2D model to a full 3D model is not expected to influence the results significantly, since the blob is elongated along the direction parallel to the magnetic field lines, which reduces the ability to refill along the field lines.

The simplified 2D model is similar to the 1D model. The plasma density and temperature profiles are fixed and constant in the poloidal direction, and blobs are modeled as 2D Gaussian perturbations that propagate radially outwards. The blobs are released at random poloidal positions with a specified frequency. The neutral transport equations are 2D versions of (13), that also include diffusion in the y-direction (poloidally) with the same diffusion constant, given by (14).

Figure 7 shows the plasma density during a blob event, and the neutral flux across the LCFS. The latter is observed to be significantly different from that of the 1D model. Even though the signature of a blob on the neutral flux across LCFS is still visible, this is strongly weakened in the 2D model.

The reason for this is that cold and hot neutrals can flow to and from the regions of decreased or increased density also in the poloidal direction, and also that the domain/blob area ratio is much larger. This allows for more neutrals to distribute in the SOL and aids to fill up regions of depletion.

Lastly we show in Fig. 8 that the localized ionization is also present in more realistic blob simulations. Here we show results from a HESEL simulation [16, 17], where neutrals have been added to react to the plasma temperature and density, but without affecting the plasma. The left column of frames shows the plasma density and temperature produced in the HESEL simulation. Note the blob emerging at the edge as well as the one in the SOL at $x = 8\,\mathrm{cm}$ from the LCFS. The upper right frame depicts the total neutral density and the lower right the ionization rate.

This figure serves as initial results of work in progress, in which we self-consistently couple the neutral model to the HESEL equations, and also include the effects of the plasma produced by impact ionization and the effects of the neutrals on the blobs and the SOL power deposition profile, to obtain a realistic plasma source profile.

5 Conclusions

The mean-field approximation, in which the plasma density and temperature or reaction rate coefficients are approximated separately by their temporal mean values, in the SOL was studied. Based on analytical estimates as well as results from the edge/SOL turbulence code HESEL, it was found that the mean-field approximation is poor in the SOL due to strong correlation between the fluctu-

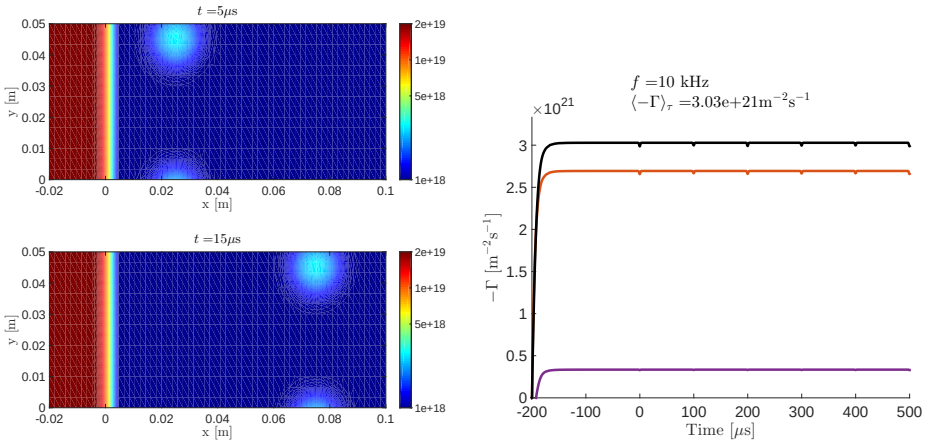

(a) (b)

Figure 7: Plasma density at various times in 2D simulation (a) (note that colorscale is logarithmic), and the poloidally averaged inward neutral density flux across LCFS as a function of time (b), where the colors have the same reference as in Fig. 4. Compare the latter to Fig. 6a.

ating signals. Applying the mean-field approximation for the profiles obtained by HESEL simulations led to an electron impact ionization rate that was only about 25 % of the value obtained when taking the proper temporal average throughout the SOL.

We have introduced a radial 1D model for plasma and neutrals in the SOL and edge regions. The model includes three neutral species of room-, SOL- and edge-temperatures. The latter two species originate from charge exchange collisions between plasma and cold neutrals. The model was used to study the effect that the frequency of blobs and thereby the fluctuation level in the SOL had on neutral atoms. It is found that more frequent blob events increase the fraction of ionization in the SOL and thus moves the ionization source outwards.

The 1D model also allowed for investigating the neutral density flux across LCFS. This is an interesting measure, as it is closely related to the fueling process of, e.g., gas puffing in tokamaks. It is found that fueling in the deep edge from warm and hot neutrals is dominating over that of cold neutrals, but that cold neutrals fuel more in the far edge. We observed that during a blob event the ionization the SOL increase and the flux of neutrals across LCFS decrease. The decrease in inward neutral desity flux is more pronounced for cold neutrals and stronger for a higher blob frequency.

Finally, the results of the 1D model were compared to those of both a similar simplified 2D model and those obtained from HESEL simulations. We see that

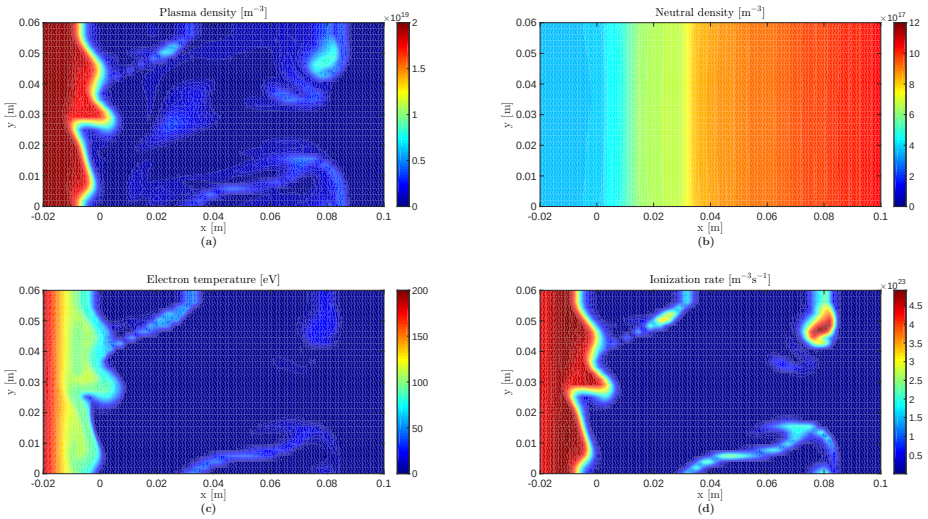

Figure 8: Plasma density (a) and electron temperature (c) plots from HESEL simulations. The HESEL model consists of a self-consistent description of electron density, electron and ion temperature, and vorticity. Neutral density (both cold, warm and hot) (b) and ionization rate (d) calculated as response to HESEL output, but without feedback to the plasma. The neutral model is identical to that used to obtain Fig. 7.

the above trends also show up in 2D models, but that the perturbations to the neutral flux across LCFS are weaker.

Here we have considered L-mode like plasmas with significant blob activity. One should expect that the ELM events in H-mode plasma may have similar and even stronger effects. The ELM events appear as a bunch of filamentary structures having similar features as blobs. Thus, with their significantly enhanced level of density and temperature - comparable to the parameters on top of the edge pedestal - we expect ELM filaments to locally fully ionize the cold neutrals in the SOL. The charge exchange collisions will additionally produce very hot neutrals, and it is therefore also expected that ELMs will give rise to an increased fueling deep into the edge plasma. This will provide a modulation of the fueling with a frequency determined by the ELM frequency. Thus, the influence of the ELMs may be traced far into the plasma by the modulation of the inward moving plasma density perturbations. Additionally, the enhanced "ELM-fueling" may add to a faster recovery of the pedestal.

Current and future work concerns a self-consistently coupling of the neutral model to the HESEL equations, which will also include the effect of the impact ionization on the plasma and thus the effects of the neutrals on the blobs.

6 Acknowledgments

This work has been carried out within the framework of the EUROfusion Consortium and has received funding from the Euratom research and training programme 2014-2018 under grant agreement No 633053. The views and opinions expressed herein do not necessarily reflect those of the European Commission.

References

[1] Zweben, S.J., et al., Plasma Phys. Control. Fusion, 49 (2007), p. S1

[2] Boedo, J.A., J. Nucl. Mater., 390-391 (2009), p. 29

[3] Naulin, V., J. Nucl. Mater., 363-365 (2007), p. 24

[4] Boedo, J.A., J. Nucl. Mater., 390-391 (2009), p. 29

[5] Darwent, B.deB., Bond Dissociation Energies in Simple Molecules, US Department of Commerce, (1970).

[6] Stangeby, P.C., The Plasma Boundary of Magnetic Fusion Devices, Institute of Physics Publishing, (2000).

[7] Goldston, R.J. and Rutherford, P.H., Introduction to Plasma Physics (Chapter 10), IOP Publishing Ltd, (1995).

[8] Garcia, O.E., Physical Review Letters 2012, Volume 108 (26)

[9] Marandet, Y., et al., Nuclear Fusion, Volume 51, Number 8, July 2011

[10] Havlíčková, E., et al., Journal of Nuclear Materials, Volume 415, Issue 1, Supplement, 1 August 2011, Pages S471-S474

[11] Vold, E.L., et al., Journal of Nuclear Materials, 176:570-577, December 1990

[12] Tokar, M.Z., Phys. Plasmas 21, 082517 (2014)

[13] Kendl, A. International Journal of Mass Spectrometry, 365-366, 106-113 (2014).

[14] Guzmán, F., et al., Journal of Nuclear Materials, Volume 463, August 2015, Pages 659-663

[15] Bernert, M., et al., Plasma Physics and Controlled Fusion, Volume 57, Issue 1, 2015

[16] Garcia, O.E., et al., Phys. Plasmas, 12 (2005), p. 062309

[17] Nielsen, A.H., et al., Conference Paper 40th European Physical Society Conference on Plasma Physics, Espoo, Finland (2013); Madsen, J. et al., *in preparation*

4.1.3 Postlude

The paper on *The influence of blobs on neutral particles in the scrape-off layer* discusses the mean-field approximation to plasma models, and reports of the initial findings from applying a model similar to nHESEL to describe the effect of blobs on the neutral atomic density. Although the paper is self-contained, there are several affiliations to later work presented in the thesis.

Most of the results in the thesis is based on 2D simulations, but in this paper a 1D model is applied. The same is true for the first of the three conference papers, and this sprouts the question on the possibility of quenching the poloidal dimension, and describe the dynamic field by a radial 1D model. Another main topic in the paper, namely the effect of blobs on the neutral density is also studied in Sec. 4.3 and in the latter two conference papers. Closely linked to this topic is that of local fuelling by ionization of neutrals. The relations of those topics, i.e., applying a 1D radial model, the effect of blobs on neutral densities, and the effect of blobs on fuelling, to those of the other papers, are further discussed.

Applying a **1D radial model for particle transport** allows for reducing the number of grid points from those in a 2D model, and thus lower the computational time for a simulation on a given radial extend. The dimensional reduction comes at a cost of the description of the physics contained in the model, as transport perpendicular to the radial direction has to be accounted for by other means, e.g., by parametrization or by assumptions on the perpendicular gradients.

A reduced radial model for the neutral particles, on the other hand, may be a good solution for reducing computational requirements. The physical motivation for applying a 1D counterpart to the neutral part of nHESEL is founded on describing the transport of neutral particles by Fick's law, and there are thus no cross-dimensional terms in the transport equations. As the transport is driven by local gradients, small gradients in the perpendicular directions result in little non-radial transport and is thus in favour of a 1D model. In the simulated domain it is evident from Fig. 8.b in the paper, that the variation of the neutral density in the y-direction is much smaller, than that of the plasma fields. As an assessment of the variation, the temporal

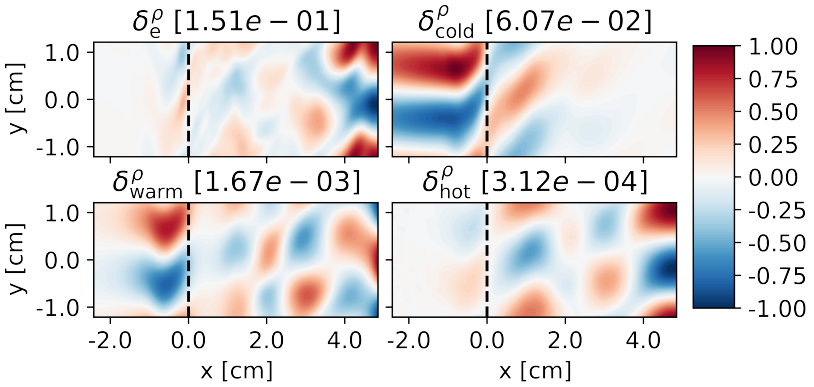

Figure 4.1: The normalized temporal average of the deviation of the densities of electrons, thermal molecules, and warm and hot atoms, from their poloidal mean value. The numbers in square brackets are the largest absolute value in the corresponding plot, and the value by which the data has been normalized.

deviation from the poloidal mean for electron and neutral density fields

$$\delta^\rho_\sigma \equiv \left\langle \frac{n_\sigma - \langle n_\sigma \rangle_\rho}{\langle n_\sigma \rangle_\rho} \right\rangle_t , \tag{4.1}$$

for $\sigma = \mathrm{e}, \mathrm{cold}, \mathrm{warm}, \mathrm{hot}$ is computed, and shown in Fig. 4.1. $\langle \cdot \rangle_\rho$ denotes the poloidal average, and $\langle \cdot \rangle_t$ the temporal average. The dataset for the computation is not that of the paper, but one where the nHESEL model is simulated. It is observed, that the electron field is that which deviates the most from the poloidal mean, which is intuitively understandable, as the blobs of enhanced density are poloidally localized. For the neutral densities, there is a common trend for the colder neutrals to deviate more from the poloidal mean. The reason for this is that blobs locally change the neutral density, and the colder neutrals are slower at levelling out the perturbation. Even though, the average deviation from the poloidal mean is only 6 percent for the thermal molecules. Thus, for studies where the local responses of the neutral densities to blobs are not essential, in particular the atomic neutral densities may be described by radial 1D models instead of the corresponding 2D model in nHESEL.

The **effect of blobs on neutral densities** is a core topic of the thesis, and the initial findings presented here are, however simplified, consistent with the other results. That is, blobs leave a non-vanishing local depletion in the neutral densities, and the effect of ionization on colder neutrals is much more

pronounced than it is for the more energetic atoms. There are two reasons for this; the first, which is however difficult to observe from the plots provided in the paper, is that the cold neutrals are much slower, which prevents a rapid refilling of a depletion in the cold neutral density, created by a blob. The second reason is, that locally enhancing the plasma pressure unambiguously increases the sink term for cold neutrals. This is not the case for the warmer neutral species, which also has source terms that increase with the plasma density, and thus competes in magnitude with the sink term from ionization. The latter effect is even more pronounced when molecules are present as a thermal neutral species, in which case various dissociation processes result in a source term for atoms that is often larger than the ionization sink term. This effect is the topic of the paper *Influence of molecular dissociation on blob induced atom density fluctuations*, and is discussed in detail in Sec. 4.3.

Finally the results on the local **fuelling from ionization of neutrals** is qualitatively compared to those reported by the other papers. As for the neutral density response to blobs, this results on this topic is also consistent with later findings for the average profiles, whereas a more detailed analysis gives a more varied picture for the instantaneous fuelling rate in the presence of blobs. The paper *Plasma particle sources due to interactions with neutrals in a turbulent scrape-off layer of a toroidally confined plasma* in Sec. 4.2 discusses the possibility of self-consistently fuelling in the nHESEL model, and the topic is touched upon by all three conference papers in Sec. 4.4.

For the steady state profiles it is found, that in the SOL region it is mainly the cold neutrals that are ionized, as the density of the cold neutrals is about an order of magnitude larger than that for the warmer neutrals. The cold neutrals penetrate only a few centimetres into the edge region where the plasma pressure is highly elevated. The warm and hot atoms on the other hand, penetrate deep into the edge region, and dominate the ionization in the edge from a few centimetres inside the LCFS and inwards. The dependence of the warmer atomic species for deep penetration is also highlighted in the conference papers *The influence of hot neutrals in simulations of gas puff modulation*, and *The influence of blob intermittency on fuelling*. In the latter the cold neutrals are molecules, and the ionization profiles are in this case consistent with those of the present paper, in the way that only the atoms penetrate the edge region.

For the time dependent ionization, the conclusion of *The influence of blob intermittency on fuelling* apparently opposes that of the paper. In the paper, a dip in the inwards neutral flux, and thus in the fuelling, result from

a blob event. Figure 2 of the conference paper, on the other hand, show a peak in the fuelling following a blob event. The reason for the discrepancy lies in the completeness of the neutral model; the conference paper includes molecules, and a source term for the warm atomic species is thus present due to dissociation of molecules. As stressed in the paper in Sec. 4.3, the source from dissociation of molecules is larger than that for ionization of atoms, and blobs thus generate more atoms than they remove, when propagating through a SOL. As it is mainly the atoms that fuel, an increase in the fuelling rate thus follows a blob event, due to the enhanced production of atoms. This effect is not observable in the present paper, and the blobs thus result in a negative response of the inwards neutral flux.

4.2 Plasma particle sources due to interactions with neutrals in a turbulent scrape-off layer of a toroidally confined plasma

4.2.1 Prelude

In the paper of this section, the full nHESEL model, which is derived in Chpt. 2, is presented. The reasoning and the main steps to obtain the transport equations are outlined, and the nHESEL equations presented.

As was stated in the introduction, the plasma dynamics in the SOL and edge regions define the overall confinement properties of tokamak plasmas. Since neutral interactions introduce potentially strong source terms to the plasma fields, neutrals may influence the confinement. It is well known that strong fuelling causes the plasma densitity to exceed the so-called Greenwald density [15], which disrupts the confined plasma. Injecting neutrals into an H-mode plasma has likewise triggered transitions to L-mode, but without disrupting the discharge [36].

Since the neutral density is difficult to measure in experiments, and the underlying mechanisms for the influence of neutrals on the plasma edge region is not completely understood, predictive modelling of plasma and neutral transport in the edge and SOL regions is a valueable tool. Since the nHESEL model treats the plasma and neutral fields in a dynamical and self-

consistent manner, future applications may explain some of the experimental observations that occur under strong gas puffing.

In the paper presented here initial results from application of the nHESEL model for medium-sized tokamak parameters are presented. A four-point scan in the flux of neutrals molecules into the system, i.e., the gas puffing rate, is carried out, so that simulations are run with a broad range of neutral densities. The effects of the gas puff rate on the plasma field profiles, as well as on the ionization rate profile and on the average radial electric field, are reported. Moreover, it is investigated how the puffing rate affects the statistics for the radial electron particle flux across the LCFS.

In addition to the analysis of the effect of puffing rates on plasma field profiles and flux statistics, it is investigated if it is possible to replace the density source that comes from the forcing of the electron density profile in the inner edge region with one that originates from local ionization of neutrals. Although it is discussable whether toroidally confined plasma is fuelled entirely at the out-board mid-plane, the possibility of allowing for this in a self-consistent manner in the simulation can be relevant for future studies, where the edge density may be ramped-up in the edge region as a result of strong fuelling, as is investigated in Sec. 4.5.1.

The paper thus presents the earliest applications of the nHESEL model, and reviews some of the consequences of changing the gas puffing rate, as well as the possibility to allow for the electron density in the nHESEL model to be self-consistently fuelled by local ionization of neutrals. It was published in *Physics of Plasmas* (Vol. 25, Issue 3) on 20 March 2018, with DOI: 10.1063/1.5019662. Reproduced from [97], with the permission of AIP Publishing.

Plasma particle sources due to interactions with neutrals in a turbulent scrape-off layer of a toroidally confined plasma

A. S. Thrysøe,[a] M. Løiten, J. Madsen, V. Naulin, A. H. Nielsen, and J. Juul Rasmussen
PPFE, Department of Physics, DTU, DK-2800 Kgs, Lyngby, Denmark

(Received 15 December 2017; accepted 28 February 2018; published online 20 March 2018)

The conditions in the edge and scrape-off layer (SOL) of magnetically confined plasmas determine the overall performance of the device, and it is of great importance to study and understand the mechanics that drive transport in those regions. If a significant amount of neutral molecules and atoms is present in the edge and SOL regions, those will influence the plasma parameters and thus the plasma confinement. In this paper, it is displayed how neutrals, described by a fluid model, introduce source terms in a plasma drift-fluid model due to inelastic collisions. The resulting source terms are included in a four-field drift-fluid model, and it is shown how an increasing neutral particle density in the edge and SOL regions influences the plasma particle transport across the last-closed-flux-surface. It is found that an appropriate gas puffing rate allows for the edge density in the simulation to be self-consistently maintained due to ionization of neutrals in the confined region. https://doi.org/10.1063/1.5019662

I. INTRODUCTION

One of the main drivers for determining the plasma confinement in magnetically confinement devices such as tokamaks is the dynamics in the edge region of the bulk plasma. This region is characterized by the transition from closed to open magnetic field lines, in which the last-closed-flux-surface (LCFS) defines the boundary between the confined plasma and the scrape-off layer (SOL), where the field lines terminate on material surfaces. The anomalous transport of particles and energy across the LCFS is strongly intermittent, and it has been found that most transport is carried by field-aligned filaments (blobs) that are formed near the plasma edge and propagate radially outwards towards the first wall.[1–4]

When the plasma filaments interact with the material surfaces, the plasma undergoes surface recombination, and neutral atoms and molecules are released through various mechanisms of which most result in low-energy neutrals.[5] This process is referred to as plasma recycling. Neutral particles can also originate from being injected into the vacuum vessel for fuelling or diagnostic purposes.[6,7] Typical SOL temperatures that are much lower than those of the bulk plasma allow for a significant population of neutrals to exist. The neutral atoms and molecules will interact with the plasma both through elastic and inelastic collisions. Elastic collisions between charged particles and neutrals are not treated in this paper, but the effect of such collisions in drift-fluid models are derived in Ref. 8. The inelastic collisions are, for example, excitation and ionization of atoms and molecules and dissociation of molecules. The ionization process, if inside the confined region, is what fuels the plasma. Ionization may also occur in the SOL and prevent the neutrals from fuelling the plasma directly. In addition to their fuelling properties, neutrals may also provide protection to the first wall from the plasma filaments by cooling down the plasma through elastic and inelastic collisions.

There exist a number of numerical models for simulating the neutral-plasma interactions. Both kinetic neutral models such as in Refs. 9–12 and fluid models[13–16] have previously been applied to study SOL and edge plasmas in the presence of neutrals. In this paper, we derive a neutral fluid model for the purpose of studying the effects of neutrals on the intermittent plasma fields. A fluid model allows for a dynamical treatment of the neutrals and thus self-consistently simulates the response of SOL plasma structures to neutrals and vice versa. This model in particular takes into account the long mean-free path of neutral atoms in the SOL region, which prevents the usual Chapman-Enskog closure[17] from being applied to the neutral fluid equations.

The source terms resulting from inelastic neutral-plasma interactions are introduced in a plasma drift-fluid model. Drift-fluid models are derived from the two-fluid equations and describe the physics of phenomena that occur on time-scales much slower than the ion cyclotron frequency and length scales much larger than the ion gyroradius. This results in a simpler fluid model which is still able to describe the low frequency turbulence in the edge and SOL regions such as interchange-driven turbulence. In this paper, we demonstrate that the presence of inelastic density and momentum sources introduce additional drift-terms, and the resulting source terms are included in an existing drift-fluid based plasma model.

This paper has two main sections: In Sec. II, the HESEL[18,19] drift-fluid model is presented (Sec. II A), and it is displayed how inelastic neutral source terms enter such a model (Sec. II C). It is also described how neutrals with a long mean-free path between collisions, for which the usual Chapman-Enskog closure scheme is no longer valid, can be described in a fluid model (Sec. II B). A combined plasma-neutral model is given in Sec. II D, where the equations for the HESEL drift-fluid model are enhanced with neutral source terms. The combined HESEL-neutral model is solved

[a]Electronic mail: alec@fysik.dtu.dk.

self-consistently, and the results are discussed in Sec. III. In this section, it is shown how the presence of neutrals affects the SOL density and temperature profiles, when gas puffing is simulated at three different puffing rates (Sec. III A). Moreover, we display in Sec. III B how fuelling in HESEL can be self-consistently described in the combined neutral-plasma model, when the electron/ion density source in the inner edge region is replaced by a source solely from ionization of neutrals. The latter will allow for future studies on the effect of gas puffing on edge plasmas and thus the effect of gas puffing on overall confinement.

II. MODELS FOR TRANSPORT AND INTERACTIONS

In this section, we present two models. The first model is a four-field drift-fluid based model for plasma variables. Drift-fluid models originate from the Braginskii fluid equations where an ordering in powers of the ion gyration frequency in the momentum equations is introduced. This technique is known as drift-ordering, and it reduces the number of variables described by eliminating the momentum equation by describing the electron and ion fluid velocities as a sum of drift-fluid velocities. The technique is described in detail in Refs. 20 and 21. The particular drift-fluid model considered in this paper is the HESEL model, and it describes the evolution of the electron/ion density, the generalized vorticity, and the electron and ion pressures. The ultimate purpose of this section is to augment an existing drift-fluid model with source terms originating from interactions with neutrals. The neutrals are described as multiple fluids to take into account both neutral molecules and atoms at distinct characteristic temperatures. The neutrals interact self-consistently with the plasma variables, so that the effect of the inelastic collisions results in source and sink terms in both the neutral and plasma transport equations.

The section is structured so that Sec. II A provides the HESEL model for the case with no source terms from neutral interactions. In Sec. II B, the derivation and validity of a neutral fluid model are discussed. Section II C displays how source terms enter the plasma drift-fluid equations, and in Sec. II D, a combined plasma-neutral model is proposed.

A. HESEL equations

The HESEL model[18,19] describes the transport of density, ion and electron pressures, and generalized vorticity at the outboard-midplane of a tokamak in a drift-plane perpendicular to the magnetic field lines. The original HESEL model describes the evolution of plasma variables without the presence of neutral particles. Here, we couple the HESEL model and a neutral model described in Secs. II B and II C. Since HESEL describes both the electron and ion temperature dynamics, the influence of neutral particles on both species can be studied in edge and SOL plasmas. The inclusion of neutrals also allows for the density source in the original HESEL equations to be partially replaced with one that self-consistently originates from ionization of neutral particles. The results of including neutrals in a plasma turbulence model are given in Sec. III.

The original HESEL equations without neutral source terms are derived from the drift-fluid equations and read

$$\mathrm{d}_t n + n\mathcal{K}(\phi) - \mathcal{K}(p_\mathrm{e}) = \Lambda_n\,, \tag{1}$$

$$\nabla\cdot\left(\mathrm{d}_t^0\nabla_\perp\phi^*\right) - \mathcal{K}(p_\mathrm{e}+p_\mathrm{i}) = \Lambda_\omega\,, \tag{2}$$

$$\frac{3}{2}\mathrm{d}_t p_\mathrm{e} + \frac{5}{2}p_e\mathcal{K}(\phi) - \frac{5}{2}\mathcal{K}(p_\mathrm{e}^2/n) = \Lambda_{p_\mathrm{e}}\,, \tag{3}$$

$$\frac{3}{2}\mathrm{d}_t p_\mathrm{i} + \frac{5}{2}p_i\mathcal{K}(\phi) + \frac{5}{2}\mathcal{K}\left(p_\mathrm{i}^2/n\right) - p_\mathrm{i}\mathcal{K}(p_\mathrm{e}+p_\mathrm{i}) = \Lambda_{p_\mathrm{i}}\,, \tag{4}$$

where n is the electron/ion density, ϕ is the potential, $p_{\mathrm{e,i}} = nT_{\mathrm{e,i}}$ are the electron and ion pressures, $\phi^* = \phi + p_\mathrm{i}$ is the modified potential, and the Λ terms on the RHS contain the terms from collisional diffusion and terms for parametrized loss along the magnetic field lines and are discussed in detail in Refs. 18 and 19. The advective derivatives are defined as $\mathrm{d}_t = \partial_t + B^{-1}\{\phi,\cdot\}$ and $\mathrm{d}_t^0 = \partial_t + \{\phi,\cdot\}$, with the anti-symmetric bracket $\{f,g\} = \partial_x f\partial_y g - \partial_y f\partial_x g$. The variables are gyro-Bohm normalized, so that

$$\Omega_{\mathrm{ci}}t \to t\,, \quad \frac{e\phi}{T_{\mathrm{e0}}} \to \phi\,, \quad \frac{x}{\rho_s} \to x\,, \quad \frac{n}{n_0} \to n\,, \quad \frac{T_{\mathrm{e,i}}}{T_{\mathrm{e0}}} \to T_{\mathrm{e,i}}\,. \tag{5}$$

with Ω_{ci} being the ion cyclotron frequency, $\rho_\mathrm{s} = \sqrt{\frac{T_{\mathrm{e0}}}{m_\mathrm{i}\Omega_{\mathrm{ci}}^2}}$ the cold-ion hybrid thermal gyro-radius, T_{e0} a characteristic electron temperature, and n_0 a characteristic density, and we have introduced the curvature operator

$$\mathcal{K} = -\frac{\rho_\mathrm{s}}{R}\partial_y\,, \tag{6}$$

where R is the major radius of the tokamak.

B. Neutral transport model

When deriving a combined neutral-plasma model, in which both neutrals and plasma are treated dynamically, it is computationally meaningful to also seek out a fluid model for the neutral particles. A neutral fluid model can be derived the same way as the plasma fluid model, i.e., by taking velocity moments of the kinetic equation but without including the terms involving electric and magnetic fields. Deriving the neutral fluid equations in this manner is a classical textbook example (see, for example, Ref. 22), in which the set of equations is usually asymptotically closed in the Chapman-Enskog scheme which leads to a set of equations similar to the Braginskii equations but again without the electric and magnetic field terms. The Chapman-Enskog closure is valid for a gas where the particles experience a mean-free path between collisions which is short compared to the characteristic length scales in the system. In the following, we examine the validity of this assumption for neutral particles in a tokamak.

In a tokamak, hydrogen isotope molecules can either be puffed into the vacuum chamber for the purpose of fuelling or perturbing the plasma or result from recombination of atoms on the first wall. Reaction rates for ion-molecule

inelastic collisions are in general low for SOL-relevant temperatures, but electrons interact with molecules in a number of ways. Electron impact collisions can lead to excited states of the molecules, ionize the molecules one or two times, or dissociate the molecule to atoms and/or ions, depending on whether the molecule was ionized before dissociation.

A dissociated molecule results in warm 2 eV neutral atoms[23] known as Franck-Condon neutrals. Warmer neutral atoms have a perpendicular mean-free path much longer than that of ions since they are not influenced by the magnetic field, and the atoms may obtain energies even higher than 2 eV from charge-exchange collisions with ions. Energetic neutrals can also originate from recombination of plasma on the first wall. For SOL parameters, the mean-free paths λ of typical neutral particles are[16]

$$\lambda = \frac{v_{\mathrm{th,n}}}{\nu} \approx \frac{\sqrt{T_{\mathrm{n}}/m_{\mathrm{n}}}}{\langle \sigma v \rangle n} \approx \begin{cases} 10^{-2}\,\mathrm{m} & \text{for } T_{\mathrm{n}} = 25\,\mathrm{meV} \\ 10^{0}\,\mathrm{m} & \text{for } T_{\mathrm{n}} = 2\,\mathrm{eV} \\ 10^{1}\,\mathrm{m} & \text{for } T_{\mathrm{n}} = 50\,\mathrm{eV}, \end{cases} \tag{7}$$

where 50 eV represents a neutral atom resulting from a charge-exchange collision with a hot ion. $v_{\mathrm{th,n}}$ is the thermal speed, $\nu = \langle \sigma v \rangle n$ is the collision frequency, T_{n} is the typical energy of neutral species n, and m_{n} is the mass. In reality, the neutrals have a continuous spread in the energy around the thermal energy, but the above comparison gives an idea of the relevant length scales.

The conclusion is that thermal neutral molecules have a mean-free path comparable to that of the gradient length scales of SOL structures, whereas hotter neutral atoms have mean-free paths much longer than those. This poses a problem for a fluid description of the neutral atoms since the conventional Chapman-Enskog closure[17] is not valid in this regime.

Neutral fluid descriptions that extend beyond the assumption of a short mean-free path are sparsely treated in the literature. It is, however, investigated in Ref. 24 when seeking a fluid description for the electron particle and heat transport in the direction of magnetic field lines in a low collisionality tokamak plasma, which also experiences a long mean-free path. This paper finds that a fluid closure is generally not obtainable in terms of profiles in the long mean-free path limit, but surprisingly the particle transport is well described, with the density flux given by Fick's law. For the neutral particle case, this results in a continuity equation of the form

$$\partial_t n_{\mathrm{n}} - \nabla \cdot (D_{\mathrm{n}} \nabla n_{\mathrm{n}}) = S^n_{\mathrm{n}}\,, \tag{8}$$

with

$$D_{\mathrm{n}} = \frac{1}{2}\frac{v^2_{\mathrm{th,n}}}{\nu}\,, \tag{9}$$

for any collisionality ν. Here, n_{n} is the density of neutral species n and S^n_{n} is the corresponding density source.

Since a heat equation on closed form is not obtainable in this regime, the neutral temperatures have to be accounted for in other manners. We propose a model that resolves the neutral velocity distribution to a finite number of isothermal neutral species, each with its own diffusion coefficient determined by the energy of that species. The main driver for such assumption is rooted in the atomic physics described above; the neutral molecules enter at thermal velocity, and the neutral atoms are created at distinct temperatures. The energy exchange rate between neutrals is low compared to their average lifetime, and they are thus assumed to maintain their initial energy until ionization. The assumption is supported experimentally, where distinct highly populated energies in the neutral velocity spectrum have also been observed, both from spectroscopic measurements of the Zeeman-split Balmer lines[25] and from laser-induced fluorescence[26] on the TEXTOR tokamak. The experimental findings report slightly lower typical energies for the dissociated neutrals than what is assumed here, most likely due to the dissociation into atoms in the $n = 3$ state, instead of the ground state.

The assumptions made by describing the neutral populations at distinct temperatures may, however, lead to an oversimplification of the physical processes that could be essential for describing observed phenomena. In particular, effects of having neutrals in a broader energy range originating from recycling and from charge exchange collisions are neglected, as the recycled neutrals are not included in the analysis presented here, and those originating from charge exchange are all assigned the same temperature. Despite this, resolving the neutral velocity distribution into three temperatures is assumed to reproduce the primary effects of a kinetic description. The characteristic decay lengths for the neutral densities are taken into account, which allows for quantifying the spatial influence of the different types of neutrals on the edge and SOL plasma.

In the model presented here, we describe the neutral atoms and molecules by three species corresponding to those with temperatures given in (7), i.e., cold neutral molecules, warm neutral atoms originating from dissociated molecules, and hot neutral atoms from charge-exchange collisions between warm neutrals and ions.

The transport equations are coupled to each other and to those of the plasma variables through inelastic collisions. The interactions with the highest cross-section in the SOL and edge domains, and that describe the neutral particle life cycle outlined in the beginning of the section, are included. The corresponding source terms enter the neutral particle transport equations (8) with n = cold, warm, and hot as

$$S^n_{\mathrm{cold}} = -n_{\mathrm{e}} n_{\mathrm{cold}} \left(\langle \sigma_{\mathrm{Dis}} v \rangle + \langle \sigma_{\mathrm{Iz}} v \rangle \right), \tag{10}$$

$$S^n_{\mathrm{warm}} = n_{\mathrm{e}} \left(n_{\mathrm{cold}} \left(2\langle \sigma_{\mathrm{Dis}} v \rangle + \langle \sigma_{\mathrm{Iz}} v \rangle \right) - n_{\mathrm{warm}} \langle \sigma_{\mathrm{iz}} v \rangle \right) - n_{\mathrm{i}} n_{\mathrm{warm}} \langle \sigma_{\mathrm{cx}} v \rangle\,, \tag{11}$$

$$S^n_{\mathrm{hot}} = n_{\mathrm{i}} n_{\mathrm{warm}} \langle \sigma_{\mathrm{cx}} v \rangle - n_{\mathrm{e}} n_{\mathrm{hot}} \langle \sigma_{\mathrm{iz}} v \rangle\,, \tag{12}$$

where n_{cold} is the density of the molecules and n_{warm} and n_{hot} are those for the atomic species.

The above set of source terms accounts for dissociation (Dis) of molecules ($\mathrm{e} + \mathrm{H}_2 \rightarrow \mathrm{e} + 2\,\mathrm{H}$), ionization followed by dissociation (Iz) of molecules ($\mathrm{e} + \mathrm{H}_2 \rightarrow 2\mathrm{e} + \mathrm{H}_2^+ \rightarrow 2\mathrm{e} + \mathrm{H}^+ + \mathrm{H}$), ionization (iz) of atoms ($\mathrm{e} + \mathrm{H} \rightarrow 2\mathrm{e} + \mathrm{H}^+$), and charge-exchange collisions (cx) between warm atoms and hot ions ($\mathrm{H}^+ + \mathrm{H} \rightarrow \mathrm{H} + \mathrm{H}^+$). H can be any hydrogen isotope, as the reaction rates only depend weakly on the

isotope mass. Those are among the dominant reaction rates in the temperature interval of interest. Other reactions could be included as well, such as charge exchange collisions between ions and molecules or dissociation of molecules into excited atomic states. Including those reactions evidently results in the same end-products as are covered by the present model, but the location and rate of the creation of atoms and ions from molecules may change. The effects of including those reactions are left for future work. The reaction rates as a function of energy are shown in Fig. 1.

This concludes the neutral model, and the effect of the interactions on the plasma drift-fluid equations are described in Sec. II C.

C. Plasma-neutral interactions

The presence of inelastic neutral interactions such as ionization of atoms introduces source terms to the transport equations. Formally, the Boltzmann equation becomes

$$\partial f_\sigma + \boldsymbol{v}\cdot\nabla f_\sigma + \frac{q_\sigma}{m_\sigma}(\boldsymbol{E}+\boldsymbol{v}\times\boldsymbol{B})\cdot\nabla_{\boldsymbol{v}} f_\sigma = \mathcal{C}_\sigma + \mathcal{S}_\sigma\,, \quad (13)$$

where an inelastic source (or sink) term $\mathcal{S}$ is introduced on the RHS. Velocity space moments of (13) result in a set of fluid equations that differ from the Braginskii two-fluid equations by the appearance of the RHS source terms

$$\partial_{t,\sigma} n_\sigma + \cdots = S^n_\sigma\,, \quad (14)$$

$$m_\sigma n_\sigma \partial_{t,\sigma}\boldsymbol{u}_\sigma + \cdots = \boldsymbol{S}^u_\sigma\,, \quad (15)$$

$$\frac{3}{2}\partial_{t,\sigma} p_\sigma + \cdots = S^p_\sigma\,, \quad (16)$$

where the source terms are formally obtained by taking moments of $\mathcal{S}_\sigma$ from (13) as discussed in Ref. 13.

For the electron impact molecular dissociation, molecular ionization and dissociation, atomic ionization, and ion-atom charge exchange, the above source terms take the form

$$S^n = S^{\mathrm{iz}} + S^{\mathrm{Iz}} = n_\mathrm{e}\left[(n_\mathrm{warm}+n_\mathrm{hot})\langle\sigma_{\mathrm{iz}}v\rangle + n_\mathrm{cold}\langle\sigma_{\mathrm{Iz}}v\rangle\right], \quad (17)$$

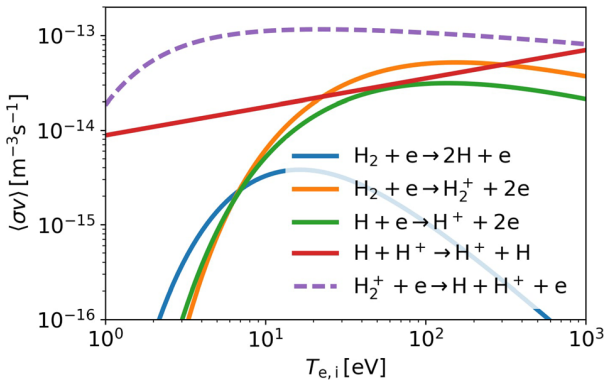

FIG. 1. Dominant reaction rates for inelastic collisions between ions or electrons and neutrals. The molecular assisted ionization is a two-step reaction, where the reaction rate for the dissociation of H_2^+ is shown by the dashed curve. Due to the high reaction rate at all relevant temperatures and the short mean-free path of H_2^+ compared to that of neutrals, this reaction is assumed to happen immediately after ionization of H_2. The reaction rates are obtained from the study by Janev *et al.*[27]

for the density source,

$$\boldsymbol{S}^u_\mathrm{e} = m_\mathrm{e}(\boldsymbol{u}_\mathrm{n}-\boldsymbol{u}_\mathrm{e})S^n\,, \quad (18)$$

$$\boldsymbol{S}^u_\mathrm{i} = m_\mathrm{i}(\boldsymbol{u}_\mathrm{n}-\boldsymbol{u}_\mathrm{i})(S^n+S^{\mathrm{cx}}) + \boldsymbol{R}^{\mathrm{cx}}_{\mathrm{in}} - \boldsymbol{R}^{\mathrm{cx}}_{\mathrm{ni}}\,, \quad (19)$$

for the momentum sources, and the energy density sources are

$$S^p_\mathrm{e} = \frac{3}{2}\frac{m_\mathrm{e}}{m_\mathrm{n}}T_\mathrm{n}S^n + \frac{1}{2}m_\mathrm{e}(\boldsymbol{u}_n-\boldsymbol{u}_\mathrm{e})^2 S^n + \frac{1}{2}m_\mathrm{e}u_\mathrm{e}^2 S^n - \phi_{\mathrm{iz}}S^{\mathrm{iz}} - \phi_{\mathrm{Iz}}S^{\mathrm{Iz}} - \phi_{\mathrm{Dis}}S^{\mathrm{Dis}}\,, \quad (20)$$

and

$$S^p_\mathrm{i} = \frac{3}{2}\frac{m_\mathrm{i}}{m_\mathrm{n}}T_\mathrm{n}S^n + \frac{1}{2}m_\mathrm{i}(\boldsymbol{u}_\mathrm{n}-\boldsymbol{u}_\mathrm{i})^2(S^n+S^{\mathrm{cx}}) + \frac{1}{2}m_\mathrm{i}u_\mathrm{i}^2 S^n + (\boldsymbol{u}_\mathrm{n}-\boldsymbol{u}_\mathrm{i})\cdot\boldsymbol{R}^{\mathrm{cx}}_{\mathrm{in}} + Q^{\mathrm{cx}}_{\mathrm{in}} - Q^{\mathrm{cx}}_{\mathrm{ni}}\,. \quad (21)$$

Here, $\boldsymbol{u}_\mathrm{n}$ is the neutral fluid velocity, which is zero in the fluid model presented in Sec. II B but included here for future reference. The charge-exchange and dissociation source terms are

$$S^{\mathrm{cx}} = n_\mathrm{i}n_{\mathrm{warm}}\langle\sigma_{\mathrm{Iz}}v\rangle\,, \quad (22)$$

$$S^{\mathrm{Dis}} = n_\mathrm{e}n_{\mathrm{cold}}\langle\sigma_{\mathrm{Dis}}v\rangle\,, \quad (23)$$

where the reaction rates in (17), (22), and (23) can be found by parameterizations of polynomial fits to experimental data in terms of $T_{\mathrm{e,i}}$ (see, for example, Ref. 27). The ion-neutral and neutral-ion frictional momentum transfer terms from charge exchange can be approximated by

$$\boldsymbol{R}^{\mathrm{cx}}_{\mathrm{in}} \approx -m_\mathrm{i}\sigma_{\mathrm{cx}}(v_{\mathrm{cx}})n_\mathrm{i}n_{\mathrm{warm}}(\boldsymbol{u}_\mathrm{i}-\boldsymbol{u}_\mathrm{n}) \times \frac{v_{\mathrm{th,n}}^2}{\sqrt{\frac{16}{\pi}v_{\mathrm{th,i}}^2 + 4(\boldsymbol{u}_\mathrm{i}-\boldsymbol{u}_\mathrm{n})^2 + \frac{9\pi}{4}v_{\mathrm{th,n}}^2}}\,, \quad (24)$$

$$\boldsymbol{R}^{\mathrm{cx}}_{\mathrm{ni}} \approx m_\mathrm{i}\sigma_{\mathrm{cx}}(v_{\mathrm{cx}})n_\mathrm{i}n_{\mathrm{warm}}(\boldsymbol{u}_\mathrm{i}-\boldsymbol{u}_\mathrm{n}) \times \frac{v_{\mathrm{th,i}}^2}{\sqrt{\frac{16}{\pi}v_{\mathrm{th,n}}^2 + 4(\boldsymbol{u}_\mathrm{i}-\boldsymbol{u}_\mathrm{n})^2 + \frac{9\pi}{4}v_{\mathrm{th,i}}^2}}\,, \quad (25)$$

where $v_{\mathrm{cx}} = \sqrt{\frac{4}{\pi}(v_{\mathrm{th,i}}^2 + v_{\mathrm{th,n}}^2) + (\boldsymbol{u}_\mathrm{i}-\boldsymbol{u}_\mathrm{n})^2}$, and the heat-exchange from charge-exchange collision can be approximated by

$$Q^{\mathrm{cx}}_{\mathrm{in}} \approx \frac{3}{4}m_\mathrm{i}\sigma_{\mathrm{cx}}(v_{\mathrm{cx}})n_\mathrm{i}n_{\mathrm{warm}}v_{\mathrm{th,n}}^2 \times \sqrt{\frac{4}{\pi}v_{\mathrm{th,i}}^2 + (\boldsymbol{u}_\mathrm{i}-\boldsymbol{u}_\mathrm{n})^2 + \frac{64}{9\pi}v_{\mathrm{th,n}}^2}\,, \quad (26)$$

$$Q^{\mathrm{cx}}_{\mathrm{ni}} \approx \frac{3}{4}m_\mathrm{i}\sigma_{\mathrm{cx}}(v_{\mathrm{cx}})n_\mathrm{i}n_{\mathrm{warm}}v_{\mathrm{th,i}}^2 \times \sqrt{\frac{4}{\pi}v_{\mathrm{th,n}}^2 + (\boldsymbol{u}_\mathrm{i}-\boldsymbol{u}_\mathrm{n})^2 + \frac{64}{9\pi}v_{\mathrm{th,i}}^2}\,, \quad (27)$$

following Refs. 13 and 28.

We will now show how the source terms enter the drift fluid equations. Following the recipe of drift-ordering, the

momentum source terms, i.e., Eqs. (18) and (19), introduce additional drifts. The drift ordering used here is identical to that of Refs. 8 and 18 and allows for solving the momentum equations iteratively, by assuming that the characteristic time- and parallel length-scales are much larger the inverse ion gyro-frequency and the ion gyro-radius. This allows for describing the perpendicular momentum vector (including terms up to first order) by

$$\boldsymbol{u}_{\perp\sigma} = \boldsymbol{u}^0_{\perp\sigma} + \boldsymbol{u}^1_{\perp\sigma}\,, \tag{28}$$

where $\boldsymbol{u}^0_{\perp\sigma}$ are the (leading-order) diamagnetic- and $E\times B$-drifts

$$\boldsymbol{u}^0_{\perp\sigma} = -\frac{\nabla_\perp p_\sigma \times \hat{\boldsymbol{B}}}{q_\sigma n B} - \frac{\nabla_\perp \phi \times \hat{\boldsymbol{B}}}{B}\,, \tag{29}$$

and $\boldsymbol{u}^1_{\perp\sigma}$ consist of the (next-to-leading-order) polarization, resistive, and viscous drifts

$$\boldsymbol{u}^1_{\perp\sigma} = \boldsymbol{u}_{\mathrm{p}\sigma} + \boldsymbol{u}_{\mathrm{R}\sigma} + \boldsymbol{u}_{\pi\sigma}\,. \tag{30}$$

Similar to the friction between ions and electrons, the neutral sources also originate from collisions at a much lower frequency than that of the ion gyration and thus introduce a first order drift $\boldsymbol{u}_{\mathrm{S}\sigma}$ to the existing sum in (30), resulting in

$$\boldsymbol{u}^1_{\perp\sigma} = \boldsymbol{u}_{\mathrm{p}\sigma} + \boldsymbol{u}_{\mathrm{R}\sigma} + \boldsymbol{u}_{\pi\sigma} + \boldsymbol{u}_{\mathrm{S}\sigma}\,. \tag{31}$$

Since the source term itself is first order in the drift-approximation, it is only the leading order velocity terms that contribute, i.e.,

$$\boldsymbol{u}_{\mathrm{S}\sigma} = \frac{\boldsymbol{S}^u_\sigma \times \hat{\boldsymbol{B}}}{n_\sigma q_\sigma B}\,, \tag{32}$$

where

$$\boldsymbol{S}^u_{\mathrm{e}} = m_{\mathrm{e}}\left(\boldsymbol{u}_{\mathrm{n}} - \boldsymbol{u}^0_{\perp\mathrm{e}}\right)S^n\,, \tag{33}$$

$$\boldsymbol{S}^u_{\mathrm{i}} = m_{\mathrm{i}}\left(\boldsymbol{u}_{\mathrm{n}} - \boldsymbol{u}^0_{\perp\mathrm{i}}\right)\left(S^n + S^{\mathrm{cx}}\right) + \boldsymbol{R}^{\mathrm{cx}}_{\mathrm{in}} - \boldsymbol{R}^{\mathrm{cx}}_{\mathrm{ni}}\,. \tag{34}$$

This results in the source drifts

$$\boldsymbol{u}_{\mathrm{Se}} = \frac{S^n}{n_{\mathrm{e}}\Omega_{\mathrm{ce}}}\left[\boldsymbol{u}_{\perp\mathrm{n}} - \left(\frac{\nabla_\perp\phi}{B} + \frac{\nabla_\perp p_{\mathrm{e}}}{q_{\mathrm{e}} n_{\mathrm{e}} B}\right)\right]\,, \tag{35}$$

$$\boldsymbol{u}_{\mathrm{Si}} = \frac{S^n + S^{\mathrm{cx}}}{n_{\mathrm{i}}\Omega_{\mathrm{ci}}}\left[\boldsymbol{u}_{\perp\mathrm{n}} - \left(\frac{\nabla_\perp\phi}{B} + \frac{\nabla_\perp p_{\mathrm{i}}}{q_{\mathrm{i}} n_{\mathrm{i}} B}\right)\right] + \frac{\boldsymbol{R}^{\mathrm{cx}}_{\perp\mathrm{in}} - \boldsymbol{R}^{\mathrm{cx}}_{\perp\mathrm{ni}}}{n_{\mathrm{i}}\Omega_{\mathrm{ci}}}\,. \tag{36}$$

Had elastic collisions with neutrals been included in the model, a yet another first order drift term would be added to (31). This is the so-called Pedersen drift, and details on the derivation of the term are found in Ref. 8.

In Sec. II D, the new source-drift terms are introduced in the HESEL drift-fluid based model for the plasma edge and SOL regions.

D. Combined model equations

The source terms from neutral interactions that were calculated in Sec. II C enter the HESEL equations as

$$\mathrm{d}_t n + n\mathcal{K}(\phi) - \mathcal{K}(p_{\mathrm{e}}) = \Lambda_n + \Sigma_n\,, \tag{37}$$

$$\nabla\cdot\left(\mathrm{d}^0_t\nabla_\perp\phi^*\right) - \mathcal{K}(p_{\mathrm{e}} + p_{\mathrm{i}}) = \Lambda_\omega + \Sigma_\omega\,, \tag{38}$$

$$\frac{3}{2}\mathrm{d}_t p_{\mathrm{e}} + \frac{5}{2}p_e\mathcal{K}(\phi) - \frac{5}{2}\mathcal{K}(p_{\mathrm{e}}^2/n) = \Lambda_{p_{\mathrm{e}}} + \Sigma_{p_{\mathrm{e}}}\,, \tag{39}$$

$$\frac{3}{2}\mathrm{d}_t p_{\mathrm{i}} + \frac{5}{2}p_i\mathcal{K}(\phi) + \frac{5}{2}\mathcal{K}\left(p_{\mathrm{i}}^2/n\right) - p_{\mathrm{i}}\mathcal{K}(p_{\mathrm{e}} + p_{\mathrm{i}}) = \Lambda_{p_{\mathrm{i}}} + \Sigma_{p_{\mathrm{i}}}\,, \tag{40}$$

where

$$\Sigma_n = S^n_{\mathrm{e}} - \nabla\cdot\left(n\boldsymbol{u}^{\mathrm{S}}_{\mathrm{e}}\right)\,, \tag{41}$$

$$\Sigma_\omega = \left(S^n_{\mathrm{i}} - S^n_{\mathrm{e}}\right) - \nabla\cdot\left[n\left(\boldsymbol{u}^{\mathrm{S}}_{\mathrm{i}} - \boldsymbol{u}^{\mathrm{S}}_{\mathrm{e}}\right)\right]\,, \tag{42}$$

$$\Sigma_{p_{\mathrm{e}}} = S^p_{\mathrm{e}} - \frac{3}{2}\nabla\cdot\left(p_{\mathrm{e}}\boldsymbol{u}^{\mathrm{S}}_{\mathrm{e}}\right) - p_{\mathrm{e}}\nabla\cdot\boldsymbol{u}^{\mathrm{S}}_{\mathrm{e}}\,, \tag{43}$$

$$\Sigma_{p_{\mathrm{i}}} = S^p_{\mathrm{i}} - \frac{3}{2}\nabla\cdot\left(p_{\mathrm{i}}\boldsymbol{u}^{\mathrm{S}}_{\mathrm{i}}\right) - p_{\mathrm{i}}\nabla\cdot\boldsymbol{u}^{\mathrm{S}}_{\mathrm{i}}\,. \tag{44}$$

The neutrals are described as three fluids, consisting of cold thermal molecules, warm atoms from dissociation of molecules, and hot atoms from charge-exchange collisions with ions. The transport of neutral particles is described by diffusion (8) with source terms (10)–(12). The diffusion coefficients are approximated by

$$D_{\mathrm{hot}} = 10^1 D_{\mathrm{warm}} = 10^3 D_{\mathrm{cold}} = 10^2\rho_{\mathrm{s}}^2\Omega_{\mathrm{ci}}\,, \tag{45}$$

which have approximately the same relative value as prescribed by (9).

Note that the neutral terms have been normalized with parameters that are related to the plasma parameters and not to those of the neutrals. If one were to treat only the neutral particles, more suitable scale-setting parameters may exist, but for the combined model, it is simpler to apply the same normalization throughout. The system of equations is solved in a slab geometry in a drift-plane at the outboard mid-plane of a tokamak, perpendicular to the magnetic field lines. The domain is depicted in Fig. 2, which has dimensions of 225 $\times 75\,\rho_{\mathrm{s}}^2$ and consists of SOL and edge sub-domains.

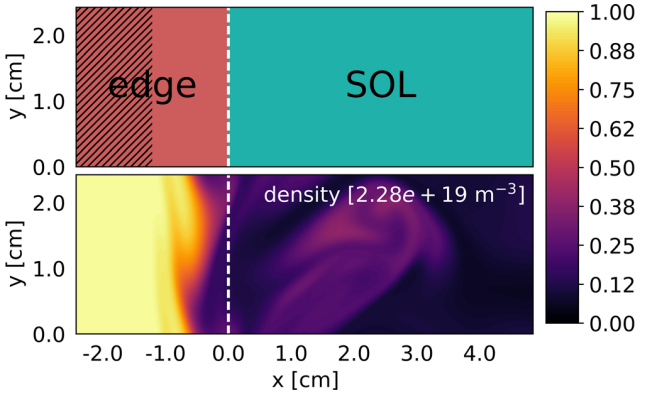

FIG. 2. The upper frame shows the domain for the combined HESEL-neutral simulations, where the x-coordinate corresponds to the radial direction and the y-coordinate corresponds to the poloidal direction. In the inner part of the edge region, marked by the shaded area, the plasma density and pressure fields are relaxed towards fixed prescribed profiles, which result in a dynamically imposed boundary condition to the core. In the SOL region, the plasma fields are damped according to parametrized parallel transport. The white dashed line shows the location of the LCFS. The lower frame displays a snapshot of the turbulent electron density during a simulation.

The boundaries are periodic in the poloidal y-direction. At the inner boundary towards the core, the boundary conditions for the plasma fields are $\omega = 0$, $n = 1.5 n_0$, and $p_e = 2 p_i = 10\, n_0 T_{e0}$, and at the outer boundary towards the first wall, the boundary conditions are $\partial_x n = \partial_x p_{e,i} = \omega = 0$, where x is the radial direction. The neutral density fields satisfy

$$-D_n \partial_x n_n = \sqrt{-\frac{D_n S_n'}{n_n}}\, n_n \,, \tag{46}$$

at the inner boundary, where S_n' are the source terms that are proportional to n_n, i.e., for n = warm, the proportional source term is

$$S_{warm}' = -n_{warm}\left(n_e \langle \sigma_{iz} v \rangle + n_i \langle \sigma_{cx} v \rangle\right) . \tag{47}$$

At the outer boundary, the neutral density boundary conditions are

$$-D_n \partial_x n_n = -\gamma \sqrt{-\frac{D_n S_n'}{n_n}}\, n_n + \Gamma_{puff}\, \delta_{n,cold} \,. \tag{48}$$

The boundary conditions in both (46) and (48) are obtained by solving (8) at a steady state, under the assumption that there are no fluctuations on the boundaries and that the density vanishes at $\pm\infty$. The outer boundary condition (48) moreover has a factor γ, which is a measure of the fraction of absorbed particles. For $\gamma = 1$, the boundary conditions for the neutrals are (apart from a sign) identical to those on the inner boundary, i.e., solutions to the corresponding steady-state equations. If $\gamma = 0$, no particles pass the boundary, and the outer boundary becomes a zero-flux boundary condition for the neutral atom densities. For the simulations used for this paper, the value is $\gamma = 0.2$. The parameter Γ_{puff} introduces a flux of thermal molecules to the system to mimic gas-puffing in a tokamak.

In Sec. III, the above model is solved in the BOUT++ framework[29] for varying input parameters for the purpose of enlightening phenomena involving interactions between neutral particles and edge and SOL plasmas.

III. APPLICATIONS

The inclusion of neutral interactions in the HESEL drift-fluid model equations allows for investigating various aspects of the edge and SOL fusion plasmas. In this section, it is illustrated how gas-puff rates affect the far edge and SOL profiles for electron density and for electron and ion temperatures. It is moreover shown that for an appropriate flux of neutrals into the system, the density source in the edge region can be replaced by a self-consistent source from ionization of neutral particles. For the results presented here, the gyro-Bohm normalization parameters from (5) correspond to the plasma parameters of a medium-sized tokamak with

$$\begin{aligned} \Omega_{ci} &= 9.57 \times 10^7\, s^{-1} \,, & T_{e0} &= 20\, eV \,, \\ \rho_s &= 3.23 \times 10^{-4}\, m \,, & T_{i0} &= 10\, eV \,, \\ n_0 &= 1.5 \times 10^{19}\, m^{-3} \,, & B_0 &= 2\, T \,, \end{aligned} \tag{49}$$

and with deuterium ions and neutrals.

A. Changing neutral molecule puffing rate

The model described in Sec. II D is solved numerically with the same initial plasma fields but for different values of flux of neutral molecules into the system at the outer boundary. The purpose is to investigate how different gas-puff rates affect the plasma density and temperature profiles and turbulent dynamics in the edge and SOL regions.

The values of the flux density Γ_{puff} are $10^{20}\, m^{-2} s^{-1}$ resembling a low puffing rate, $10^{21}\, m^{-2} s^{-1}$ for a medium puffing rate, and $10^{22}\, m^{-2} s^{-1}$ for a high puffing rate. The low and medium puffing rates resemble realistic puffing rates for experiments. For all puffing rates, the plasma density and pressure sources in the edge region are maintained, and the effect of the puffing rate on the profiles is thus only visible in the far edge and SOL regions.

It is observed from Fig. 3 that a higher puffing results in a higher average density and lower average electron and ion temperatures. This is particularly visible for the high puffing rate case.

Other profiles of interest are the electron/ion density source profiles, which are shown in Fig. 4. The density source profile provides the total ionization rate of atoms and molecules as a function of the radial position and can thus be used to estimate the location of the fuelling. There is a clear tendency in the density source profiles for an increased gas puffing to increase the magnitude of the ionization source as expected from (17). It is moreover observed that for an increased gas puffing, the profile peaks in both the edge and SOL move towards the LCFS. Relatively more neutrals are ionized in the SOL for the lower fuelling cases, and we believe that the reason for this is that the higher fuelling cases cool the outermost electrons more, which allows for a deeper penetration of the neutral molecules before they are ionized. In Fig. 5, the radial electric field is shown. The radial electric field is known to correlate with the formation of an edge transport barrier due to the sheared poloidal flow

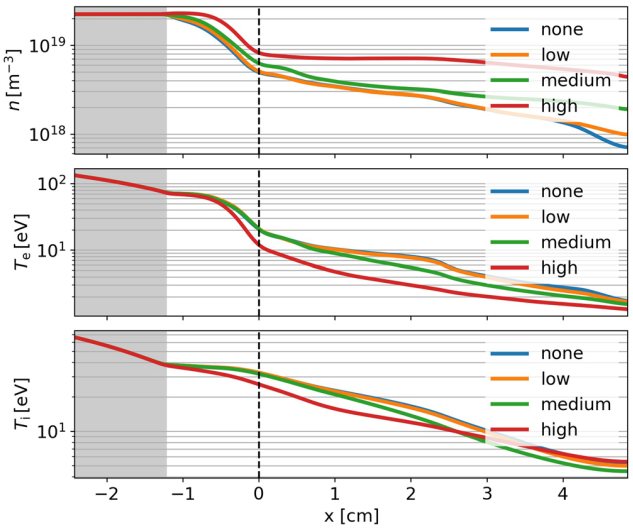

FIG. 3. Temporally averaged electron density and ion and electron temperature profiles for "none," "low," "medium," and "high" gas puffing rates. Neutral gas puffing increases the density and decreases the temperatures in the edge and SOL regions. The gray region marks the forcing region.

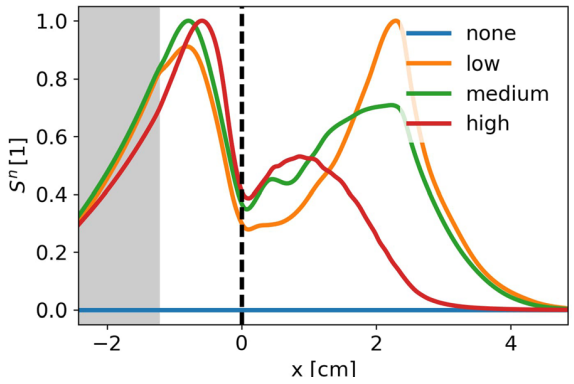

FIG. 4. The normalized density source for "none," "low," "medium," and "high" gas puffing rates. The profiles are normalized with the values 1, 1.41 $\times$ 10^{21}, 1.33 $\times$ 10^{22}, and 1.18 $\times$ 10^{23}, respectively, all in units of $m^{-3}s^{-1}$. The density source increases with the amount of neutrals, and the source in the SOL in particular is shifted towards the LCFS for higher fuelling rates. The gray region marks the forcing region.

resulting from the $E \times B$-drift. A negative radial electric field corresponds to an $E \times B$ flow in the electron-diamagnetic velocity direction, which is usually observed in experiments. It is observed that the radial electric field changes slightly with the puffing rate, where in particular for the case of high gas puffing, the profile of the radial electric field shifts away from that where neutrals are absent.

The plasma edge dynamics also change when the gas puffing is increased. This can be observed by monitoring the particle flux across the LCFS. Among the leading order drifts, only the $E \times B$-drift advects the density, and the radial particle flux Γ_x is thus obtained from

$$\Gamma_x = -n\frac{\partial_y \phi}{B}. \tag{50}$$

From Fig. 6, it appears that there is a tendency for the average radial density flux to increase with a higher puffing rate, which is consistent with the increased fuelling in the edge region. The flux characteristics are also different for different cases, which is apparent in Fig. 7 showing the probability density functions (PDFs) for Γ_x. The mean, standard deviation, skewness, and kurtosis for the PDFs are shown in

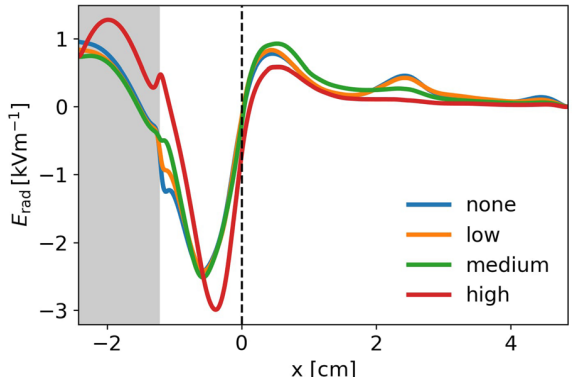

FIG. 5. The radial electric field for "none," "low," "medium," and "high" gas puffing rates. It is observed that the radial electric field changes slightly both in the magnitude and shape with increased neutral flux. The gray region marks the forcing region.

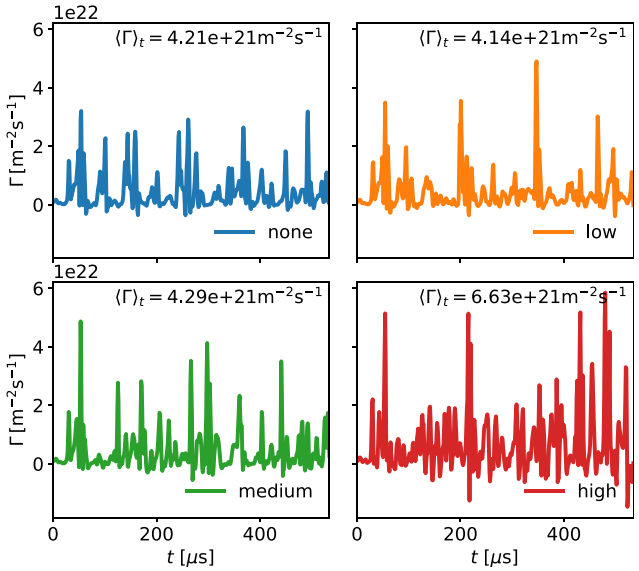

FIG. 6. Radial particle flux across LCFS for "none," "low," "medium," and "high" gas puffing rates. The general tendency is that the flux increases with the increased puffing rate, and the characteristics of the transport do likewise appear to be influenced by the neutral density.

Table I. For all gas puff cases, except for that with no puffing, there is a trend that the mean and standard deviation increase, and the skewness and kurtosis decrease, for a higher puffing rate. It is unclear why the values for the simulation without gas puffing deviate so much from that with low puffing, but it is our belief that larger datasets will show a better consistency between the statistics of the flux for different puffing rates. A more detailed analysis on the effect of the fuelling rate on blob characteristics is planned for a future publication. The topic is related to the results in Ref. 30, where the effect of neutrals on blob transport is attributed to their insulating behavior in the divertor region. It is interesting that we see similar effects but without any inclusion of physics near the divertor. Future studies with the model should likewise enlighten whether the rise of density in the SOL observed in Fig. 3 is mainly due to increased ionization in this region or a larger radial particle flux across the LCFS as a result of increased fuelling.

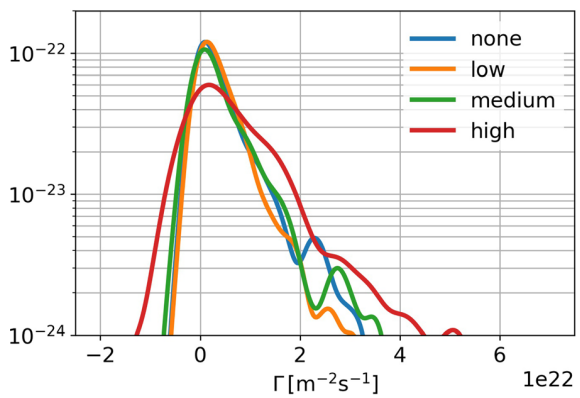

FIG. 7. Probability density of the flux across LCFS for "none," "low," "medium," and "high" gas puffing rates. Descriptors for the PDFs are given in Fig. 1.

B. The effect of the puffing rate on self-consistent fuelling

In this section, we investigate the possibility of removing the forcing of the density that is responsible for the stiffness in the innermost part of the domain, as shown by the shaded area in Fig. 3. The forcing has been necessary in previous plasma simulations since the profiles are naturally flattened due to transport. Here, the density source is supplemented by a self-consistent source from local ionization of neutrals, and the forcing at the inner boundary acts as a source (or as a sink) to constitute an appropriate coupling towards the core plasma.

With the inclusion of the density source from local ionization of neutrals, it is, however, possible to remove the forcing altogether. Removing the forcing is desirable since for tokamak experiments, fuelling is entirely caused by ionization of neutrals. It is unknown whether the fuelling from gas puffing is approximately evenly distributed across the plasma surface, which would correspond to removing the profile forcing as done here. Alternatively, more neutrals may cross the LCFS locally, for example, near the x-point after recycling at the divertor, and the resulting plasma is then transported upstream. The fuelling from particles recycled in the simulated domain is also not included although those may contribute with a significant amount.[5] Neutrals originating from recycling can be included in the model by introducing a term for the atomic species similar to that for the flux of molecules on the outer boundary in (48) or by increasing the value of Γ_{puff}, which would then represent a sum of flux from puffed and recycled neutral molecules.

For the simulations treated in Sec. III A, both the integrated forced density source, i.e.,

$$\text{force} = \int_{\text{edge}} \mathrm{d}x\mathrm{d}y\,(n_{\text{fixed}} - n)/\tau\,, \tag{51}$$

where n_{fixed} is the fixed density profile and τ is the relaxation time, and the integrated source from ionization of neutrals, i.e.,

$$\text{fuel} = \int_{\text{edge}} \mathrm{d}x\mathrm{d}y\,S^n\,, \tag{52}$$

are shown in Fig. 8. This should give a hint of the amount of gas puffing necessary for keeping the edge density up. It appears that the density source at low puffing is completely dominated by factors other than local ionization of neutrals,

TABLE I. Mean, standard deviation, skewness, and kurtosis for the PDF of the radial particle flux across the LCFS. The mean only changes significantly when going from medium to high fuelling, whereas the skewness and kurtosis appear to depend stronger on the gas puff rate.

	Mean (10^{21} m^{-2} s^{-1})	Standard dev. (10^{21} m^{-2} s^{-1})	Skewness	Kurtosis
None	4.21	5.92	2.08	7.80
Low	4.14	5.95	3.29	18.9
Medium	4.29	6.87	2.51	11.4
High	6.63	9.92	1.92	8.25

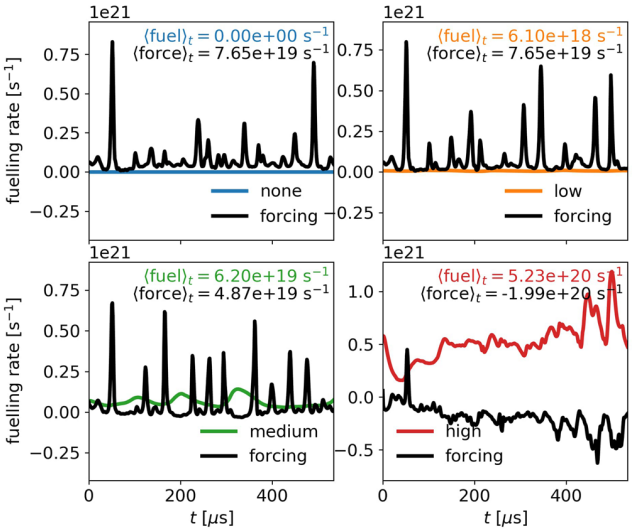

FIG. 8. Fuelling in the edge for "none," "low," "medium," and "high" gas puffing rates. The black curves show the forcing applied to maintain the density in the inner edge region and the colored curves the amount of fuelling provided by ionization of neutrals. For the high puffing rate, the neutrals fuel more than what the system is targeted for and the forcing becomes negative in order to maintain the density in the inner edge.

at medium puffing the two sources contribute approximately equally, and at a high puffing rate, the source from local ionization of neutrals is so big that the forcing becomes negative. Note that for the "none," "low," and "medium" cases where the neutrals do not fuel the plasma sufficiently, the blob events are visible as peaks in the forcing graph. This feature, however, ceases to exist when the neutrals fuel the plasma, and the forcing turns negative. The change in the characteristics of the "high" puffing plot in Fig. 8 from that of the other plots is thus due to a change in the degree of local fuelling from neutrals, going from under-fueled to over-fueled, and not due to a change in the blob formation mechanism itself.

The ideal puffing rate result in a vanishing average forcing, and from the above observations, this should be expected to lie somewhere in between the cases with the medium and high fuelling rate. It appears that with a puffing rate of $\Gamma_{\text{puff}} = 2 \cdot 10^{21}\,\text{m}^{-2}\text{s}^{-1}$, the plasma edge density is maintained at approximately $n = 1.5\ n_0$, which allows for a scenario where the edge region in the simulation is entirely fueled from the local ionization of neutrals.

IV. CONCLUSIONS

In Sec. II, it is displayed how inelastic source terms enter a drift-fluid model. It is found that density sources give rise to an additional drift term in the electron and ion drift velocities and that yet another term is added to the ion drift velocity due to charge-exchange collisions with neutrals.

Neutral atoms originating from dissociation of molecules, and to an even greater extend atoms that have undergone charge-exchange collisions with ions, experience a mean-free path between collisions in the SOL, which is on the order of meters and thus much larger than any gradient length-scales perpendicular to the magnetic field lines. For this reason, a neutral model that is valid in the long

mean-free path limit has been formulated. The neutral model is coupled to the HESEL drift-fluid model for the plasma fields, and the resulting system of equations describes the evolution of plasma and neutral fields in a self-consistent manner.

The coupled HESEL-neutral model allow for investigation of various phenomena in Sec. III. It is observed how increasing the amount of neutrals raises the electron and ion densities and lowers the temperatures in the SOL and far edge regions. It is moreover observed that change in the flux of neutrals into the system affects the radial electric field and the statistical properties of the electron and ion particle fluxes across the LCFS. The self-consistent model moreover allows for removing the forcing of the density source in the inner edge region present in the original HESEL equations and introduces a source from local ionization of neutrals in the edge region.

A combined plasma-neutral model as the one described in this paper allows for a wide range of studies on the neutral-plasma interactions. It is possible to further illuminate how the interactions with neutrals affect blobs and how blobs affect neutrals, with a model that includes both dynamical neutrals and plasma fields. Moreover, a range of experimentally observed phenomena that are most likely due to neutrals influencing the plasma fields, such as shoulder formation[30] and the fuelling triggered H-mode density limit,[31] are expected to at least be partially explained by future simulations with this model.

ACKNOWLEDGMENTS

This work was carried out within the framework of the EUROfusion Consortium and received funding from the Euratom research and training programme 2014–2018 under Grant Agreement No. 633053. The views and opinions expressed herein do not necessarily reflect those of the European Commission.

[1]S. J. Zweben, J. A. Boedo, O. Grulke, C. Hidalgo, B. LaBombard, R. J. Maqueda, P. Scarin, and J. L. Terry, Plasma Phys. Controlled Fusion **49**, S1 (2007).
[2]O. E. Garcia, V. Naulin, A. H. Nielsen, and J. Juul Rasmussen, Phys. Plasmas **12**, 62309 (2005).
[3]D. A. D'Ippolito1, J. R. Myra, and S. J. Zweben, Phys. Plasmas **18**, 060501 (2011).
[4]V. Naulin, J. Nucl. Mater. **363-365**, 24 (2007).
[5]U. Samm and the TEXTOR-94 Team, Plasma Phys. Controlled Fusion **41**, B57 (1999).
[6]S. J. Zweben, J. L. Terry, D. P. Stotler, and R. J. Maqueda, Rev. Sci. Instrum. **88**, 041101 (2017).
[7]E. de la Cal and The TJ-II Team, Nucl. Fusion **56**, 106031 (2016).
[8]M. Løiten, Ph.D. thesis, Department of Physics, Technical University of Denmark, 2017.
[9]C. Wersal and P. Ricci, Nucl. Fusion **55**, 123014 (2015).
[10]D. Reiter, M. Baelmans, and P. Börner, Fusion Sci. Technol. **47**, 172 (2005).
[11]D. Heifetz, D. Post, M. Petravic, J. Weisheit, and G. Bateman, J. Comput. Phys. **46**, 309 (1982).
[12]K. Shimizu, T. Takizuka, S. Sakurai, H. Tamai, H. Takenaga, H. Kubo, and Y. Miura, J. Nucl. Mater. **313-316**, 1277 (2003).
[13]E. T. Meier and U. Shumlak, Phys. Plasmas **19**, 072508 (2012).
[14]E. L. Vold, A. K. Prinja, F. Najmabadi, and R. W. Conn, J. Nucl. Mater. **176-177**, 570 (1990).
[15]D. Schwörer, N. R. Walkden, H. Leggate, B. D. Dudson, F. Militello, T. Downes, and M. M. Turner, Nucl. Mater. Energy **12**, 825 (2017).
[16]A. S. Thrysøe, L. E. H. Tophøj, V. Naulin, J. Juul Rasmussen, J. Madsen, and A. H. Nielsen, Plasma Phys. Controlled Fusion **58**, 044010 (2016).
[17]S. Chapman and T. G. Cowling, *The Mathematical Theory of Non-uniform Gases* (Cambridge, 1953).
[18]J. Madsen, V. Naulin, A. H. Nielsen, and J. Juul Rasmussen, Phys. Plasmas **23**, 032306 (2016).
[19]A. H. Nielsen, J. Juul Rasmussen, J. Madsen, G. S. Xu, V. Naulin, J. M. B. Olsen, M. Løiten, S. K. Hansen, N. Yan, and L. Tophøj, Plasma Phys. Controlled Fusion **59**, 025012 (2017).
[20]F. L. Hinton and C. W. Horton, Jr., Phys. Fluids **14**, 116 (1971).
[21]A. Zeiler, J. F. Drake, and B. Rogers, Phys. Plasmas **4**, 2134 (1997).
[22]C. Cercignani, *The Boltzmann Equation and Its Applications* (Springer, New York, NY, 1988).
[23]P. C. Stangeby, *The Plasma Boundary of Magnetic Fusion Devices* (Institute of Physics Publishing, Bristol, 2000).
[24]R. D. Hazeltine, Phys. Plasmas **5**, 3282 (1998).
[25]J. D. Hey, C. C. Chu, P. Mertens, S. Brezinsek, and B. Unterberg, J. Phys. B: At. Mol. Opt. Phys. **37**, 2543–2567 (2004).
[26]P. Mertens and A. Pospieszczyk, J. Nucl. Mater. **266–269**, 884–889 (1999).
[27]R. K. Janev, W. D. Langer, K. Evans, Jr., and D. E. Post, Jr., *Elementary Processes in Hydrogen-Helium Plasmas* (Springer-Verlag, Berlin, 1987).
[28]H. L. Pauls, G. P. Zank, and L. L. Williams, J. Geophys. Res. **100**, 21595, https://doi.org/10.1029/95JA02023 (1995).
[29]B. D. Dudson, M. V. Umansky, X. Q. Xu, P. B. Snyder, and H. R. Wilson, Comput. Phys. Commun. **180**, 1467 (2009).
[30]D. Carralero, J. Madsen, S. A. Artenea, M. Bernert, G. Birkenmeier, T. Eich, G. Fuchert, F. Laggner, V. Naulin, P. Manz *et al.*, Nucl. Mater. Energy **12**, 1189 (2017).
[31]M. Bernert, T. Eich, A. Kallenbach, D. Carralero, A. Huber, P. T. Lang, S. Potzel, F. Reimold, J. Schweinzer, E. Viezzer, and H. Zohm, Plasma Phys. Controlled Fusion **57**, 014038 (2015).

4.2.3 Postlude

The paper is the backbone of the thesis, and contains, although in less detail, much of the information provided in Chpt. 2. Most of the results, such as the profiles for the radial electric fields, and the statistical analysis of the radial electron particle flux, are not comparable to what is produced in the other papers presented here. It should, however, be noted that the ionization profile in Fig. 4, qualitatively agrees well with that in the first paper in Sec. 4.1. In that paper only one ionization rate peak, that in the edge region, is observable. The reason for that is, that all the neutrals considered there are atoms, and the SOL ionization is thus limited. The claim that it is the atoms, and not the molecules, that are responsible for the ionization in the edge region is backed by Fig. 2 in the conference paper *The influence of blob intermittency on fuelling* and discussed in Sec. 4.1.3.

The statistical analysis presented in the paper focuses on the effect of neutrals on the flux across the LCFS. The interactions between plasma and neutrals in the SOL also affect how blobs propagate further away from the edge region. A more detailed study on the particular effect of the different neutral interactions on blobs is initiated in Sec. 4.5.2. However, for the paper in consideration, there are some data available, which may hint on some of the significant features of the effect of neutrals on blobs. Similar to the PDF for the radial flux across the LCFS, shown in Fig. 7 in the paper, the PDF for **radial plasma flux across a plane in the mid-SOL** is shown in Fig. 4.2, and the corresponding statistical descriptors provided in Tab. 4.1. It is observed that increasing the neutral molecule particle flux also increases the mean and the standard deviation of the probability density functions (PDFs), whereas the skewness and kurtosis again display a somewhat inconsistent response to the increment in the puffing rate. In particular the case for high gas puffing shows signs of a complete alteration in the transport dynamics. The higher values for the mean and the standard deviation are consistent with the preliminary findings presented in Sec. 4.5.2, where it is observed that the ionization interactions have the potential to alter the blob dynamics by significantly increasing the density, while the electron and ion temperatures are lowered. More detailed studies on the effects of neutral interactions on blobs are intended to be carried out in the near future.

Although the current paper is self-contained, an obvious question would be that regarding the **self-consistent fuelling** at a puffing rate of $\Gamma_{\text{puff}} =$

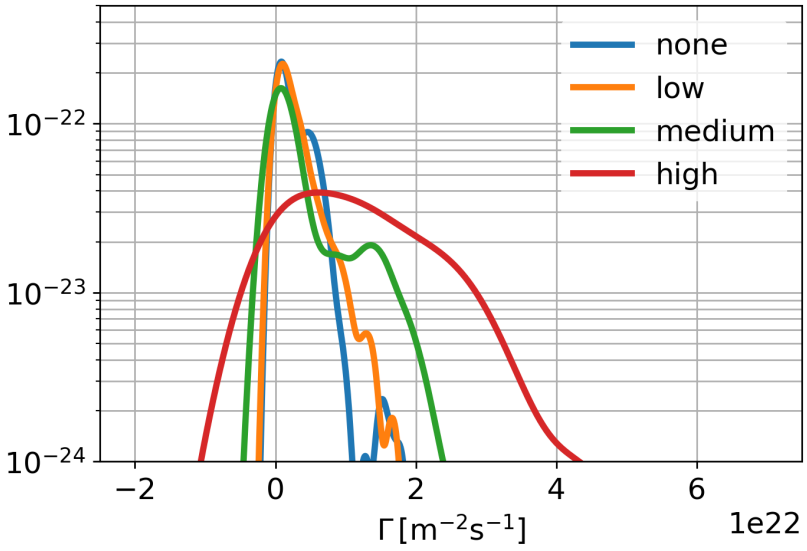

Figure 4.2: Probability density of the flux across a plane in the middle of the SOL for 'none', 'low', 'medium', and 'high' gas puffing rates. Descriptors for the PDF are given in Tab. 4.1.

Table 4.1: Mean, standard deviation, skewness and kurtosis for the PDF of the radial particle flux across a plane in the middle of the SOL.

	mean $[10^{21}\,\mathrm{m^{-2}s^{-1}}]$	standard dev. $[10^{21}\,\mathrm{m^{-2}s^{-1}}]$	skewness	kurtosis
none	2.63	2.57	1.73	8.15
low	2.66	2.84	1.93	7.39
medium	3.68	5.27	1.66	4.75
high	13.4	15.9	3.52	19.4

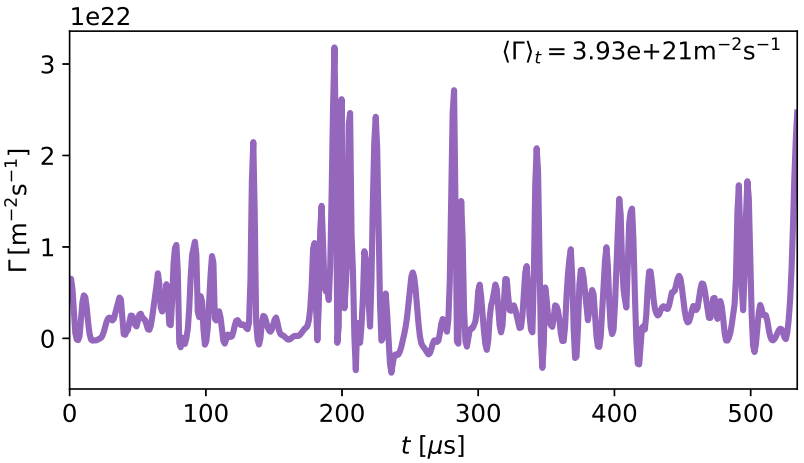

Figure 4.3: Radial particle flux across LCFS for self-consistent fuelling from neutrals at puffing rate $\Gamma_{\text{puff}} = 2 \cdot 10^{21}\,\text{m}^{-2}\text{s}^{-1}$.

$2 \cdot 10^{21}\,\text{m}^{-2}\text{s}^{-1}$. In the paper, it is mentioned that fuelling at this rate results in a vanishing average contribution from the forcing to the fuelling in the edge, and the density forcing can thus be entirely removed, so that the fuelling depends only on local ionization of neutrals in the simulated domain. Figures 6-8 of the paper are reproduced for the case, where the neutrals self-consistently fuel the edge region locally.

In Fig. 4.3 the radial flux across the LCFS is shown. The appearance of the flux is visibly similar to those in Fig. 6 of the paper. The average radial flux of $\langle\Gamma\rangle_t = 3.93 \cdot 10^{21}\,\text{m}^{-2}\text{s}^{-1}$ is lower, but in the same range, as those resulting from the simulations with forcing. This hints, that the flux resulting from maintaining the density in the edge is not only dependent on the edge density, but also on the shape of the density source.

Figure 4.4 shows the corresponding PDF for the radial flux across the LCFS, and in Tab. 4.2 the statistical descriptors are provided. Comparing the shape of the PDF in Fig. 4.4 to those presented in the paper Fig. 7, one observes good consistency between the simulations with and without density forcing in the edge region. The significant broadening of the PDF observed for the higher gas-puffing schemes is, however, absent for the simulation with self-consistent fuelling, which may also explain the lower average radial particle flux across the LCFS. The other descriptors in are also more similar to those for a lower puffing rate, although the inwards flux of molecules to the system for this simulation is higher than the 'medium' case for the paper.

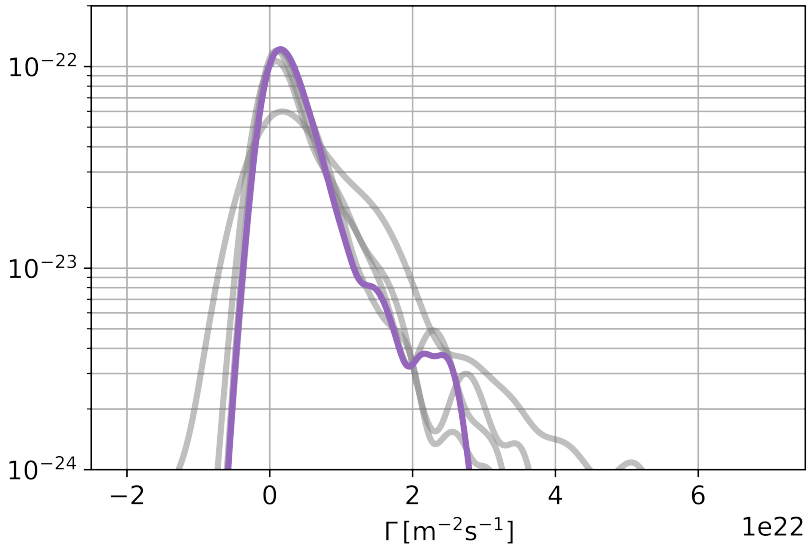

Figure 4.4: Probability density of the flux across LCFS for self-consistent fuelling from neutrals at puffing rate $\Gamma_{\text{puff}} = 2 \cdot 10^{21}\,\text{m}^{-2}\text{s}^{-1}$. The PDFs from the simulations in the paper are outlined for comparison. Descriptors for the PDF are given in Tab. 4.2.

Table 4.2: Mean, standard deviation, skewness and kurtosis for the PDF of the radial particle flux across the LCFS for a simulation where fuelling is entirely from local ionization of neutrals.

Γ_{puff} $[10^{21}\,\text{m}^{-2}\text{s}^{-1}]$	mean $[10^{21}\,\text{m}^{-2}\text{s}^{-1}]$	standard dev. $[10^{21}\,\text{m}^{-2}\text{s}^{-1}]$	skewness	kurtosis
2	3.93	5.24	2.17	8.66

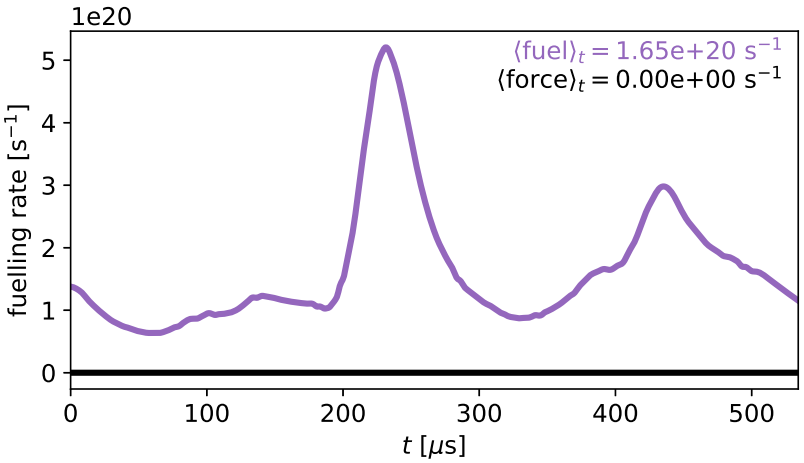

Figure 4.5: Fuelling in the edge for self-consistent fuelling from neutrals at puffing rate $\Gamma_{\text{puff}} = 2 \cdot 10^{21}\,\text{m}^{-2}\text{s}^{-1}$. The black curve at constant zero show that no forcing is applied to maintain the density in the inner edge region. The amount of fuelling provided by ionization of neutrals is shown by the coloured curve.

Finally the plot of the fuelling as a function of time, i.e., Fig. 8 of the paper is shown for the self-consistent fuelling simulation in Fig. 4.5. Here the plot is again qualitatively similar to those in the paper, with the difference that the fuelling from density forcing in the edge is now zero throughout the simulation. The average fuelling rate of $\langle \text{fuel} \rangle_t = 1.65 \cdot 10^{20}\,\text{s}^{-1}$ is comparable to the values of total average fuelling shown in Fig. 8 in the paper, and is constituted entirely of local ionization of neutrals.

As discussed in the paper, fuelling only from local ionization in the edge region of the out-board mid-plane is computationally possible, but it is questionable if it physically corresponds to the fuelling process in a tokamak experiment. In reality fuelling is most likely not evenly distributed across the edge region, and more particles may enter the bulk plasma near the colder x-point region. Moreover, the effect of fuelling from recycled neutrals is not included in this analysis, although they may constitute the majority of the fuelling rate, depending on the wall material.

4.3 Influence of molecular dissociation on blob-induced atom density perturbations

4.3.1 Prelude

In this paper, the focus has been put on the response of neutral densities to a perturbation in the plasma pressure in the SOL. This study is in particular relevant for calculations related to the gas puff imaging technique, which is a SOL and edge diagnostic.

For the GPI diagnostic a neutral gas is puffed into the vacuum chamber. Energetic electrons excite the atoms in the gas, which subsequently decay to lower excited states under emission of photons. The emitted photons are captured by fast cameras at various locations. The intensity I of the emitted light is approximated by

$$I = n_{\mathrm{e}} n_{\mathrm{n}} r_{\mathrm{emit}} \,, \tag{4.2}$$

where n_{e} is the electron density, n_{n} is the density of the puffed neutrals, and r_{emit} is the emission rate coefficient, which depends on the electron density and temperature. Multiple fast cameras at various locations allow for temporal and spatial resolution of the intensity, and various characteristics of SOL structures, such as the density, temperature, velocity, width, etc., can thus be calculated, aided by measurements of the plasma fields by other techniques.

In GPI calculations the neutral density is often assumed constant, as this is difficult to measure by other diagnostics. It is, however, clear from, e.g., Sec. 4.2, that there is a large gradient in the neutral SOL density for the thermal neutrals. But even accounting for that by including a neutral background with a finite gradient will often result in incorrect estimates for n_{n}. In [64, 98] it is shown, that the elevated electron pressure in a blob results in a local depletion of the atom density, since the ionization rate increases with blob pressure, and neutrals are thus ionized in the blob. This effect leads to underestimating the average neutral density when calculated from (4.2) as the signal originates from the volume of depleted neutral density.

Since the evolution of neutral and plasma fields is calculated dynamically in the nHESEL model, and in a region relevant to GPI imaging, it is an ideal

environment to asses the effect of blobs on neutral densities. The nHESEL model does in particular offer new information on the subject, as it also includes molecules, which prove to play a crucial rule to the perturbation of the deuterium atom density. It is found, that for neutrals that are under the same conditions as those investigated in [64, 98], the resulting perturbations to the neutral densities are in agreement. For deuterium atoms originating from dissociated molecules, however, the particle source is shown to exceed the ionization sink, leading to perturbations in the atom density of opposite sign of that for neutrals, that do not originate from dissociation. This effect is shown to possibly be present in the whole SOL, and thus relevant when assuming a neutral density for GPI calculations.

The numerical setup is similar to that used in Sec. 4.2, with the addition of an auxiliary neutral density of thermal helium atoms. The helium species is passive in the sense, that it changes according to sinks from interactions with plasma, but the corresponding source terms are not present in the plasma field equations.

The paper only considers a single blob-event. A more generic analysis, including scans in neutral densities, and electron and ion density and temperatures would allow for a more quantitative assessment of the response of the neutral density to blobs. It would also be an obvious move to implement a synthetic GPI diagnostic on top of the code, to asses the effect of the perturbations on the emitted light. The purpose of the paper is to add to the discussion on use of static neutral profiles in GPI calculations the possible effect that sources from dissociation of molecules may have on the atom density perturbation, for which neither a parameter scan, nor a synthetic diagnostic, is required. Those have thus been left for future studies in order to focus the content of the paper.

The paper was submitted for publication in *Nuclear Fusion* on 24 March 2018.

Influence of molecular dissociation on blob-induced atom density perturbations

A.S. Thrysøe, J. Madsen, V. Naulin, and J. Juul Rasmussen

PPFE, Department of Physics, DTU, DK-2800 Kgs, Lyngby, Denmark

E-mail: alec@fysik.dtu.dk

21 March 2018

Abstract. The effect of enhanced electron and ion pressure perturbations mediated in filamentary structures (blobs) on the densities of neutral atoms and molecules are investigated through a self-consistent dynamical fluid model for plasma and neutral fields. The electron and ion densities and pressures, and the generalized vorticity, are simulated by a 2D drift-fluid model in an edge and scrape-off layer slab domain of a toroidally magnetically confined plasma. The plasma dynamics are coupled with a diffusion model for densities of neutral atoms and molecules. The combined model allows for determining the response of the density of neutrals with various energies to blobs. It is found that blobs locally deplete densities of molecules and atoms that do not originate from dissociation of molecules, whereas the density of atoms created by dissociation may increase during blob events. The neutral species, their temperature, and origin should thus be taken into consideration when estimating the effect of blobs on neutral density perturbations when calculating emission rates, e.g., for gas puff imaging.

1. Introduction

The conditions in the edge and scrape-off layer (SOL) regions of magnetically confined plasmas contribute significantly in determining the overall confinement properties, as they function as boundary conditions for the confined plasma [1]. The edge and SOL regions are separated by the last-closed-flux-surface (LCFS), across which the outwards transport of particles and energy is known to be highly intermittent. In the SOL the plasma is mainly transported in field-aligned structures of enhanced electron and ion

pressure, known as blobs, which are formed near the LCFS and propagate radially outwards [2, 3].

The spatial structure of blobs can be observed using the gas puff imaging (GPI) technique [4, 5, 6]. Neutral gas, for example hydrogen isotopes or helium, is puffed into the SOL, and the electrons from the blob excite the atoms, which emit radiation in the visible spectrum. Fast cameras monitor the location and magnitude of radiation, and the data allows for deriving information about the magnitude and location of the electron density and temperature fields. In the GPI calculations it is common to assume a static background of neutral particles. However, in recent papers [7, 8, 9] this assumption has been questioned, and simulations reveal an anti-correlation between the electron pressure and neutral atom density, caused by the ionization of atoms.

In this paper it is investigated how the density of neutral particles respond to a blob through a self-consistent 2D model, with dynamical plasma and neutral fields. The neutrals consist of both deuterium molecules, which are puffed into the system, and deuterium atoms originating from dissociation of the molecules. This model is explained in detail in [10]. In addition to this, a passive species of helium atoms is simulated to highlight the difference between neutral atoms that are created from dissociation of molecules in the chamber, and those which enter the system as atoms.

It is found that densities of thermal molecules and atoms which do not originate from dissociative processes behave as reported in [7, 8], i.e., the neutral density decreases locally due to interactions with the electrons in the filament. The density of atoms from dissociated molecules, however, displays an opposite behaviour if the reaction rate for dissociation of molecules is bigger than that for ionization of atoms, which is the case for the SOL region for the results presented here. The implications for GPI calculations are that the temperature of the neutral gas, as well as the origin of the neutral atoms, dictate the magnitude, extend, and sign of the neutral density perturbation during interactions with blobs.

2. Correlated perturbations in the scrape-off layer

The reaction rate R for electron impact reactions with neutrals have the general form

$$R = n_{\mathrm{e}} n_{\mathrm{n}} r(n_{\mathrm{e}}, T_{\mathrm{e}}) \,, \tag{1}$$

where n_{e} is the electron density, n_{n} is the density of the neutral species, and $r(n_{\mathrm{e}}, T_{\mathrm{e}})$ is the reaction rate coefficient which can often be parametrized as a function of electron density and temperature (see e.g. [11]). It is common practice to decompose the field

into a mean field term and a fluctuating therm, i.e.,

$$f = \langle f \rangle + \Delta f \,, \tag{2}$$

for $f = n_\mathrm{e}, T_\mathrm{e}, n_\mathrm{n}$. The implications of approximating the electron density and temperature fields in the SOL region with their average value when calculating (1) are discussed in [12, 13]. Ignoring the fluctuations result in a significant difference when calculating reaction rates for blobs due to the correlation between Δn_e and ΔT_e. Recently, the error resulting from assuming a static neutral density when calculating emission rates have been studied as well [7, 8]. Both papers draw attention to the fact that the neutral density perturbation anti-correlates with that of the electron density, as the two are coupled trough the ionization process

$$\mathrm{A} + \mathrm{e} \rightarrow \mathrm{A}^+ + 2\mathrm{e} \,, \tag{3}$$

where A is an atomic species such as helium He (as for [7]) or deuterium D (as for [8]). The ionization process implies that for structures with enhanced electron pressure, such as blobs, the amount of neutrals is expected to decrease and the amount of electrons and ions increases, effectively anti-correlating Δn_n with Δn_e, ΔT_e.

The importance of including molecules in addition to the atomic species for which the emission is experimentally measured is supported by the dominant interactions

$$\begin{aligned} &\mathrm{D}_2 + \mathrm{e} \rightarrow 2\mathrm{D} + \mathrm{e} \,, && \mathrm{D} + \mathrm{e} \rightarrow \mathrm{D}^+ + 2\mathrm{e} \,, \\ &\mathrm{D}_2 + \mathrm{e} \rightarrow \mathrm{D}_2^+ + 2\mathrm{e} \rightarrow \mathrm{D} + \mathrm{D}^+ + 2\mathrm{e} \,, && \mathrm{D} + \mathrm{D}^+ \rightarrow \mathrm{D}^+ + \mathrm{D} \,, \end{aligned} \tag{4}$$

which are expressed in the deuterium atom density source term

$$S_\mathrm{D}^n = n_\mathrm{e} n_{\mathrm{D}_2} [2 r_\mathrm{dis}(T_\mathrm{e}) + r_\mathrm{m.iz}(T_\mathrm{e})] - n_\mathrm{e} n_\mathrm{D} r_\mathrm{iz}(T_\mathrm{e}) \,, \tag{5}$$

where n_{D_2} is the density of deuterium molecules, n_D is the density of deuterium atoms, r_dis is the molecule dissociation reaction rate, $r_\mathrm{m.iz}$ is that for molecular assisted ionization, and r_iz is the ionization rate coefficient for deuterium atoms. All reaction rates are parametrized in terms of T_e according to [11]. For the interactions in (4) involvining D_2 and D_2^+, there is a finite probability that some of the resulting atoms are born in an excited state, and thus emit a D-alpha photon without a prior electron impact collision. This dissociation path is well known, see e.g. [14], and result in overestimating the deuterium atom density in GPI calculations. Excited atomic states are, however, not included in the model. The first term of (5) results from the molecule sink term

$$S_{\mathrm{D}_2}^n = -n_\mathrm{e} n_{\mathrm{D}_2} [r_\mathrm{dis}(T_\mathrm{e}) + r_\mathrm{m.iz}(T_\mathrm{e})] \,, \tag{6}$$

and the second term in (5) is the electron impact ionization of atoms. For a model with only atoms, only the last term of (5) persists, and the neutral density source is always negative, resulting in the anti-correlation between the atom density and the electron

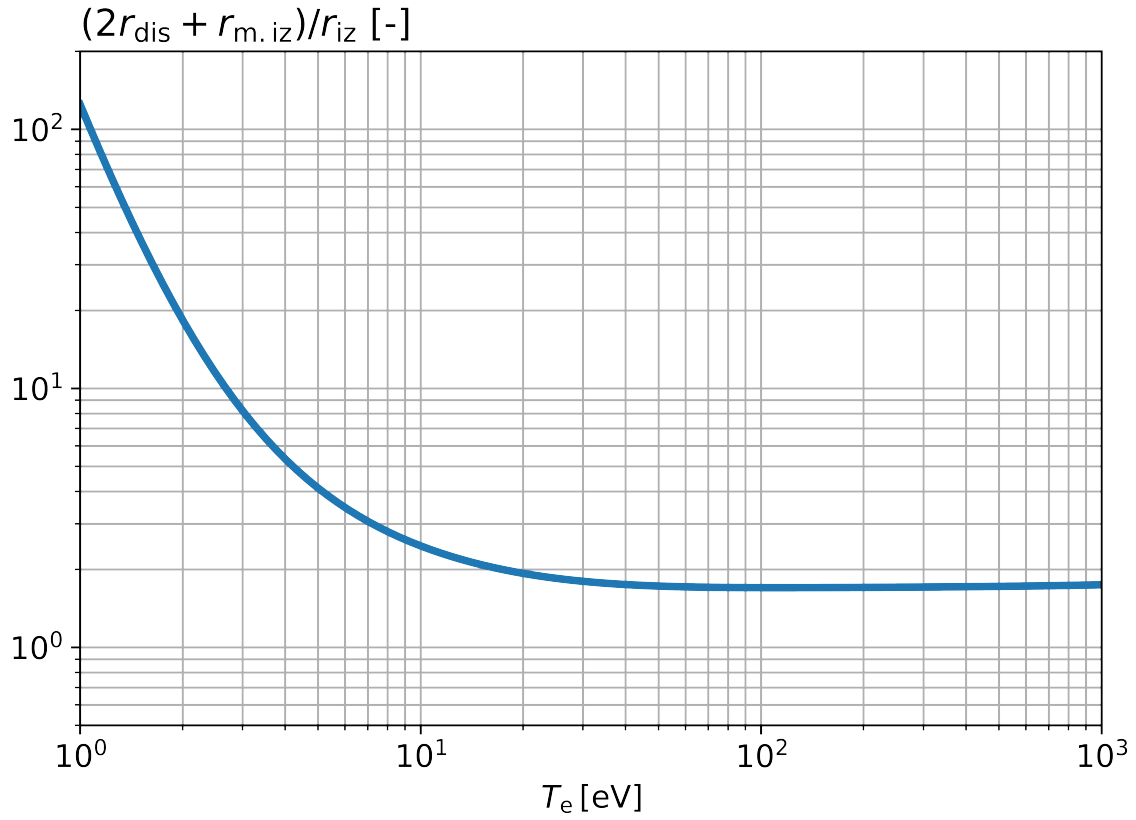

Figure 1. The ratio of the reaction rate coefficients for creation of neutral atoms by dissociation and molecular assisted ionization, to that for removal of neutral atoms by ionization, as a function of electron temperature. It is observed that for all temperatures, the ratio larger than one.

density as observed in [7, 8]. For the source of deuterium atoms in (5), however, the sign is determined by the ratio of the absolute value of the two terms

$$\eta = \frac{n_{\mathrm{e}} n_{\mathrm{D}_2} [2r_{\mathrm{dis}}(T_{\mathrm{e}}) + r_{\mathrm{m.iz}}(T_{\mathrm{e}})]}{n_{\mathrm{e}} n_{\mathrm{D}} r_{\mathrm{iz}}(T_{\mathrm{e}})} = \frac{n_{\mathrm{D}_2}}{n_{\mathrm{D}}} \frac{2r_{\mathrm{dis}}(T_{\mathrm{e}}) + r_{\mathrm{m.iz}}(T_{\mathrm{e}})}{r_{\mathrm{iz}}(T_{\mathrm{e}})}\,, \tag{7}$$

which dictates that the atom source term is negative for $0 < \eta < 1$ and positive for $\eta > 1$. The last fraction in (7), i.e., the ratio of the reaction rates, is plotted in Fig. 1. It is observed that for all relevant energy scales this factor is larger than one, and increases rapidly for smaller electron energies below 10 eV. Thus, for regions where the neutral molecule density is sufficiently high, perturbations to the electron pressure result in a positive perturbation of the neutral atom density.

3. Numerical model

The effect of blobs on the neutral density is investigated numerically through a combined plasma and neutral fluid model. The plasma module solves the HESEL [15, 16] four-field drift-fluid model for the electron/ion density, electron and ion pressures, and the generalized vorticity. The neutral module solves a three-field diffusion model, which has a thermal D_2 molecule species, and two more energetic atomic D species to include both the Franck-Condon atoms produced from dissociation and those energized by atomic charge exchange collisions with ions. The plasma and neutral modules are coupled through the source terms, and the plasma and neutrals interact self-consistently through molecule dissociation, molecular assisted ionization, atomic ionization, and atomic charge exchange collisions with ions, i.e., the interactions in (4). The combined neutral-plasma model is described in detail in [10].

In addition to the neutral deuterium species described in the model in [10], a passive fluid model for neutral helium gas has been added to the code. The transport equations for the helium density is identical to that of D_2, as the mass and temperature of the particles are assumed to be the same, i.e.,

$$\partial_t n_{\mathrm{He}} - \nabla \cdot (D_{\mathrm{He}} \nabla n_{\mathrm{He}}) = S^n_{\mathrm{He}} \,, \tag{8}$$

with $D_{\mathrm{He}} = D_{\mathrm{D}_2}$, and the source term

$$S^n_{\mathrm{He}} = -n_{\mathrm{e}} n_{\mathrm{He}} r_{\mathrm{iz,He}}(T_{\mathrm{e}}) \,, \tag{9}$$

and where $r_{\mathrm{iz,He}}$ is the ionization reaction rate coefficient for helium in the ground state, for which the parametrization in terms of T_{e} is found in [11]. The source term (9) is calculated according to the dynamical helium density, and electron density and temperature fields, but information from interactions with helium does not feed back into the drift-fluid equations for the plasma fields as is the case for the other neutrals.

The full model is implemented in the BOUT++ framework [17], and the equations are solved in a 2D slab perpendicular to the magnetic field lines at the outboard mid-plane. The domain overlaps both parts of the edge and SOL regions, and has dimensions of $225 \times 75\, \rho_{\mathrm{s}}^2$. In the poloidal y-direction the boundaries are periodic, and at the inner edge boundary, the conditions are for the generalized vorticity $\omega = 0$, density $n = 1.5 n_0$, and electron and ion pressures $p_{\mathrm{e}} = 2p_{\mathrm{i}} = 10\, n_0 T_{\mathrm{e}0}$. At the outer boundary, the conditions are $\partial_x n = \partial_x p_{\mathrm{e,i}} = \omega = 0$, where x is the radial direction. The normalization values are

$$\begin{aligned} \Omega_{\mathrm{ci}} &= 9.57 \cdot 10^7\, \mathrm{s}^{-1} \,, & \rho_{\mathrm{s}} &= 3.23 \cdot 10^{-4}\, \mathrm{m} \,, \\ n_0 &= 1.5 \cdot 10^{19}\, \mathrm{m}^{-3} \,, & T_{\mathrm{e}0} &= 20\, \mathrm{eV} \,, \end{aligned} \tag{10}$$

which correspond to typical parameters for a medium-sized tokamak [16]. The neutral density fields for the atomic deuterium atoms (n = warm, hot), the deuterium molecules

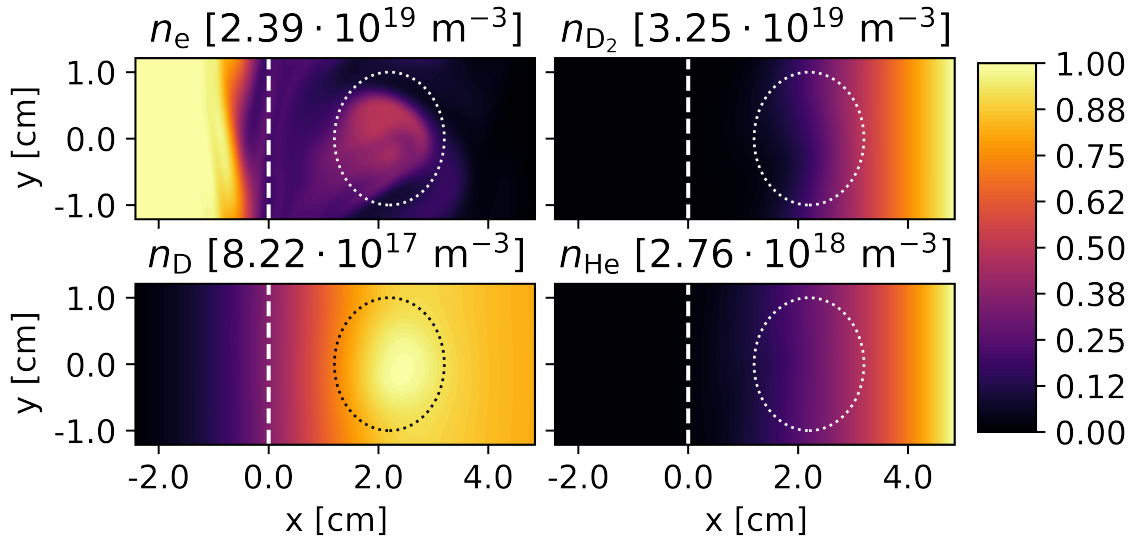

Figure 2. Normalized electron density, deuterium molecule density, deuterium atom density, and helium atom density during a blob. The blob is clearly observable from the electron density, whereas perturbations to the neutral densities are relatively smaller. The dotted straight line is the last closed flux surface, and the circle is inserted as a reference for the blob position in this and the following figures.

($\mathrm{n} = \mathrm{D}_2$), and helium atoms ($\mathrm{n} = \mathrm{He}$) satisfy

$$-D_\mathrm{n}\partial_x n_\mathrm{n} = \sqrt{-\frac{D_\mathrm{n} S'_\mathrm{n}}{n_\mathrm{n}}}\, n_\mathrm{n}\,, \tag{11}$$

at the inner boundary, and

$$-D_\mathrm{n}\partial_x n_\mathrm{n} = -\gamma\sqrt{-\frac{D_\mathrm{n} S'_\mathrm{n}}{n_\mathrm{n}}}\, n_\mathrm{n} + \Gamma_{\mathrm{n,puff}}\delta_{\mathrm{n},(\mathrm{D}_2,\mathrm{He})}\,, \tag{12}$$

at the outer boundary, where S'_n are the source terms that are proportional to n_n. The parameters used for the neutral fields are

$$\begin{aligned} D_\mathrm{hot} = 10^1 D_\mathrm{warm} = 10^3 D_{\mathrm{D}_2} = 10^2 \rho_\mathrm{s}^2 \Omega_\mathrm{ci}\,, \qquad & \Gamma_{\mathrm{D}_2,\mathrm{puff}} = 1\cdot 10^{21}\,\mathrm{m}^{-2}\mathrm{s}^{-1}\,, \\ \gamma = 0.2\,, \qquad & \Gamma_{\mathrm{He,puff}} = 1\cdot 10^{20}\,\mathrm{m}^{-2}\mathrm{s}^{-1}\,, \end{aligned} \tag{13}$$

and the atomic deuterium density reported here is related to that of the deuterium warm and hot subspecies by $n_\mathrm{D} = n_\mathrm{warm} + n_\mathrm{hot}$.

A snapshot of the densities during a blob is shown in Fig. 2. Here the atom density is the sum of the two distinct (warm and hot) deuterium atom fluid densities at different temperatures, whereas the density of helium atoms is shown separately.

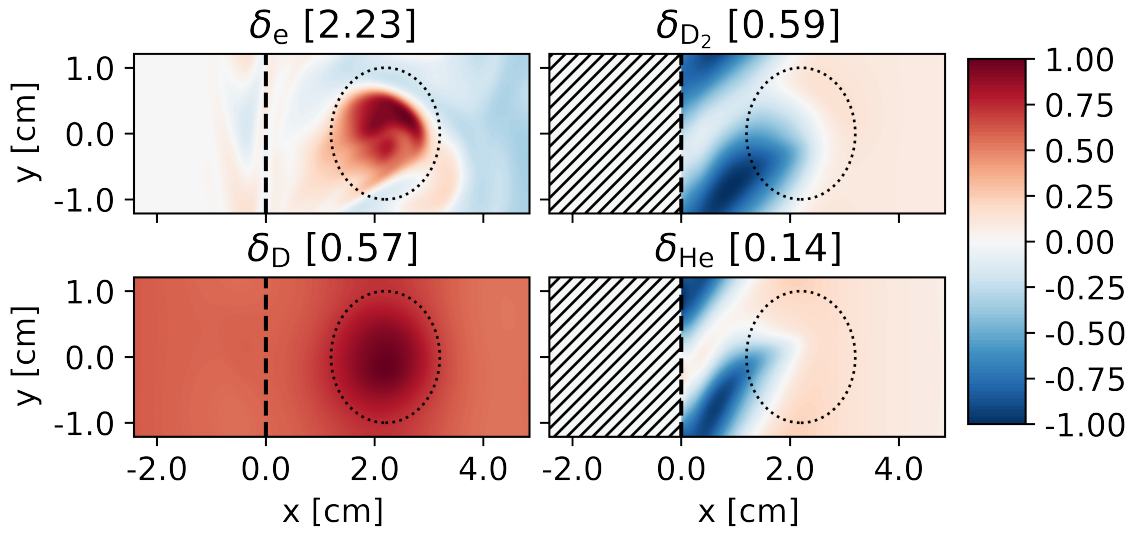

Figure 3. Deviation of the electron and neutral densities from their temporal mean values. The blob result in a negative perturbation in the thermal deuterium molecule and helium atom densities, and a positive perturbation in the deuterium atom density. The data for the thermal neutrals in the shaded areas are excluded, as the neutral density here is so low that the relative fluctuations outshine those resulting from the blob interactions.

4. Neutral response to blob

The impact of the blob on the neutral densities is slightly visible from Fig. 2, and the relative deviation from the temporal mean

$$\delta_\sigma = \frac{n_\sigma - \langle n_\sigma \rangle_t}{\langle n_\sigma \rangle_t}, \tag{14}$$

for $\sigma = \mathrm{e}, \mathrm{D}, \mathrm{D}_2, \mathrm{He}$ is shown in Fig. 3. Here $\langle n_\sigma \rangle_t = \frac{\int \mathrm{d}t\, n_\sigma}{\int \mathrm{d}t}$ is the temporal average of the density of σ. The blob induce a negative perturbation to the thermal neutral deuterium molecule and helium densities, and a positive perturbation to the deuterium atom density. The perturbation to the deuterium atom density is of similar amplitude to that of molecules, but the effect is visible in the whole domain. The perturbation to the molecule density is much more localized, and the trail remains visible after the blob has moved further outwards. Thermal transport time-scales are much larger for the thermal species than those for deuterium atoms, which is the reason why the 'footprint' of the blob remains in deuterium molecule and helium atom densities, but not in the deuterium atom density. For helium atoms, the perturbation is also of smaller amplitude, as the ionization energy for helium is several times larger than the dissociation energy for deuterium molecules, and thus less helium atoms are ionized than molecules are dissociated under the same conditions.

The influence of plasma pressure perturbations, e.g. in blobs, on the neutral atom density thus depends on several factors. It is observed, that it makes a difference whether the atoms are injected directly into the system (as for He), or if they originate from dissociation of molecules (as for D). For the latter case, the source of atoms due to dissociation of molecules may be larger than the sink due to ionization, resulting in a positive correlation with the electron density perturbations. Whether this is the case depend on the ratio of molecules to atoms, and on the electron temperature. However, if the ratio of molecules to atoms, $n_{\mathrm{D}_2}/n_{\mathrm{D}}$ is above 0.58, this will always be the case. Secondly, the temperature of the neutrals determines how local the response to the electron pressure perturbation is. If the neutrals are thermal, the equalization of a depletion or enhancement of the density is slow and the effect of the blob is more local. If the neutrals are warmer, such as those created by dissociation or charge exchange collisions, the perturbation is more localized in time.

The value of η defined in (7) is shown for the whole domain in Fig. 4. It is observed that the value of η is larger than one in most of the SOL, and that the blob brings this value closer to unity as expected from Fig. 1, and because increased plasma density remove molecules and create atoms. Note that the value of the source ratio η only determines the sign, and not the magnitude, of the perturbation. Thus, for blobs pushing η closer to unity still result in an enhanced perturbation, since the magnitude of the sources increase with the blob pressure. Although the effects of a single blob created from one set of plasma and neutral input parameters is studied, the results are expected to reproduce well in the range of realistic SOL pressures. At lower temperatures, less molecules are removed, and the ratio of the reaction rate coefficients shown in Fig. 1, increases drastically, which increases η and enhance the positive response of the neutral density to blobs reported here. Higher pressures may result in a lower η. At higher temperatures, the ratio of the reaction rate coefficients in Fig. 1 retains a value of approximately 1.7, but a decrease in the density of D_2 as a result of enhanced electron pressure, causes the value of η to decrease as well. This is the case to the left of the solid line in the edge region in Fig. 4, and for higher edge pressures blobs drag the line further into the SOL region, as a result of the increased depletion of D_2.

The simulated thermal helium density shows a behaviour similar to that observed for neutral atoms in [7, 8], and thus the conclusion on the effect of assuming a constant neutral background in calculations based on GPI measurements is the same. That is, the neutral atoms anti-correlate with the electron pressure perturbations, and when calculating reaction rates of the form in (1) the product is therefore overestimated if a static neutral density is assumed. The results for the density of non-thermal neutral atoms that originate from dissociation of molecules, however, may have a much lower, or even the opposite, effect for GPI if this is based on radiation of such atoms, which for example is the case for atomic D-alpha measurements.

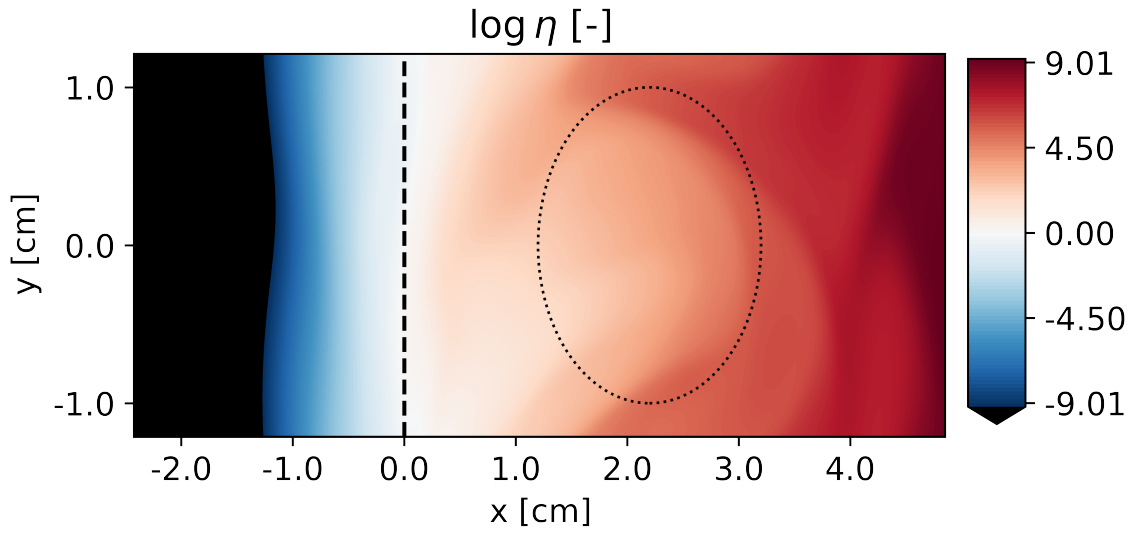

Figure 4. The logarithm of the ratio of creation of neutral atoms to that of ionization of neutral atoms η, defined in Eqn. (7). The ratio is larger than one in most of the SOL region.

5. Conclusions

The effect of electron pressure perturbations mediated in blobs on the densities of neutral atoms and molecules in the SOL is investigated by a numerical model. The densities of the neutrals and of the electrons are strongly coupled through in-elastic sources, and perturbations in the electron pressure result in an immediate perturbation to the neutral density.

The neutral density response to blobs is investigated by a coupled neutral-plasma model, that self-consistently describe the interplay between neutral densities, and the turbulent density and pressure fields of electrons and ions. The neutral part of the model describes the evolution of deuterium atom and molecule densities, as well as that of a passive helium species.

For molecules, the blob induced perturbation anti-correlates with that for electron density, which result in increased magnitude of the molecule density sink terms. The same is the case for atoms, that do not originate from dissociation of molecules (e.g. helium atoms). However, for atoms that are created from dissociative processes the density perturbation can correlate with that of the electron pressure, as more atoms are created from dissociation of molecules than removed by ionization.

The response of the atom densities to blobs is important when interpreting atomic emission, e.g., GPI, measurements, since assuming a constant neutral background

will either lead to over- or under-estimating the magnitude of the electron pressure perturbation, depending on the SOL conditions and on the origin of neutrals. Thus, when correcting for the neutral density mean-field approximation, one should also take those parameters into account.

6. Acknowledgements

The authors thank Eduardo de la Cal for insightful discussions on neutral density perturbations and sources of D-alpha radiation.

This work has been carried out within the framework of the EUROfusion Consortium and has received funding from the Euratom research and training programme 2014-2018 under grant agreement No 633053. The views and opinions expressed herein do not necessarily reflect those of the European Commission.

7. References

[1] A. Loarte, et al., Nucl. Fusion **47** S203, (2007)
[2] S.J. Zweben, et al., Plasma Phys. Control. Fusion **49**, S1 (2007)
[3] D.A. DIppolito et al., Physics of Plasmas **18**, 060501 (2011)
[4] J.L. Terry, et al., J. Nucl. Mater. **290** 757, (2001)
[5] S.J. Zweben, et al., Physics of Plasmas **9** 1981, (2002)
[6] R.J. Maqueda, et al., Review of Scientific Instruments **74** 2020, (2003)
[7] E. de la Cal and The TJ-II Team, Nucl. Fusion **56**, (2016)
[8] C. Wersal and P. Ricci, Nucl. Fusion **57**, (2017)
[9] D. Moulton, et al., J. Nucl. Mater. **463** 893, (2015)
[10] A. Thrysøe, et al., Physics of Plasmas **25**, 032307 (2018)
[11] R.K. Janev, et al., *Elementary Processes in Hydrogen-Helium Plasmas*, Berlin: Springer-Verlag, (1987)
[12] E. Havlíčková, et al., J. Nucl. Mater. **415** (2011) S4714
[13] A. Thrysøe, et al., Plasma Phys. Control. Fusion **58**, (2016) 044010
[14] E. de la Cal, et al., Nucl. Fusion **48**, (2008)
[15] J. Madsen, et al., Physics of Plasmas **23**, 032306 (2016)
[16] A.H. Nielsen, et al., Plasma Phys. Control. Fusion **59**, 025012 (2017)
[17] B.D. Dudson, et al., Computer Physics Communications **180** (2009), pp. 1467-1480

4.3.3 Postlude

The paper presented in this section is somewhat more narrow topic wise, than the former two. The ties to the other papers are, however, strong as the discussion of the effect of molecular dissociation on the atomic density is relevant for all density source related results. In Section 4.1 it was, aided by the results in *The influence of blob intermittency on fuelling*, discussed how the inwards flux of neutral atoms across the LCFS actually increases following blobs, as an effect of molecular dissociation.

The effects of the blob induced fluctuations on experimental measurements, such as GPI is, however, unique to this paper, and leaves room for a more elaborate discussion than what is provided in the paper. In particular it is asserted how including a dynamical description of the neutrals influences the **light emission from blobs**. The dynamic reaction rate

$$S_\sigma = n_\mathrm{e} n_\sigma r_\rho(T_\mathrm{e})\,, \tag{4.3}$$

is compared to that with static neutrals

$$S^*_\sigma = n_\mathrm{e} \langle n_\sigma \rangle_t r_\rho(T_\mathrm{e})\,, \tag{4.4}$$

where $\sigma = \mathrm{D}, \mathrm{He}$, and r_ρ is the reaction rate coefficient for that reaction which brings the atom to the excited state, from which it emits light under de-excitation. It is not straightforward to include physical effects such as a finite decay time in the present model, and the reaction rates from ground state to the relevant excited state are thus used as proxies for the more accurate reaction rates. Here we consider the excitation of deuterium from the ground state to the $n = 3$ state, from which it emits D_α radiation, which is a commonly observed spectral line in tokamak experiments. For helium the $(1\mathrm{s}^2|^1\mathrm{S}) \rightarrow (1\mathrm{s}2\mathrm{p}|^1\mathrm{P})$ transition is used.

The reaction rates that proxies for the emission rates in (4.3) and (4.4) are shown at the same time instance as is studied in the paper in Fig. 4.6 for deuterium and helium. Several observations are made from this figure. The signal from helium only reveals the blob, and not the edge region, as is the case for emission from deuterium atoms. The reason for this is found in Fig. 2 in the paper, which shows that due to the higher temperature, the deuterium atoms penetrate the SOL much more efficiently, which allows for resolving the edge region as well. Secondly, the difference in the cross-sections of the two reactions results in different pictures of the blob, of which

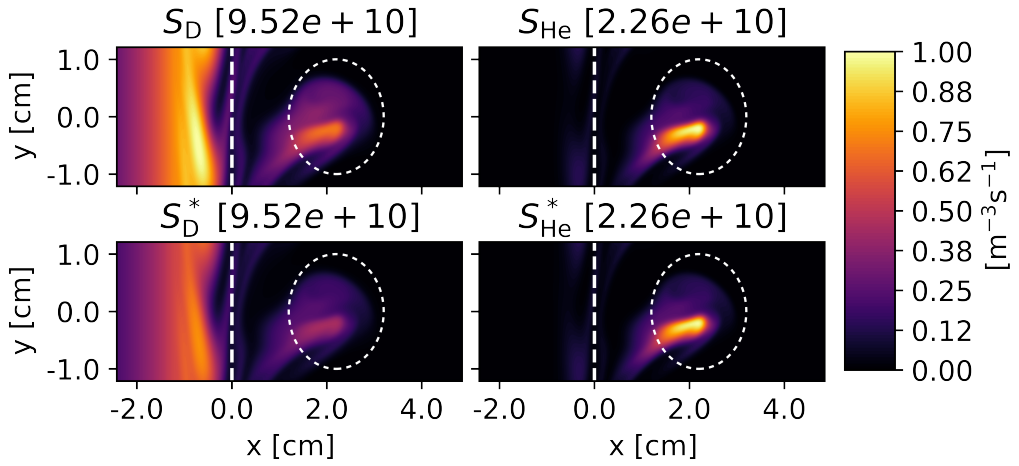

Figure 4.6: The reaction rates for the $(n = 1) \rightarrow (n = 3)$ state for deuterium (left), and for the $(1s^2|^1S) \rightarrow (1s2p|^1P)$ state for helium (right), as a proxy for the emission intensity. The top row show the emission with dynamic neutrals, and the bottom row with static neutrals. The plots are normalized with the values in square brackets.

the helium emission seems to be more localized at the hotter core of the blob. Finally, the effect of averaging the neutral densities is more pronounced for deuterium, which most likely results from having a lower excitation energy and thus a larger fluctuation response in the density.

The error in the calculated emission by assuming a static neutral background is quantified by the relative difference of S_σ from S_σ^*, i.e.,

$$\delta_\sigma^* \equiv \frac{S_\sigma - S_\sigma^*}{S_\sigma^*} = \frac{n_\sigma - \langle n_\sigma \rangle}{\langle n_\sigma \rangle}\,, \tag{4.5}$$

which are plotted for deuterium and helium in the lower row of Fig. 3 in the paper. As is suggested in the paper, assuming a static neutral background results in an overestimation of the actual average neutral density for deuterium, and an underestimation of that for helium.

4.4 Conference papers

This section presents published, non-peer reviewed, conference papers for the 42^{nd}- 44^{th} European physical society (EPS) conferences on plasma physics. The three papers deal with various aspects of neutral-plasma interactions, and in addition to the reported observations, the papers reflect the progress towards developing the combined plasma-neutral model described in Chpt. 2.

In the earliest paper, titled *The influence of hot neutrals in simulations of gas puff modulation*, the effect of including hot neutral atoms originating from charge-exchange collisions in a 1D radial neutral model is examined. The neutrals enter the plasma in a manner where the puffing rate is modulated to simulate an experiment in which gas puff modulation was applied. This allows for tracking the phase shift and the amplitude resulting from enhanced ionization, and for observing the changes as a function of radial position. It is found that including hot neutral atoms weakly influences the phase shift, but has a high impact on the amplitude of the perturbation. The results were presented on a poster at the 42^{nd} EPS conference on plasma physics.

The second conference paper, *Simulation of neutrals in a turbulent scrape-off layer*, presents another predecessor to the nHESEL model, where molecules are included, but only the density source term feeds back into the HESEL equations. In the paper the neutral transport equations are presented, and the resulting plasma density source from ionization of neutrals is discussed. The need of hot atomic species to penetrate the edge region is re-established, and the possibility of fuelling the plasma entirely by local ionization of neutrals (as was done in the paper presented in Sec. 4.2) is pondered upon. The results were presented in an oral at the 43^{rd} EPS conference on plasma physics, and highly recommended for the Itoh Project Prize 2016.

The last paper, titled *The influence of blob intermittency on fuelling*, treats the effect of blobs on the fuelling rate. The model is here the complete nHESEL model, and the integrated density source in the edge and SOL regions is monitored in order to assess the response of the fuelling rate to blobs. The results again confirm, that the warmer atomic species are essential for fuelling the edge region, but also highlight the importance of dissociation of molecules as a source of neutral atoms. It is found that the fuelling is increased following a blob event, as more neutral atoms are created from dissociation than removed by ionization in the blob. The results were presented on a poster at the 44^{th} EPS conference on plasma physics.

The influence of hot neutrals in simulations of gas puff modulation

A.S. Christensen[1], J. Madsen[1], V. Naulin[1], J.J. Rasmussen[1],
A. Salmi[2], L.E.H. Tophøj[1] and JET contributors[*3]
[1]*PPFE, DTU Physics, Technical University of Denmark, Denmark,* [2]*VVT, Espoo, Finland,*
[3]*EUROfusion Consortium, JET, Culham Science Centre, Abingdon, OX14 3DB, UK*

Introduction

Experiments utilizing the gas puff modulation technique have been carried out in JET for the purpose of studying plasma fueling as well as particle transport [1]. It is of great interest to simulate such experiments, as this allows for deeper insight in the mechanics that determines the fueling rate when applying gas puffing, as well as providing knowledge of the dynamics of neutral particles. This has to some extend been achieved in numerical simulations, which have proved successful in reproducing profiles for the modulation experiments in [1].

In this paper we make progress towards a simple to use model which allows to explore parameter space in a dynamical fashion and can treat modulation experiments in a meaningful way. We present numerical investigations on how the gas puff modulation characteristics are affected by the neutral particle model. Two 1D models are studied; the first model includes only one species of neutral atoms originating from the gas puffing, whereas the second model also accounts for the hot neutrals created in charge exchange collisions between hot plasma and the cold neutrals ($ion_{\mathrm{hot}} + neutral_{\mathrm{cold}} \underset{\mathrm{cx}}{\rightarrow} neutral_{\mathrm{hot}} + ion_{\mathrm{cold}}$).

It is found that the neutral model does not affect the transport of the modulated signal significantly, but the amplitude of the modulation is several times larger in the two-species neutral model. Also, the hot neutrals are seen to penetrate deeper into the edge, which along with the increased amplitude for the hot neutral model indicates a significant difference in fueling in the two models.

Models

To simulate the transport of heat and particles, we apply a system of 1D transport equations [2]. The density equation for the quasi-neutral plasma species reads

$$\partial_t n_{\mathrm{p}} + \tfrac{1}{r}\partial_r \left(r\Gamma_{\mathrm{p}}\right) = S_{\mathrm{p}}\,, \qquad \Gamma_{\mathrm{p}} = -D_{\mathrm{p}}\partial_r n_{\mathrm{p}} + v n_{\mathrm{p}}\,, \tag{1}$$

---

[*] See the Appendix of F. Romanelli et al., Proceedings of the 25th IAEA Fusion Energy Conference 2014, Saint Petersburg, Russia

where n_p is the plasma density, v is vthe convective velocity, $D_\mathrm{p} = D_\mathrm{p}(\chi_\mathrm{e})$ is the diffusion coefficient and S_p is the plasma particle source. The electron temperature equation reads

$$\tfrac{3}{2}\partial_t\left(n_\mathrm{p}T_\mathrm{e}\right) + \tfrac{1}{r}\partial_r\left(r\left[q_\mathrm{e} + \tfrac{5}{2}T_\mathrm{e}\Gamma_\mathrm{p}\right]\right) = Q_\mathrm{e} + \frac{\Gamma_\mathrm{p}}{n_\mathrm{p}}\partial_r\left(n_\mathrm{p}T_\mathrm{e}\right), \qquad \frac{q_\mathrm{e}}{n_\mathrm{p}} = -\chi_\mathrm{e}\partial_r T_\mathrm{e} + uT_\mathrm{e}, \tag{2}$$

where u is the electron heat convection velocity, χ_e the heat diffusivity and Q_e is the heat source. In order to account for turbulent effects, the electron heat diffusivity is described by a critical electron temperature gradient model [3], such that the heat diffusion grows when the electron temperature gradient exceeds a critical level κ

$$\chi_\mathrm{e} = \chi_{\mathrm{e}0} + \lambda T_\mathrm{e}^{\alpha}\left[\frac{|\nabla T_\mathrm{e}|}{T_\mathrm{e}} - \kappa\right]^{\beta} H\left(\frac{|\nabla T_\mathrm{e}|}{T_\mathrm{e}} - \kappa\right), \tag{3}$$

where H is the Heaviside step function, $\chi_{\mathrm{e}0}$ is the collisional heat diffusion coefficient and λ a coefficient.

Two models for the neutral particles are applied. In the two-species model the neutral population consists of a cold neutral species which enters the system by gas puffing, and a hot neutral species which is created in charge exchange collisions between hot plasma and cold neutrals. Both hot and cold neutral densities $n_{\mathrm{n_{c,h}}}$ are described by a diffusion model

$$\partial_t n_{\mathrm{n_{c,h}}} + \tfrac{1}{r}\partial_r\left(r\Gamma_{\mathrm{n_{c,h}}}\right) = S_{\mathrm{n_{c,h}}}, \qquad \Gamma_{\mathrm{n_{c,h}}} = -D_{\mathrm{n_{c,h}}}\partial_r n_{\mathrm{n_{c,h}}}, \tag{4}$$

where $D_{\mathrm{n_{c,h}}}$ are the diffusion coefficients.

The plasma and neutral equations are coupled through the sources

$$S_\mathrm{p} = \left(n_\mathrm{n}k_\mathrm{iz} - n_{\mathrm{n_c}}k_\mathrm{cx}\right)n_\mathrm{p}, \qquad Q_\mathrm{e} = -k_\mathrm{iz}n_\mathrm{n}T_\mathrm{iz}, \tag{5}$$

$$S_{\mathrm{n_c}} = -\left(k_\mathrm{cx} + k_\mathrm{iz}\right)n_{\mathrm{n_c}}n_\mathrm{p}, \qquad S_{\mathrm{n_h}} = \left(n_{\mathrm{n_c}}k_\mathrm{cx} - n_{\mathrm{n_h}}k_\mathrm{iz}\right)n_\mathrm{p}, \tag{6}$$

where $n_\mathrm{n} \equiv n_{\mathrm{n_c}} + n_{\mathrm{n_h}}$, $T_{iz} = 13.6\,\mathrm{eV}$ is the ionization energy and k_iz and k_cx are the ionization and charge exchange rates which both depend on the plasma temperature [4]. External plasma and cold neutral sources are imposed through boundary conditions, and in particular the gas puffing is simulated by modulating the cold neutral source on the wall.

The one-species model for neutrals is similar to the above, but the charge exchange reaction rate k_cx is quenched such that no hot neutrals are created.

Results

By solving the system of equations (1)-(6) numerically we obtain the neutral profiles shown in Figure 1, modulated plasma density profiles in Figure 2 and phase shift and amplitude for the modulation in Figure 3. The plots for experimental data shown in Figures 2 and 3 are constructed from a measured plasma density profile in phase 1 of JET shot #87425 with GIM7 modulation (for details, see [5, 6]). These, along with experimental electron temperature data, were also used when the free parameters of the model were estimated.

In Figure 1 it is seen, that in both models the cold neutrals have a small penetration depth and the densities vanish inside the last-closed-flux-surface (LCFS) which lies at approximately at $R = 3.80\,\mathrm{m}$. The hot neutrals have a much lower density at the wall (at $R = 3.864\,\mathrm{m}$), but penetrate far deeper into the plasma edge. This indicates that hot neutrals may play a significant role in plasma fueling.

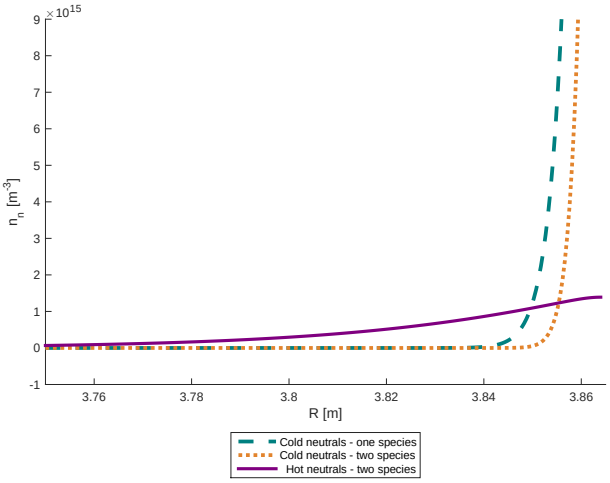

Figure 1: Neutral profiles in steady state, shown both for the one-species model (dashed), and for the two-species model with cold (dotted) and hot (full) neutrals for JET geometry.

Figure 2 shows the modulation of the density as a function of time. Both simulations mimic the plasma behavior to gas puffing well by reproducing a modulation phase shift which increases, and an amplitude which decreases when approaching the center. The phase shift and amplitude are depicted in Figure 3. This shows that the calculated phase shift only depends weakly on which of the two models is applied, and that the ionization source region is deeper for the model which includes hot

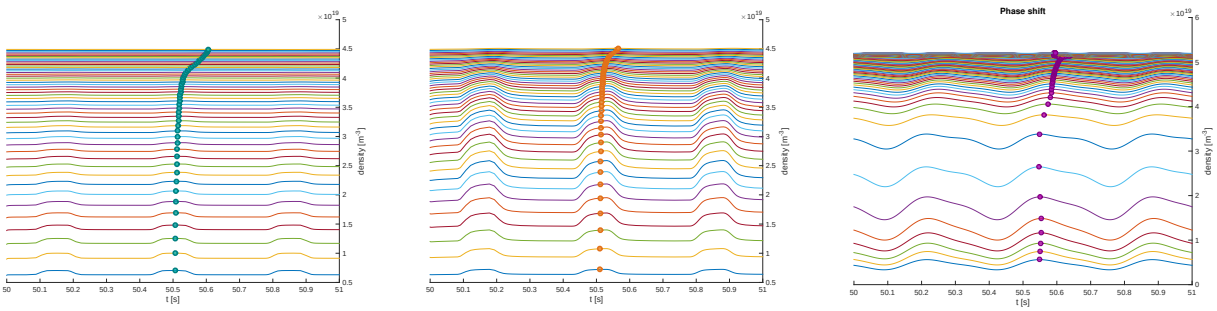

(a) One neutral species. (b) Two neutral species. (c) Experimental data.

Figure 2: Simulations of and experimental data for gas puff modulation of plasma density. One of the perturbations is tracked and marked by colored circles.

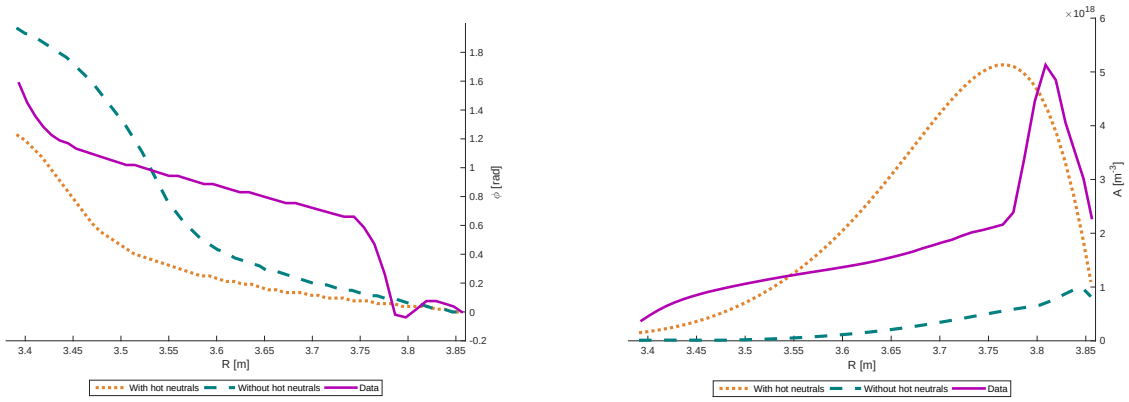

(a) Phase shift.

(b) Amplitude.

Figure 3: Phase shift and amplitude of plasma density modulation for one-species model (dashed), two-species model (dotted) and experimental data (full).

neutrals. The latter is concluded from the flatter phase shift of the two-neutral-species model in the outer region. It is also observed that the amplitude of the modulation is several times larger for the model that includes hot neutrals. This effect is due to the deeper penetration of the hot neutrals inside LCFS.

Discussion and conclusion

The effect on the gas puff modulation characteristics are investigated for two different models for neutral particles. A comparison shows that the phase shift in the plasma density modulation is similar for the two neutral models, whereas the amplitude of the modulation is significantly larger for the model which includes hot neutrals produced in charge exchange collisions.

The weak influence on the phase shift suggests that the choice of neutral model is not significant for the plasma particle transport. In contrast the strong influence that the choice of neutral model has on the amplitude of the density modulation indicates that the fueling rate inside LCFS is very dependent on whether hot neutrals are included or not.

This work has been carried out within the framework of the EUROfusion Consortium and has received funding from the Euratom research and training programme 2014-2018 under grant agreement No 633053. The views and opinions expressed herein do not necessarily reflect those of the European Commission.

References

[1] A. Salmi et al. 41st EPS conference on Plasma Physics, Berlin, 2014, P1.008

[2] P. Mantica, F. Ryter, C. R. Physique 7 (2006)

[3] F. Imbeaux et al, Plasma Phys. Control. Fusion 43 (2001)

[4] P.C. Stangeby, IoP Publishing, (2000)

[5] A. Salmi et al. 42nd EPS conference on Plasma Physics, Lisbon, 2015, conference poster

[6] T.T.J. Tala, 20th joint US-EU TTF workshop, Salem, 2015, conference oral presentation

Simulation of neutrals in a turbulent scrape-off layer

A.S. Thrysøe, J. Madsen, V. Naulin, A.H. Nielsen, J. Juul Rasmussen

PPFE, Department of Physics, DTU, DK-2800 Kgs. Lyngby, Denmark

Introduction

In future magnetic confinement fusion devices, such as ITER, high efficiency fuelling with deep penetration is required for maintaining a sufficient plasma core density. One possible fuelling method is gas puffing, in which neutral molecules are puffed into the scrape-off layer (SOL), where they dissociate, and if the resulting atoms are ionized inside the last closed flux surface (LCFS), they fuel the plasma effectively. To investigate the direct fuelling efficiency from gas puffing in a turbulent SOL, the HESEL model for SOL turbulence is coupled to a fluid-like neutral model.

The HESEL model [1] is a 4-field drift-fluid model that describes interchange driven turbulence in the SOL region. The simulated domain is 2D slab perpendicular to the magnetic field lines, at the outboard-midplane of a tokamak. The reaction rates of the plasma-neutral interactions that shape the neutral profiles in the SOL depend strongly on both electron density, and electron or ion temperature. As fluctuations in these fields are highly correlated in the SOL, a turbulence model such as HESEL is necessary for investigating the reaction rates in a proper way.

Neutral Model

The choice of model for the neutrals is made from a series of requirements. First from Fig. 1a[†] it appears that both molecular and atomic neutrals are important for describing the interactions with the plasma. Secondly, the so-called Franck-Condon neutrals that result from molecular dissociation will have a temperature of a few eV [2], whereas neutral atoms that have undergone charge-exchange collisions typically have much higher temperatures similar to that of the ions. Moreover, it is seen from Fig. 1b that in the SOL region the cold neutrals typically have a short mean-free path (mfp), whereas the mfp for the atoms is much longer than the typical perpendicular length-scales of SOL structures that are of the order of cm. Finally, the neutral gas transport is described by a fluid model. Using a fluid model rather than a more detailed kinetic model is motivated by computational expediency, and allows for solving the coupled system of plasma and neutral transport equations simultaneously.

[†]The molecular ionization is actually a two-step process: $D_2 + e \rightarrow D_2^+ + 2e \rightarrow D + D^+ + 2e$. The cross-section for the second step is, however, so high, that the dissociation can be assumed to happen immediately after ionization, and only the reaction rate of the first step is used.

The resulting neutral model is a 3-field diffusive model for the neutral densities[‡], similar to that used in [4], i.e,

$$\partial_t n_s - \nabla \cdot (D_s \nabla n_s) = S_s\,, \qquad s = \text{cold, warm, hot}\,, \tag{1}$$

where n_s are the neutral densities, the diffusivities $D_{\text{hot}} = 10^1 D_{\text{warm}} = 10^3 D_{\text{cold}} \approx 10^2 \frac{\text{m}^2}{s}$ are estimated from neutral temperatures of $T_{\text{hot}} = 20\,\text{eV}$, $T_{\text{warm}} = 2\,\text{eV}$, and $T_{\text{cold}} = 25\,\text{meV}$, ρ_s is the cold-ion hybrid thermal gyro-radius and Ω_{ci} is the ion cyclotron frequency. The neutral density sources are

$$\begin{aligned} S_{\text{cold}} &= -n n_{\text{cold}} \left(\langle \sigma_{Dis} v\rangle + \langle \sigma_{Iz} v\rangle\right)\,, \qquad S_{\text{hot}} = n\left(n_{\text{warm}} \langle \sigma_{cx} v\rangle - n_{\text{hot}} \langle \sigma_{iz} v\rangle\right)\,, \\ S_{\text{warm}} &= n\left[n_{\text{cold}} \left(2\langle \sigma_{Dis} v\rangle + \langle \sigma_{Iz} v\rangle\right) - n_{\text{warm}} \left(\langle \sigma_{iz} v\rangle + \langle \sigma_{cx} v\rangle\right)\right]\,, \end{aligned} \tag{2}$$

where n is the electron density, and $\langle \sigma_r v\rangle$ is the reaction rate coefficient for reaction r, and the reaction rates are defined in Fig. 1a. By demanding that the neutral densities should vanish to dissociation and/or ionization inside the edge, and that the wall is absorbing a fraction γ of colliding neutrals the boundary conditions become

$$\partial_x n_s\big|_{\text{edge}} = \sqrt{\frac{S_s'}{D_s}} n_s\,, \qquad \partial_x n_s\big|_{\text{wall}} = -\gamma \sqrt{\frac{S_s'}{D_s}} n_s\,, \tag{3}$$

along with an evenly distributed auxiliary molecular neutral deuterium source on the wall boundary for simulating gas puffing. Here s again denote the different neutral species, S_s' are the source terms proportional to n_s and $\gamma = 0.2$.

Density Sources

A first step in coupling the neutral and HESEL equations, is to include the 0^{th} moment source term

$$S_{\text{n}} = n\left[n_{\text{cold}} \langle \sigma_{Iz} v\rangle + \left(n_{\text{warm}} + n_{\text{hot}}\right) \langle \sigma_{iz} v\rangle\right]\,, \tag{4}$$

in the continuity equation. Including this density source in the HESEL equations allows for probing the potential of simulating gas-puff fuelling from the outboard-midplane, as well as investigate to which extent neutrals are ionized in the SOL, and thus lost for direct fuelling purposes. Ideally higher-moment sources, such as cooling from charge-exchange collisions or ionization of warm neutrals, should be included as well. It is however believed that these sources do not affect the fuelling properties much, and including them is thus left for future work.

The molecular neutral source that imitates a steady state gas-puffing is formulated in such a way, that enough neutrals are puffed in to maintain the plasma edge density from direct fuelling.

[‡]Even though the neutral atoms experience a long mfp in the SOL, the particle transport can be well described by Fick's laws [3].

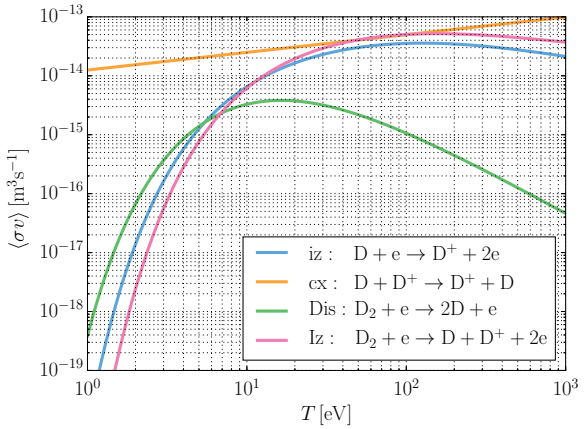

(a) *Reaction rates for dominant inelastic collisions between neutral particles and plasma. They are referred to as* iz, cx, Dis *and* Iz *respectively.*

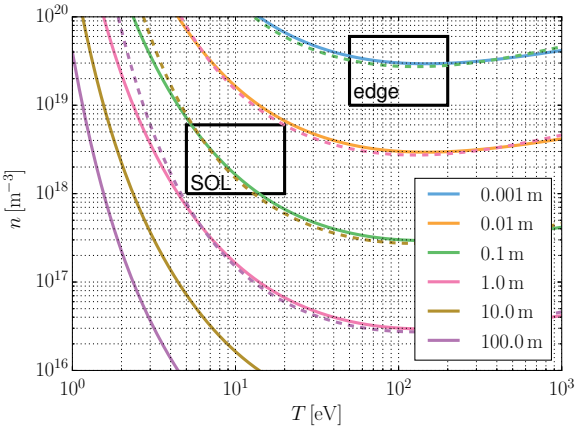

(b) *Ionization and dissociation mfp of cold neutral molecules (solid), and ionization mfp for hot neutral atoms (dashed).*

Figure 1: *Reaction rates for neutral-plasma collisions, and mean-free paths (mfp) for cold and hot neutrals. Reaction rate coefficents are obtained from [5].*

It is found that for sustaining the plasma edge density by direct fuelling, the density flux must yield a total neutral pressure

$$P_{\text{wall}} = \sum_{\substack{s=\text{cold,} \\ \text{warm,hot}}} n_s T_s \big|_{\text{wall}}, \tag{5}$$

of $P_{\text{wall}} \approx 0.1\,\text{Pa}$. This pressure is consistent with what is measured in experiments.

Another interesting result that the coupled model yields, is the fraction of different neutral species that cross the LCFS, and thus fuel the plasma directly. It is found that approximately 60 % of the flux is constituted by hot neutrals, that are created by interactions between blobs and warm neutrals in the SOL. The remaining 40 % of the flux comes from warm neutrals, and the amount of cold neutrals reaching the LCFS is negligible. This testifies to the importance of a dynamical treatment of the SOL plasma, as well as the inclusion of the hot neutral species. It is also observed that the fuelling briefly increases during a blob event, which can be explained by a temporary increase in the hot neutral production rate. Some of the fields and the resulting ionization rate are shown in Fig. 2.

Conclusions and Outlook

In this paper the initial results from implementing a neutral model in the HESEL code are presented. It is displayed how simulating gas puffing as a molecular neutral source at the wall yields a realistic fuelling scenario, in which the molecular neutral density self-consistently takes values comparable to those in todays gas-puffed tokamaks. It is found, that most of the direct

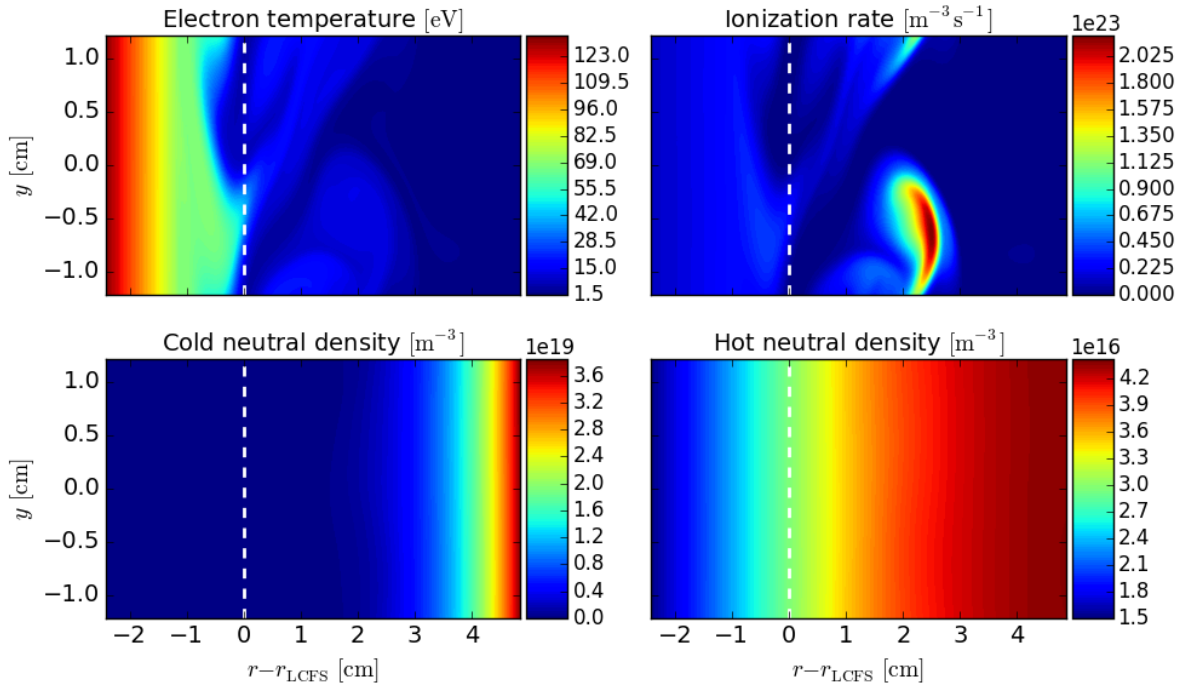

Figure 2: *Plasma and neutral fields solved by the combined neutral-HESEL simulation, and the resulting ionization rate. The dashed line indicates the position of the LCFS.*

fuelling originates from hot neutrals created in charge-exchange collisions the SOL, and also that blobs shortly increase fuelling due to a brief increased production hot neutrals with a long mean-free path.

Future extensions of the combined neutral-HESEL model will involve inclusion of higher moment sources, and consideration of wall and divertor recycling effects. This will allow for a better understanding of the influence of the neutrals on the blobs, as well as a more consistent fuelling scheme.

This work has been carried out within the framework of the EUROfusion Consortium and has received funding from the Euratom research and training programme 2014-2018 under grant agreement No 633053. The views and opinions expressed herein do not necessarily reflect those of the European Commission.

References

[1] J. Madsen et. al, Physics of Plasmas **23**, 3 (2016)

[2] P. Stangeby, G. McCracken, Nucl. Fusion **30**, 7 (1990)

[3] R. Hazeltine, Physics of Plasmas **5**, 9 (1998)

[4] A.S. Thrysøe et. al, Plasma Physics and Controlled Fusion **58**, 4 (2016)

[5] J.K. Ratko et. al, Springer Series on Atoms and Plasmas **4** (1987)

The influence of blob intermittency on fuelling

A.S. Thrysøe[1], J. Madsen[1], V. Naulin[1], A.H. Nielsen[1], J. Juul Rasmussen[1]

[1]*PPFE, Department of Physics, DTU, DK-2800 Kgs. Lyngby, Denmark*

Introduction

The overall performance in a tokamak is strongly affected by the dynamics in the edge and Scrape-Off Layer (SOL) regions. This region is characterized by the transition from closed to open magnetic field lines, and the last-closed-flux-surface (LCFS) defines the boundary between the confined plasma and the SOL region. The anomalous transport of heat and particles across the LCFS is strongly intermittent, and the plasma mainly escapes the confined region in field-aligned filaments (blobs) that are formed near the LCFS and propagate radially outwards.

The edge and SOL regions also contain a significant amount of neutral particles. The neutrals can either be puffed into the SOL for fuelling or diagnostic reasons, or originate from recycling of plasma on material surfaces. The presence of neutrals is known to affect the edge and SOL plasma through various interactions such as dissociation and ionization reactions, or charge-exchange collisions.

In this paper we present the results of a combined plasma-neutral model that allow for studying the effects of plasma turbulence and the associated transport on neutrals and vice versa. Both the plasma and neutral parts of the model are formulated in the fluid picture, which allow for studying the interactions between neutrals and turbulence self-consistently. In particular it is investigated how blobs affect the fuelling rate during gas-puffing at the outboard-midplane of a medium-sized tokamak.

Combined plasma-neutral model

A slab perpendicular to the magnetic field lines at the outboard-midplane is simulated in a model that describe the interactions between plasma and neutral particles in a self-consistent manner. The evolution of plasma fields is described by the HESEL model [1], which is a four-field drift-fluid model for the density, electron and ion pressures, and the vorticity. The HESEL model describes the edge and SOL dynamics, including the formation and propagation of field aligned filaments.

The neutrals are described in a three-fluid neutral diffusive model similar to that of [2], but with the difference that thermal molecules are now included. The three neutral fluids correspond to thermal deuterium molecules, deuterium atoms originating from dissociation of molecules and a hotter species of atoms that are created in charge-exchange collisions with hot ions. The

three species interact with the plasma and one another through the reactions

$$\begin{aligned} &\mathrm{e}+\mathrm{D}_2 \rightarrow \mathrm{e}+2\mathrm{D}\,, \qquad &&\mathrm{e}+\mathrm{D}_2 \rightarrow 2\mathrm{e}+\mathrm{D}_2^+ \rightarrow 2\mathrm{e}+\mathrm{D}+\mathrm{D}^+\,, \\ &\mathrm{e}+\mathrm{D} \rightarrow 2\mathrm{e}+\mathrm{D}^+\,, \qquad &&\mathrm{D}^+ + \mathrm{D} \rightarrow \mathrm{D}+\mathrm{D}^+\,, \end{aligned} \tag{1}$$

which are denoted dissociation and ionizing dissociation of molecules, and ionization and charge-exchange collision of atoms respectively.

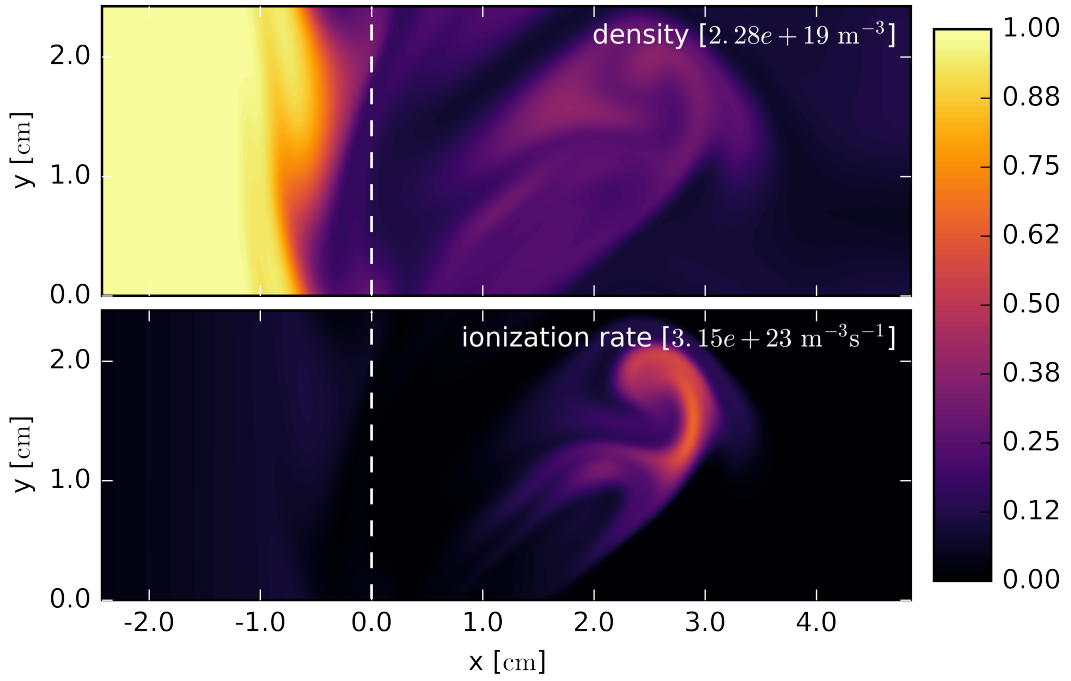

Figure 1: *Density (upper), and ionization rate (lower) event calculated by the HESEL code. The area to the left of the LCFS (dashed vertical line) is the edge region, and that to the right of the LCFS is the SOL region. The domain as a slab perpendicular to the magnetic field lines at the outboard-midplane.*

The interactions in (1) result in a set of fluid source terms. For the purpose of studying fuelling the source term of most interest is that for the density

$$S^n = n_\mathrm{e}\left(n_\mathrm{n}\langle\sigma_{iz}v\rangle + n_\mathrm{N}\langle\sigma_{IZ}v\rangle\right)\,, \tag{2}$$

where n_e is the electron density, n_n and $\langle\sigma_\mathrm{iz}v\rangle$ are the neutral atom density and ionization reaction rate, and n_N and $\langle\sigma_\mathrm{IZ}v\rangle$ are the neutral molecule density and ionization reaction rate. The reaction rates are non-linear functions of the electron temperature obtained from [3]. The density and the density source, i.e., the ionization rate, are shown for a blob event in Fig. 1.

Blobs and fuelling

The combined HESEL-neutral model is suitable for studying fuelling and ionization in edge and SOL regions with fluctuating plasma and neutral fields, since no approximations are made

to simplify the products in (2). It is of interest to asses to what degree neutrals penetrate the SOL region and thus fuel the plasma, as well as understand the effects that blob filaments have on the fuelling.

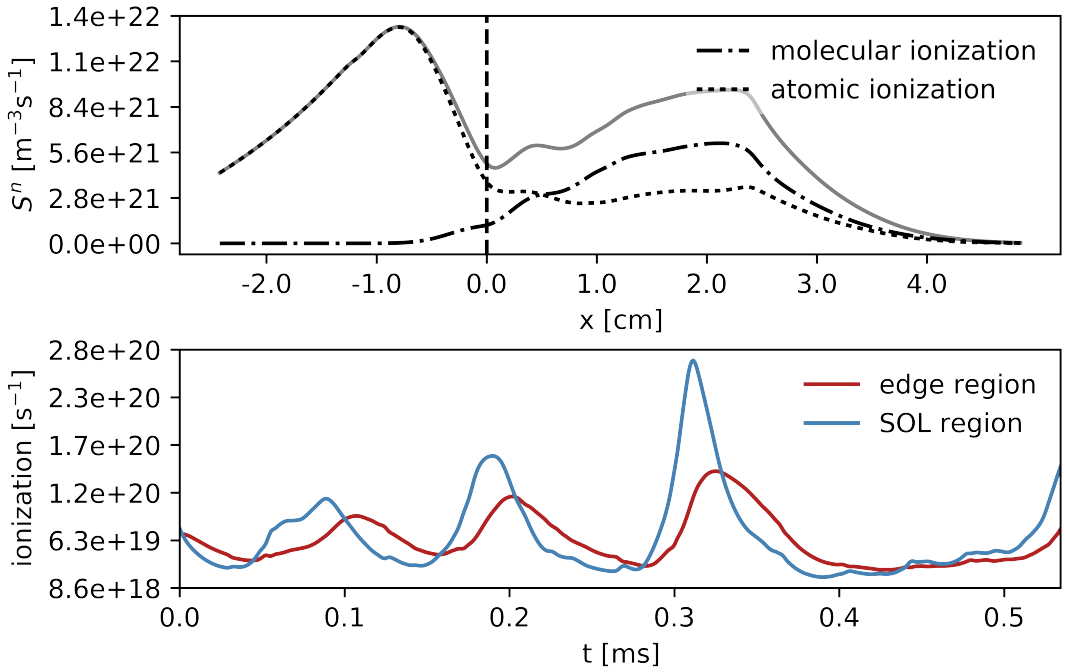

Figure 2: *Time-averaged density source profile (upper), and integrated ionization in the edge and SOL regions as a function of time (lower). It is observed that the ionization level in the two regions is comparable, and that the ionization in the edge region, i.e., the fuelling, increases significantly following a blob event.*

In Figure 2 the density source profile reveals that a the edge and SOL regions experience a comparable amount of ionization. The main part of the ionization in the edge region is due to ionization of atoms, whereas the SOL ionization is dominated by ionizing dissociation of molecules.

The spatially integrated density source is a measure of the amount of ions and electrons created in ionization processes

$$\text{ionization} = \int \mathrm{d}x\mathrm{d}y\, S^n\,. \tag{3}$$

The ionization between the inner domain boundary and the LCFS is the main fuelling of the plasma, whereas electrons and ions created in SOL do not contribute directly to the fuelling. For the simulated domain the edge and SOL ionization is approximately equal.

It is observed from Fig. 2 that the SOL ionization is significantly increased when a blob emerges into the SOL region. This is in good agreement with the positive effect of the increased

pressure on the ionization reaction rate in (2). It is moreover observed that shortly after a blob event, the fuelling is likewise increased.

The increase in the fuelling rate can be explained by the neutral dynamics resulting from the increased electron pressure of the blob. During a blob event the ionization of both neutral atoms and molecules increase. The dissociation of molecules into atoms, and the number of charge-exchange collisions likewise increase. The fuelling is effectively unaffected by the ionization of molecules, since the edge is primarily fuelled by atoms, and since the density of molecules is much larger than that of atoms in the SOL, the blob creates more atoms than it ionizes. Due to their long mean-free path the atoms can penetrate the SOL and reach the edge region where they are ionized and thus contribute to fuelling.

Outlook

The results on the effects of blobs on fuelling were obtained from a combined plasma-neutral fluid model that include hot ions and treats the interactions between plasma and neutrals in a self-consistent way. Those features are thought to be essential to ongoing research in edge and SOL relevant experimentally observed phenomena such as shoulder formation [4] and the fuelling triggered H-mode density limit [5].

This work has been carried out within the framework of the EUROfusion Consortium and has received funding from the Euratom research and training programme 2014-2018 under grant agreement No 633053. The views and opinions expressed herein do not necessarily reflect those of the European Commission.

References

[1] J. Madsen et al., Physics of Plasmas **23**, 032306 (2016)

[2] A.S. Thrysøe et al., Plasma Phys. Control. Fusion, **58**, 044010 (2016)

[3] R.K. Janev, et al., 1987 *Elementary Processes in Hydrogen-Helium Plasmas* (Berlin: Springer-Verlag)

[4] D. Carralero et al., Nuclear Materials and Energy (2016)

[5] M. Bernert, et al., Plasma Phys. Control. Fusion **57** (2015) 014038

4.5 Preliminary results

In this section a selection of somewhat mature, but not yet published, results are presented. The topics covered here constitute a basis for near-future work. Other future topics that could possibly be elucidated by nHESEL simulations are discussed in Sec. 5.2. The section consists of two related parts; in the first part in Sec. 4.5.1 the initial investigations on the effect of ionization in the SOL region on shoulder formation is presented, and in Sec. 4.5.2, the effect of inelastic collisions with neutrals on seeded blobs is studied.

4.5.1 Shoulder formation due to SOL ionization

In the resent years, it has been experimentally observed, that an increased gas puffing result in a broadening of the plasma density profile into the SOL region. This phenomenon is referred to as *shoulder formation*, and the physical mechanisms behind the formations of the density shoulder is discussed in various papers, e.g., [99, 100, 101]. Two mechanism are theorized to contribute significantly to the density shoulder formation; the divertor detachment, and cooling of the edge region. Common for most papers is that the effect of local ionization in the SOL is neglected when discussing the formation of density shoulders. The nHESEL model provides a framework for studying the contribution of local ionization of neutrals to the SOL plasma density.

Two simulations are compared. In one simulation there is no forcing in the edge region, and the edge is thus fuelled entirely from ionization of neutrals. The neutral puffing rate is $\Gamma_{\text{puff}} = 5{\cdot}10^{21}\,\text{m}^{-2}\text{s}^{-1}$, and the system is thus 'over-fuelled', which result in an increasing edge density as a function of time. In the other simulation there are no neutrals present, instead a time-dependent forcing of the plasma edge density ensures, that the density in the edge region is similar to that of the first simulation. The average electron density at the inner edge region is shown for the two simulations in Fig. 4.7. Here it is observed, that the edge density in the two simulations rises consistently from $n_{\text{e}} = 2.25\,\text{m}^{-3}$ to $n_{\text{e}} = 3.65\,\text{m}^{-3}$ throughout the simulations.

The fixed increase of the edge density for the two simulations should ensure, that the outwards radial particle flux across the LCFS stays consistent across the simulations. The flux is shown in Fig. 4.8, and the values only

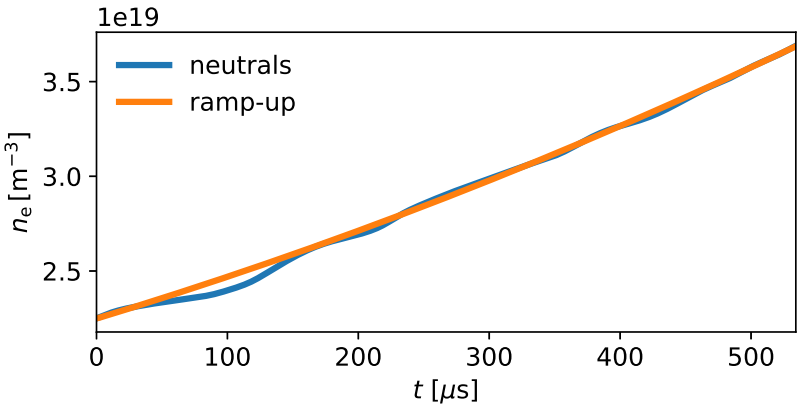

Figure 4.7: Poloidally averaged density at the inner edge region for the two simulations. The edge density for the simulation with forcing is matched only that with fuelling from local ionization of neutrals.

differ slightly from one another, with a larger outwards flux from the edge region for the simulation, where the edge density is ramped up.

With the edge density fixed and the outwards particle flux similar for the two simulations, the only source to excess increment of SOL density in the nHESEL framework is that from local ionization of neutral particles. Figure 4.9 shows the density profiles for the two simulations at various time instances. The inner density grows consistently for the two simulations as expected. For both simulations the SOL density likewise increases, but with a much more rapid increase for the simulation with neutrals. The higher increase in SOL density for the simulation with the neutrals present is also observed in Fig. 4.10. In this figure the average density of the SOL region, i.e.,

$$\langle n_\mathrm{e} \rangle_\mathrm{SOL} = \frac{\int_\mathrm{SOL} \mathrm{d}x\mathrm{d}y\, n_e}{\int_\mathrm{SOL} \mathrm{d}x\mathrm{d}y}\,, \tag{4.6}$$

is shown as a function of time. It is clear that although the increased edge density results in an increase in the SOL density, as is the case for the simulation with the density ramp-up, most of the density in the SOL results from local ionization of neutral particles.

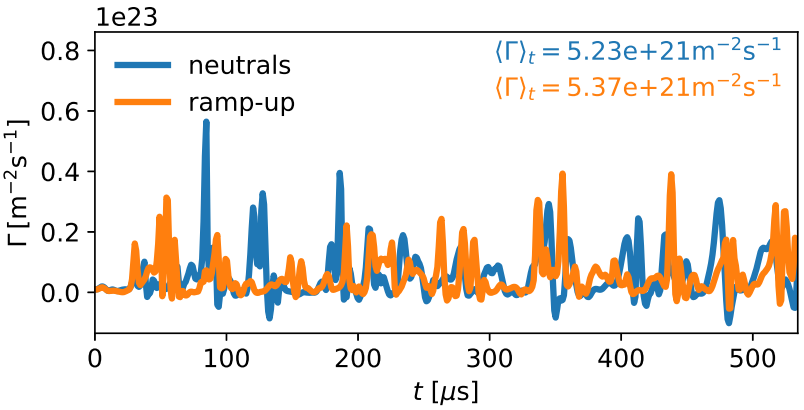

Figure 4.8: Radial flux of electrons across the LCFS as a function of time for the two fuelling scenarios. The temporal mean of the fluxes are displayed in the upper right corner, and only differs slightly.

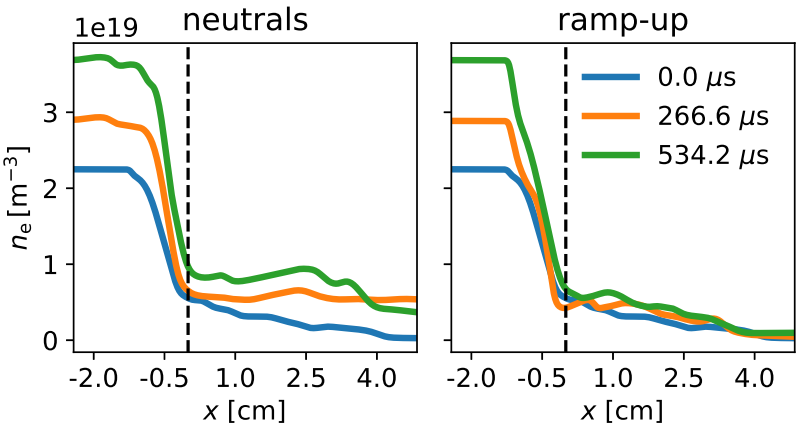

Figure 4.9: Poloidally averaged electron density fields for the two simulations. The density profiles are depicted at three different instances, and it is observed, that although the density in the inner edge region is the same for the two simulations, the SOL density increases much more for the simulation with neutrals.

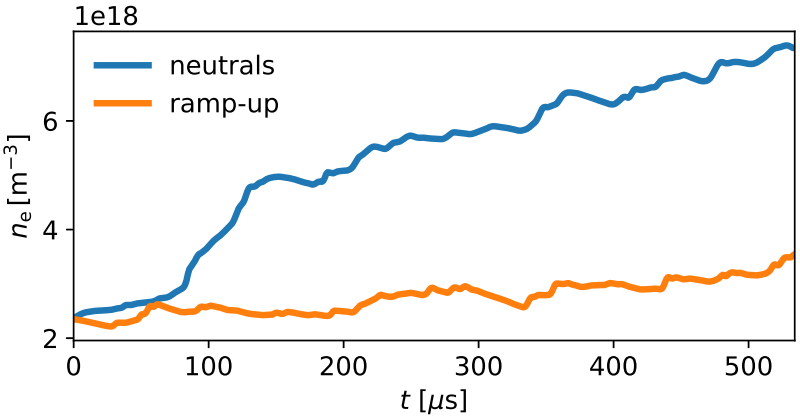

Figure 4.10: Average density in the SOL region for the two simulations. Despite having a similar flux across the LCFS, the density in the SOL is much larger for the simulation with neutrals, due to local ionization of neutrals in the SOL.

4.5.2 Effect of neutral interactions on seeded blobs

One aspect that has been somewhat neglected in the published papers is that of the effect of the individual neutral-plasma interactions on the blobs. The presence of neutral particles introduces several terms to the existing HESEL equations, which enter both as direct source terms and as contributions to the drift-velocity in (2.128)-(2.131). Both contributions influence the evolution of density, temperature, and vorticity fields, which affect the blob shape and thus its velocity [102, 103, 104].

In order to keep as many parameters fixed as possible, the set-up is different from that of the default nHESEL domain. Here we consider flat density and pressure profiles for the electron and ion fields with

$$n = 1 \cdot 10^{18}\,\mathrm{m}^{-3}\,, \qquad T_\mathrm{e} = T_\mathrm{i} = 10\,\mathrm{eV}\,. \tag{4.7}$$

On top of the field is a Gaussian perturbation of, so that $f \to f + \Delta f$, with

$$\Delta f = \frac{f}{2} \exp\left(\frac{x^2 + y^2}{2\sigma^2}\right)\,, \tag{4.8}$$

and $f = n, T_\mathrm{e}, T_\mathrm{i}$, and the width $\sigma = 10\rho_s$. The initial perturbations are shown as the first collection of subplots (at $t = 0$) in Figs. 4.11-4.13.

The neutral background is static, with an equal density of molecules, warm atoms and hot atoms of

$$n_{\text{cold}} = n_{\text{warm}} = n_{\text{hot}} = n\,, \tag{4.9}$$

where n refers to the background electron density without the blob. The value of the neutral background is chosen, so that the effects of the interactions are visible, but do not alter the plasma fields on a time-scale that is too short for the blob to evolve dynamically. Note that in particular the atom densities are much larger than those present in the usual nHESEL simulations. The neutral background is furthermore static, as results from a dynamical background would be more sensitive to initial neutral profiles and molecule-to-atom ratios. Finally, 95% of the plasma background fields are subtracted when calculating the source terms, as it is the intention to study the effect of the interactions on the perturbation only, and not on the background. The dampening of the plasma fields due to parallel transport has likewise been disabled.

In Figures 4.11-4.13 the evolution of the electron density, temperature, and the ion temperature are shown at various time-instances. For all fields, the plot at some time contains six sub-plots. The sub-plots depict the evolution of the blob without the influence of neutral interactions (denoted 'none'), the evolution under the influence of only one interaction, which is either dissociation of molecules (dis), molecular assisted ionization of molecules (Iz), ionization of atoms (iz), or charge-exchange collisions between atoms and ions (cx), and finally the evolution of the blob under the influence of all interactions ('all').

For the density of the seeded blob in Fig. 4.11, it is observed that neither dissociation nor charge-exchange collisions has a major impact on the density evolution. Neither of those interactions introduces a plasma particle source, as opposed to the ionization interactions. For molecular assisted ionization and atomic ionization, the density perturbation is significantly altered, both by an increase in magnitude and in poloidal asymmetry.

It is also the ionization reactions that have the bigger impact on the evolution of the electron temperature perturbation shown in Fig. 4.12. In this case dissociation also introduces a direct source term in the transport equations, but of much smaller magnitude than that from the ionization reactions. For the neutral background level applied here, the electrons are almost cooled to the their background temperature when all interactions are applied.

The ion temperature shown in Fig. 4.13 appears to be much more robust to neutral interactions. The reason for this is most likely, that the ionization and dissociation potentials do not enter the ion pressure equations, as is the case for the electron pressure. Therefore, it is also surprising that molecular assisted ionization has such a large impact on the ion temperature, in particular compared to that from atomic ionization. Charge-exchange collisions, on the other hand, show as little effect on the ions as it does on the electrons, even though it only enters the ion pressure equations.

The results presented here are still in their infancy, and more studies on the subject are planned for future work. In particular, it could be interesting to compare how much of the change of the blob structure is due to the additional source terms from neutral interactions, and how much is caused by the additional drift terms. Preliminary results suggest, that it is the former of the two that dominates.

This concludes the results section. In Chapter 5 the main features of the nHESEL model, and the most important results, are summarized, and near-future work plan with the code is mapped out.

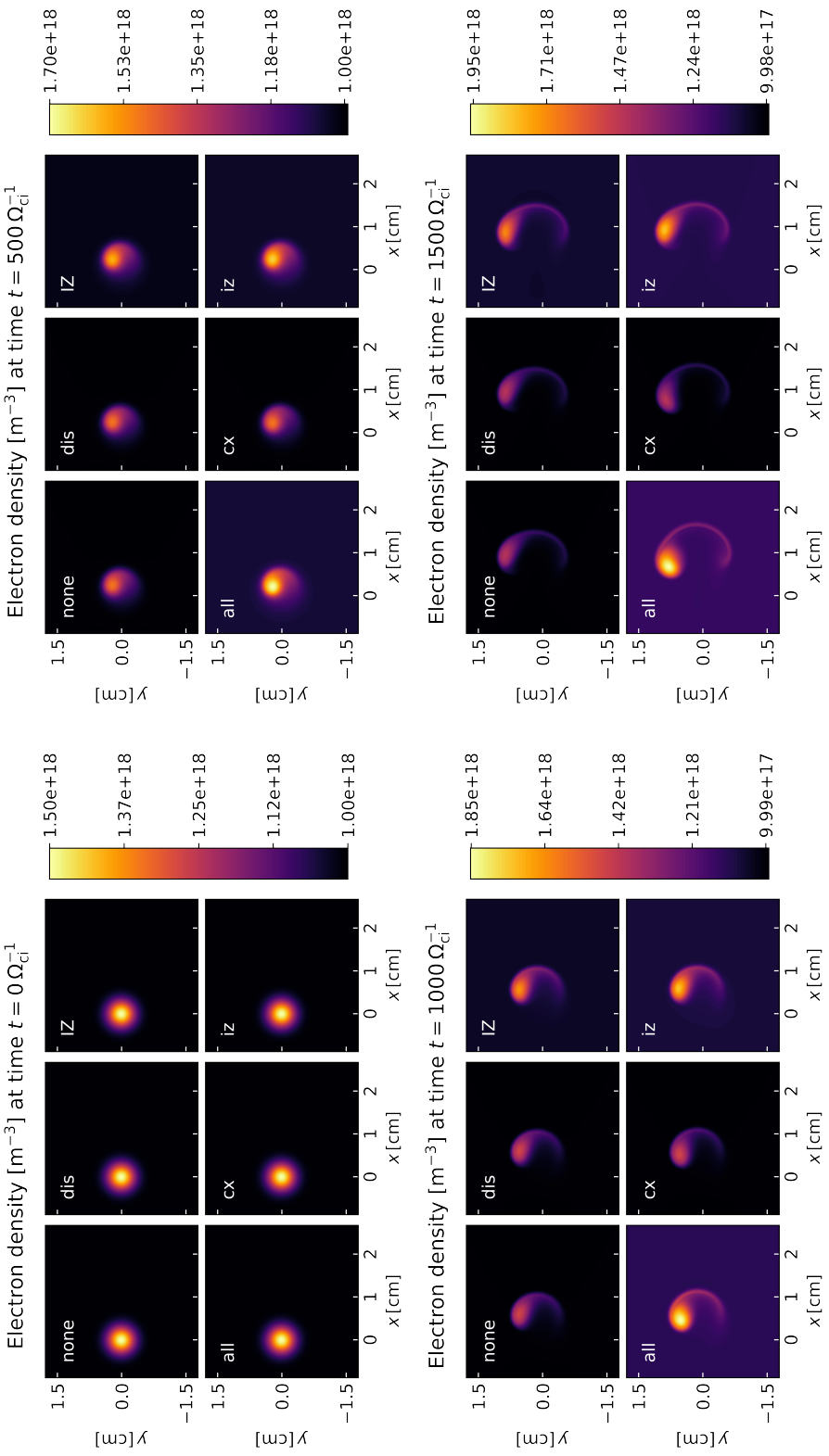

Figure 4.11: Evolution of electron density for seeded blob in a neutral background, and subject to different in-elastic neutral interactions with molecules and atoms.

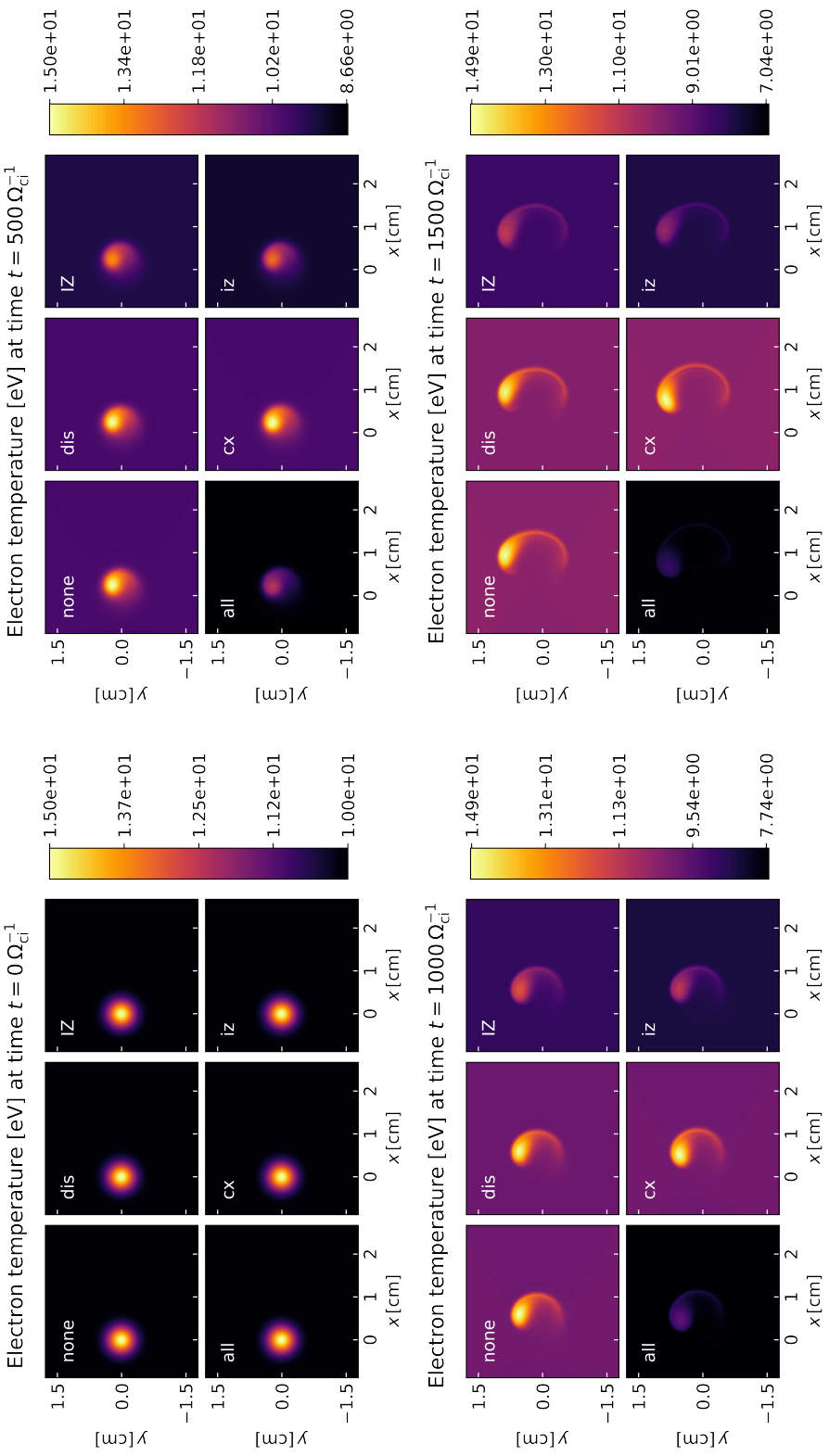

Figure 4.12: Evolution of electron temperature for seeded blob in a neutral background, and subject to different in-elastic neutral interactions with molecules and atoms.

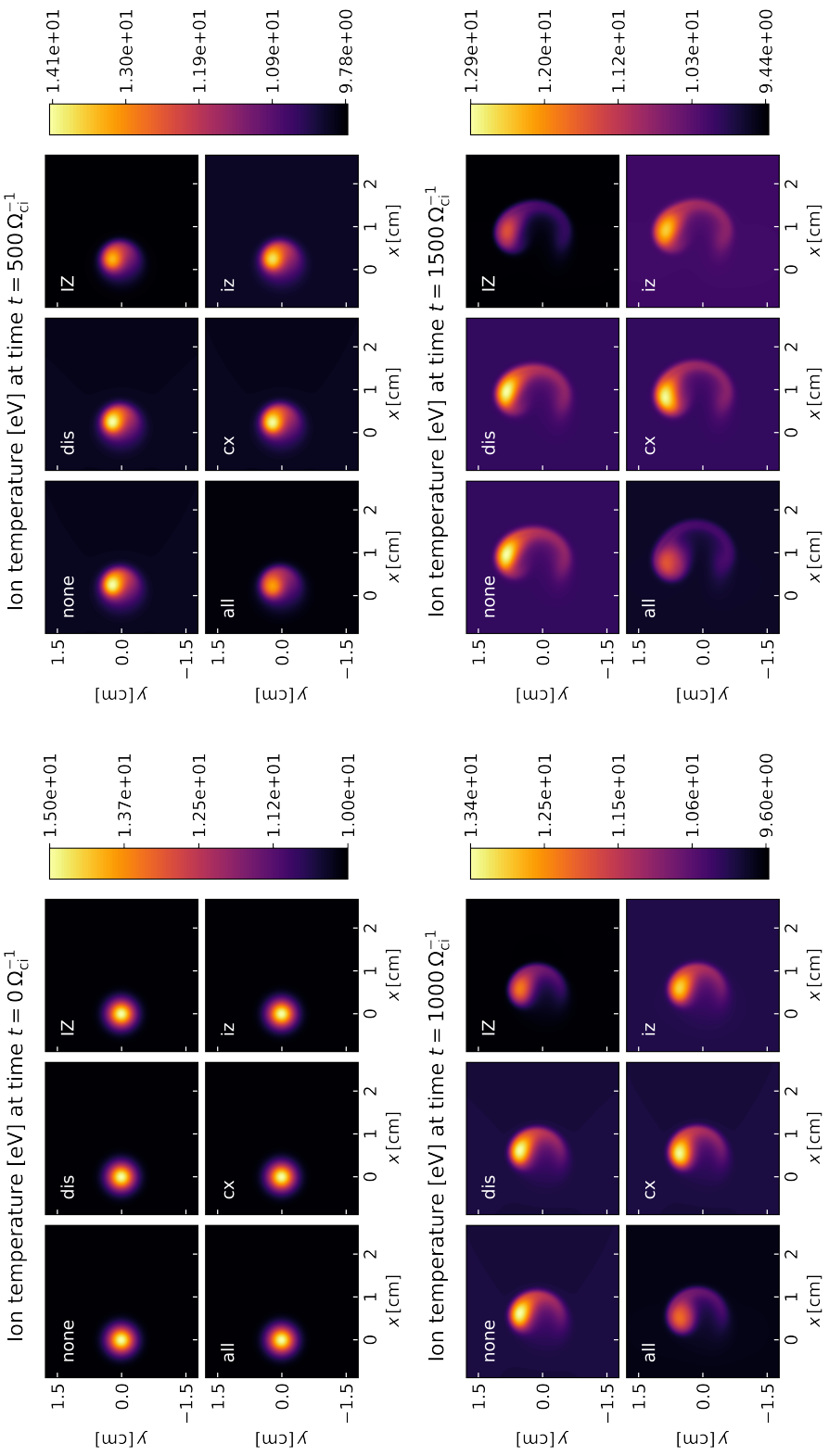

Figure 4.13: Evolution of ion temperature for seeded blob in a neutral background, and subject to different in-elastic neutral interactions with molecules and atoms.

Chapter 5

Conclusions and outlook

In Chapter 1 the trends for fossil fuel consumption and reserves are reviewed, and serves as a strong motivator for the quest for alternative base-load energy sources. Reactor-based thermonuclear fusion is promoted as a candidate for future power production, and promises a source of electric energy which is clean, safe, and sustainable. Currently most research is done on the tokamak design, where hot fusion plasma is suspended in a toroidal magnetic field. In current reactors the energy loss is larger than that required for maintaining the environment required for a high fusion reaction rate. The main particle and heat loss is by turbulent transport in the plasma edge region. Studies of the dynamics of the edge and the surrounding scrape-off layer (SOL) regions is a large field in fusion research, and analysis of experimental data, numeric simulations, and analytical models are required for mapping out the transport phenomena that prevent a large energy confinement time.

A potential player in understanding and controlling the plasma edge and SOL dynamics is neutral atoms and molecules. Neutral particles are either created in the far SOL or at the first wall, which have temperatures that allow for chemical bonds to persist, or they are injected into the vessel for diagnostic or fuelling purposes. The neutrals interact strongly with the edge and SOL plasma and affect both electron and ion densities, momenta, and temperatures, and thus the transport of the charged particles.

In Chapter 2 two models are presented. One model is for transport of plasma and one is for neutral transport, and the two are joined into the nHESEL model of plasma and neutral transport and interactions in the edge

and SOL out-board mid-plane regions of a magnetically confined plasma. The plasma model transport is described by the HESEL model, which is based on the drift-fluid approximation of the Braginskii plasma transport equations, which describe phenomena at time scales larger than the inverse ion gyro-frequency. The neutral molecules and atoms are described in a fluid-like model, which calculate electron and ion density, pressure, and drift source terms, that are self-consistently added to the HESEL equations. The neutral fluid model is derived from the kinetic equation with a closure that allows for a long mean-free path between collisions, which is the case for the neutrals in the SOL and far edge regions.

The combined nHESEL model consists of seven coupled non-linear differential equations, which are solved by numerical means. The model is implemented into the numeric BOUT++ framework, and the numerical machinery has been verified by the method of manufactured solutions as discussed in Chpt. 3.

The nHESEL model, or similar predecessors thereof, are in Chpt. 4 applied in a series of studies of plasma edge and SOL dynamics in an environment strongly influenced by neutral interactions. This has allowed studying the influence of the neutrals on the plasma fields as well as of the plasma on the neutral densities. The conclusions of the papers presented here, and additional related topics, are summarized in Sec. 5.1. In Section 5.2 near-future applications of the nHESEL model, and potential additions to the model are discussed.

5.1 Conclusions

In this section the main conclusions from Chpt. 4 are reviewed. The conclusions cover both the effect of neutrals on plasma, and the effect of plasma on the neutral densities, as well as assessments of which neutral populations are required to describe different aspects of neutral-plasma interactions.

The effect of neutrals on toroidally confined plasmas is mainly dealt with in the paper of Sec. 4.2, and in the preliminary results of Sec. 4.5. In a plasma drift-fluid model, density and momentum sources from interactions with neutrals result in next-to-leading order drift terms. Along with the additional drift terms, the plasma experiences direct density and temperature

sources from inelastic neutral interactions that influence the plasma dynamics in the edge and SOL regions. It has been observed that increasing the flux of neutrals into the system, and thus increasing the neutral density, affects the edge dynamics in the following ways. The intermittency of radial flux, as well as the magnitude of the average flux, of charged particles across the LCFS is increased. The change in flux statistics is also present in the PDFs, which broaden as the neutral density increases. Increasing neutral densities also shift the ionization profiles towards the LCFS, as the far SOL region is cooled more, and thus allows for a deeper penetration of neutrals. Besides cooling both electrons and ions in the SOL, a high neutral density increases the plasma SOL density significantly. It is speculated whether the change of edge dynamics or temperature sinks and density sources in the SOL from neutral interactions may have a bigger effect on shoulder formation and preliminary results suggest, that the effects from the latter dominates.

For the effect of plasma on the neutral particles, the densities and the ratio of different neutral species are influenced. This is reported in the papers of Secs. 4.1 and 4.3, as well as the conference paper entitled *The influence of blob intermittency on fuelling* in Sec. 4.4. The overall neutral profiles are determined by the plasma profiles, but local fluctuations in the plasma fields influence the neutral densities locally, as well as globally for the non-thermal neutral species. It is observed that the density of thermal neutrals such as molecules strongly decay in the SOL region, and it is dominantly atoms which cross the LCFS and thus fuel the plasma. Although blobs increase the local ionization, the fuelling increases following blob events, as more atoms are created from dissociation of molecules than removed due to ionization by the blob. This effect is likewise important for gas puff imaging diagnostic, as the light is emitted in a volume of perturbed neutral density, and the intensity is thus not proportional to the average neutral density.

The neutral particles exist as different species, such as molecules and atoms, and at various characteristic energies. It is found, e.g., in *The influence of hot neutrals in simulations of gas puff modulation* in Sec. 4.4 that effects of including energetic neutral atoms from charge-exchange collisions, and potentially also from Franck-Condon dissociation, is important for describing the effects of neutrals on the edge plasma, as it is only those energetic neutrals that penetrate deeper into the edge region. Likewise, the paper of Sec. 4.3 and *The influence of blob intermittency on fuelling* emphasizes the importance of including molecules if SOL dynamics are explored, as those act as strong volume sources for the atoms. In the following section further applications of the nHESEL model, and possible improvements to the model,

are discussed.

5.2 Outlook

The derivation of the nHESEL model and the application to various case studies presented here is self-contained, but further applications as well as enhancements of the model are envisaged for the future. This section summarizes the potentially fruitful near-future paths that could be followed in the use and improvement of the nHESEL model.

After applying the nHESEL model, certain shortcomings of the model have surfaced, which, if accounted for, could elevate the usability of the neutral part of the model. There are two major points from which the model would strongly benefit from more attention; the treatment of excited atomic (and molecular) states and inclusion of a neutral density source from plasma recycling at the first wall. The excited states have not been included in the initial model, as each state would require its own neutral species, and the number of coupled equations to solve would be overwhelming. One possible option to circumvent this issue could be introducing a field, which represent the average ionization energy of, e.g., atoms. By making a weighted average, with the electron temperature dependent reaction rates determining the weights, of the possible excitation states, the model could take into account the electron energy lost in excitation of neutrals, and the lower energy required to ionize excited atoms, in a statistical manner.

The wall recycling would be more straightforward to implement, as the recycling channels are already mapped out, and the numerical machinery for a finite neutral particle flux at the wall is already implemented and tested. In practice the code would monitor the flux of charged particles to the wall, and redistribute them to the neutral species, according to various recycling scenarios. Besides not being the focal point of the thesis, the main reason that this has not been done for the current code is, that the plasma density obeys Neumann boundary conditions at the wall, and the flux is thus zero. One could, however, use the particles removed, e.g., in the wall shadow region in the outermost SOL, and calculate the corresponding flux based on those values.

As for future use cases, the ones of Sec. 4.5 are the most obvious to move

forward with; both the study of the effect of neutrals on seeded blobs as well as the direct influence of ionization of neutrals on the SOL shoulder formation are concerned with how blobs react in a SOL heavily populated by neutral particles. Another topic which is currently being investigated in another project is that of supersonic molecular beam injection, where a poloidally shaped neutral molecule profile with a finite value of the advection velocity is utilized. Finally, another related topic that could be explored in the future is that regarding the influence of strong neutral fuelling on the experimentally observed H-L transition [36].

As the numerical model is implemented in the BOUT++ framework, changes to transport equations, source terms, and boundary conditions are straightforward to implement. It is our belief and intention that future projects result in enhancement and new applications of the nHESEL model, in order to further investigate the influence of neutral particles on edge dynamics of magnetically confined plasmas.

Bibliography

[1] *BP Statistical Review of World Energy 2017.* [online] London: BP Statistical Review of World Energy. Available at: https://www.bp.com/statisticalreview [Accessed March 2018].

[2] *Climate Change 2014: Synthesis Report.* Contribution of Working Groups I, II and III to the Fifth Assessment Report of the Intergovernmental Panel on Climate Change [Core Writing Team, R.K. Pachauri and L.A. Meyer (eds.)]. IPCC, Geneva, Switzerland, 151 pp.

[3] M.V. Ramana, Bulletin of the Atomic Scientists **67**, 4 (2015)

[4] Marques, J. G. (2011). Review of Generation-III/III+ Fission Reactors. In Nuclear Energy Encyclopedia (eds S. B. Krivit, J. H. Lehr and T. B. Kingery).

[5] G. Locatelli, et al., Energy Policy **61**, (2013), 1503–1520

[6] G. Audi, et al., Nuclear Physics **A729**, 337–676 (2003)

[7] H.A. Bethe, Phys. Rev. **55**, 436–456 (1939)

[8] P. Batistoni, et al., 2012, Nucl. Fusion **52** 083014

[9] N.J. Peacock, et al., Nature Vol. **224**, November 1, 1969

[10] Available at: https://www.euro-fusion.org/2011/09/tokamak-principle-2/ [Accessed March 2018]

[11] M. Keilhacker, et al., 1982 Phys. Scr. **1982** 443

[12] M. Kikuchi, et al., Fusion physics, Vienna : International Atomic Energy Agency, 2012.

[13] J.D. Lawson, "Some Criteria for a Useful Thermonuclear Reactor", Atomic Energy Research Establishment, 1955 Culham Report No: A.E.R.E. GP/R – 1807.

[14] A.A. Harms, et al., Principles of Fusion Energy, World Scientific Publications, ISBN 978-981-238-033-3.

[15] M. Greenwald, et al., 1988, Nucl. Fusion **28** 2199

[16] F. Wagner, et al., Phys. Rev. Lett. **49**, 1408 (1982)

[17] S.J. Zweben, et al., 2007, Plasma Phys. Control. Fusion **49** S1

[18] B. LaBombard, Physics of Plasmas **9**, 1300 (2002)

[19] E. Mazzucato, Phys. Rev. Lett. **36**, 792 (1976)

[20] H.J. Hartfuss, et al., 1997, Plasma Phys. Control. Fusion **39** 169

[21] A. Huber, et al., 1999, J. Nucl. Mater. **266–269** 546

[22] S. Zoletnik, et al., Rev. Sci. Instrum. **76** 073504 (2005)

[23] S.J. Zweben, et al., Rev. Sci. Instrum. **88**, 041101 (2017)

[24] D.A. D'Ippolito, et al., Physics of Plasmas 9, 222 (2002)

[25] D.A. D'Ippolito, et al., Physics of Plasmas **18**, 060501 (2011)

[26] J.R. Myra, et al., 2013, Nucl. Fusion **53** 073013

[27] P.M. Bellan, (2006). *Fundamentals of Plasma Physics*, Cambridge: University Press. ISBN-13: 978-0-521-82116-2.

[28] R. Fitzpatrick (2015). *Plasma Physics: An Introduction*, Boca Raton: CRC Press. ISBN-13: 978-1-4665-9427-2

[29] Y. Lianghua, et al., 2010, Plasma Sci. Technol. **12** 529

[30] C.A. Foster, et al., 1977, Nucl. Fusion **17** 1067

[31] J.D. Hey, et al., J. Phys. B: At. Mol. Opt. Phys. **37**, 2543-2567 (2004)

[32] J.D. Hey, et al., J. Phys. B: At. Mol. Opt. Phys. **38**, 3517-3534 (2005)

[33] G.F. Matthews, 1995, J. Nucl. Mater. **220-222** 104-116

[34] S.I. Krasheninnikov, et al., Physics of Plasmas **23**, 055602 (2016)

[35] D. Carralero, et al., Nuclear Materials and Energy **12**, 1189 (2017)

[36] M. Bernert, et al., 2015, Plasma Phys. Control. Fusion **57**, 014038

[37] J. Madsen, et al., Physics of Plasmas, **23**, 032306 (2016)

[38] A.H. Nielsen, et al., 2017, Plasma Phys. Control. Fusion **59**, 025012

[39] R. Schneider, et al., Contrib. Plasma Phys. **46**, No. 1-2, 3 - 191 (2006)

[40] T.D. Rognlien, et al., 1992, J. Nucl. Mater. **196-198** 347-351

[41] G.J. Radford, et al., (1996), Contrib. Plasma Phys., **36**: 187-191

[42] P. Tamain, et al., Journal of Computational Physics **229** (2010) 361–378

[43] B.D. Dudson and J. Leddy, 2017, Plasma Phys. Control. Fusion, **59** 054010

[44] P. Ricci, et al., 2012, Plasma Phys. Control. Fusion **54** 124047

[45] S.I. Braginskii, Rev. Plasma Phys. **1**, 205 (1965)

[46] S.H. Müller, et al., 2009, Plasma Phys. Control. Fusion **51** 105014

[47] E.T. Meier and U. Shumlak, Physics of Plasmas **19**, 072508 (2012)

[48] S. Chapman and T.G. Cowling, 1953, *The Mathematical Theory of Non-uniform Gases*, Cambridge. ISBN-13: 978-0-5214-0844-8

[49] R.J Goldston and P.H Rutherford (1995). *Introduction to Plasma Physics*, IoP Publishing Bristol and Philadelphia. ISBN-13: 978-0-7503-0183-1

[50] H.L. Pauls, et al., J. Geophys. Res. **100**, 21595 (1995)

[51] F.L. Hinton and C.W. Horton Jr., The Physics of Fluids, **14**, 116 (1971)

[52] A. Zeiler, et al., Physics of Plasmas, **4**, 2134 (1997)

[53] W. Baumjohann and R. Treumann, (1997),*Basic Space Plasma Physics.* Imperial College Press

[54] M.L. Magnussen, et al., (2017). *Global numerical modeling of magnetized plasma in a linear device.* Department of Physics, Technical University of Denmark.

[55] O.E. Garcia, et al., Physics of Plasmas **12**, 62309 (2005)

[56] A. I. Smolyakov, Can. J. Phys. **76**, 321 (1998)

[57] D.J. Tritton, (1988). *Physical Fluid Dynamics*. Oxford University Press. ISBN-13: 978-0-19-854493-7

[58] F.L. Hinton and R.D. Hazeltine, Rev. Mod. Phys. **48**, 239 (1976)

[59] L. Spitzer and R. Härm, Phys. Rev. 89, 977 (1953)

[60] P.C. Stangeby, (2000), *The Plasma Boundary of Magnetic Fusion Devices*, IoP Publishing Bristol and Philadelphia. ISBN-13: 978-0-7503-0559-4

[61] D. Reiter, et al., Fusion Science and Technology, **47**, 172 (2005)

[62] B. LaBombard, (2001). MIT Plasma Science and Fusion Center

[63] D. Stotler and C. Karney, (1994), Contrib. Plasma Phys., **34**: 392-397

[64] C. Wersal and P. Ricci, 2015, Nucl. Fusion **56**, 123014

[65] E.L. Vold, et al., 1990, J. Nucl. Mater., **176-177**, 570

[66] D. Schwörer, et al., Nuclear Materials and Energy **12**, 825 (2017)

[67] P. Helander, et al., Physics of Plasmas **1**, 3174 (1994)

[68] Y.L. Zhou, et al., Physics of Plasmas **22**, 012503 (2015)

[69] Z.H. Wang, et al., 2014, Nucl. Fusion **54** 043019

[70] D.A. Knoll and P.R. McHugh, Physics of Plasmas **3**, 293 (1996)

[71] M. Rensink, et al., Contributions to Plasma Physics, **38**(1-2):325–330, 1998

[72] R.K. Janev, et al., (1987). *Elementary Processes in Hydrogen-Helium Plasmas*, Berlin: Springer-Verlag

[73] S.A. Astashkevich and B.P. Lavrov, Journal of Physical and Chemical Reference Data **44**, 023105 (2015)

[74] Ya.F. Verolanen and A.Ya. Nikolaich 1982 Sov. Phys. Usp. **25** 431

[75] E.U. Condon, 1928, Phys. Rev. **32** 858–72

[76] G. Herzberg and A. Monfils, Journal of Molecular Spectroscopy, **5**, 482-498 (1960)

[77] J. Liu, et al., The Journal of Chemical Physics **130**, 174306, (2009)

[78] G.M. McCracken and P.E. Stott, 1979, Nucl. Fusion **19** 889

[79] Ph. Mertens, et al., 2001, Plasma Phys. Control. Fusion **43** A349

[80] U. Samm and the TEXTOR-94 Team, 1999, Plasma Phys. Control. Fusion **41** B57

[81] R.D. Hazeltine, Physics of Plasmas **5**, 3282 (1998)

[82] J.R. Albritton, et al., Phys. Rev. Lett. **57**,1887 (1986)

[83] S. I. Krasheninnikov, Phys. Fluids **B 5**, 74 (1993)

[84] P L. Bhatnagar, et al., Phys. Rev. **94**, 511 (1954)

[85] B.D. Dudson, et al., Computer Physics Communications **180**, 1467 (2009)

[86] A. Arakawa, Journal of Computational Physics **135**, 103–114 (1997)

[87] G.D. Byrne and A.C. Hindmarsh, The International Journal of High Performance Computing Applications, **13**, 4, 354-365, (1999)

[88] W. Oberkampf and C. Roy, (2010). *Verification and Validation in Scientific Computing*, Cambridge University Press

[89] K. Salari and P. Knupp, (2000). *Code Verification by the Method of Manufactured Solutions*, SAND2000-1444. Albuquerque: Sandia National Laboratories

[90] B.D. Dudson, et al., Physics of Plasmas **23**, 062303 (2016)

[91] O.E. Garcia, et al., 2006, Plasma Phys. Control. Fusion **48** L1

[92] W. Fundamenski, et al., 2007, Nucl. Fusion **47** 417

[93] F. Militello, et al., 2013, Plasma Phys. Control. Fusion **55** 025005

[94] N. Yan, et al., 2013, Plasma Phys. Control. Fusion **55** 11500

[95] Lingyan Xiang, private communication, DTU 2018

[96] A.S. Thrysøe, et al., 2016, Plasma Phys. Control. Fusion, **58**, 044010

[97] A.S. Thrysøe, et al., Physics of Plasmas **25**, 032307 (2018)

[98] E. de la Cal and The TJ-II Team, 2016, Nucl. Fusion, **56**, 106031

[99] B. LaBombard, et al., Physics of Plasmas **8**, 2107 (2001)

[100] D.L. Rudakov, et al., 2005, Nucl. Fusion **45** 1589

[101] D. Carralero, et al., 2015, J. Nucl. Mater. **123-127**, 463

[102] O.E. Garcia, et al., Physics of Plasmas **12**, 090701 (2005)

[103] P. Manz, et al., Physics of Plasmas **20**, 102307 (2013)

[104] J. Olsen, et al., 2016, Plasma Phys. Control. Fusion **58** 044011